HIGH SPIN STATES IN THE TRANSITIONAL NUCLEI $^{116,117,118,119}Te$

by

Daniel Conley

A thesis submitted for the degree of
Doctor of Philosophy
at the Australian National University

Canberra, February 1982

PREFACE

This thesis describes work done at the Department of Nuclear Physics, The Australian National University, using beams of carbon ions provided by the University's 14UD Pelletron accelerator.

The project was suggested by Professor J.O. Newton and Dr. R.M. Diamond. I was assisted in the collection of experimental data during the course of the project by Professors J.O. Newton and H. Evans, Drs. R.M. Diamond, W. Galster and S. Sie, and Mr. D. Hinde.

The data analysis was performed by myself, using existing tape sorting programs. Some least squares fitting programs were written by myself. The computer program to calculate level energies in the triaxial rotor plus particle model was provided by Professor Meyer-ter-Vehn. Modifications to this and other programs were performed by myself.

The interpretation of the data was, apart from helpful comments by Professor J.O. Newton, performed by myself.

No part of this thesis has been submitted for a degree at any other University.

Daniel Conley.

Daniel Conley

ACKNOWLEDGEMENTS

I would like to thank Professor J.O. Newton for providing the opportunity for me to work in this laboratory during the last four years. I would also like to thank him for his supervision, assistance and support throughout the course of this project.

Many thanks also go to Dr. S. Sie for his valuable assistance and comments on all phases of the work. Thanks also go to Professor R.M. Diamond, Professor H. Evans, Dr. W. Galster, and Mr. D. Hinde for their assistance, at various stages, in the collection of the data. Thanks also go to Dr. G. Dracoulis for his comments on an early draft of this thesis.

I am grateful to Dr. I.G. Graham for his assistance in the computing field, to the technical staff for their maintenance of the 14UD accelerator; to Mr. G. Clarkson and Mr. G. Gilmour for their assistance with the photography and to Ms N. Chin for her skilful typing of this thesis.

I would also like to acknowledge the financial assistance of an A.N.U. post-graduate scholarship, for which I am most thankful.

Finally, I would like to thank my wife, Karen, for her invaluable support during the course of this work.

CONTENTS

ABSTRACT

High spin states in the transitional nuclei $^{116,117,118,119}Te$ have been populated using (^{13}C,4n) and (^{13}C,5n) reactions on Palladium targets. States were identified up to excitation energies of approximately 8 MeV and to a maximum spin of $I = 41/2$ (in ^{119}Te).

The even mass nuclei were found to be easily deformed, being neither good rotors nor good vibrators. In ^{119}Te and ^{117}Te bands based on the $1h_{11/2}$ and $1g_{7/2}$ neutron Nilsson orbitals were well described by a triaxial rotor plus particle model. The model also gave an estimate of the deformation of the core induced by extra neutron.

Quasiparticle configurations were assigned to many of the high spin states on the basis of level energy systematics. Two main influences, that of the lowering of the $1h_{11/2}$ orbital excitation and that of the relative lowering in the energy of two quasiproton excitations as the Tellurium mass increased, were recognised.

CHAPTER 1

INTRODUCTION

1.1 INTRODUCTION — AND NUCLEAR SHAPES

Much of the effort in Nuclear Physics is directed at understanding the structure of the nucleus, and, through this knowledge, attempting to determine the nature of nuclear forces. Reaching this goal is difficult, as the very small size of the nucleus, approximately 10^{-12} cm, makes data collection difficult. Indirect experiments are necessary for the obtaining of any information; also, as a nucleus is a finite many-body system, its mathematical description is highly complex.

However, the desire for progress resulted in a series of mathematical models being produced, each of which attempted to reduce the structural description of a nucleus to simply grasped concepts. Those models deemed "successful" were able to both describe previously observed phenomena and also predict new results — although gross failure was sometimes as informative. The following section will briefly introduce three of these "successful" models and it will be upon these (extreme) examples that the majority of later discussion will be based.

In their attempts at describing the nuclear structure, these models will, at times, need to refer to the shape of the nucleus. Even this is a concept which must be simplified in order for its meaning to be grasped. It is relevant then, to review the procedure and nomenclature for describing nuclear shapes, before discussing nuclear models.

Generally, when speaking of a nucleus' shape we describe a surface, representing some equipotential, which can then be described in a fashion similar to that used for classical bodies. Such a surface can be represented by defining the radius vector, using spherical co-ordinates as,

$$R = R_0\left[1 + \sum_{\mu,\lambda} a_{\lambda\mu} Y_\lambda^\mu(\theta,\phi)\right] , \quad \left\{ \begin{array}{l} \lambda = 0,1,2,\ldots \\ \mu = -\lambda,-\lambda+1,\ldots,+\lambda \end{array} \right\} , \qquad (1)$$

where the Y_λ^μ are Spherical Harmonic Functions, and the $a_{\lambda\mu}$ are the parameters which describe the shape with respect to axes fixed in space. Some common terms which are used in describing deformation parameters of differing λ value are:

$$\lambda = 2 \Rightarrow \text{Quadrupole}$$

$$\lambda = 3 \Rightarrow \text{Octupole}$$

$$\lambda = 4 \Rightarrow \text{Hexadecapole} .$$

However, if a nucleus rotates, the $a_{\lambda\mu}$ will change in time, even though we would not say that the "shape" is changing. To circumvent this somewhat unwanted feature, the deformations are usually defined relative to *body-fixed axes*. By using symmetry conditions, the *quadrupole* parameters can then be written as,

$$\begin{aligned} a_{21} &= a_{2-1} = 0 \\ a_{22} &= a_{2-2} = \frac{1}{\sqrt{2}}\,\beta\,\mathrm{Sin}\gamma \qquad (2) \\ \text{and} \quad a_{20} &= \beta\,\mathrm{Cos}\gamma . \end{aligned}$$

Here, β and γ are introduced as variables having more easily grasped physical significance than the $a_{\lambda\mu}$; for it can be shown (using Eqn (1)), that

$$\beta^2 = \sum a_{2\mu}^2 \qquad (3)$$

and is therefore a measure of the total deformation of the nucleus. The quantity γ, on the other hand, is a measure of the degree of *axial* asymmetry of the nucleus, which can be seen from the expression representing the principal axes, written as (from Eqns (1) and (2)),

$$R_\kappa = R_0 + \sqrt{\frac{5}{4\pi}}\,R_0\,\beta\,\mathrm{Cos}\left(\gamma - \kappa\,\frac{2\pi}{3}\right) , \qquad \kappa = 1,2,3 , \qquad (4)$$

where κ denotes a body axis.

Thus if $\gamma = 0$, $2\pi/3$ or $4\pi/3$, the nucleus is a prolate spheroid, whereas if $\gamma = \pi$, $\pi/3$, or $5\pi/3$, it is an oblate spheroid.

Of course, there are other ways of defining shape. Although we will not go into the details of their origins here, the following are some common measures of axially symmetric deformations.†

Degree	Term	Relation
Quadrupole	δ	$\approx .95\ \beta$
Quadrupole	ε (or ε_2)	$\approx \delta + \frac{1}{6}\delta^2 + 0(\delta^3)$
Hexadecapole	ε_4	

1.2 INDEPENDENT PARTICLE MODEL

This model, first proposed in the 1930's [E134], assumes that all the nuclear particles move independently of each other, subject only to an *average* nuclear potential. This is similar, in concept, to the movement of electrons in atomic physics. The fundamental difference is that, in Atomic Physics, there is a well defined "centre", or "source", of the potential, whereas in Nuclear Physics, there is not. However, one could expect some features to occur in the nuclear system, which have an analogue in the atomic system.

One such feature, which is observed in both systems, is "shell structure". That is, states are grouped in energy, with (relatively) large energy differences between adjacent groups of states. (Each group is termed a "shell"). This is supported by the observation that many nuclear properties, e.g. the quadrupole distortion shown in Fig. 1.1 (from [Se64]), exhibit discontinuities at certain neutron or proton numbers. These "Magic Numbers" represent the filling of various shells, and differ from the corresponding numbers of the atomic system. The nuclear Magic Numbers are 2, 8, 20, 28, 50, 82, and 126.

Naturally, nuclear potentials used in calculations of nuclear level energies are restricted by the calculation's ability to

† These are generally used in single particle energy calculations. The definitions are chosen to ease calculations.

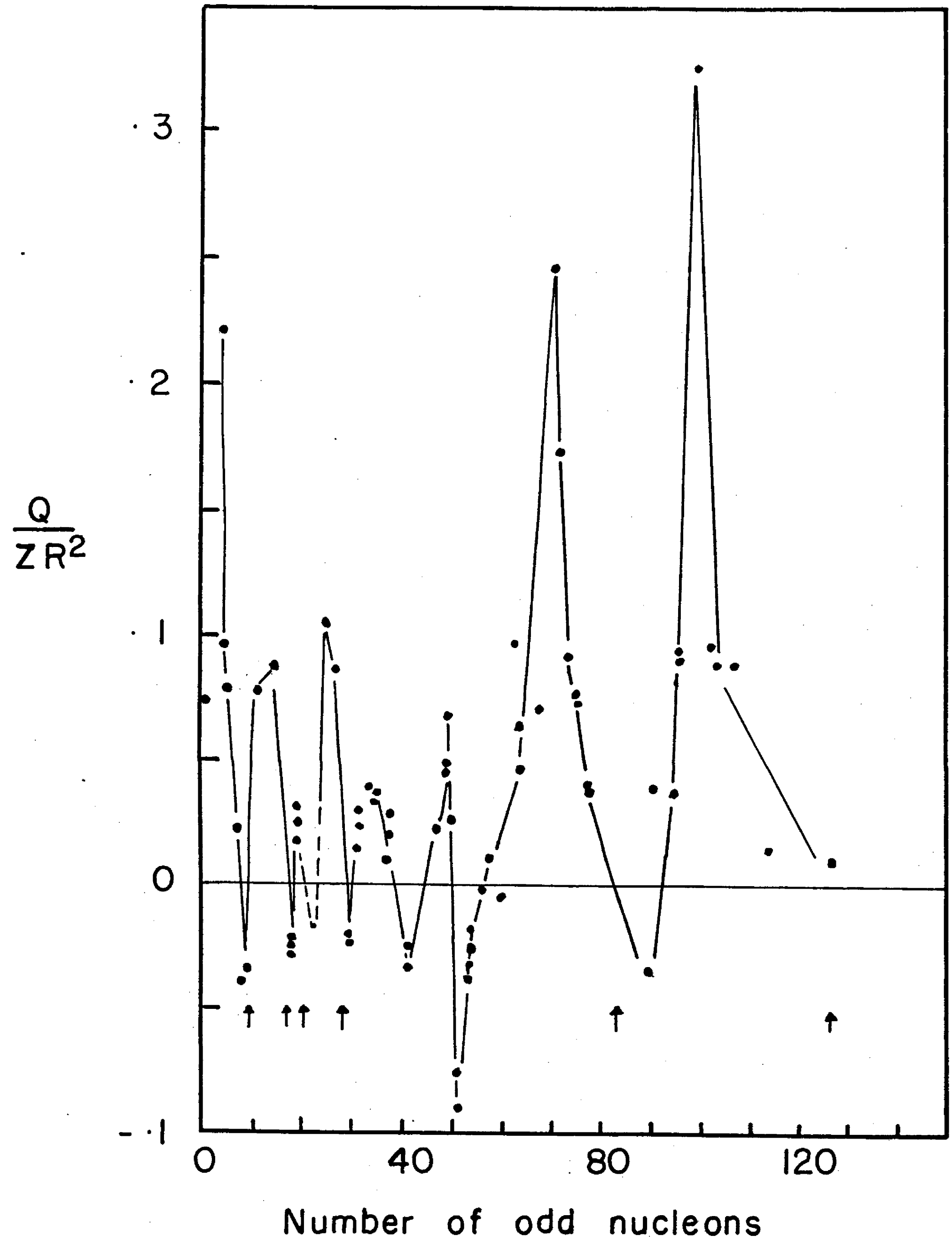

Fig. 1.1: Quadrupole distortion Q/ZR^2 ($\approx \Delta R/R$) for odd-A nuclei versus the odd nucleon number, Z or N.

reproduce the Magic Numbers. Figure 1.2 shows the level orderings predicted by the use of various potentials, ranging from the simple Harmonic Oscillator, to more complex examples. Although shell structure is seen in all the schemes in Fig. 1.2, only the example on the right of the figure is capable of reproducing the correct Magic Numbers.

This, and similarly successful potentials have two distinctive features: one, they approximately map the mass distribution of the nucleus [as with the "square well with rounded edges", or the "Woods-Saxon" potential], and two, they incorporate a potential dependant upon the coupling of the intrinsic and orbital angular momentum (Spin-Orbit coupling), as first suggested by Mayer, in 1949 [Ma49]. The use of such potentials in the Independent Particle Model (I.P.M.) is also highly successful in predicting other nuclear features, including ground state spins throughout most of the Periodic Table.

The model, though, is not omnipotent. Calculations (based on the I.P.M.) of the rates at which transitions occur between the ground state, and the first excited 2^+ state of even nuclei are a spectacular failure — the model assumes that only a single nucleon is involved in a transition. This failure can be seen in Fig. 1.3, where the *ratio* of the observed rate to the calculated rate is plotted against nuclear mass. If the model were successful, the ratio would equal 1 for all masses. The ratio, though, reaches values in excess of 200, indicating that many particles are involved in the transition. Such action suggests a form of *collective* nuclear motion, which will be discussed further in the next two models.

Also, there exists a short-range interaction between particles (see e.g. [Ed52]). This force, which tends to pair particles, destroys the assumption, required by the I.P.M., of independent particles. The mathematical simplicity of the model can be regained, though, by introducing the concept of "quasiparticles".

Quasiparticles are generalised Fermions which are partly particles and partly holes. They arise from the pairing force altering the probability with which an orbital is occupied. This is illustrated in Fig. 1.4 where, on the top, is shown the probability of orbital occupation in the I.P.M. Note that the nucleus is, here,

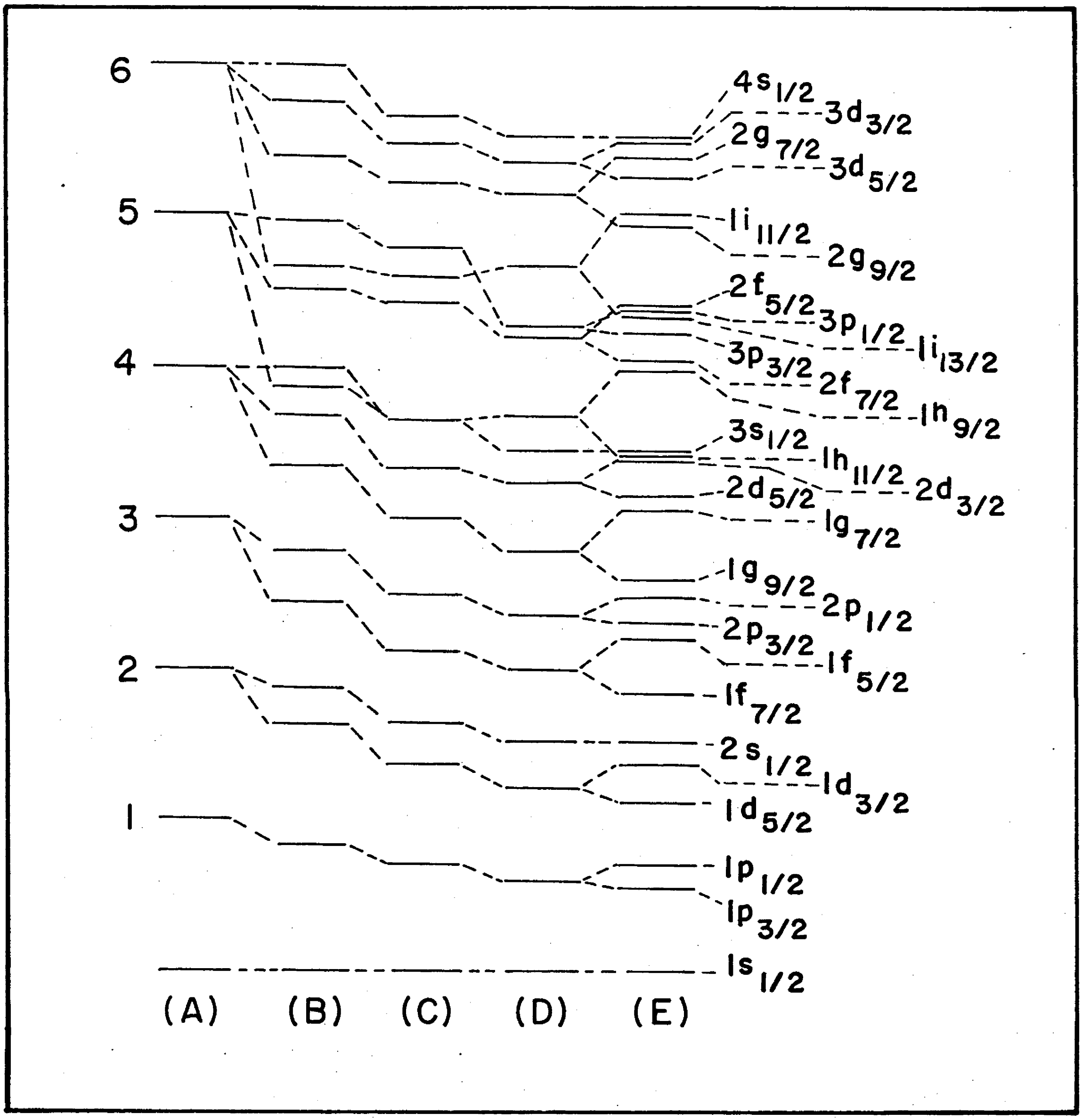

Fig. 1.2: Order of energy levels according to the independent particle model with the potentials (A) Harmonic Oscillator, (B) Infinite Square Well, (C) Finite Square Well, (D) Square Well with "Rounded Edges", (E) Potential (D) Plus Spin-Orbit Coupling.

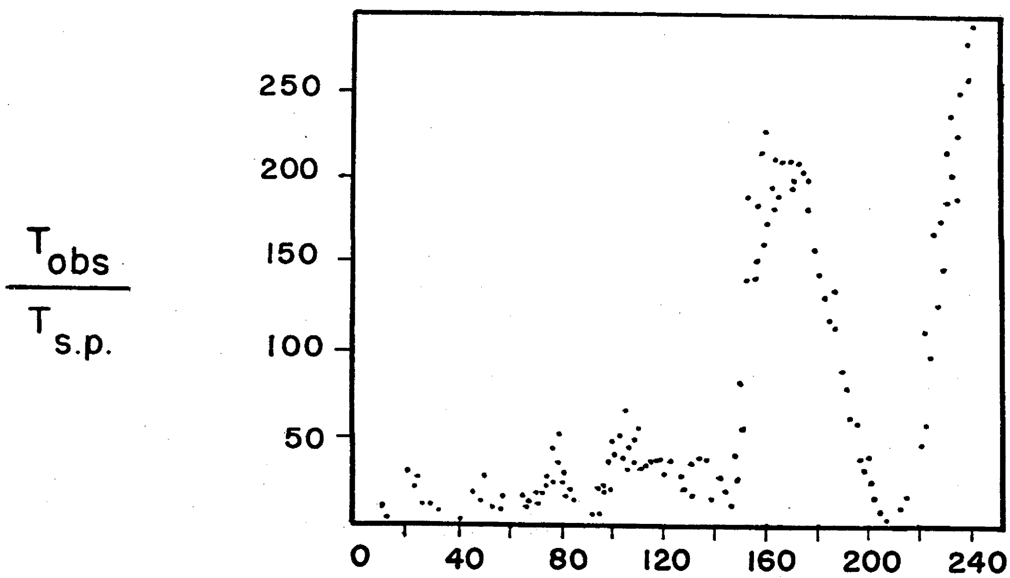

Fig. 1.3: The observed transition probability for the excitation of the first 2^+ state in even-even nuclei (in units of the single proton estimate for the same transition) versus mass number.

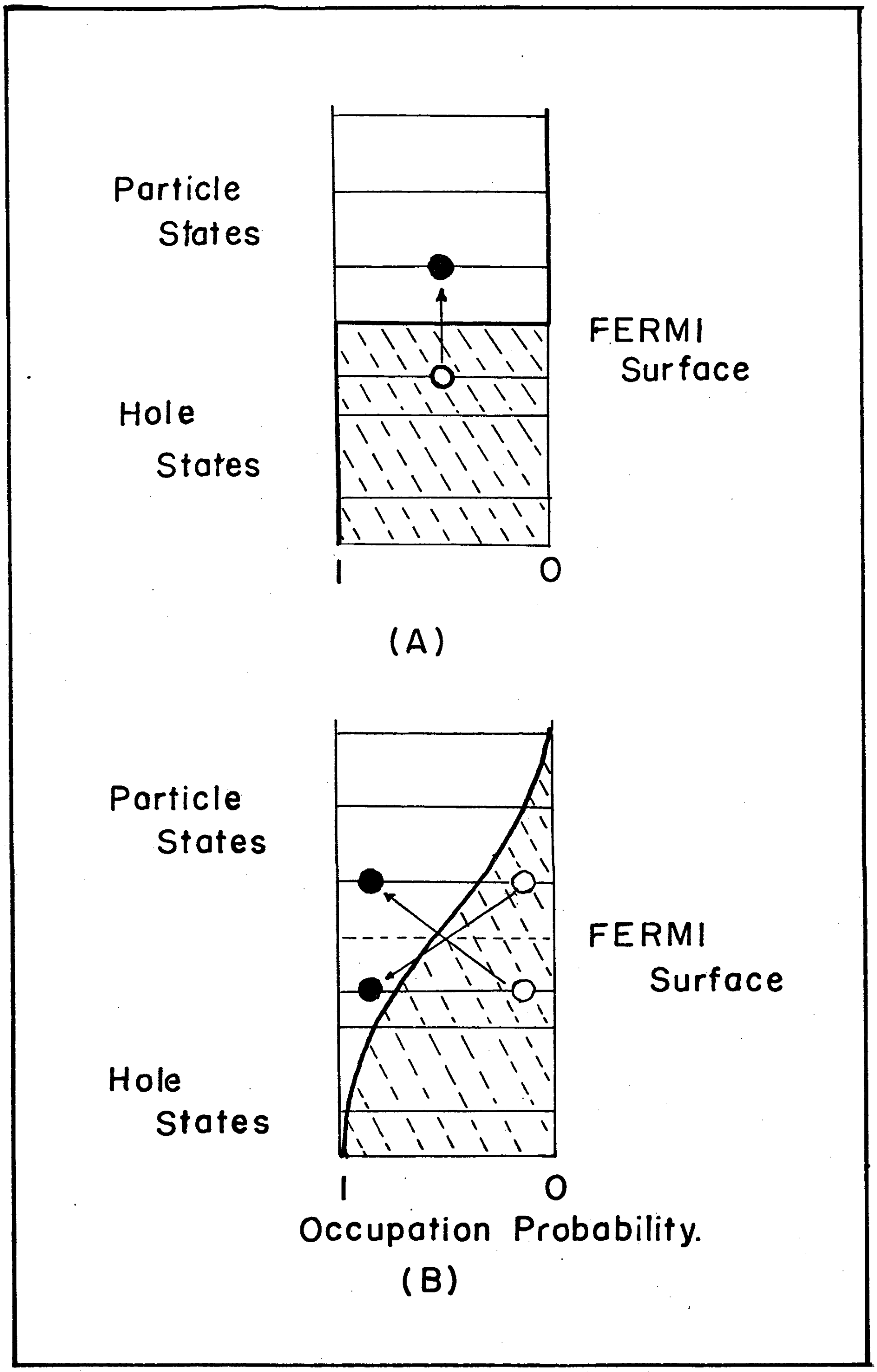

Fig. 1.4: Occupation probabilities of single particle orbitals (A) in the Independent Particle Model, (B) with the inclusion of short-range pairing forces. The arrows indicate possible excitations of the nucleus induced by the transfer of a particle.

completely filled up to a certain point; the point being determined by the number of nucleons present. This is termed the Fermi level (λ_F). The probability of orbital occupation under the influence of pairing forces is shown on the bottom in Fig. 1.4. The Fermi level is now the level at which the probability of orbital occupancy is equal to 0.5.

The energy of a quasiparticle is found from the single particle energies, as

$$E_\nu = [(\varepsilon_\nu - \lambda_F)^2 + \Delta^2]^{\frac{1}{2}}, \tag{5}$$

where ε_ν is the single particle energy ignoring the pairing force, λ_F is the energy of the Fermi level, and Δ is the pairing energy, which, apart from local deviations, can be well described by the relation,

$$\Delta = 12A^{-\frac{1}{2}}. \tag{6}$$

This holds for both protons and neutrons and is illustrated in Fig. 1.5.

The model, which has now become an "Independent Quasiparticle Model", can now be used to predict some broad features of nuclear behaviour.

Firstly, we can consider the energy of quasiparticle excitations. Using Eqn (5), we see that the energy of states of even nuclei with two quasiparticles excited is of order 2Δ — typically two to three MeV for $A \approx 120$. In contrast, an odd mass nucleus can have excited states at low energy. In these nuclei, one is concerned with the *difference* in energy between two orbitals (ν_1 and ν_2 say). Thus the excitation energy of a single quasiparticle state can be approximated by

$$[E_{\nu_2} - E_{\nu_1}] \approx (\varepsilon_{\nu_2} - \varepsilon_{\nu_1}) \times \left(\frac{(\varepsilon_{\nu_2} + \varepsilon_{\nu_1} - 2\lambda_F)}{2\Delta}\right); \quad \text{if } (\varepsilon_\nu - \lambda_F) << \Delta . \tag{7}$$

Three quasiparticle states will then have excitation energies approximately equal to the sum of this (Eqn (7)) energy and the energy for breaking a pair ($\sim 2\Delta$).

Secondly, we can consider the shape of a nucleus. As we saw in Fig. 1.1, the shape of a closed shell nucleus is spherical. The addition of a particle to such a nucleus will generate a non-spherical

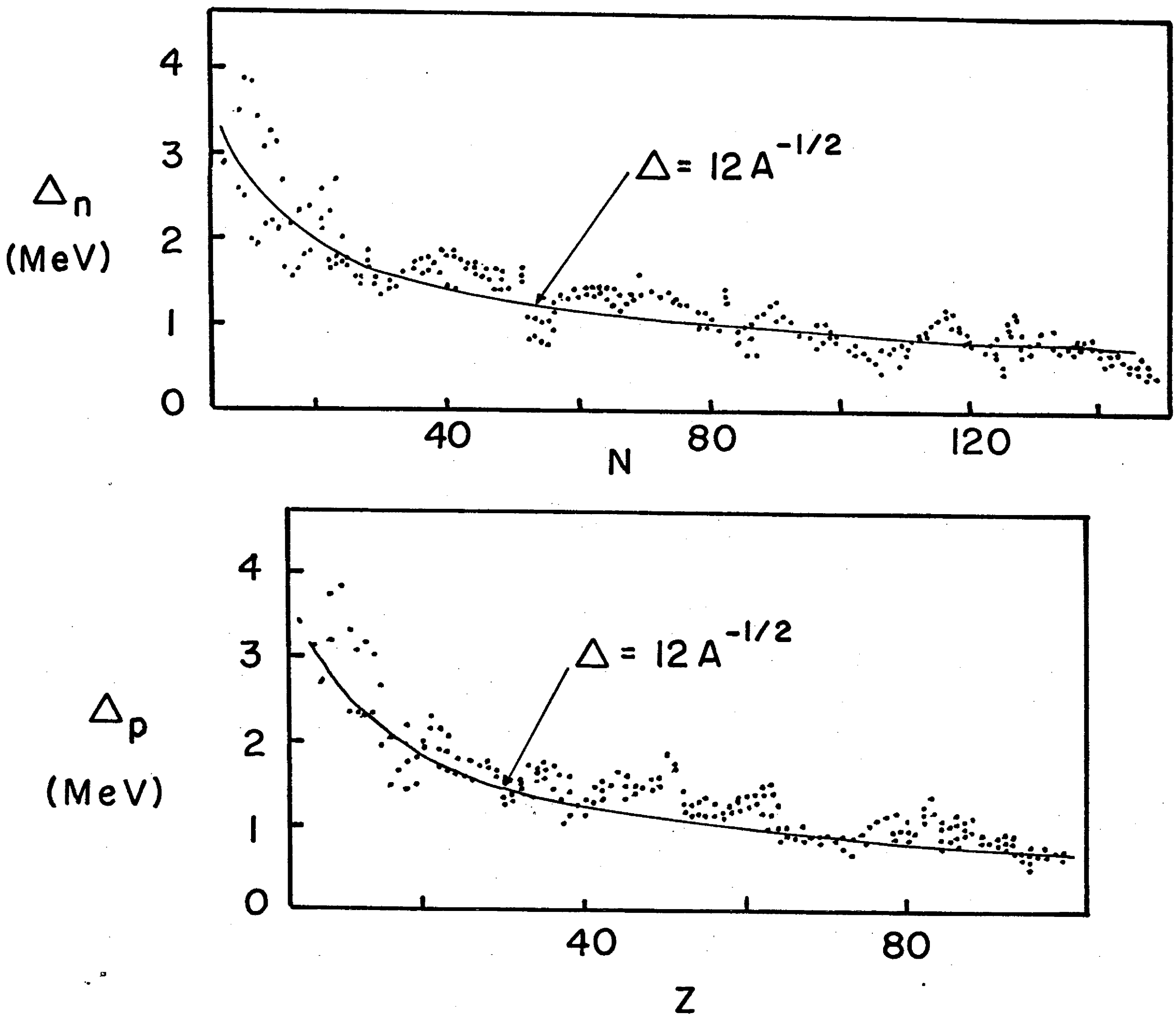

Fig. 1.5: Odd-even mass differences for neutrons and protons.

density distribution and hence, a non-spherical potential. Additional particles will then tend to align their orbital planes with the first, or rather, as much as they are allowed to by the Pauli Principle. The pairing force, though, opposes this deforming action, so that near magic nuclei are still spherically distributed.

We have then, in addition to the regions of magic nuclei in which the pairing force dominates (giving spherical nuclei), and nuclei in the middle of shells where deformation is well defined, a third region in which the two effects almost cancel — Transitional nuclei. This last region could be expected to be spherical, yet easily deformed by perturbing interactions.

Knowing, broadly, the energy of quasiparticle states, we will now turn to the *collective* excitation levels of, first, vibrational, and then, rotational, nature.

1.3 COLLECTIVE VIBRATIONAL MODEL

Excited states caused by vibrational motion occur when the nucleus, as a whole, oscillates. Many particles are therefore involved. Using the nomenclature of §1.1, there exists a band of vibrationally excited states for each deformation degree λ. The energy of these vibrational states is given by

$$E_{vib} = n\hbar\omega_\lambda \, , \tag{8}$$

where ω_λ is the frequency of vibration of the λ-mode, and n is the number of oscillator quanta involved.

As the oscillator quanta (phonons) are identical bosons, they can only couple such that the combination is symmetric about the principal axes. If we consider only quadrupole ($\lambda = 2$) vibrations, then a one phonon state has spin 2, whereas two phonons can couple to give states of $J^\pi = 0^+$, 2^+, and 4^+. (Sometimes called two phonon states.) The degeneracy of this triplet of states is usually split by anharmonic effects, but, when they are observed, they are found to cluster about an energy of $2\hbar\omega_2$. An example of this can be seen in Fig. 1.6, where the partial level scheme of ^{106}Pd, a "good" vibrator, is shown.

Another feature of the vibrational model can also be seen in Fig.

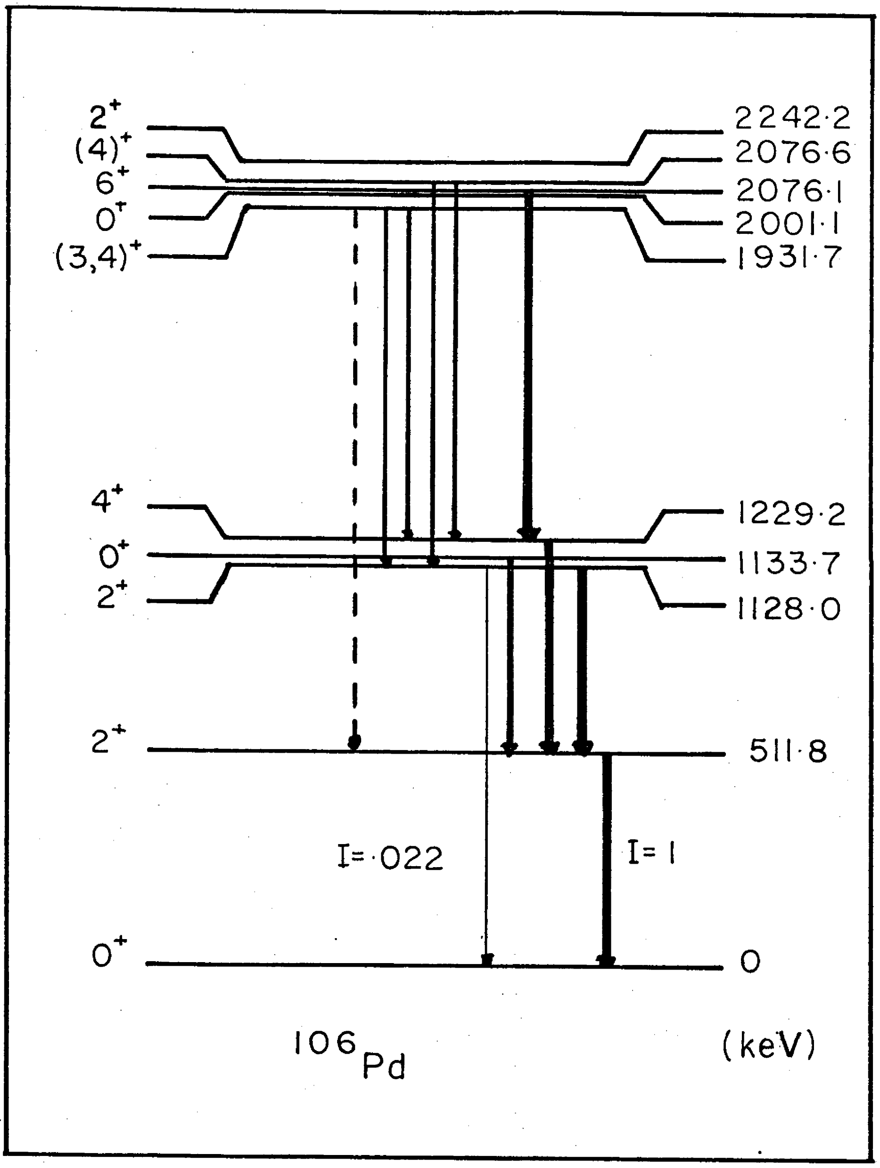

Fig. 1.6: Partial level scheme of a "good" vibrator — ^{106}Pd [Le79].

1.6. There, the $2_2^+ \rightarrow 0_1^+$ transition is very weak, when compared to the $4_1^+ \rightarrow 2_1^+$ or $2_1^+ \rightarrow 0_1^+$ transitions. This is in line with the model prediction of allowed transitions involving a change of phonon number by one, only. (The $2_2^+ \rightarrow 0_1^+$ transition involves a transition from a two phonon state to a zero phonon state and therefore should not occur according to the simple vibrational model.)

It is interesting to note that as the deformation of a uniformly charged fluid by vibration does not produce a magnetic moment, then no magnetic transitions should occur.

1.4 COLLECTIVE ROTATIONAL MODEL

Rotational motion in macroscopic bodies is an easily understood concept. However, the small size and particle nature of nuclei are the cause of some interesting effects. To start with, we will assume that the nuclear shape rotates so slowly that individual nucleons can follow the motion adiabatically, i.e.

$$\omega_{rot} << \omega_{intrinsic} \, .$$

This allows the rotation to be described independently of the particle motion.

Now quantum mechanics forbids rotation about any symmetry axis, hence any rotating nuclei *must* be deformed. A further consequence is that nuclei with an axis of symmetry (prolate or oblate) can only rotate about axes perpendicular to the symmetry axis.

If we consider an axially symmetric nucleus, of which the z axis is the axis of symmetry, then the angular momenta couple according to the sketch of Fig. 1.7, and the rotational Hamiltonian is

$$H_{rot} = \frac{\hbar^2}{2\mathcal{I}_0} (R_x^2 + R_y^2) \, , \tag{9}$$

where $\mathcal{I}_0$ is the moment-of-inertia. Because $\underset{\sim}{I} = \underset{\sim}{j} + \underset{\sim}{R}$, Eqn (9) becomes

$$H_{rot} = \frac{\hbar^2}{2\mathcal{I}_0} (I^2 + j^2 - 2\underset{\sim}{I}.\underset{\sim}{j}) \, . \tag{10}$$

For the ground state of an even mass nucleus, this results in a level spectrum whose energies are determined by

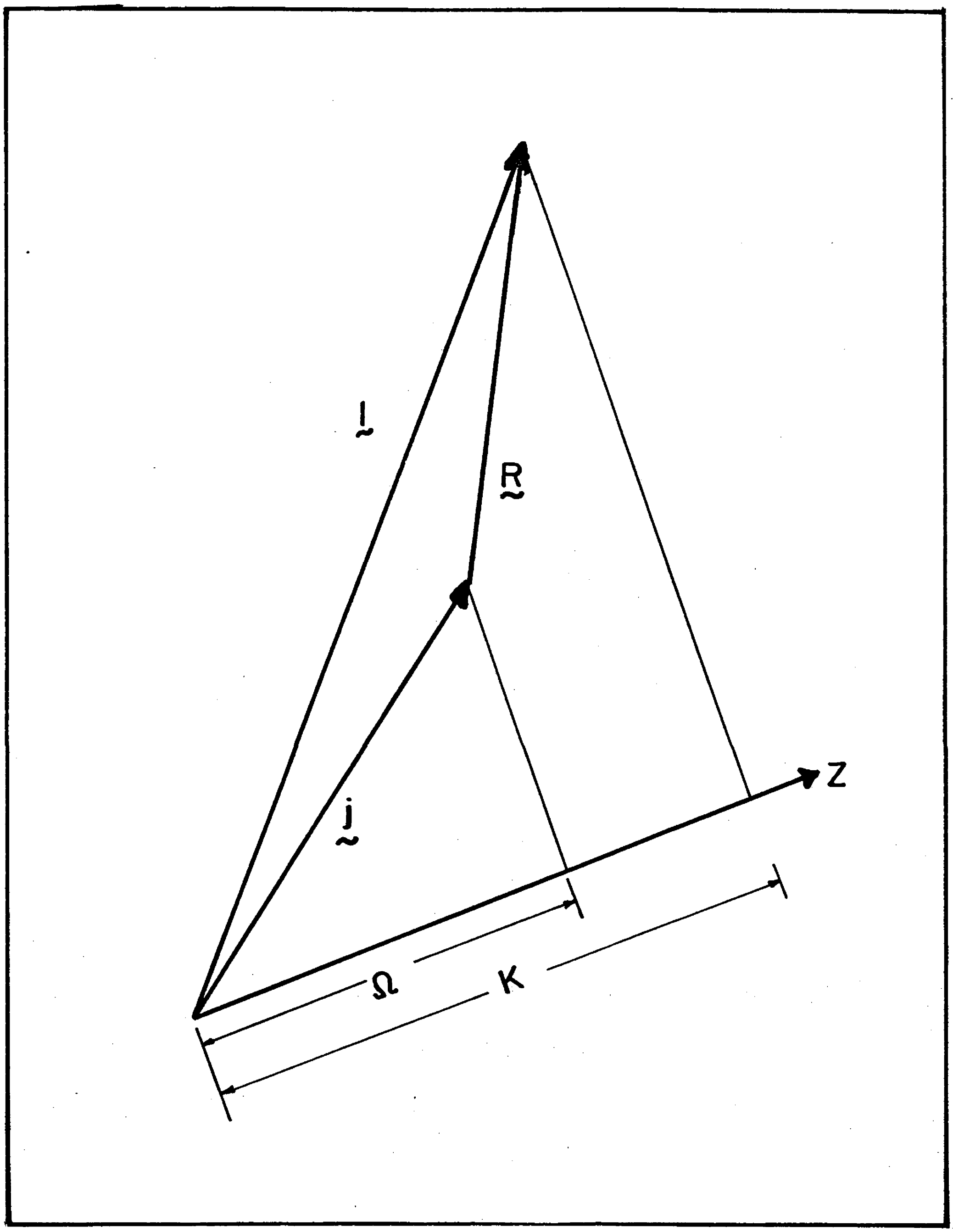

Fig. 1.7: Coupling of the angular momentum in a non-spherical nucleus. If Z is an axis of symmetry, $K = \Omega$.

$$E_{rot} = \frac{\hbar^2}{2\mathcal{I}_0} I(I+1) \,. \tag{11}$$

The manner by which a nucleus rotates is reflected in the value of $\mathcal{I}_0$. Because of the nucleus' particle nature, the rotation can be anything between the extremes of rigid-body rotation and the irrotational flow of fluids. In the former the nucleus bodily rotates, but in the latter, only a surface wave rotates.

Values of the moment-of-inertia determined from experimental data are found, invariably, to both lie between those predicted by the above two extremes and also to increase as the total spin increases. Bohr and Mottelson [Bo75] have shown that while Independent Particle Motion and Rotational flow result in a moment-of-inertia equal to the rigid body value, pairing correlations cause a reduction in the value of $\mathcal{I}_0$. They were, in fact, able to reproduce observed values.

The general increase of $\mathcal{I}_0$ with spin is caused by the effects of the Coriolis and Centrifugal "forces". These "forces" are not actual forces, but are merely mathematical artefacts caused by our choice of frame of reference — because it is rotating relative to the laboratory frame of reference. If one considers the directions in which these "forces" act, one can see how they may affect the moment-of-inertia.

The Centrifugal "force" is, classically, equal to $m\Omega^2\underset{\sim}{r}$, and is directed radially outwards. It tends to stretch the nucleus, thereby increasing $\mathcal{I}_0$.

The Coriolis "force", classically, equals $-2m\underset{\sim}{\Omega} \times \underset{\sim}{v}$ and thus exists only if a particle has a velocity relative to the rotating frame. The effect of this force on a time-reversed pair of particles is to attempt to align their intrinsic spin vectors, thereby breaking down the pairing correlations. The magnitude of this effect will, of course, increase as the core rotation increases ($\underset{\sim}{\Omega}$ increases). Hence, according to [Bo75], the moment-of-inertia will increase with spin. (This effect is known as Coriolis Antipairing.)

Both the Coriolis and Centrifugal "forces" are included within the $\underset{\sim}{I}.\underset{\sim}{j}$ term of Eqn (10). Generally, they are lumped together and termed a "Coriolis" force.

The Coriolis effects become very important in odd mass nuclei, and this will be discussed in the next section.

The more complicated effects of rotation of nuclei without axial symmetry will be dealt with in Chapter 4.

1.5 COLLECTIVE MOTION IN ODD MASS NUCLEI

In odd mass nuclei, the type of level spectrum observed depends, to a large extent, on the magnitude of the Coriolis effects. The maximum value of the Coriolis force on the unpaired particle is of the order

$$E_{Cor(max)} \approx 2\left(\frac{\hbar^2}{2\mathcal{I}_0}\right) I_j , \tag{12}$$

where j is the spin of the unpaired particle.

It is obvious, then, that the effects will be greatest for the high spin orbitals, for high total spin values, and low moment-of-inertia.

However, if the nuclear core is well deformed, and the extra particle is strongly coupled to it, then the particle has little velocity relative to the nuclear frame of reference. As $E_{Coriolis} \ll E_{core}$, the effects of the Coriolis force can then be treated as a perturbation on top of the normal rotational spectrum — which can be represented by (for axially symmetric nuclei)

$$E_I = \frac{\hbar^2}{2\mathcal{I}_0} [I(I+1) - K^2] , \qquad (K \neq \tfrac{1}{2}) , \tag{13}$$

where K is the component of I parallel to the symmetry axis, and all values of $I \geqslant K$ are possible. Such a spectrum is also called a "Deformation aligned" rotational spectrum.

If the core nucleus is almost spherical, the extra particle will be only weakly coupled to it, and the moment-of-inertia will be small. The level energies are then better approximated by the solutions of the Weak-Coupling model of de-Shalit [Sh62].

It is also possible to describe a coupling scheme where the extra particle is aligned with the rotation axis (see e.g. [St75]). When the projection of the particle's spin on the rotation axis [α] is large and defined, K is small and undefined. This is just the situation, i.e. rotational and particle spin aligned, which produces the greatest Coriolis effects. The energy levels can be described by the relation (for axially symmetric nuclei)

$$E(Ij\alpha) = A[(I-\alpha)(I-\alpha+1)+j(j+1)-\alpha^2],$$

where j is the particle spin.

To find the deformation regions in which these coupling schemes are applicable, the total Hamiltonian of the system, i.e.

$$H_{tot} = H_{part} + H_{rot}$$

must be solved exactly. This is done in Fig. 1.8, where the dots represent the exact solution for the lowest $I = {}^{11}/_2$ state of an odd A rotor ($j = {}^{11}/_2$). The "$K = {}^1/_2$" and "$K = {}^{11}/_2$" curves represent the extreme solutions of the "Deformation Aligned" Coupling scheme. The "$\alpha = {}^1/_2$" and "$\alpha = {}^{11}/_2$" curves represent the extreme solutions of the "Rotation Aligned" coupling scheme, and the "$R = 0$" curve represents the solution of de-Shalit [Sh62]. The projection of the particle's spin on the axes is also shown.

It is obvious (from Fig. 1.8) that the weak coupling model should only be used when $|\beta| \leqslant .1$, that the "rotation aligned" scheme can be used when $0.1 \leqslant \beta \leqslant 0.3$, and that the deformation aligned scheme is generally applicable elsewhere. If one considers a "hole" coupled to a rotor, Fig. 1.8 is not changed except for the inversion of the β axis, i.e. Rotation aligned schemes occur in oblate nuclei.

1.6 TRANSITIONAL TELLURIUM NUCLEI

1.6.1 Transitional Nuclei

We have previously considered the spectra of deformed (rotational) and spherical (vibrational) nuclei. The structure of many nuclei, however, cannot be described by these simple approximations. The present study is of nuclei of one such region; the Tellurium nuclei of masses 116 to 119.

Being two protons away from a closed proton shell, one would expect Tellurium nuclei to be "spherical" in their ground states. The neutron numbers, though, (64 to 67), lie midway through a major shell.

Fig. 1.8: The energy of the lowest $I = {}^{11}/_{2}$ state (in units of the even-even $I = 2^{+}$ energy) for a $j = {}^{11}/_{2}$ particle. Three coupling schemes and their approximate solutions (lines) and the results of exact diagonalization are shown. Schematic vector diagrams of the various couplings are also shown.

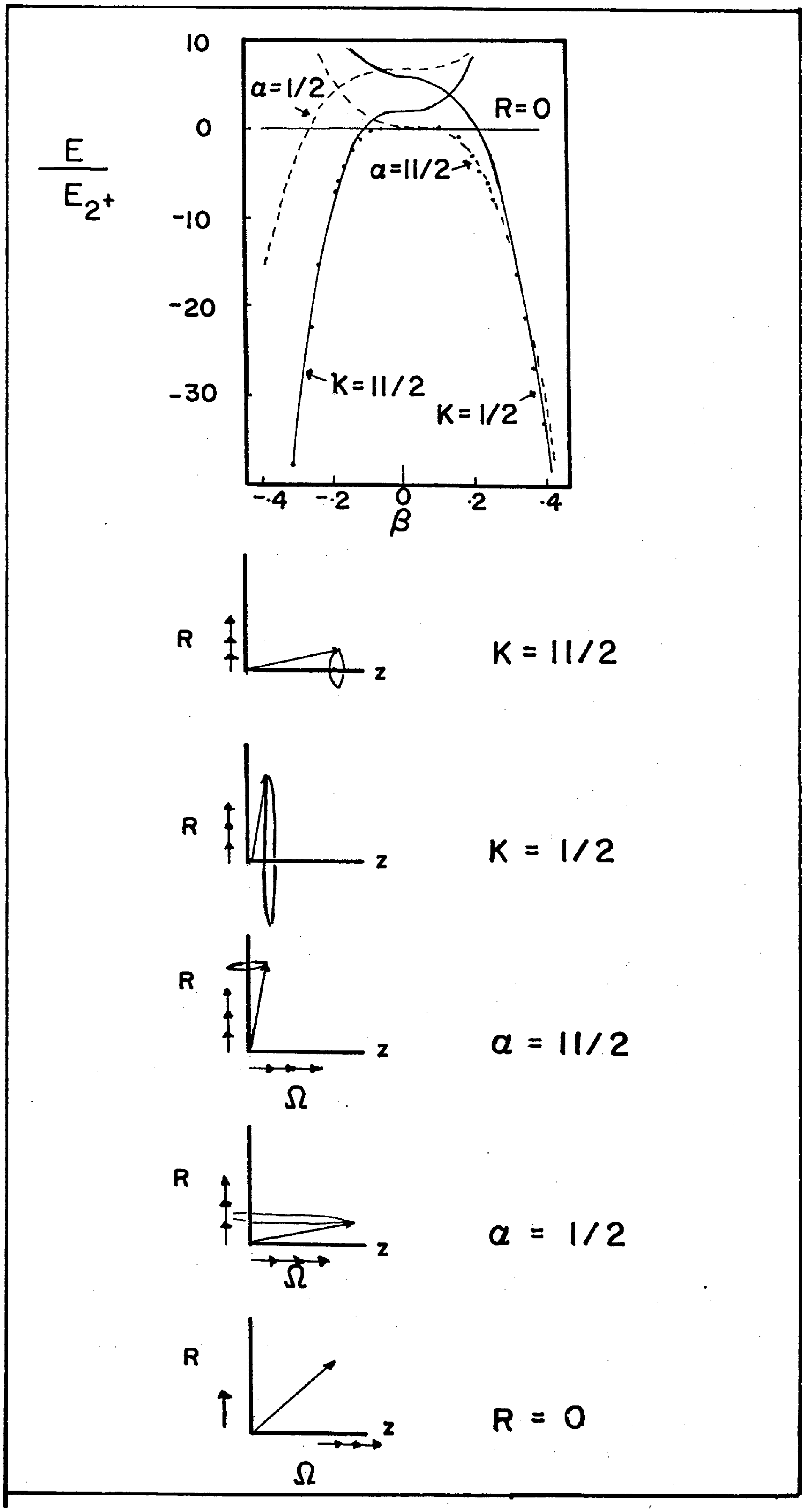
10
0
-10
-20
-30
E / E2+
α=1/2
R=0
α=11/2
K=11/2
K=1/2
-.4
-.2
0
.2
.4
β
R
z
K = 11/2
R
z
K = 1/2
R
z
Ω
α = 11/2
R
z
Ω
α = 1/2
R
z
Ω
R = 0

The neutrons could then be suspected of having a deforming influence on the core. Recalling the level schemes of Fig. 1.2, we find that the orbitals of the N = 50 to 82 major shell consist of two groups of levels; almost splitting the shell into two "subshells". This point will be discussed further in Chapter 4, but here we point out that any effects of a subshell closure should become evident at N = 64, when both the $1g_{7/2}$ and $2d_{5/2}$ orbitals are filled.

To picture some of the effects of the above opposing influences, we could look at the potential energy surfaces of the Tellurium nuclei. Such a surface indicates not only the preferred shape of a nucleus, but also, how tightly bound the nucleus is to that shape. For example Fig. 1.9 shows examples of the potential energy surfaces, as a function of β and γ, of several commonly occurring nuclear shapes. The shape of the contours, which represent equipotentials, vividly show the difference between the "γ stable" nucleus, Fig. 1.9(b), and a "γ unstable" nucleus, Fig. 1.9(c).

Fortunately, the potential energy surfaces of some of the even Tellurium nuclei have been calculated [Ha74], and these are shown in Fig. 1.10 as a function of β and γ. The calculations utilised the generalised collective model of Gneuss and Greiner [Gn71], and available experimental data.

The shaded regions of Fig. 1.10 represent the (calculated) spread of the ground state wavefunction. It is obvious that although the even Tellurium nuclei appear to be spherical vibrators, they are very soft. It can be shown that they, in fact, have r.m.s. values of β up to $\langle\beta_{rms}\rangle \approx .2$ [Ha74].

Excitation of the nuclei, or addition of a particle to them may cause their shape to alter. As the energies of the various particle orbitals depend on the deformation in different ways (see Chapter 4), it is not difficult to imagine that the shape of the nucleus may depend on whichever orbital is occupied by the extra particle. Such effects have been observed, for example, in the Antimony nuclei, close neighbours of the nuclei under study [He76] and [Sh79].

As an example, the calculated total potential energy surface, as a function of β only, is shown, in Fig. 1.11, for ^{115}Sb. Fig. 1.11

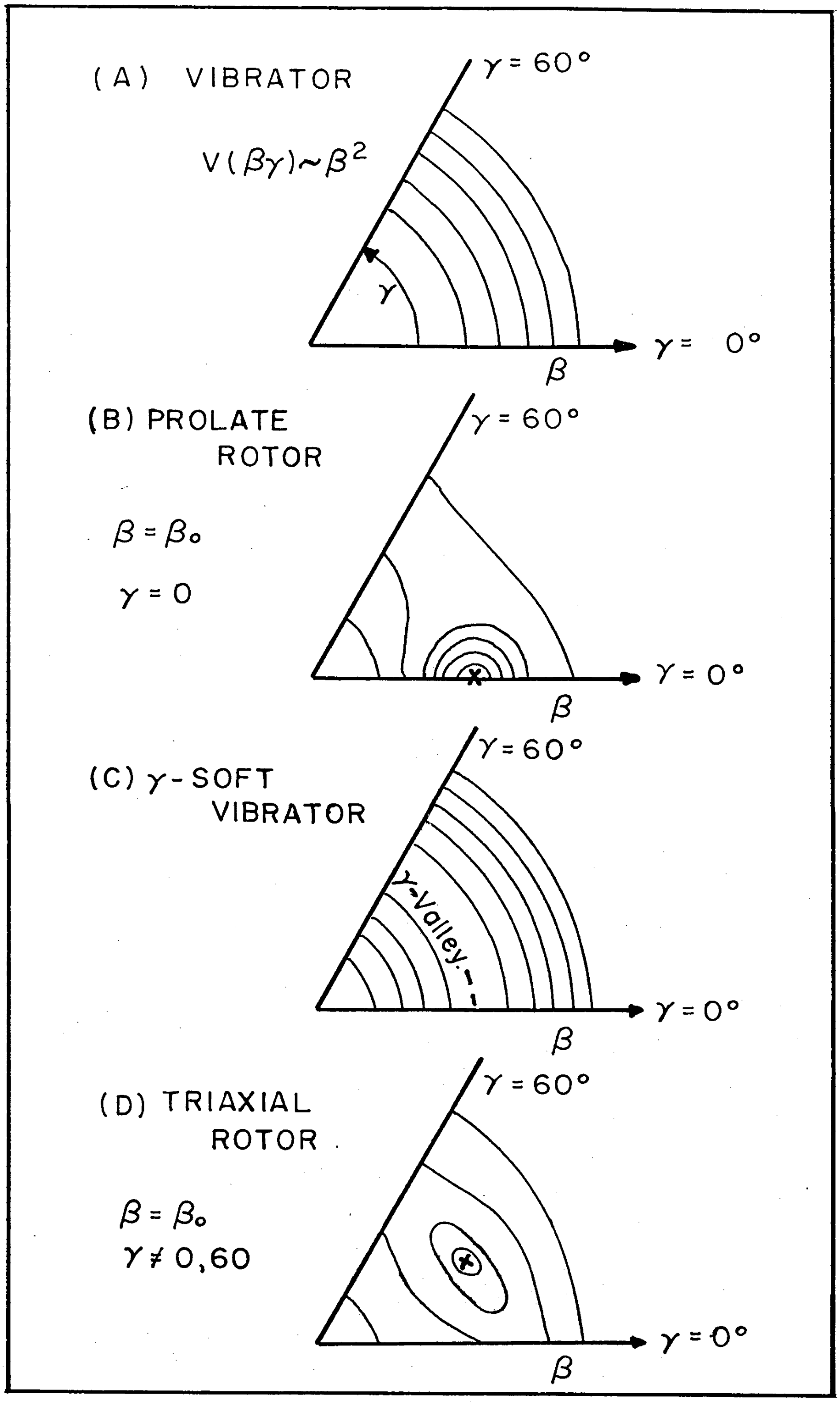

Fig. 1.9: Idealised examples of potential energy surfaces.

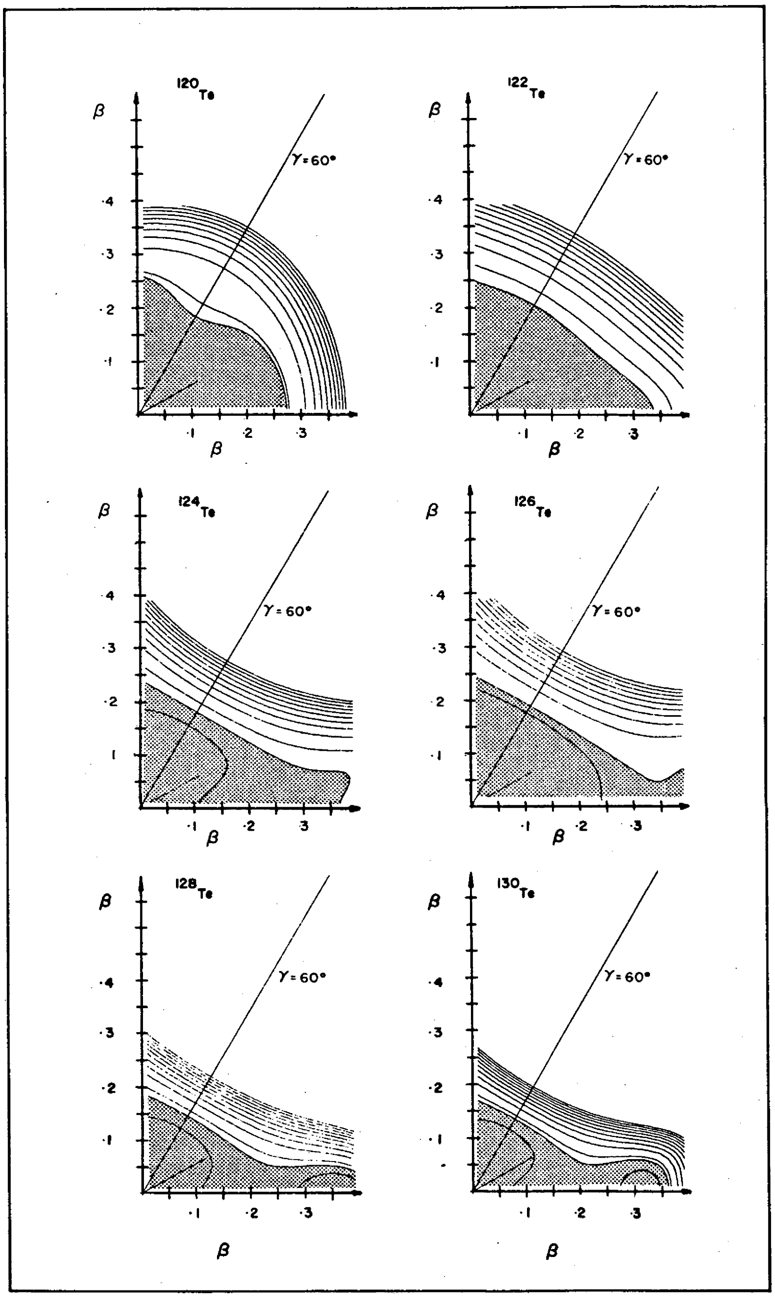

Fig. 1.10: Potential energy surfaces of the Tellurium nuclei with $A \geq 120$ [Ha74].

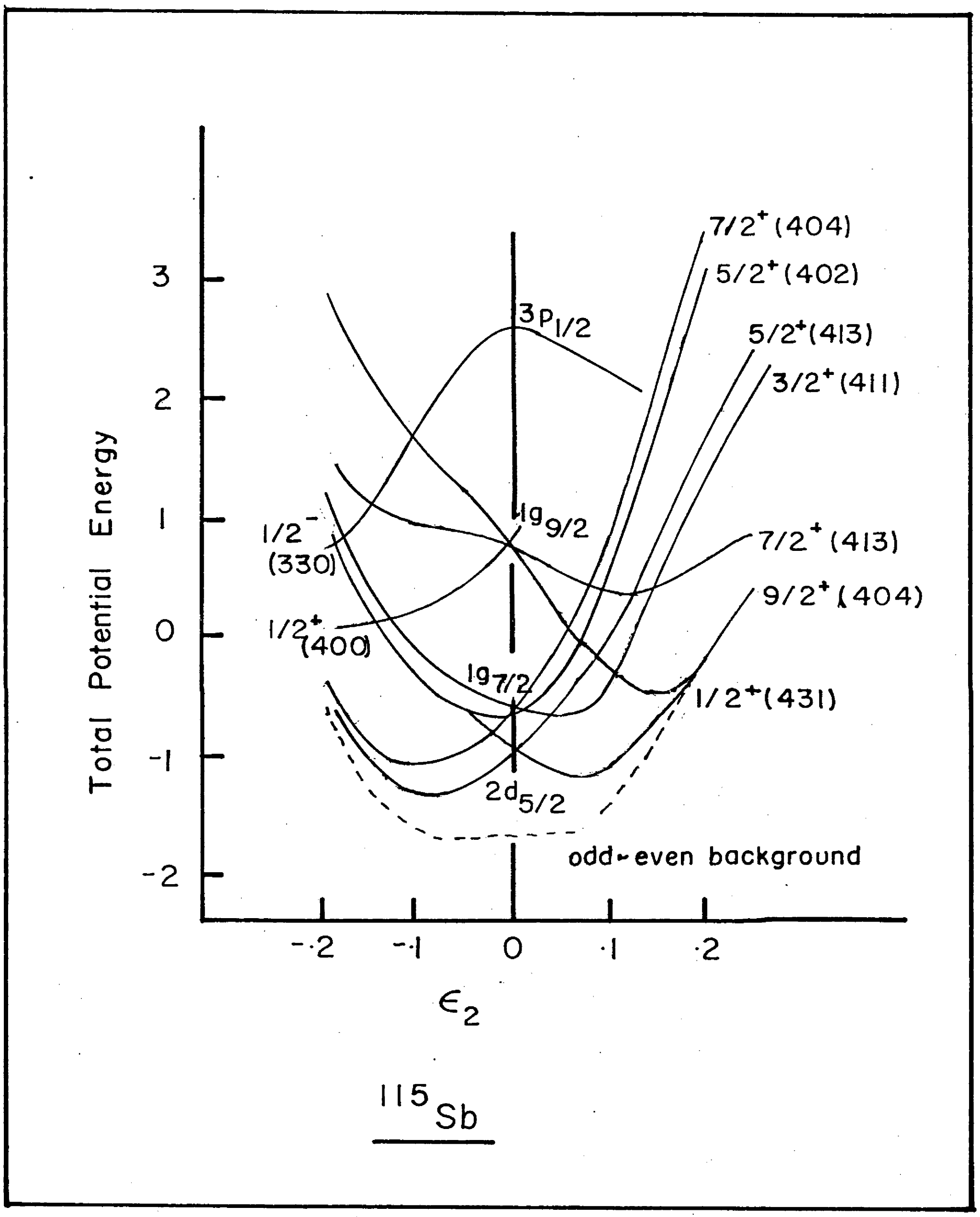

Fig. 1.11: Total potential energy surface of ^{115}Sb with the odd particle placed in different Nilsson orbitals as indicated. The odd-even background is also given with a dashed line.

is a composite, summarising many sets of potential energy calculations, each one assumes that the extra proton occupies a different orbital (e.g. $7/2^+[404]$, $3/2^+[411]$, etc.).

One could then hope to observe similar effects in the Tellurium nuclei.

1.6.2 Previous Work

At the commencement of this project, little was known about the level schemes of the neutron deficient Tellurium nuclei. Studies of the radioactive decay of Iodine nuclei had yielded levels of up to 2^+ in ^{116}Te [Go76], $5/2^+$ in ^{117}Te [La69] and [Se69], 6^+ in ^{118}Te [Sp69] and $5/2^+$ and $11/2^-$ in ^{119}Te [Sp70], [Se68] and [La69].

Vibrational-like band structure up to levels of 8^+ have been observed in both ^{116}Te and ^{118}Te [Wa70], [Lu69], [Se69], [Sa74] with the nuclei being formed by (α,xn) [Wa70], [Lu69], [Se69] and (p,xn) [Sa74] reactions. Sakai *et al.* [Sa74] also found states which are candidates for the 2_2^+ and 3_1^+ levels. The multipolarity of the transitions in the main band was confirmed as E2 by Wyckoff and Draper [Wy73]. A search for low lying 4p - 2h bands in ^{118}Te [Ch78] similar to the 2p - 2h bands observed in the Tin nuclei [Br79] has so far been inconclusive.

The odd mass nuclei, ^{117}Te and ^{119}Te, have only recently been studied by (α,xn) reactions. Positive parity states up to spin $15/2$ in ^{119}Te and $9/2$ in ^{117}Te have been reported by Hagemann *et al.* [Ha79a]. Negative parity states, based on the $1h_{11/2}$ orbital have been observed up to spin $23/2$ in both nuclei [Ha79b]. Both the $5/2^+$ and $11/2^-$ levels in ^{117}Te and ^{119}Te have been observed to be isomeric [Ha79a], [Br72], [Br69a], [Le78] and the decay of these is discussed in Chapter 3.

Of the heavier Tellurium nuclei, [Wa70], [Lu69] and [Wy73] give levels up to spin parity 8^+ in all the even nuclei up to mass 126. Other studies include decay studies on Iodine and Antimony nuclei [Ke71], [Wa76], [Ga70], particle scattering [Sa79] and transfer reactions [Ro80], [Li77]. In none of these studies have states of spin greater than 10^+ or $13/2^-$ been observed. An (α,3n) reaction [Ke72] has enabled states up to $23/2^+$ to be observed in ^{125}Te.

Hagemann *et al.* [Ha79a], [Ha79b] have also identified states up to $J^{\pi} = {}^{23}/_{2}^{-}$ in ^{121}Te.

Observation of transitions between higher spin states in Tellurium nuclei has been confined to continuum gamma rays following the ^{110}Pd(^{12}C,xn)Te and ^{82}Se(^{40}Ar,xn)Te reactions [Si79]. This study argued against the existence of deformed rotational bands below spin 30 $\hbar$, and also showed that shell structure effects play an important role in the determination of transition energies.

The present work extends the level schemes of $^{116-119}$Te to much higher spin (e.g. $\sim {}^{41}/_{2}$ in ^{119}Te).

CHAPTER 2

EXPERIMENTAL PROCEDURE AND DATA ANALYSIS TECHNIQUES

2.1 INTRODUCTION

In order for the phenomena mentioned in the previous chapter to be investigated, we needed to form the desired nuclei ($^{116-119}$Te) in such a manner that high spin states were preferentially populated. The modes of decay of these states should then provide the structural information that we seek.

Nuclear formation by fusion-evaporation reactions (commonly called (HI,xn) reactions) provides a suitable angular momentum population distribution. It will be seen also (§2.2) that characteristics of this reaction mechanism allow relatively simple experiments to be used to determine level spins. This chapter outlines the reaction mechanism, experiments completed, and methods of data analysis which were utilised in the derivation of the level schemes presented in Chapter 3.

2.2 (HI,xn) REACTIONS

The use of these reactions as a spectroscopic tool was first suggested by Marinaga and Gugelot in 1963 [Mo63]. Since then, many works have utilised the (HI,xn) reactions, and a review of the reaction mechanism and its uses has been given by Newton [Ne74]. Here we shall describe the salient features by considering the progress of a ^{13}C ion incident upon a ^{110}Pd target. This choice is made as it is one example of the experiments conducted.

Although other reasons for the particular choice of projectile and target will become apparent, an obvious reason is that complete fusion of the two particles produces a Tellurium nucleus (^{123}Te) that is somewhat heavier than those being studied.

Using hindsight, we will assume that the projectile (^{13}C) has 59 MeV energy, in the laboratory frame. At this energy, the particle has a de Broglie wavelength of only .16 f. This is small compared to the nuclear radius of 3.3 f, and permits us to describe the reaction, to a fair approximation, by classical mechanics. Also, the particle has sufficient energy to overcome the Coulomb barrier ($\sim$ 43 MeV), and collide with the ^{110}Pd nucleus.

During the collision, many different types of reaction may occur, of which complete fusion is but one example. However, after penetration of the Coulomb barrier, there is only 14 MeV of energy left, and complete fusion is the dominant reaction. The collision, being inelastic, results in a highly excited compound nucleus (55 MeV of excitation in the present case) being formed.

Another feature of the reaction is that the system, in all cases but that of direct head-on collisions, has non-zero angular momentum. The actual value depends on the reduced mass of the system, the energy of bombardment, and the impact parameter. If one assumes that fusion occurs whenever it is possible, then it can be shown that the partial cross section for the production of the compound nucleus is proportional to the input angular momentum — up to a value ℓ_{max}, which is determined by the maximum impact parameter. Thus it is more likely that a nucleus with large rather than small angular momentum is formed.

This situation is shown in Fig. 2.1. Fig. 2.1a depicts the situation in which the maximum angular momentum is obtained, i.e. grazing collisions, and Fig. 2.1b shows the relation between fusion partial cross section and angular momentum. The average angular momentum with which the ^{123}Te nuclei are formed is then simply two-thirds of the maximum value. An estimate of this can be found by the relation,

$$\bar{\ell} = \frac{2}{3} \times [.219 \times R \times [\mu(E_{CM} - E_{CB})^{\frac{1}{2}}]] , \qquad (1)$$

where μ is the reduced mass,

E_{CM} is the bombarding energy (in the centre-of-mass frame),

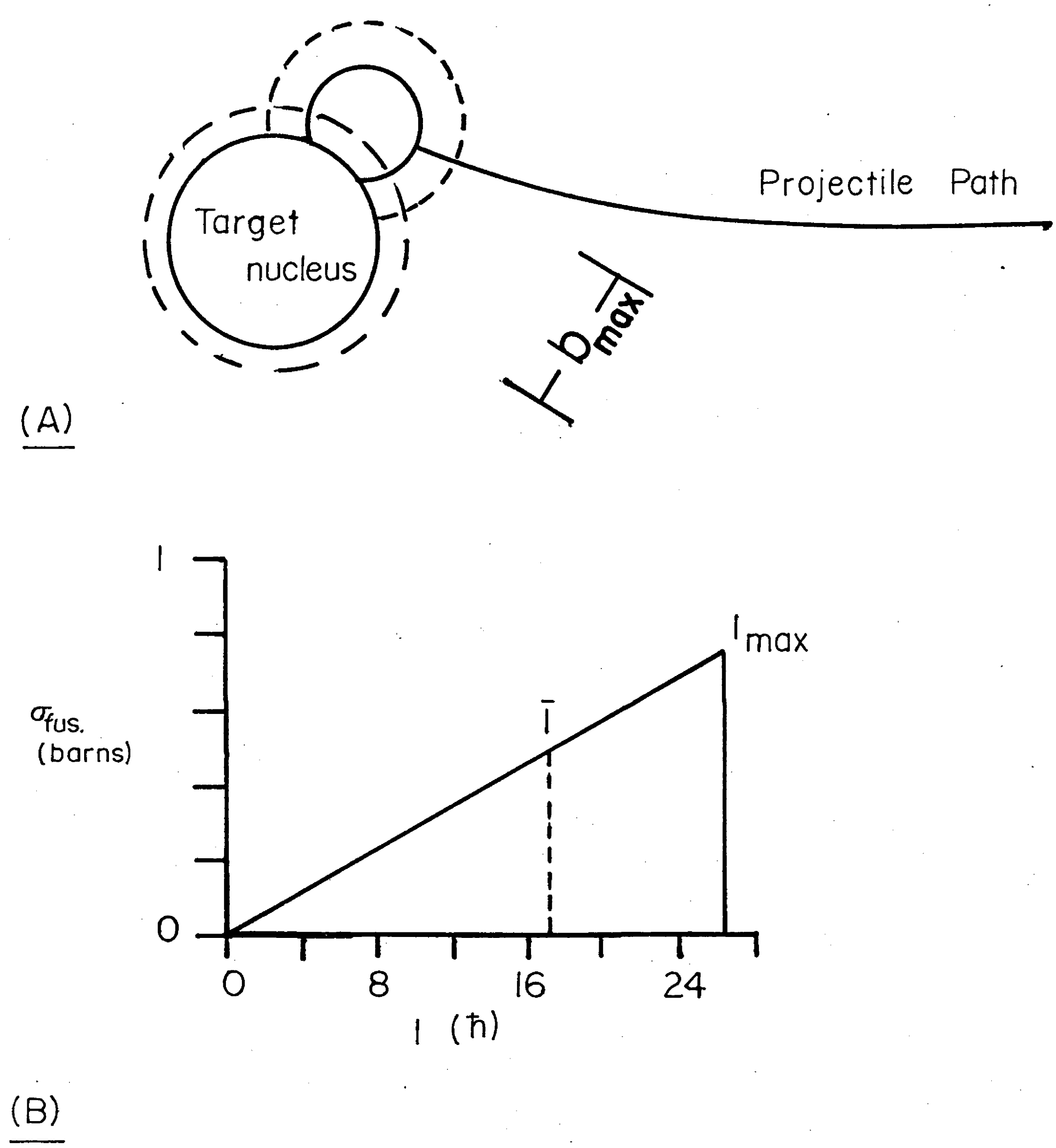

Fig. 2.1: Classical example of colliding nuclei. (A) The situation producing maximum angular momentum in a fusion reaction. (B) Relative cross section for formation of the compound nucleus versus spin.

E_{CB} is the Coulomb energy (in the centre-of-mass frame), and

R is the sum of the projectile and target radii.

In applying this equation to the present example, we find that the ^{123}Te is formed with $\bar{\ell} \approx 17\ \hbar$ ($\ell_{max} = 26\ \hbar$). If a similarly energetic ^{12}C nucleus was used as the projectile, the compound nuclei (^{122}Te) would have been formed with a slightly less average angular momentum.

Hence we are likely to find that, after a fusion reaction, a highly excited and rapidly spinning compound nucleus is formed. The excitation energy of the compound nucleus is far above the binding energies of neutrons (~ 8 MeV), protons (~ 6 MeV) and alpha particles (~ .3 MeV). It appears then, that these particles may be evaporated by the compound nucleus in its de-excitation process. There are several factors though, that inhibit their emission rates relative to each other.

Firstly we must realise that for any given spin* of the nucleus, there exists a minimum energy, below which a nucleus with that spin* cannot exist (e.g. recall from Chapter 1, $E_J \propto J(J+1)$). The locus of these minima, best seen in an E vs. J diagram such as Fig. 2.2, is called the *Yrast line*.

Also, in emitting a particle with spin* greater than zero, the centrifugal barrier must be overcome. As this barrier increases with spin*, particles which carry off high spin* values are less likely to be emitted than those taking away no spin.* In combining this with the above observation, we see that, in the first instance, it is the excitation of the compound nucleus relative to the Yrast line, *not* the total excitation, which is the important quantity. This energy helps to determine the level density of the compound nucleus (at the particular spin* value), which increases as the energy above Yrast increases. The probability of emission of a particle is therefore dependent on the amount of energy it takes away, for, in emitting a particle, the nucleus "moves" from a region of high level density to a region of lower level density. This assumes that properties of E vs. J level density diagrams are similar for neighbouring nuclei.

The same is true in the case of gamma ray emission, so that the

*Errata: for "spin", read "angular momentum".

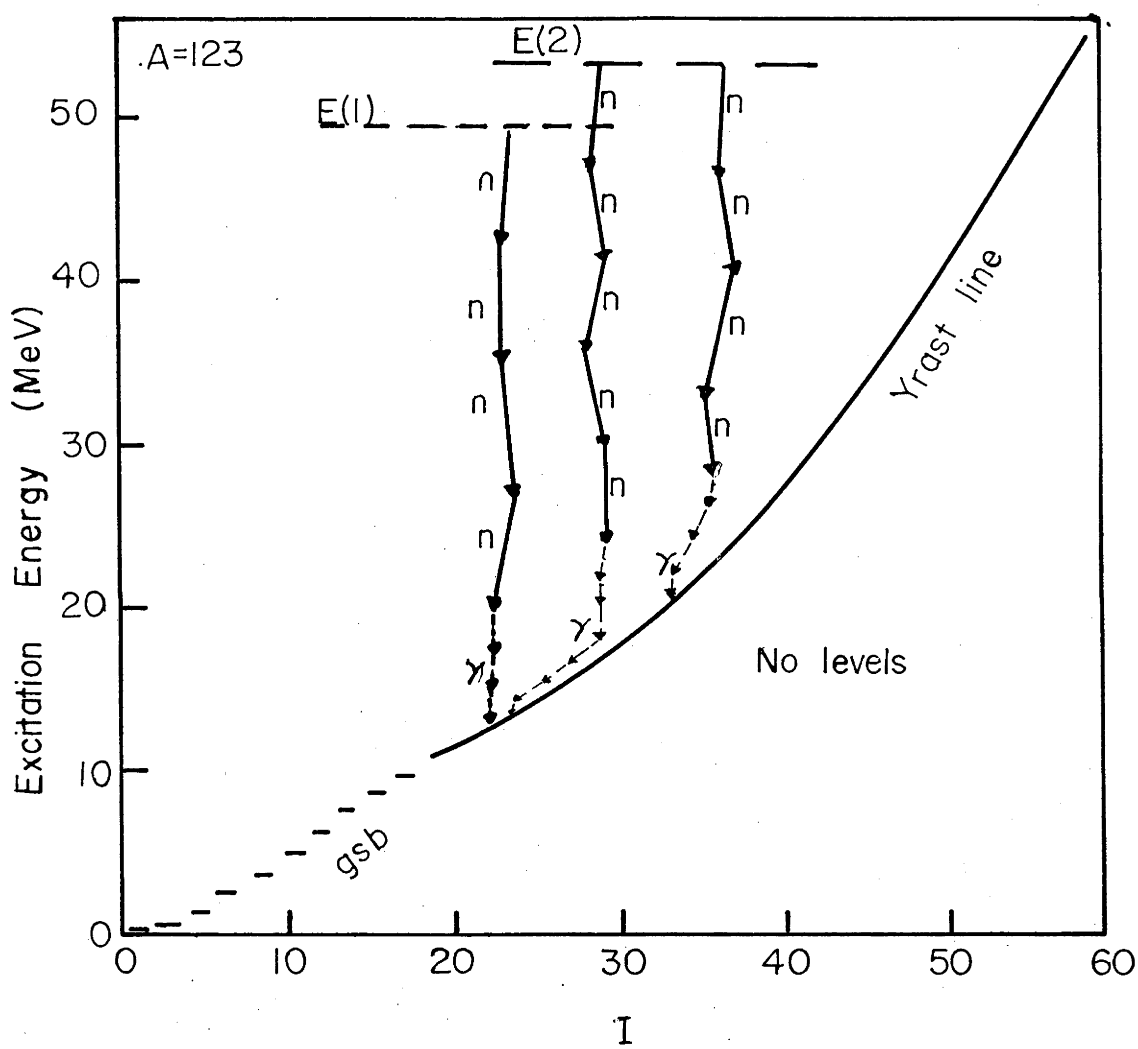

Fig. 2.2: Energy versus spin (E vs J) diagram showing some possible decay modes of the compound nucleus.

four processes compete for the most probable decay mode of the compound nucleus. In general, the following observations can be made:

(a) Of particle evaporation, neutron evaporation is most probable for neutron rich nuclei. This is because the neutrons carry off the least energy (no Coulomb energy), leaving the nucleus in a region of relatively high level density. However, the binding energies of alphas and protons decrease more rapidly with decreasing compound nucleus neutron number than the neutron binding energy does. The evaporation of these particles then becomes relatively more likely as the neutron deficiency increases.

(b) At excitation energies less than one neutron binding energy above Yrast, any evaporated neutrons must carry off angular momentum. If they did not, there would be no state available to which the nucleus could decay (below Yrast). The neutrons then have to overcome the centrifugal barrier, causing gamma emission to become more probable.

These processes continue until a nucleus is formed which must decay by gamma emission. If that nucleus is formed sufficiently often, so that discrete gamma rays can be observed, its properties can be studied.

Now, given a compound nucleus' position on an E vs. J diagram, the probability of formation of any one daughter nucleus can be calculated by repetitive application of the probabilities of the above processes. As a result, the probability of formation of a nucleus by a fusion-evaporation reaction is determined by the projectile-target combination and the energy of the projectile, for these are the factors which determine the position of the fused nucleus on the E vs. J diagram. This is the basis of complex computer programs such as that developed by Sikkeland [Si64].

The results of using that programme on the present case are seen in Fig. 2.3. The peaking of the xn channels can be understood by reference to Fig. 2.2. As the energy is increased, the probability of emitting more neutrons is increased. However, the angular momentum distribution of the compound nuclei has also changed (see Eqn (1)), spreading the possible entry points on the E vs. J diagram. As a

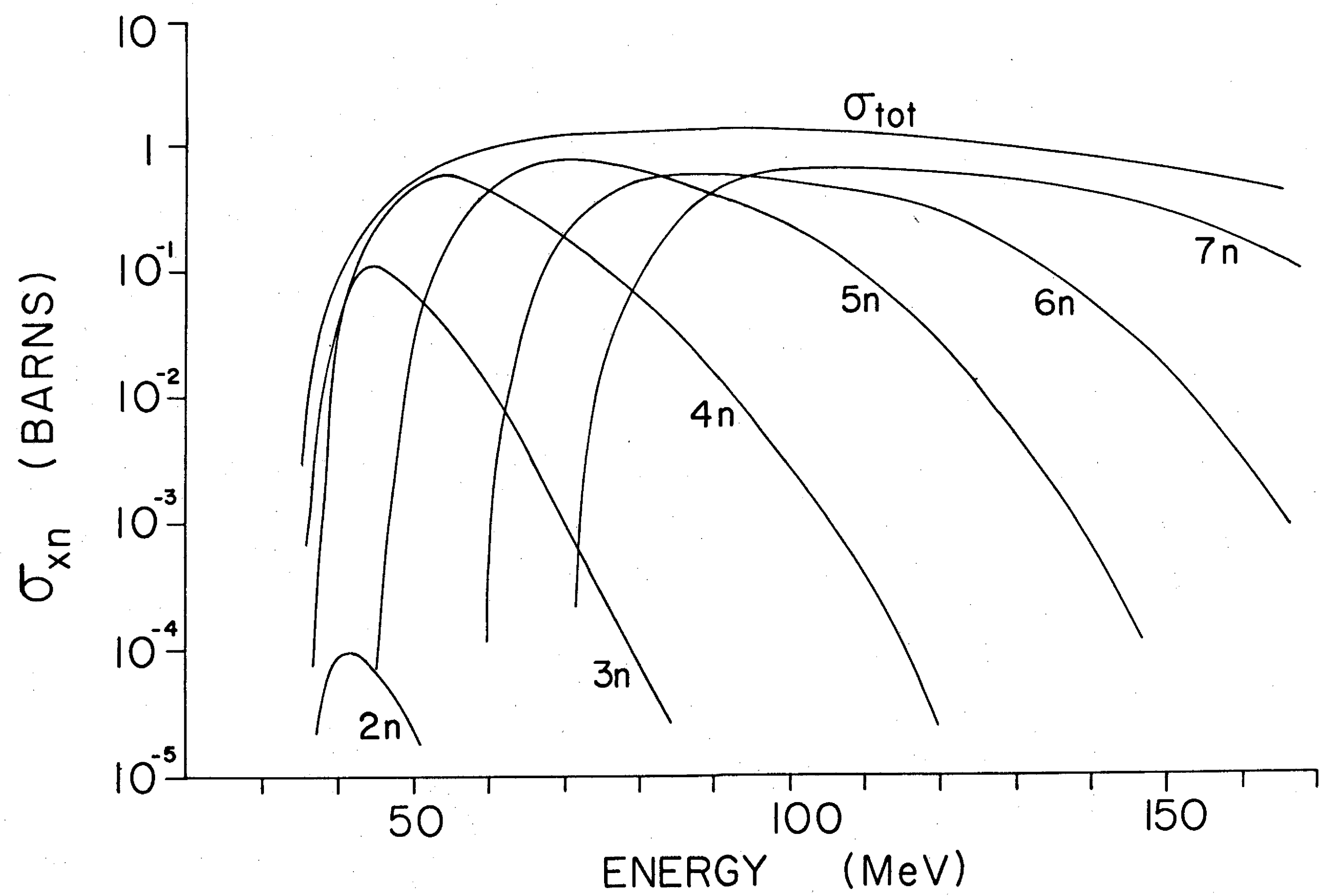

Fig. 2.3: Calculated probabilities for neutron emission following a $^{110}Pd(^{13}C,xn)^{123-x}Te$ reaction versus projectile bombarding energy. Note the Log scale.

result, the ability to cleanly produce one xn channel is diminished. This is even further enhanced by the finite width of the neutron spectrum. The effect of these is clearly seen in the tailing of the xn cross sections in Fig. 2.3.

However, if one wished to pursue a particular xn channel as the energy of bombardment were increased (by, say, gamma-gamma coincidence measurements), one would find that the average initial nuclear spin would increase.

In the present example, ^{119}Te is formed most abundantly, and with very high cross section. The reaction is also fairly "clean", i.e. relatively little formation of the other xn channels.

In carrying out a fusion experiment, all the projectiles approach the target from the one direction. Classically, then, all the angular momentum is aligned perpendicular to the beam direction. Quantum mechanically though, this is impossible. What does occur is that the distribution of nuclei over the M (= $2J+1$) substates is symmetrical and is peaked at $M=0$ (for even nuclei) or $M=\pm\frac{1}{2}$ (for odd nuclei) — where $M=0$ is taken along the beam axis. If both the projectile and target are of spin $I=0$, then only the $M=0$ substate is populated in the compound nucleus.

As the process of particle evaporation does not greatly affect (for reasons discussed previously) the angular momentum of the compound nucleus, then one could expect the alignment to persist until gamma ray emission occurs. This has been found to be so — see for example Diamond *et al.* [Di66]. The reaction mechanism then effectively carries out the first step of a correlation experiment, by providing a non-random distribution of nuclei over the M substates. Direct ("singles") measurements of the intensity of a transition, made as a function of angle away from the beam axis, should then provide information as to the difference in spin between the transition's initial and final states. If one spin and the level spectrum are known, the spin of most levels should be easily determined. Much use of this feature is made in Chapter 3.

When gamma ray (and conversion electron) emission first begins to successfully compete with particle emission, the level density is still much higher than it is near the ground state. This implies that there are many paths available by which the nucleus can decay; hence no one transition receives sufficient intensity to render it observable by present techniques. This gives rise to a quasicontinuum spectrum.

It is not until the level density is much lower, i.e. near the Yrast line, that individual transitions can be delineated.+ The excitation energy, and spin, to which discrete transitions can be observed depends on the input angular momentum and the type of transitions occurring in the quasicontinuum region. As the quasicontinuum is not well understood (e.g. [Ne74]), it will not be considered further.

The population of any one level can be thought of as being derived from two "sources". The first is directly, via the quasicontinuum, and the second is via discretely observed transitions originating from levels at higher excitation energy. For levels near the origin of an E vs. J diagram (i.e. low spin, low excitation energy), the former is relatively less important than the latter. The reverse is true for levels of high excitation and high spin. If the initial angular momentum distribution is changed (e.g. by increasing the bombarding energy), then the relative importance of these feeding processes change.

The position of a level, or rather, a gamma transition originating at that level, can then be estimated by the response of its intensity to changing bombarding energy. The intensity of gamma rays originating at high spin will, of course, vary more rapidly than that of gamma rays originating at low spin. These "excitation functions" are also used extensively in Chapter 3. One example is reproduced in Fig. 2.4 which shows the rapid increase which may be observed. The rapidity of the increase observed is more easily explained if the bombarding energy values were replaced by the values of "energy above the Coulomb barrier", which, as shown in Eqn (1), is the effective energy of the reaction.

One feature of the (HI,xn) reactions is that because of the many different paths possible, the population of any one level is almost independent of that level's structure.

+ In later chapters, the term 'Yrast Cascade' will be used to describe the sequence of transitions that connects the Yrast states. Also, the term 'Yrare Cascade' will be used to describe that cascade which appears closest to the Yrast cascade when both are viewed in an E vs J diagram

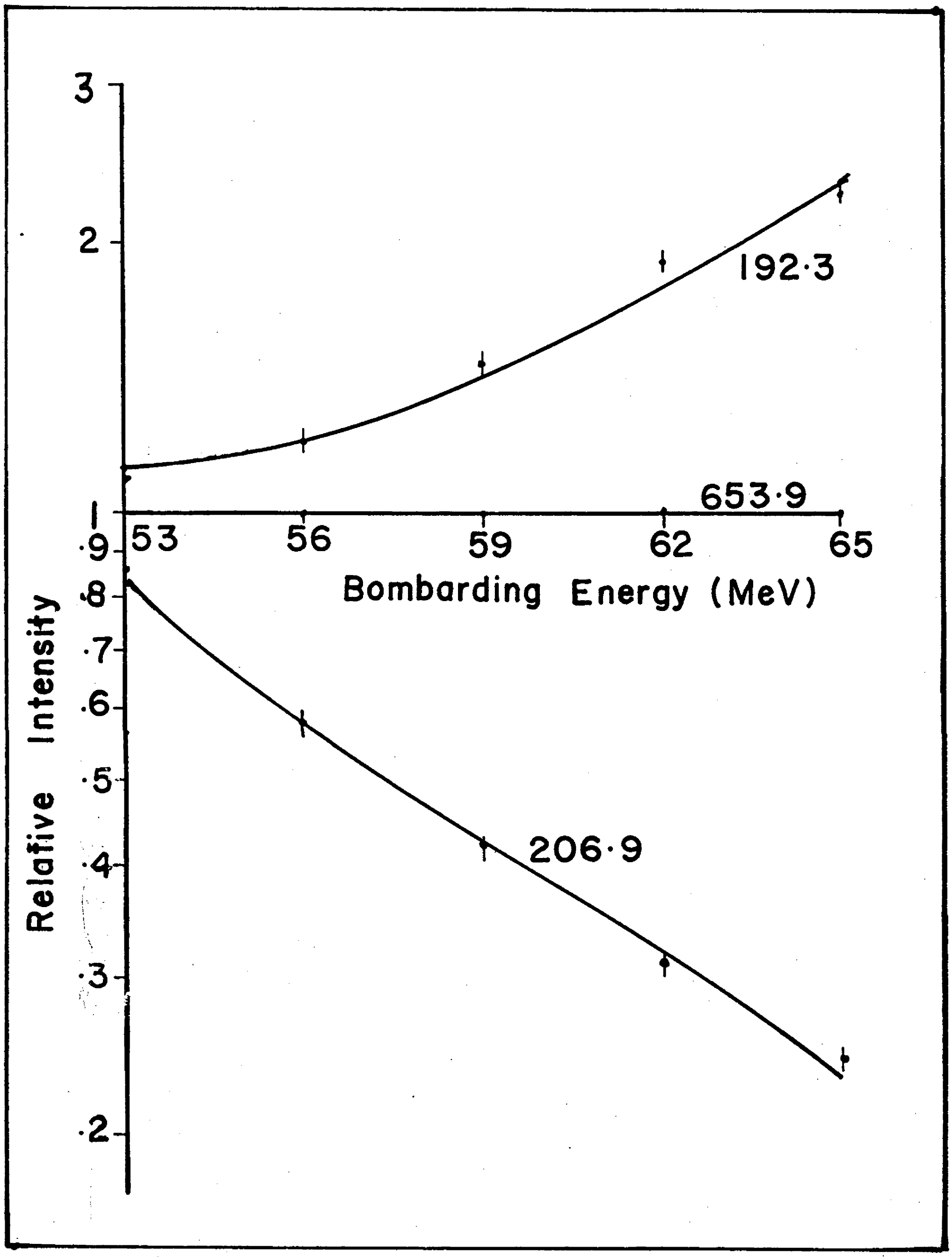

Fig. 2.4: Examples of relative excitation functions — extracts from Fig. 3.4.

One final feature of (HI,xn) reactions will be mentioned. Conservation of linear momentum implies that the compound nucleus has a high recoil velocity — in the present case, 1% of the velocity of light. This velocity gives any emitted radiation a Doppler shift, which can be utilised in various experiments. However, for accurate energy and intensity measurements, the nuclei must be stopped. This can be achieved by "backing" targets with a piece of material thick enough to stop the recoiling nuclei. By the time the compound nuclei have stopped (several picoseconds), several particles and/or gamma rays may have been emitted. The nuclei though, have not had time to decay to the point where transitions can be discretely observed. As a result, no Doppler shifting of the discrete transitions is observed.

2.3 EQUIPMENT REQUIREMENTS

2.3.1 Beams and Targets

The beam-target combination was chosen so that it provided the highest angular momentum distribution in the nuclei studied, while giving a stable target and a beam capable of being produced and accelerated. This limited the choice to the Carbon-Palladium combination.

^{13}C beams were used in all the experiments, with negative ^{13}C ions being provided by a Sputter Ion source. Cones used by the ion source were comprised of either a 50-50 mixture of ^{12}C and ^{13}C, or powdered ^{13}C bonded onto a cone of natural carbon. Using either cone, the source output was capable of exceeding 100 nA of ^{13}C. With that quantity of beam input, the accelerator easily stabilised, and a steady beam was achieved on target. The beam was sufficiently intense to not be a deciding or critical factor in any experiment.

The beam was accelerated by the Department of Nuclear Physics' 14UD Pelletron accelerator. Terminal voltages used ranged from 10.6 MV for 53 MeV ^{13}C (4^+) to 13.0 MV for 65 MeV ^{13}C (4^+). The beam was stripped of electrons in the centre of the accelerator by passage through a thin Carbon foil. Generally the 4^+ or 5^+ charge states were selected; the choice being determined by their relative abundances and/or by the voltage limitations of the accelerator.

The target was made of rolled, isotopically enriched metallic foils. The isotopic analysis of the two target materials used is given in Table 2.1. The target thicknesses were chosen such that the ^{13}C beam lost less than 7 MeV during its passage of the foil. This restriction was made in an attempt to limit the reaction to one xn channel (as 9 MeV is approximately one neutron binding energy). As a result, the various xn channels were able to be studied independently.

Table 2.1

Isotopic Analysis of the Target Material

^{108}Pd Isotopic Analysis			^{110}Pd Isotopic Analysis		
Isotope	Atomic Per Cent	Precision	Isotope	Atomic Per Cent	Precision
102	< 0.03	-	104	0.07	±0.02
104	0.12	±0.03	105	0.24	±0.05
105	0.35	±0.03	106	0.36	±0.05
106	1.04	±0.05	108	2.35	±0.05
108	98.11	±0.05	110	96.98	±0.10
110	0.38	±0.03	102	< 0.02	-

Thicknesses used were 2.8 mg/cm^2 from ^{110}Pd and 3.4 mg/cm^2 for ^{108}Pd, which allowed for the positioning of the target at 45° to the beam. The targets were made as thick as possible in order to gain a large production rate.

For the measurement of electrons, a target of 1.8 mg/cm^2 thickness was placed at 63° to the beam direction, giving an effective thickness of 2.0 mg/cm^2 to both the beam and detected electrons. The thinner target was needed here in an attempt to increase the resolution of the electron measurement.

The beam, and any recoiling nuclei, were stopped in lead backing (41 mg/cm^2 thickness). The energy loss experienced by the beam in its passage of the target ensured that for all bar the highest energies used, the Coulomb barrier for lead was not exceeded. The effect of reactions occurring in the backing was checked by bombarding the lead, as a target, with ^{13}C beams of up to 70 MeV energy. No discrete gamma rays were observed. The backing was not used during low energy gamma ray measurements, nor during electron measurements. In the former, it was because of the intense lead X rays given off, and in the latter, because of the flux of stopping electrons emitted. In both cases, the beam was stopped at least 60 cm from the target so that any radiation emitted in the stopping process could not affect the measurements. A list of the reactions investigated is given in Table 2.2.

Table 2.2

Reactions Investigated

Reaction	Bombarding Energy (for coincidence data)
$^{110}Pd(^{13}C,4n)^{119}Te$	59 MeV
$^{110}Pd(^{13}C,5n)^{118}Te$	75 MeV
$^{108}Pd(^{13}C,4n)^{117}Te$	68 MeV
$^{108}Pd(^{13}C,5n)^{116}Te$	68 MeV

2.3.2 Detection of Gamma Rays

The gamma rays emitted during the nuclei's decay were detected by the use of Lithium drifted Germanium detectors [Ge(Li)], operated at liquid nitrogen temperature. The radiation interacted with the semiconductor crystals by the photoelectric, Compton, and pair production processes. These resulted in the formation of electron particle-hole pairs which were collected at the electrodes, forming the signal to be analysed. The spectrum observed as the result of the detection of a gamma ray then depends on the relative efficiencies of the above three processes.

Pair production only occurs above a threshold of 1.022 MeV, when, in the presence of a nucleus, the photon can be converted into an electron-positron pair, with any excess energy being converted into kinetic energy. The eventual annihilation of the position produces the usual annihilation quanta, which in turn may be detected by one or both of the other two processes. When one or both of the quanta escape from the crystal, the total energy of the photon which can be absorbed by the crystal is thereby reduced by the corresponding amount. This gives rise to secondary "escape" peaks in the spectrum which can be confused with full energy peaks due to other transitions. However, in the present experiments, few intense gamma transitions were observed above the pair threshold, and no examples of escape peaks were observed.

The photoelectric effect occurs when a gamma ray is completely absorbed by an electron, giving rise to a free electron of an energy equal to that of the gamma ray, less the atomic binding energy of the electron. This reaction is most likely to occur at low energies and produces a highly localised disturbance of the crystal. As the X rays which are emitted when the electron vacancy is filled are also absorbed in the detector, the observed spectrum, often called the "photopeak" represents the full energy of the photon.

The Compton process occurs when a gamma ray is inelastically scattered by an electron. This process can occur many times until either the photon escapes the crystal, or until the resultant low energy photon is absorbed by the photoelectric process. If the latter occurs, a full energy peak similar to the photopeak is observed. This process is the dominant detection process for photon energies of the range $\sim$ 200 keV to 1500 keV. The probability of detection depends, naturally, on the size and shape of the crystal.

Coaxial Ge(Li) detectors have cylindrical crystals, and can be made quite large — typically $\sim$ 4 cm diameter by $\sim$ 4 cm in length. One of the electrodes is inserted along the axis of the cylinder for most of the crystal length. The electric field radiates from this electrode to the crystal surface. The effective detection volume would then be annular in cross section except near the front of the detector, where some regions of poor field strength may occur.

Low energy photons which are unable to penetrate to the region of constant field are then susceptible to incomplete, and relatively slow, charge collection. In contrast, planar Ge detectors, which have uniform field distributions at the front of the detector exhibit good timing and relatively high detection efficiency for low (< 200 keV) energy gamma rays. As planar detectors are generally quite thin (< 1 cm), the detection efficiency decreases rapidly as the photon energy increases.

So, although coaxial Ge(Li) detectors were generally used, a planar detector was used to detect gamma rays of $E_\gamma < 200$ keV. To enhance the detection of the low energy photons, a detector which was covered by only a thin Beryllium window was used.

An integral part of all the experiments was the measurement of the relative efficiencies of all the detectors used. Care was taken to evaluate the relative efficiencies at all the detector angles employed, and for all conditions under which the experiment was conducted. This was done by placing a radioactive source in the target position (^{152}Eu [Ri70] and ^{133}Ba [Be74]) with the data being collected in "singles" mode.

The electronic units used in the detection of coincident gamma rays differed from those used for the measurement of gamma rays in singles. To effectively measure the relative efficiency of the coincidence circuitry, a "dummy" coincidence experiment was conducted, by splitting the signal from the Timing Filter Amplifier (T.F.A.) (see later) and using it for both start and stop signals to the Time Amplitude Converter (T.A.C.) (see later).

Examples of the relative efficiency curves for coaxial and planar detectors are shown in Figs. 2.5a and 2.5b respectively. The decrease in efficiency at low energies is caused, in part, by the absorption of photons by the material between the source and the detector. When the targets were backed with lead, additional absorbers were placed immediately in front of the detectors in an attempt to reduce the flux of lead X-rays. Absorbers used for this purpose were two sheets, each .5 mm thick, of Cadmium and Copper.

Efficiency measurements must necessarily be conducted out of beam. However, the flux of gamma rays which enters the detector when the beam is on, can subtly alter the electric field. The energy calibration of the system can then be measurably different between the "in" and "out of" beam conditions. Therefore, as a precaution, energy

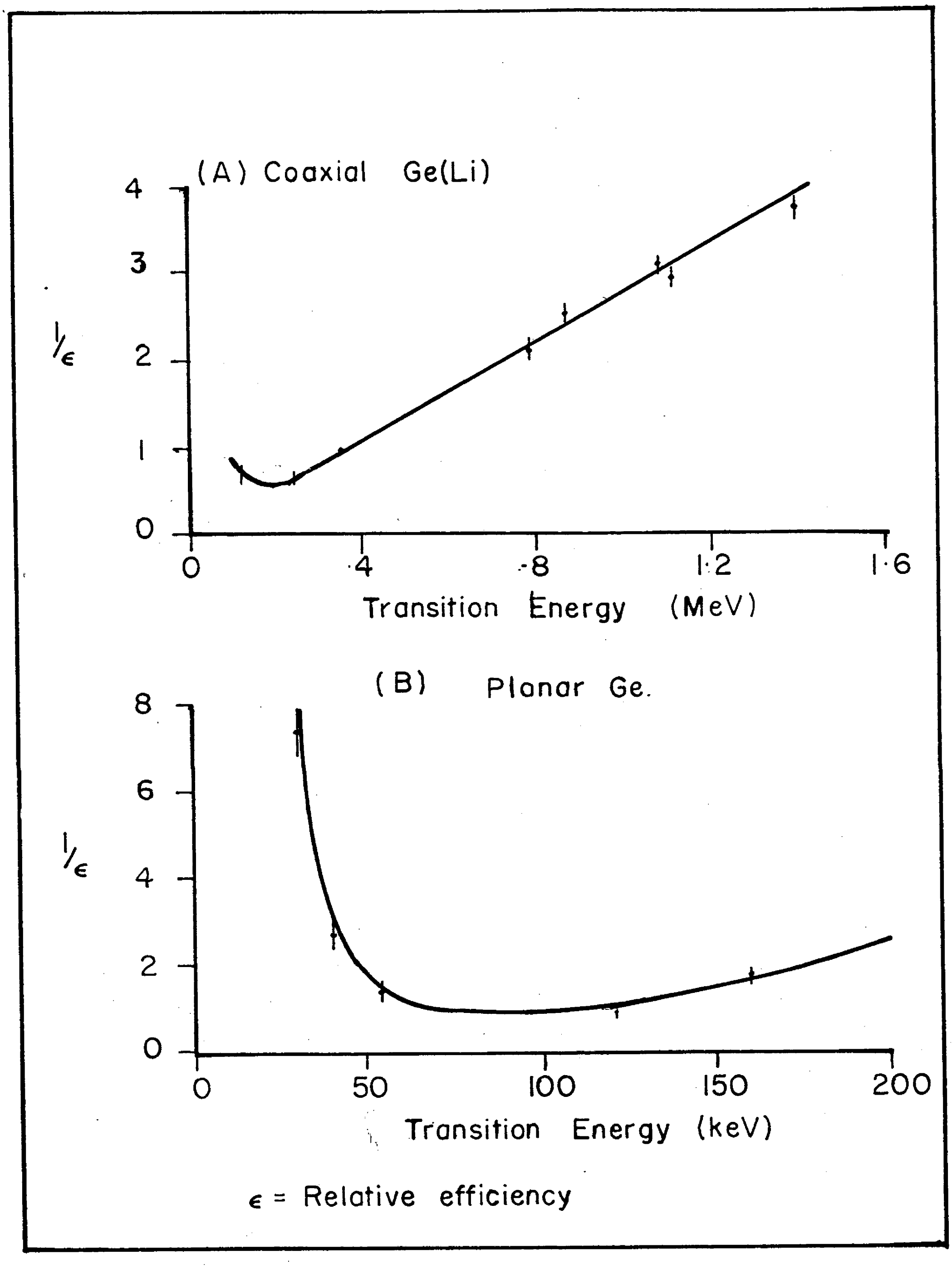

Fig. 2.5: Characteristic measure relative efficiency curves for gamma ray detectors. (A) Coaxial Ge(Li), (B) Planar Ge. The inverse of the efficiency is plotted against transition energy.

calibrations of the detector systems were conducted by placing a radioactive source (^{152}Eu or ^{133}Ba) near the target chamber, when the beam was on target.

The electric charge collected in the detectors was converted to an electronic signal by a pre-amplifier (ORTEC 120-4 for coaxial detectors) attached to the detector. The pre-amplifier had two outputs, one of which was used for energy analysis, the other for timing analysis. As the signals became distorted through noise and signal reflections over long lengths of cable, timing analysis, which required a very clean signal, was conducted very close to the detectors. Energy analysis, which was not so critically dependent on the signal shape, was usually conducted at a more convenient point (i.e. near the data collection computer).

A Tennelec TC205A amplifier was used to shape and amplify the pre-amplifier output for later energy analysis. The other pre-amplifier output was shaped by a Timing Filter Amplifier (ORTEC TFA 454) before being passed to a companion module, the Constant Fraction Discriminator (ORTEC CFD 473) for timing analysis. The output of this module was a negative logic pulse timed so that it related directly to the time of the original signal.

The method used to achieve this was the "Constant Fraction" technique. With this technique, the input signal to C.F.D. is split, one inverted and delayed, while the other is compressed in amplitude by a given fraction. When the two signals are added again, the resultant will pass through zero at a time which is almost independent of the original peak height (given that the fraction and delay were carefully chosen). The output pulse is therefore timed to commence when the above summed signal passes through zero. The fraction and delay utilised when coaxial Ge(Li) detectors were used were .30 and 14 ns respectively. This technique also obviates problems which may be caused by the initial slow rise of the Ge(Li) signals.

The difference in time between signals from two such systems was measured with a Time-to-Amplitude Converter (CANBERRA 1443 T.A.C.) unit. The output of this unit was used in determining coincident events. The rest of the electronics required were used in common with the other detection systems, and are discussed in §2.4.1. Fig. 2.12

of that section shows the above system in use.

The planar detector pre-amplifier system (ORTEC 117B) differed somewhat in that only one output was given. To get around the problems discussed previously, this signal was fed to an Extrapolated Zero Strobe unit (CANBERRA 1426). Not only did this unit provide a timing signal (determined by extrapolating the incoming signal back to zero voltage), but it also provided an output signal that was identical to the input signal. It was this secondary signal which was used for energy analysis.

After analysis, the spectrum from a Ge(Li) detector appeared like the idealised version shown in Fig. 2.6. Here it is evident that there are four separate regions to the spectrum. The first, of most interest, is the peak corresponding to total absorption of the photon energy (photopeak). Secondly, at lower energies, there is a large background due to incomplete absorption of the photon energy (Compton background). The third section is the low energy peak corresponding to the energy deposited when the gamma ray is scattered by 180° and then escapes the detector (back-scatter peak). At all energies lower than the total energy there is a small background (the fourth region) which is due to incomplete charge collection in the detector. In the vicinity of the photopeak, this gives the impression of a "step" background as shown by the dotted line in Fig. 2.6.

Not all the gamma rays detected come from fusion products after the (HI,xn) reaction. Other events can give rise to gamma transitions which are detectable and which may possibly be confused with transitions of interest. Some of the more common are:

(a) Coulomb excitation of the target. The target nucleus is often excited to its first excited state, but only rarely to states of higher energy. As a result, a very intense transition is often seen in singles spectra. In gamma-gamma coincidence spectra though, the intensity drops off markedly.

(b) Inelastic neutron scattering. Observable in singles spectra, it is a particular problem in neutron-gamma coincidence measurements. The neutrons can scatter off any of the material surrounding the target, but those that scatter from the target chamber, the Germanium

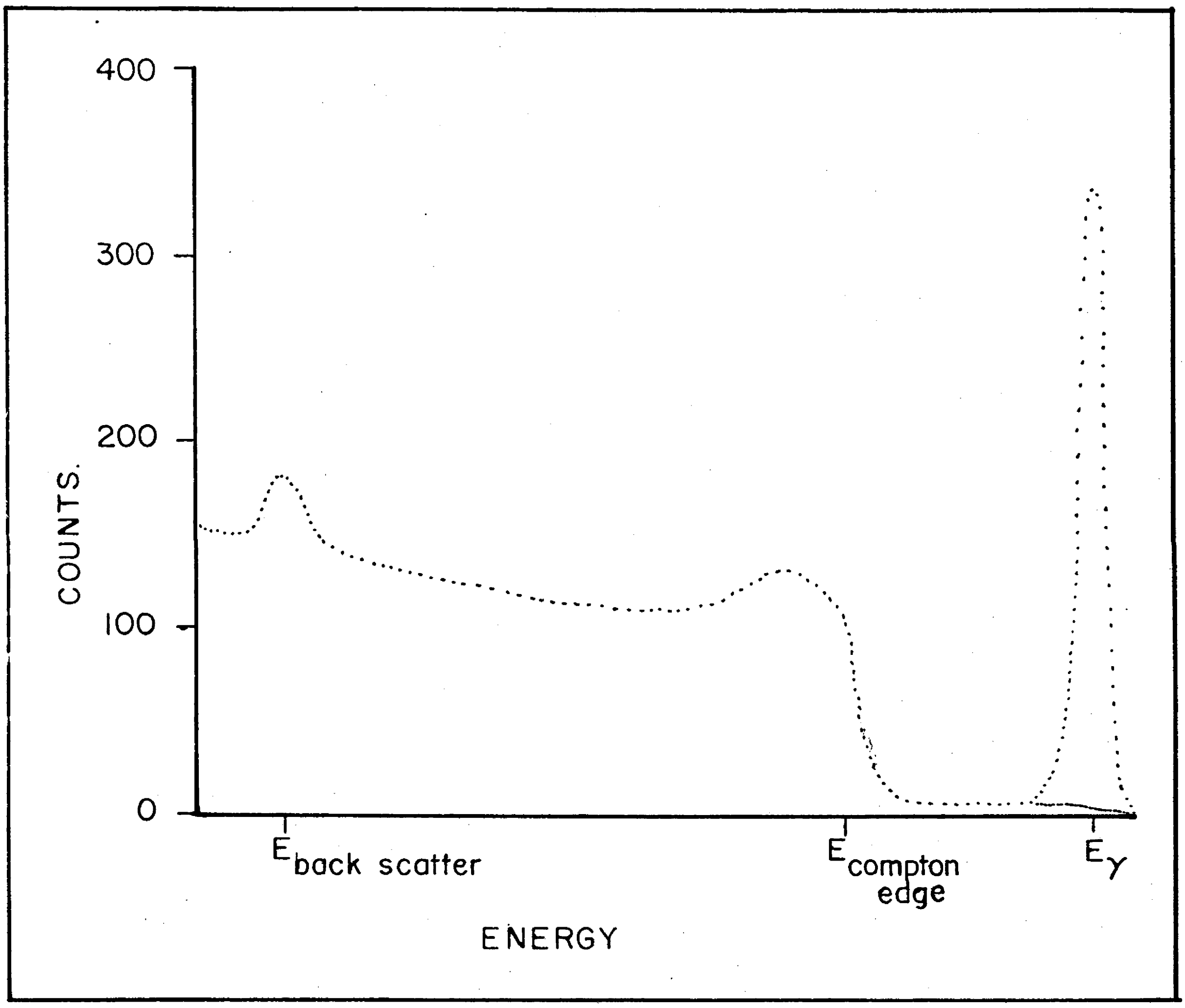

Fig. 2.6: Idealised spectrum resulting from the detection of a gamma ray of less than 1 MeV energy. The dotted line represents a continuation of the background due to incomplete charge collection.

of the detector, or Teflon (used as an absorber in front of the Ge(Li) crystal and in the collar of the detector canister) are observed most. The first gives rise to an 847 keV gamma ray from ^{56}Fe. The second gives gamma rays which can be easily identified by their high energy tail — caused by collection of energy from the recoiling nucleus. The last of the above gives a gamma ray of energy 197 keV (from ^{19}F). This transition is often of use, as its known 89 ns half life can be used as an internal check on the time contribution of the system.

(c) Escape Peaks. When the k X ray of Germanium escapes the crystal after a photon is absorbed, a secondary peak ("escape peak") can be observed. This occurs mostly when the photon absorption happens near the crystal surface as the probability of the escape of the k X ray is higher there. These peaks were observed, but only for the intense Paladium X rays.

2.3.3 Detection of Neutrons

Neutrons, being uncharged particles, cannot be detected directly. Their detection depends on their being scattered by some other medium. The NE213 liquid scintillator used in the present experiments actually detects protons which have been scattered by the neutrons. The scintillator also detects gamma rays and so some method of discrimination must be used to determine which are the neutron associated events. Fortunately, this is possible with the above detector.

The light output of the scintillator has two main components. The first, a "fluorescence" component ($\sim$ 90% of the total light intensity), has a decay time of approximately 3.7 ns. The second is a "delayed fluorescence" component ($\sim$ 10% of the total light intensity) which has an approximately 1 μs decay time. Now the recoiling protons cause ionisation quenching to occur in the scintillator, which in turn decreases the *intensity* of the "fluorescence" component. It has little effect on the "delayed fluorescence" component or the lifetimes of the two components.

This effect allows for the discrimination of neutron associated events from gamma ray associated events as the two will have different effective rise times of their light output (and therefore in the output pulse of the detector as well).

The output pulse was shaped by a delay line amplifier (ORTEC 460) in order to preserve the rise time of the signal. The shape of the pulse is now such that the fall time is also proportional to the rise time. Pulse shape analysis is then done by the ORTEC 458 P.S.D. unit. This unit measures the time the pulse takes to fall from 90% of its maximum height to 10% of its maximum height. By using the fall time, the process is virtually independent of the pulse height. Pulse height discrimination was also used as this allowed the rejection of many low energy events. Fig. 2.7 shows a practical application of the system. The first, sharper peak, is caused by gamma rays, and the other, broader, peak by neutrons. The separation of the peaks, which is typical of experimental results, is adequate to successfully distinguish between the two types of events.

The photomultiplier attached to the scintillator also gave a sharply defined negative pulse of sufficient amplitude (~ -2 V) to allow the pulse to be fed directly to an ORTEC 473 C.F.D. unit. Leading edge timing was used.

2.3.4 Detection of Electrons

For the detection of electrons, a cooled lithium drifted Silicon (Si(Li)) detector was placed in the target chamber. The detector, when in operation, was cooled by liquid nitrogen. To focus electrons at the detector, and at the same time shield the detector from gamma rays, a magnetic lens of the "Mini-Orange" type was used [Is75]. The detector system so formed is shown in Fig. 2.8.

In the "Mini-Orange", a central plug of lead 2.5 cm long effectively shielded the Si(Li) detector from gamma rays of less than 1500 keV energy. Surrounding the central plug, five rectangular rare-earth magnets (each of 1 kG) were symmetrically arranged. The axis of symmetry of the detector was at 125° to the beam. The magnetic field bent electron paths originating at the target, towards the detector. The geometry of this system effectively determined the relative efficiency of electron detection; for high and low energy electrons

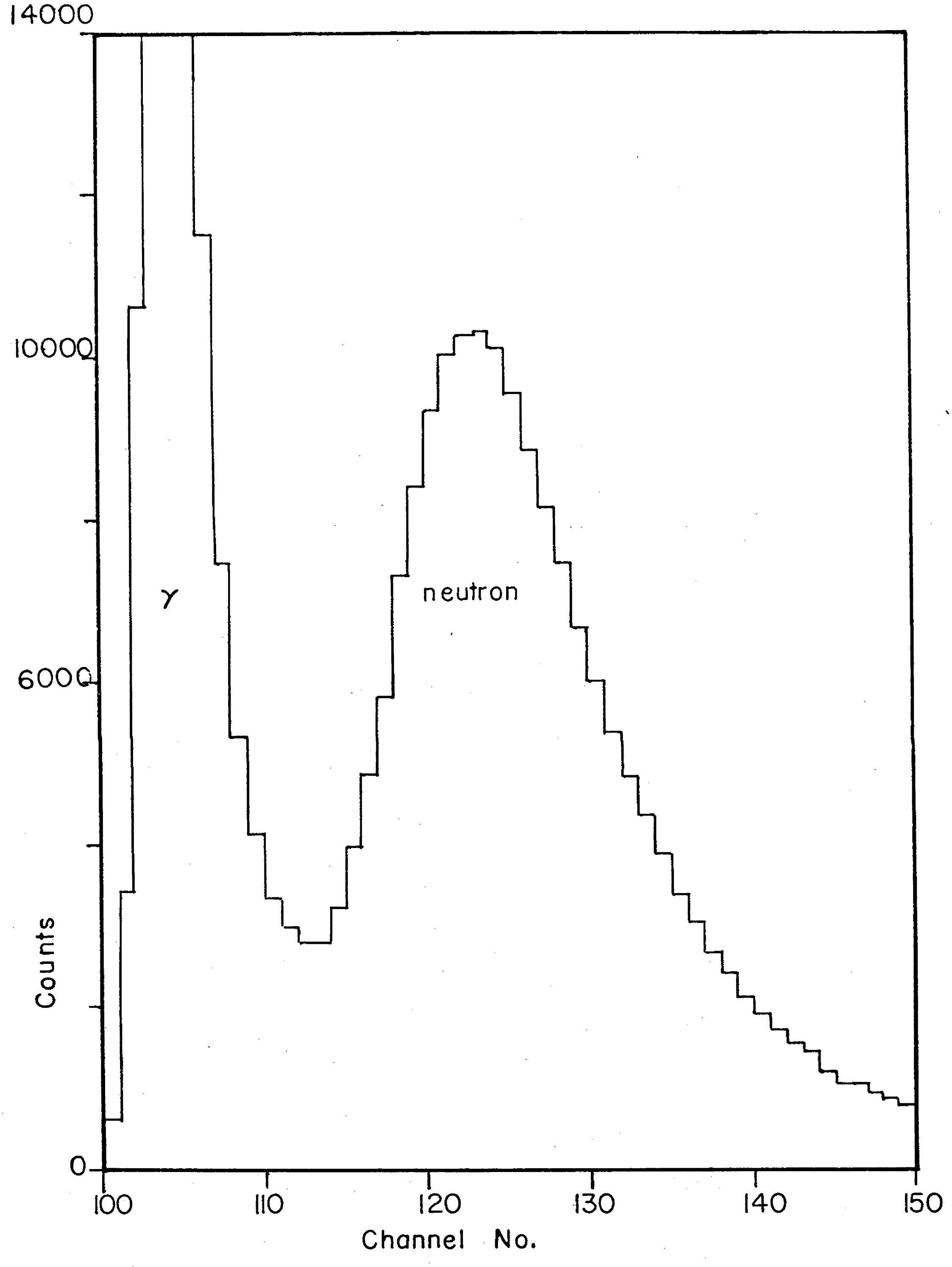

Fig. 2.7: Pulse shape discrimination achieved during a $^{110}Pd(^{13}C,4n)^{119}Te$ (59 MeV) reaction.

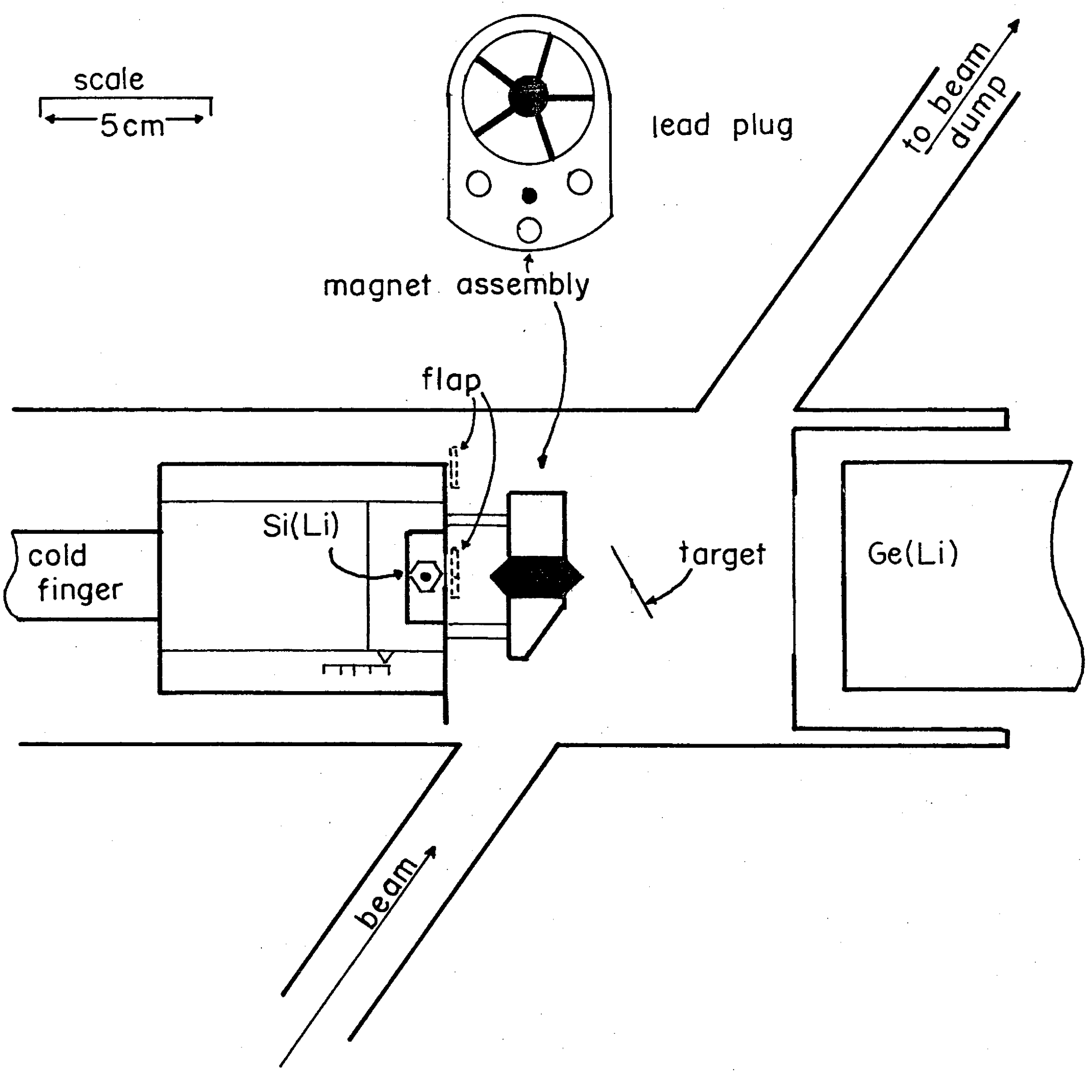

Fig. 2.8: Block diagram of the Mini-Orange electron spectrometer.

(which are bent either too little or too much) are not focused properly at the detector. The measured relative efficiency (using a ^{152}Eu source [Ma66]) is shown in Fig. 2.9.

The magnet system also serves to increase the effective solid angle of the detector relative to the situation where the magnet assembly is not present (by a factor of ~ 3). A purpose in which the magnet is less successful is in screening the electron detector from the large flux of Delta rays arising from the passage of the beam through the target. To stop these, a thin Nickel foil, sufficient to stop 30 keV electrons, had to be placed in front of the detector. Without the foil, measurements were not possible.

To minimise the collection of Compton scattered electrons, the material surrounding the target was reduced to the minimum possible, and was constructed from Aluminium. Compton scattering could also produce gamma rays which had the ability to reach the detector. To check the seriousness of this situation, an Aluminium flap ($\sim$ 2 mm thick) was placed in front of the detector, and the experiment re-run. The flap was sufficiently thick to absorb electrons of energy up to 1 MeV, yet not so thick as to greatly affect the gamma rays. As no discrete gamma rays were observed, no further precautions were taken; the analysis of the experiment not being altered.

The choice made in target thickness and position was the result of several compromises. Firstly, if the beam spot moved during an experiment, the position of the target moved off axis, thereby changing the range of angles in which electrons were detected. The thickness of the target as seen by the electrons therefore changed as well. To minimise the effects of this movement, a target angle of 62.5° to the beam was chosen (this is the angle giving "mirror reflection" for the beam and detector axis). Given this angle, the target thickness was chosen as 1.8 mg/cm^2. This thickness allowed reasonable resolution to be obtained ($\sim$ 4 keV) even with the presence of the (necessary) Nickel foil. It was also thick enough to stop approximately 50% of the recoiling nuclei in the target.

The effect of the nuclei recoiling into vacuum was not severe if the electrons were emitted promptly, for then the "source" position does not change appreciably. If, however, the transition is delayed,

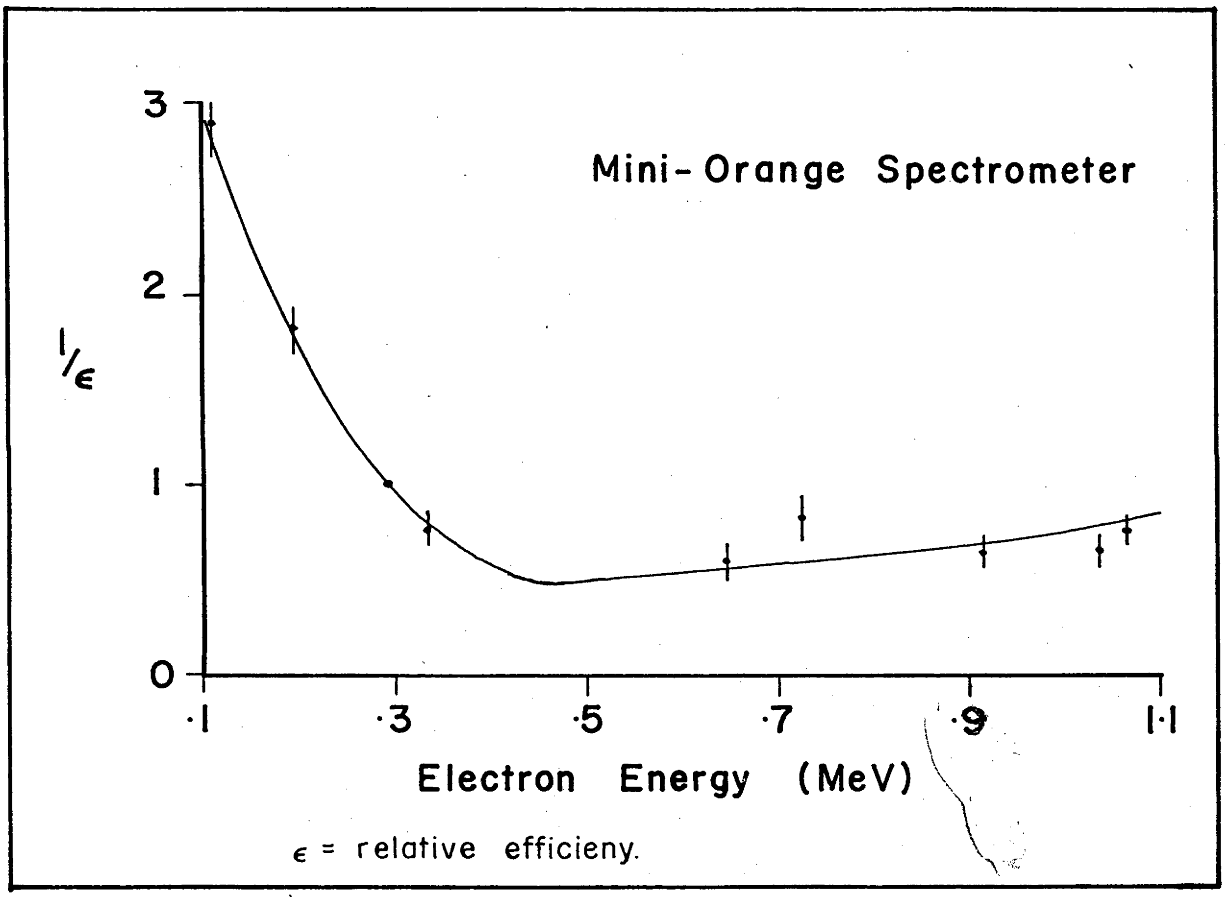

Fig. 2.9: Measured relative efficiency curve of the Mini-Orange electron spectrometer. The inverse of the efficiency is plotted against electron energy.

then the nuclei has time to move both away from the detector and off the detector axis (~ 3 mm total movement per nanosecond of delay).

A small amount of movement (< 1 cm) *away* from the detector should have little effect on the efficiency as the magnet focuses the electrons onto a broad target — the 1 cm wide detector. Movement away from the detector axis, however, introduces an asymmetry into the angles accepted by the Mini-Orange. This effect was measured using a ^{152}Eu source and the results are plotted in Fig. 2.10. The results shown here can be used in attempts at correcting for this effect.

A Doppler shift which is caused by the recoil velocity produces a broadening of the electron spectrum; this did not affect the efficiency of detection.

The angular distribution of the emitted electrons can also affect the efficiency of the Mini-Orange. This will be discussed further in §2.4.3.

The signals output from the detector were analysed by electronic units similar to those used for Ge(Li) detectors. However, as mentioned before, the delay for the constant fraction timing technique depends on the detector, and must be carefully chosen. Constants used for the Si(Li) detector were a fraction of .3 and a delay of 8 ns.

2.3.5 Target Chambers

A variety of target chambers were used, all being made from stainless steel, with thin walls (.3 - .5 mm) in the detection plane. The particular shape and size was determined by experimental requirements. The targets were mounted on a stainless steel ladder, which allowed rapid exchange of targets and radioactive sources with accurate repositioning.

Two chambers deserve special mention: the first being the target exchange chamber of the Mini-Orange detector (shown in Fig. 2.11). This chamber allowed targets and sources to be exchanged without having to warm up the Si(Li) detector. With care and practice, the target could be repositioned within approximately .3 mm of its original setting.

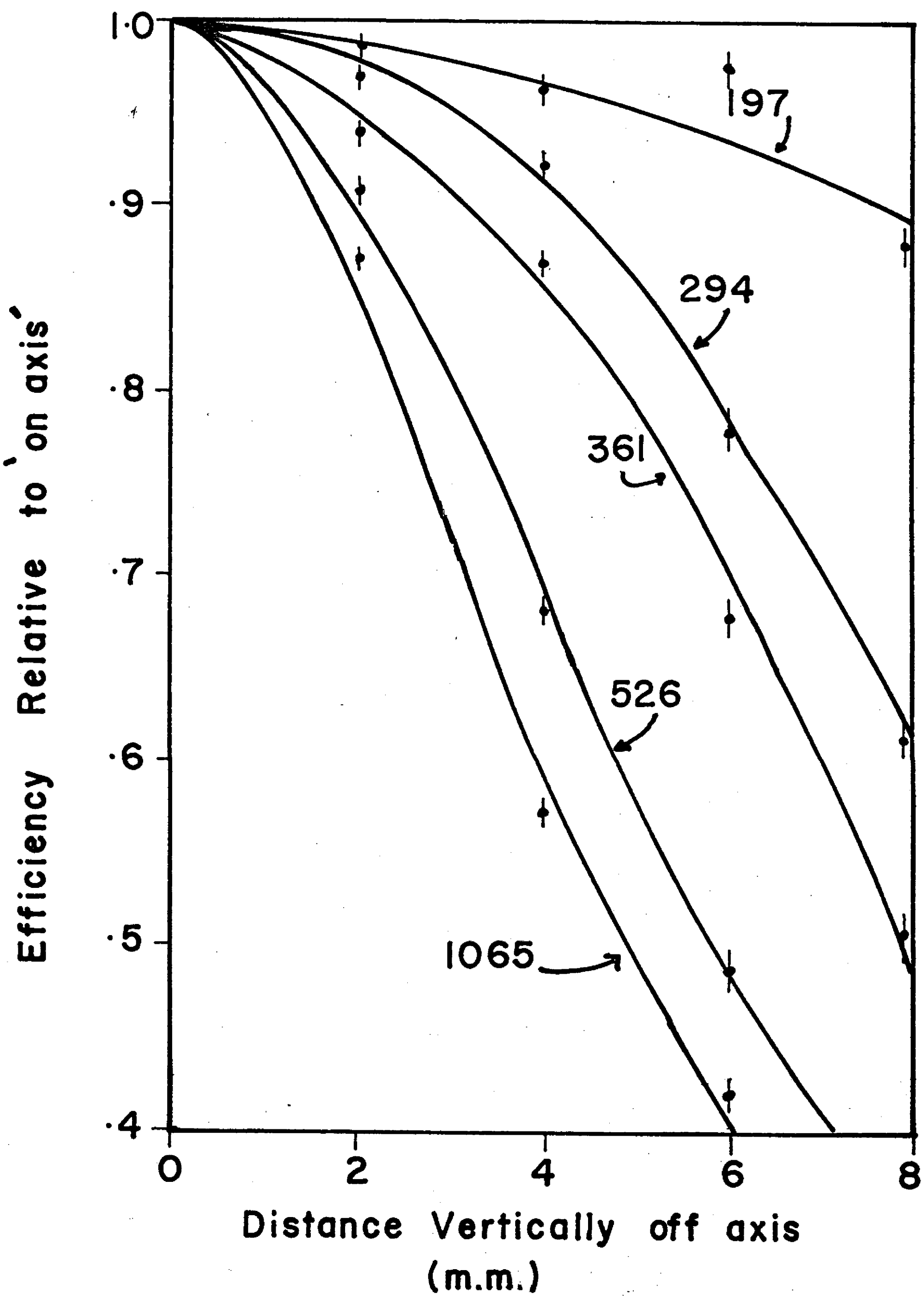

Fig. 2.10: Effect, on the Mini-Orange relative efficiency, of the radioactive source being placed "off" axis. The intensities relative to the intensities observed "on" axis are given for some of the conversion electrons emmitted by a ^{152}Eu source. The curve numbers represent the electron energy in keV.

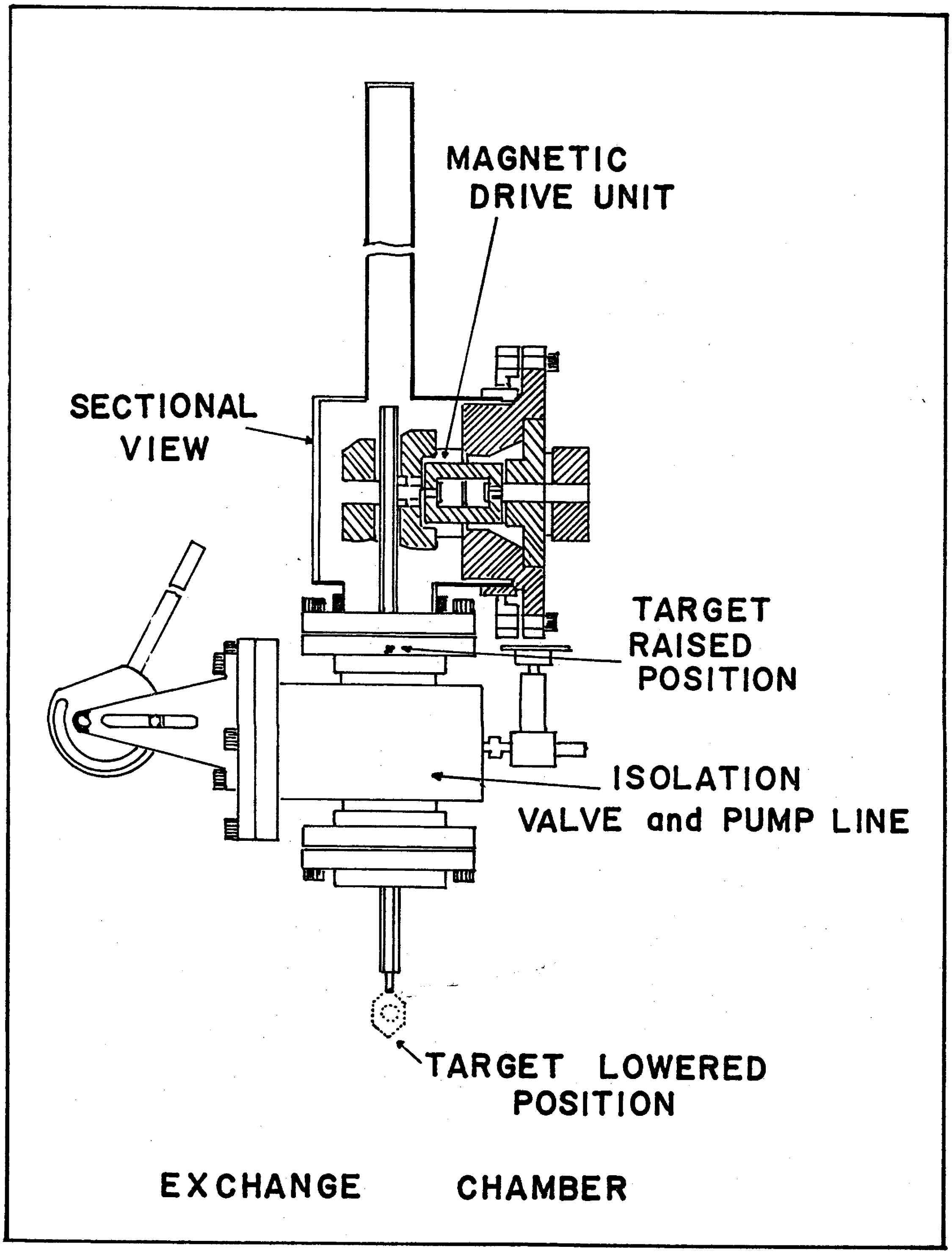

Fig. 2.11: Target exchange chamber for the Mini-Orange.

The second chamber had a thin window of .3 mm Mylar mounted on a port at 90° to the beam. This special chamber made possible the detection of a 39.8 keV transition. Gamma and X rays of less than 20 keV were also observed.

2.4 PROCEDURE AND ANALYSIS

2.4.1 Acquisition of Data

A block diagram of the physical set-up of a typical experiment is shown in Fig. 2.12 — a gamma-gamma coincidence experiment in this case. A block diagram of the electronic units used in this experiment is given in Fig. 2.13. The pulse shapes are also shown throughout the circuit.

It will be noticed in Fig. 2.13 that the "singles" and "coincident" gamma ray data are analysed in a similar manner — the main difference being that the T.A.C. signal is used as a gate for determining the coincident events.

The purpose of the Timing Single Channel Analyser (ORTEC TSCA 454) was to restrict the range of pulses (and hence events) to those voltages acceptable by the Analog to Digital Converter (CANBERRA ADC 8060). This was managed by gating with the output of the TSCA, a linear gate and stretcher (CANBERRA 1454), which in turn shaped the pulses for input to the ADCs. The output of the ADCs was transferred via an interface to the data collection computer (HP-2100A). The coincidence information was stored on magnetic tape in event-by-event mode. The singles spectra were collected in the computer and were periodically written onto the magnetic tape.

The efficiency of transferring the analog signal to the computer was less than unity. Some signals were lost in the electronics due to dead time effects. The major source of these losses was between the linear gate and stretcher (L.G. and S.) and the computer. By recording the number of gate pulses arriving at the L.G. and S., and the number of counts in the stored spectrum, this effect could be estimated.

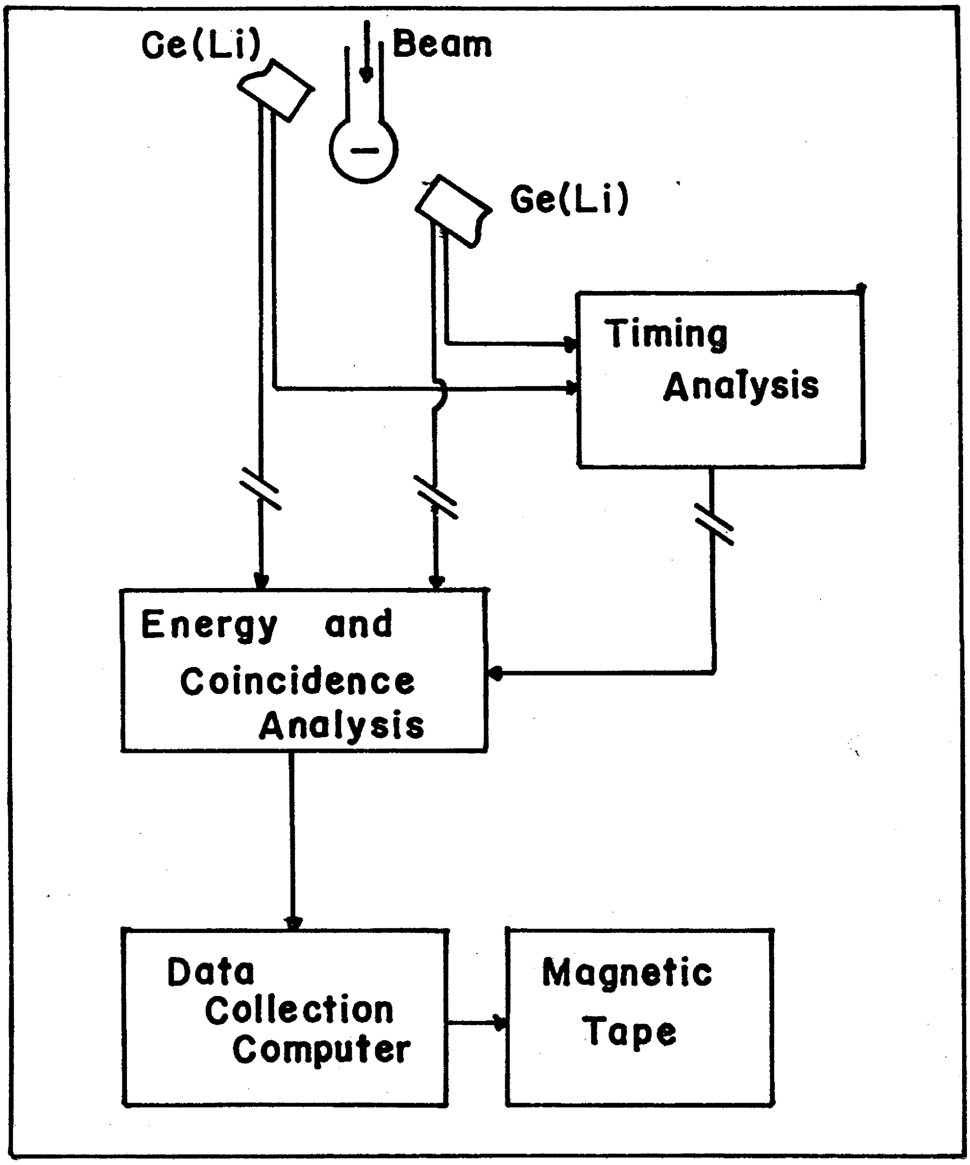

Fig. 2.12: Block diagram of a typical γ-γ experiment.

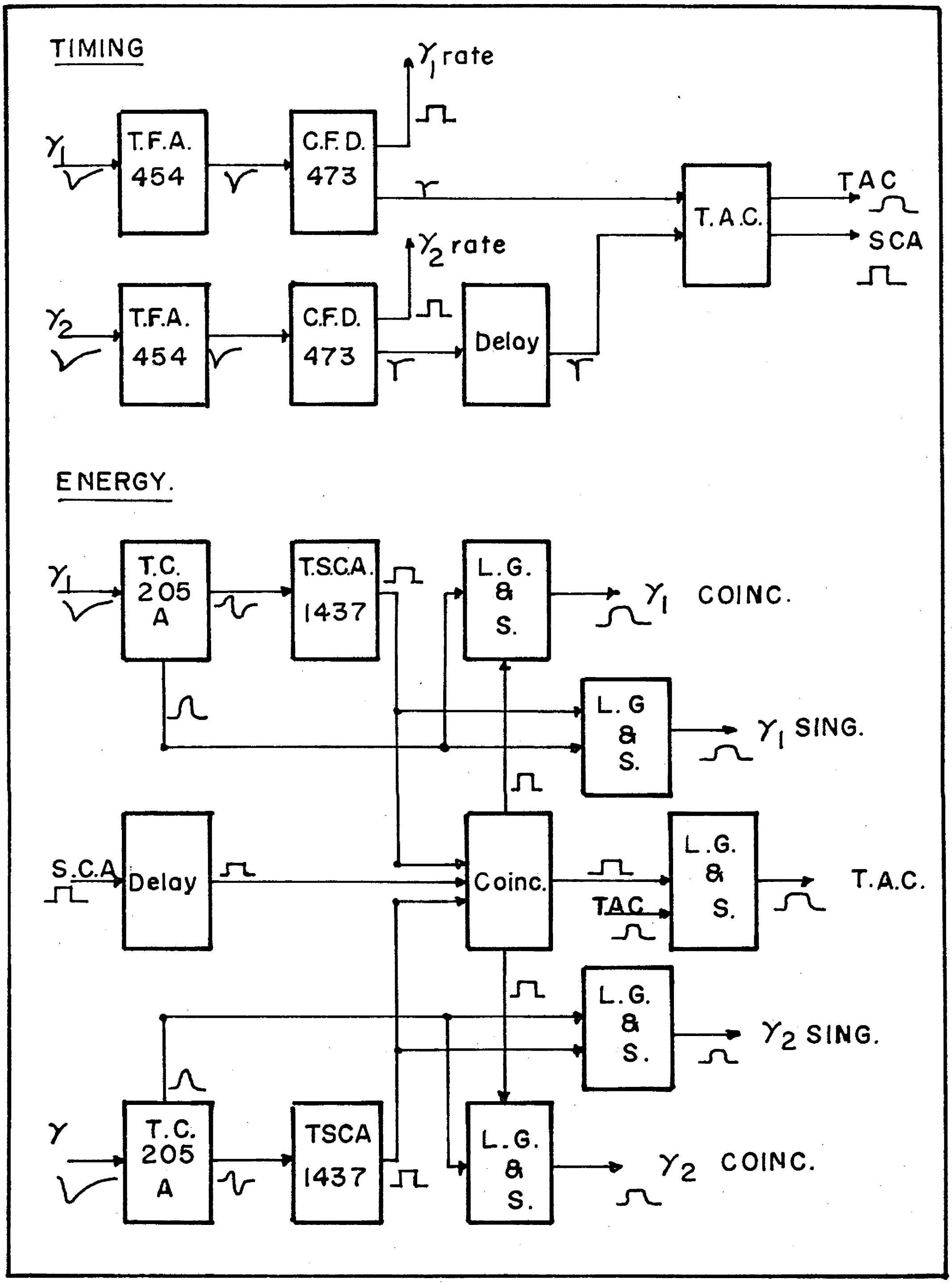

Fig. 2.13: Block diagram of the electronic circuitry required for the experiment shown in Fig. 2.12. Pulse shapes are also shown.

2.4.2 Analysis of Coincidence Data

The coincidence data was analysed with the aid of the computer programs SUPER and HPSRT. Energy and/or time windows were set [up to 96 being accepted by SUPER] and tape sorting provided the corresponding coincident spectra. Fig. 2.14 gives an example of a three parameter sort, where windows are set on the gamma (one) spectrum and the time spectrum, while the second gamma spectrum is projected. The gates labelled (A) represent peaks of interest. In order to approximate the spectra due to the background under the peaks, gates labelled (B) were set. In the event of many peaks lying close together, it was often not possible to place the background gate close to the peak gate. When these situations occurred, background gates at higher and lower energies than the peak energy were set (e.g. B_1 and B_2 in Fig. 2.14), and a representative background found by linear interpolation.

Gates were also set on the T.A.C. (time) spectrum. Gate (C) represents prompt plus random events and gate (D) represents delayed plus random events. Assuming no delayed component, correction for random coincidences can be made. To obtain the estimate of gamma rays in *prompt* coincidence with transitions in gate A the following manipulations must be made, given that the sorted spectra gating simultaneously on gates (A) and (C) is represented by $[(A) \otimes (C)]$:

$$\{[(A) \otimes (C)] - X[(B) \otimes (C)]\} - Y\{[(A) \otimes (D)] - [(B) \otimes (D)]\} ,$$

where X scales the number of counts in the background gate to the background under the peak. Y similarly scales the time spectra.

Areas are then taken for *all* the peaks observed in the net coincident spectrum. In determining these areas, the background was assumed to take the form of a step function for reasons mentioned in §2.3.2. For peaks of poor statistics, the first approximation to the step function — a straight line — was used. As the peaks after background subtraction can be well represented by a shape, a program was incorporated in HPSRT to fit the sum of up to four Gaussians to a peak region, allowing the intensities of partially resolved peaks to be estimated.

At times, backscattering of intense transitions produced true

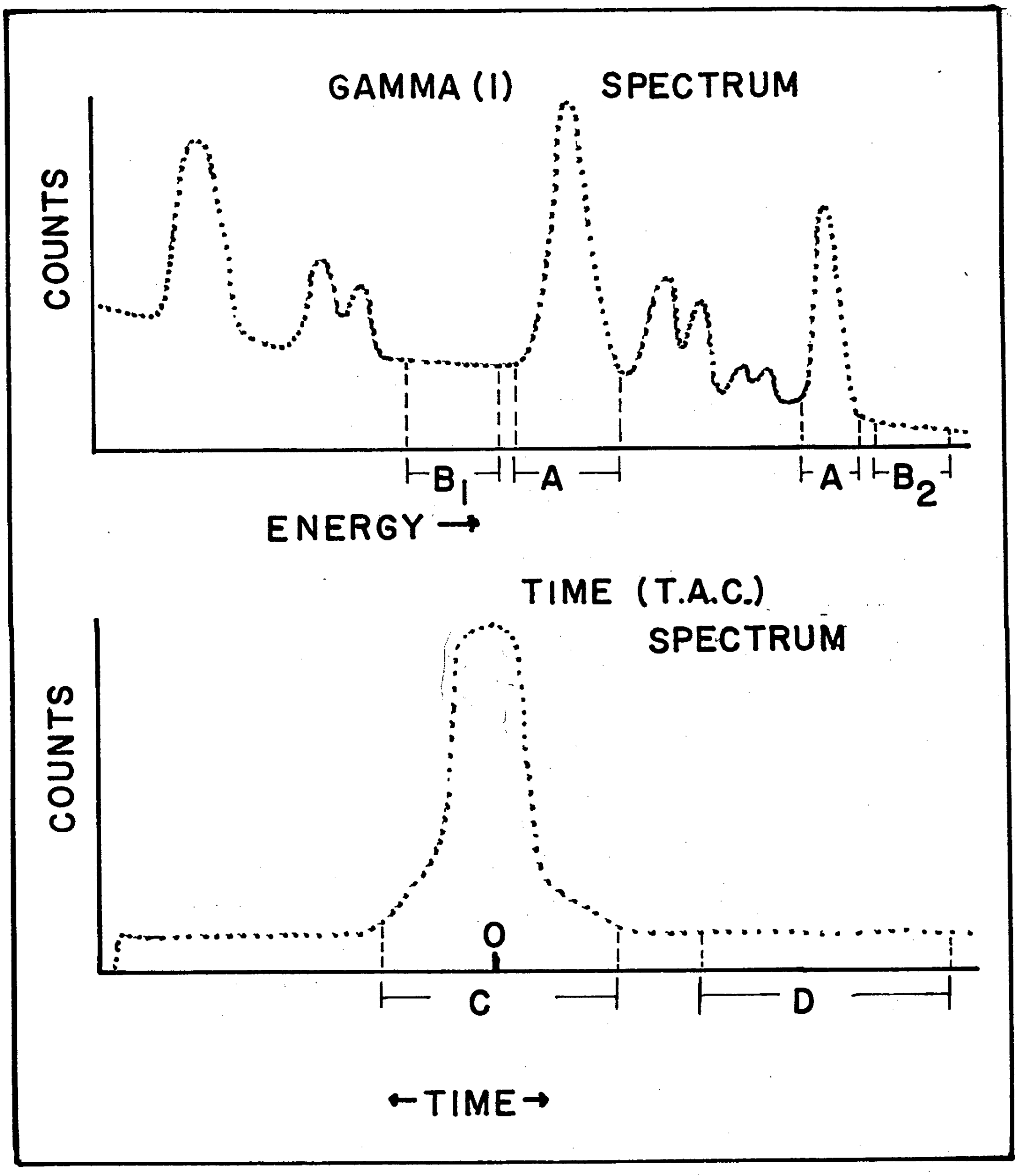

Fig. 2.14: Idealised spectra showing where energy windows for sorting would be set. (A) On a gamma total coincidence spectrum. (B) On a time (T.A.C.) spectrum.

coincident events in the Ge(Li) detectors. If one of these coincides in energy with a peak gate, a small peak is observed in the sorted spectrum. Conversely, if one of the events coincides with a background gate, oversubtraction will occur, leaving a dip in the net spectrum.

After finding peak areas from many sorted spectra, corrections for the detector efficiencies are made, the information summarised in a "Coincidence Matrix", and the level scheme deduced.

To measure lifetimes of excited states, the time spectra of transitions were projected. Despite all precautions the time zero of the T.A.C. spectra changed as a function of energy.

The magnitude of the change was found by plotting the "$t = 0$" points against energy for T.A.C. spectra over a range of energy windows. It was also possible for the shape of the T.A.C. spectra to change slowly with energy. To obtain a true representation of a "background" T.A.C. spectrum, the spectrum had to be manufactured from observed T.A.C. spectra. A weighted average of the spectra from "background" gates both higher and lower in energy than the transition energy [after each had been shifted by the required amount] formed a T.A.C. spectrum that had been corrected not only for any time shift, but also for any change in shape of the T.A.C. spectra. This manufactured spectrum was then subtracted, channel by channel, from the T.A.C. of the peak gate.

Observed time spectra of transitions of the form P(t), where

$$P(t) = \int_0^\infty F(t)\, G(t-t')\, dt' ,$$

where G(t) is the T.A.C. response curve, and F(t) represents the form of decay. E.g. if only one state has a measurable half life, F(t) is an exponential. It can be shown that away from the region of the prompt response, P(t) approximates F(t) [Si65].

The extraction of half-lives is more complicated if more than one state has a measurable half life, especially if they are in cascade. Gating on appropriate gamma transitions in γ-γ coincidence experiments can effectively eliminate all bar one of the isomers but this requires reasonably intense transitions if one is to obtain half-lives with small errors. If the intense transitions are not available, as in the masurement of the half-life of the 5187 + x keV level in ^{119}Te, n - γ coincidence measurements provide spectra with good statistics. In these measurements, allowance must be made for lifetimes other than the one being measured, and the amount of direct feeding to the state of interest. An example of the decay, in series, of two states with comparable half-lives is shown in Fig. 2.15. It can be seen from this that the time zero must be known in order to fit the data, and that certain combinations of parameters can give rise to a function which can be mistaken for the decay of a single state — given that prompt radiation will mask the form near $t = 0$. This was found to be the case in ^{119}Te. Fortunately, most of the parameters could be estimated and given errors. The time spectra away from the prompt region were then fitted by a non-linear least squares procedure.

2.4.3 Angular Distribution Effects

As mentioned in §2.1, the angular distribution of the gamma rays, as measured by "singles" data collection, contains information on the spin of initial and final states of the transition. The measured distribution can be fitted by the expansion,

$$W(\theta) = W_0[1 + A_2P_2(\mathrm{Cos}\theta) + A_4P_4(\mathrm{Cos}\theta)] ,$$

where $P_k(\mathrm{Cos}\theta)$ are Legendre Polynomials, with θ representing the angle relative to the beam direction.

The parameters A_k can of course be evaluated by theoretical models. The interpretation of angular distribution data in this thesis relies on the tables published by Yamazaki [Ya67]. These tables list values of A_k which have been calculated for both totally and partially aligned initial states. The degree of alignment is represented in the calculations by a Gaussian distribution of the nuclei about the $M = 0$ substate (or $M = \pm\frac{1}{2}$), for Diamond *et al.* [Di66] showed that this was a reasonable assumption after (HI,xn) reactions.

Using these tables, one can determine the multipolarity and mixing ratios of transitions. Practical applications are given in Chapter 3.

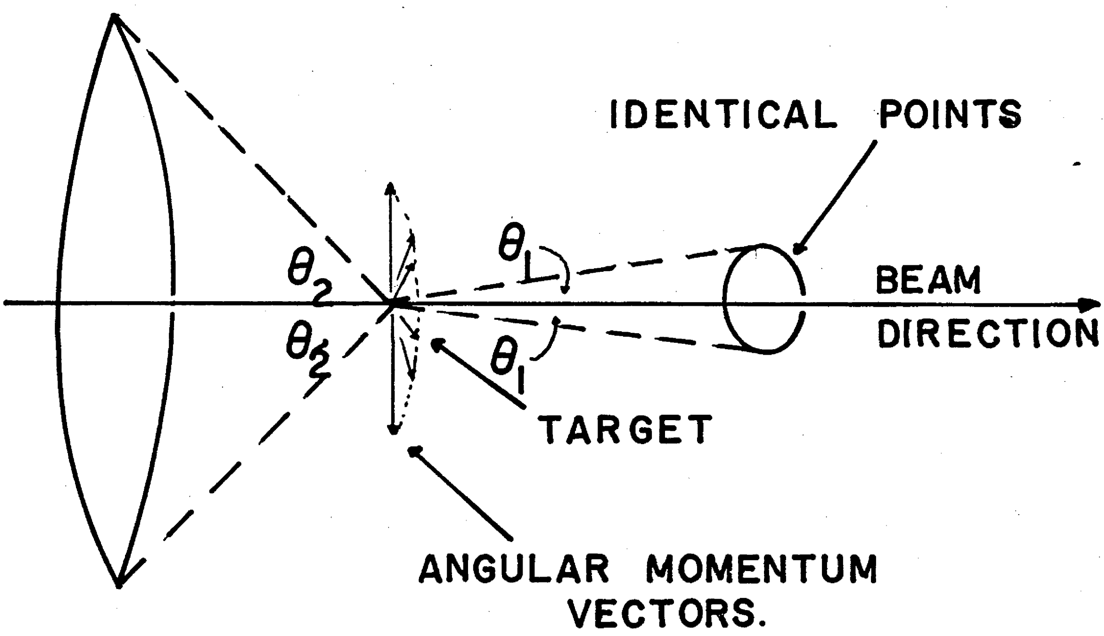

Fig. 2.16: Cylindrical symmetry about the beam axis caused by angular momentum alignment following (HI,xn) reactions.

If the angle at which the detector is placed is chosen with care, the angular distribution effects can be ignored, and the total intensity measured. The angles at which this is possible are those where the second term in the above explanation goes to zero, i.e. when $P_2(\cos\theta) = 0$, which occurs at $\theta \approx \pm 55°$ and $\theta \approx \pm 125°$. At these angles, the third term in the expansion is usually quite small, i.e.

$$|A_4 P_4(\cos 55°)| \leq .01$$

which allows the approximation to be made.

To be more general, though, the coefficients of the above expansion need to be expanded as

$$A_i = Q_i \, \alpha_i \, b_i \, A_i^{max} ,$$

where A_i^{max} is the value which corresponds to a gamma transition from a completely aligned nucleus. This is the maximum value that A_i can take.

α_i are attenuation coefficients which allow for incomplete alignment of the nucleus. It is A_i^{max} and $\alpha_i A_i^{max}$ which are tabulated in [Ya67].

b_i are particle parameters. These are defined to be unity for transitions involving the emission of gamma rays. For transitions of other types, e.g. emission of conversion electrons, the b_i values are dependent on the multipolarity of the transition. Values of b_i for conversion electrons are tabulated in [Ha68b].

Q_i are attenuation coefficients which allow for the finite solid angle of the detector (Geometric Attenuation). The efficiency of detection of gamma rays, or particles, across the width of a detector will depend on both the detector efficiency, and the angular distribution of the emitted radiation.

Values of Q_i for detectors of cylindrical cross section (especially coaxial Ge(Li) detectors) have been calculated — e.g. [Ro53] and [Fe55]. These determinations have all assumed that the radioactive source was unaligned, thereby preserving the cylindrical symmetry about the detector axis. For nuclei aligned as a result of a (HI,xn) reaction, this is no longer a valid assumption.

Using the beam direction as axis, the angle, θ, at which "spot" measurements would be identical, defines a *cone* about the axis. This is shown in Fig. 2.16. The intersection of these cones with a cylindrical detector will result in an angular dependency of the Geometrical Attenuation coefficients.

The effect of this was made negligible in the case of gamma ray angular distribution measurements by simply placing the detectors sufficiently distant from the target. The Mini-Orange, however, subtends an angle of approximately 90° at the target, and the correction may not be trivial. It was necessary to calculate the correction, for all efficiency measurements were conducted using unaligned radioactive sources.

The efficiency of detection of full energy peaks in the electron spectrum is determined by the angular range of electrons of given energy that is accepted by the magnet assembly. For a first approximation, this can be considered as a ring, centred on the Mini-Orange axis, whose width and radius depend on the energy of the electron. The calculation of Q_i for such a ring is given in Appendix 1. The calculation can easily be extended to more complicated cylindrical detectors, e.g. Ge(Li) detectors, but we will not discuss this further.

It is interesting to note that when the detector axis is aligned with a zero point of $P_2(\mathrm{Cos}\theta)$, as is the case with the Mini-Orange, then Q_2 is equal to zero no matter what angular range is accepted! The value of Q_4 is not so simply evaluated, but it is noted that one example when Q_4 equals zero is the angular range, about the Mini-Orange axis, of $0° \rightarrow 40°$. This corresponds, roughly, to full acceptance by the Mini-Orange magnet.

Values of Q_4 for some other angular ranges are given in Table 2.3. When these are combined with the (usually) small values of $\alpha_4 b_4 A_4^{max}$ (see Chapter 3), the overall effect is very small. Conversion coefficients determined with the aid of a Mini-Orange spectrometer at 125° to the beam are therefore affected little by the angular distribution of the electrons.

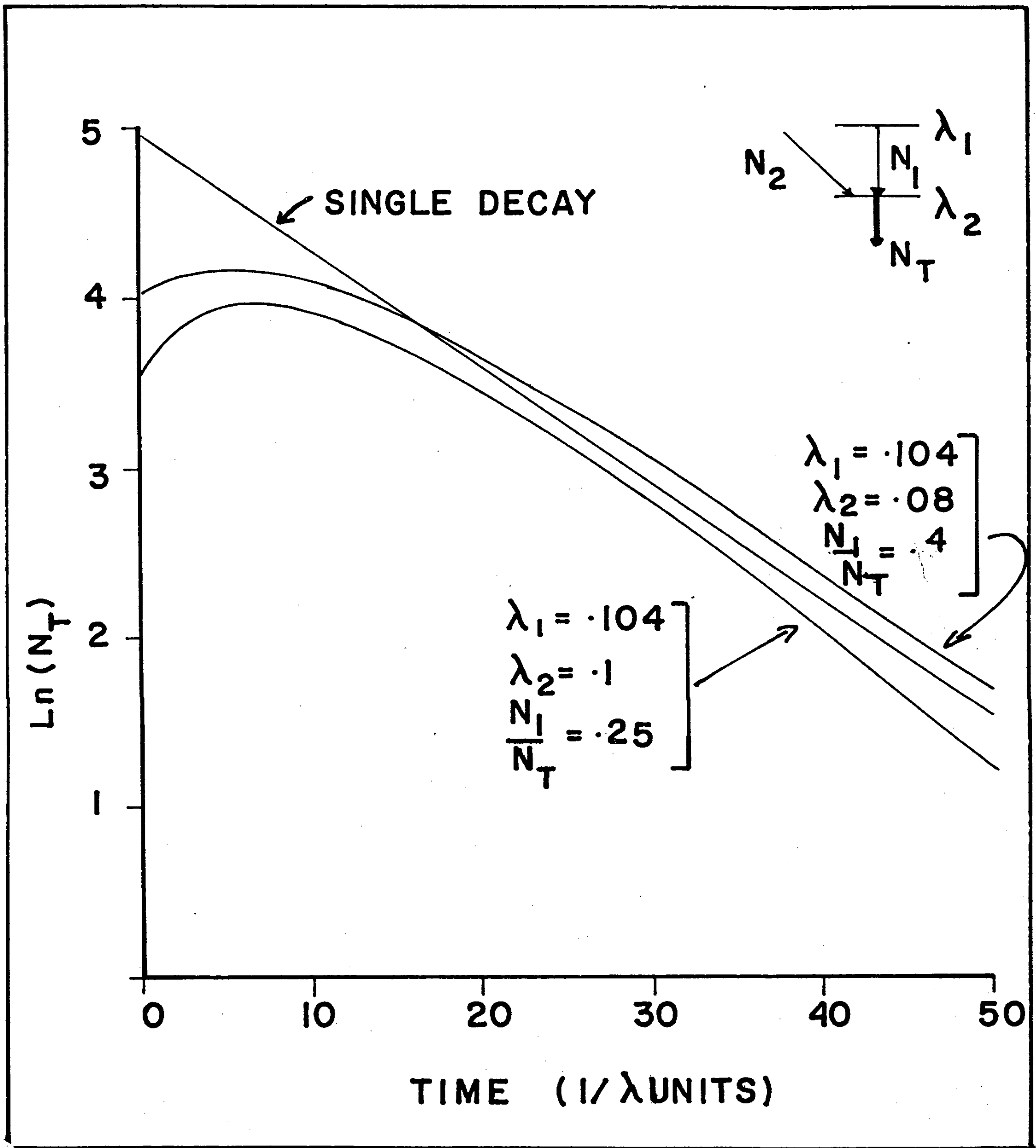

Fig. 2.15: Some examples where two decay components can produce spectra that can be mistaken as being caused by only one decay component.

Table 2.3

Values of Q_4 for Detector Angle of 54.74°, and smallest angle accepted of zero degrees

θ_2	Q_4
10°	-.36
20°	-.28
30°	-.18
40°	0.00
45°	-0.02

2.4.4 Multipolarities

Angular distribution measurements are only able to indicate the magnitude of the difference in spin between initial and final levels, and so are insensitive to a change of parity. There are several ways of determining when a parity change occurs, and two of them are used in this thesis — i.e. measurement of conversion coefficients, and partial half lives of transitions.

For any given nucleus, the magnitude of the conversion coefficients depends on the energy of the transition. An example of these, for the k shell conversion in Tellurium nuclei, α_k [Ma74] is shown in Fig. 2.17. If we consider the simple case of only dipole or quadrupole transitions occurring, then it can be seen from Fig. 2.17 that E1 and M2 transitions should be capable of being uniquely determined. All other transitions (i.e. of E2, M1, E2/M1, and E1/M2 type) may be confused in various energy regions.

Sometimes this ambiguity can be resolved if the ℓ shell conversion coefficient can be determined — the k/ℓ ratio being a sensitive measure of multipolarity. However, the ℓ shell conversion coefficient is often difficult to obtain experimentally because of its much smaller value. Another method of resolving the ambiguity is by determining the relevant partial half lives.

Using this method, one measures the half life of a level, and, using the observed α_k, determine the partial half life for all

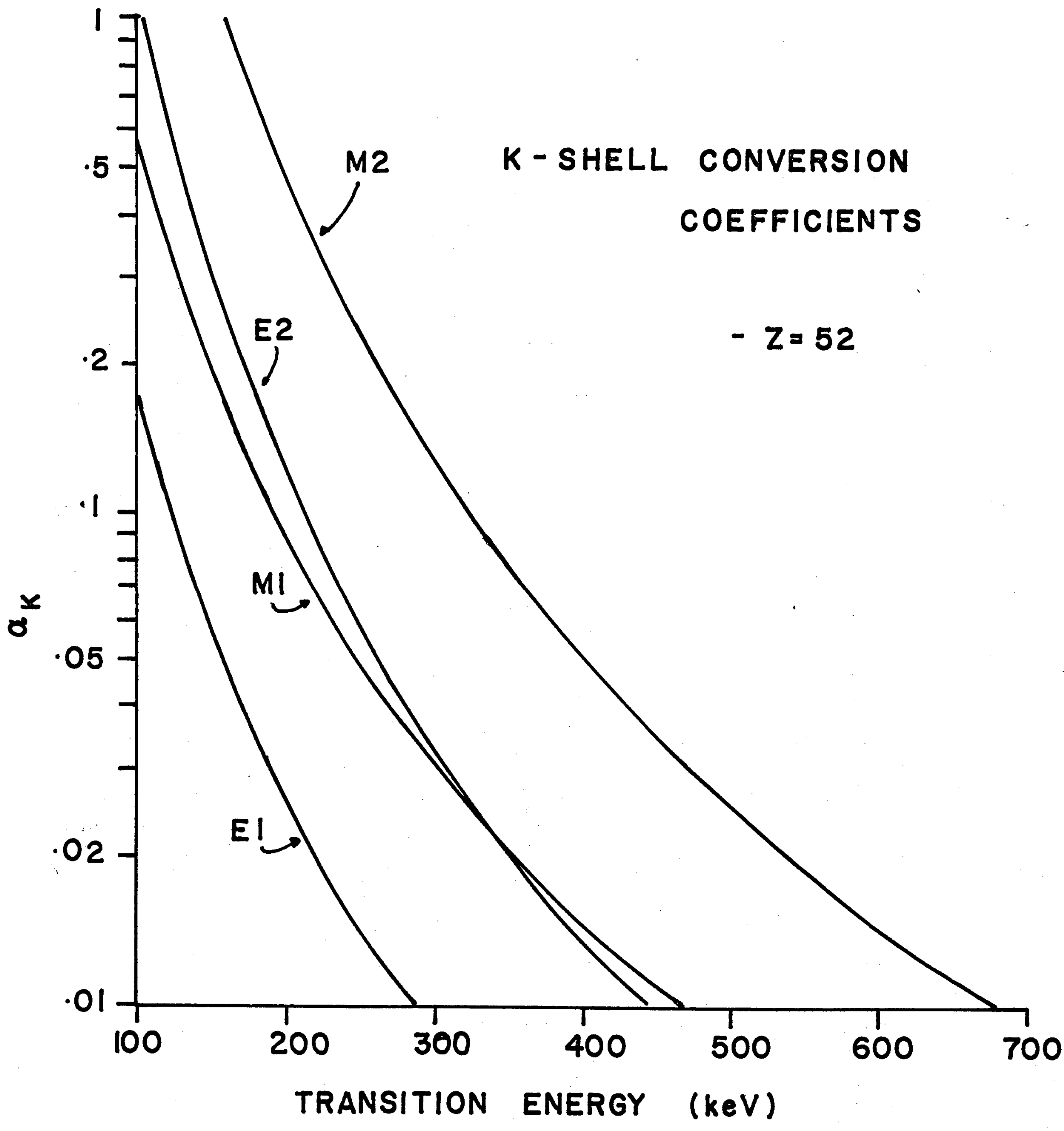

Fig. 2.17: Theoretical K conversion coefficients in ^{119}Te.

possible combinations of multipolarities for the observed transition. These can then be compared with theoretical estimates.

The theoretical estimates used are made for the simple case of a single proton changing its state, with the assumption that the initial and final particle wavefunctions overlap as much as possible. The calculated probability of such a transition taking place sets an approximate upper limit to the expected value. These are called Weisskopf units and are given, for ^{119}Te, by

$$T_W(E1) = 26.11 \times \left(\frac{\hbar\omega}{197}\right)^3 \times S \times 10^{21} \ \mathrm{sec}^{-1}$$

$$T_W(M1) = .221 \times \left(\frac{\hbar\omega}{197}\right)^3 \times S \times 10^{21} \ \mathrm{sec}^{-1}$$

$$T_W(E2) = 23.8 \times \left(\frac{\hbar\omega}{197}\right)^5 \times S \times 10^{21} \ \mathrm{sec}^{-1}$$

$$T_W(M2) = .816 \times \left(\frac{\hbar\omega}{197}\right)^5 \times S \times 10^{21} \ \mathrm{sec}^{-1} ,$$

where S is a statistical factor of the order of unity and $\hbar\omega$ is the energy of the transition in MeV.

It is not surprising then, that observed single particle transitions generally show a hindrance when compared to the relevant Weisskopf unit ($T_{exp}/T_W < 1$). Of course, in a transition, many particles may be coherently involved — giving a collective transition. This increases the probability of the transition occurring and an enhancement of the Weisskopf estimate may be observed.

It is easy to see how collective transitions can enhance the E2 transition probability, but it is not easy to see how they could be involved in M2 transitions. The generally observed enhancement of E2 transitions, and hindrances of M2 transitions is displayed in [Si65]. Comparisons such as these can be used to eliminate some of the possible transitions.

Used together, conversion coefficients, angular distributions, and lifetime estimates can often resolve ambiguities concerning parity assignments.

2.4.5 Experimental Procedure

The list of reactions studied was given in Table 2.2. The following details the overall procedure followed in the study of the Tellurium nuclei.

An excitation function was the first measurement conducted for the study of each isotope. It was from the results of these measurements that the bombarding energies, given in Table 2.2, were determined.

Gamma-gamma coincidence data, and singles data were gathered simultaneously for each nucleus. When the coaxial detectors were used (for the majority of the data collection), the angles at which they were set were ±55° and ±125° to the beam for reasons discussed earlier. For most measurements of low energy gamma rays — with the planar detector — the detectors had to be placed at 90° to the beam due to the chamber's shape causing unwanted absorption of the gamma rays at ±55°.

Checking of the effect of any backscattering was conducted in all experiments. When the detectors were placed at an angle other than 180° to each other, lead shielding was placed between them in order to reduce the detection of scattered radiation.

Activity spectra, both in coincidence and singles were collected during each experiment. This provided a check on the purity of the desired reaction. During lengthy experiments (2-3 days), the activity spectra were recorded at several intervals.

The angles of 90°, 60°, 45°, 30°, 15°, and 0° to the beam were used to collect singles data for angular distribution measurements. Collection at all angles was repeated, and counts were normalised by using a monitor detector at a fixed angle (125°).

Timing information was gained from both gamma-gamma and neutron-gamma coincidences. The time calibration was conducted by insertion of known delays to one of the T.A.C. inputs.

To check the lineshapes produced by prompt radiation, ^{176}W was formed by the $^{164}Dy(^{16}O,4n)^{176}W$ (80 MeV) reaction. Known prompt transitions in this nucleus covered the energy range of interest and

Table 2.4

Intense Transitions Observed in ^{176}W
Following a $^{164}Dy(^{16}O,4n)^{176}W$ [Dr77]

Energy	Relative Intensity of γ Ray
109.1	42
240.2	100
351.2	91
440.7	68
558.1	27.5
596.2	20.1
625.5	7.8
876.8	6.4

had several transitions at energies conveniently close to those of interest in the Tellurium nuclei. The main transitions are listed in Table 2.4.

Conversion electron measurements were made for ^{119}Te only. Gamma and electron data were simultaneously collected in singles mode and in coincidence with neutrons. The relative efficiencies were measured using a ^{152}Eu source. Absolute normalisation was made using the known multipolarities of transitions in ^{152}Eu [Ma66] and [Ma74]. The confirmation of known multipolarities in ^{119}Te (see Chapter 3) confirmed the viability of this technique.

APPENDIX 1

CALCULATION OF THE GEOMETRIC ATTENUATION FACTORS FOR CYLINDRICAL DETECTORS WHEN THE RADIOACTIVE SOURCE IS ALIGNED BY (HI,xn) REACTIONS

For the case in question we need only to consider that angular range which is accepted by the Mini-Orange. This can be represented by a ring, as shown in Fig. A.1, where the figure represents the three dimensional situation.

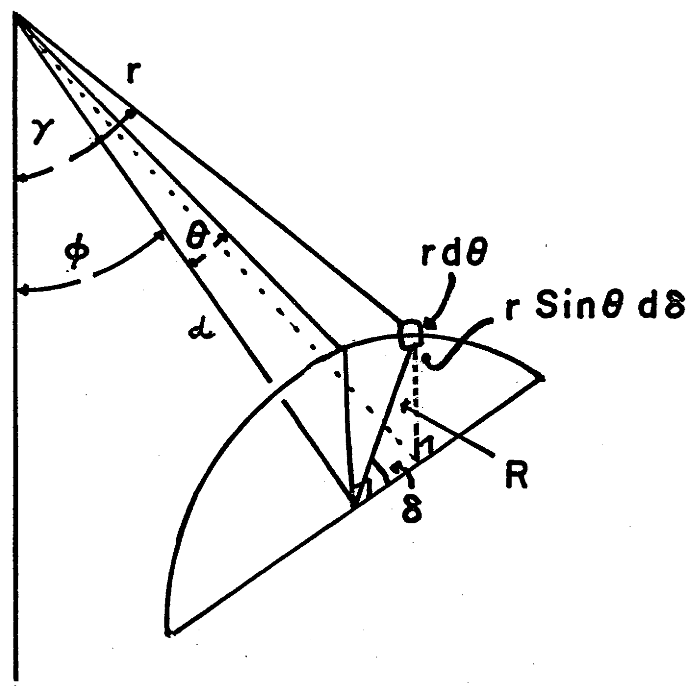

Fig. A.1: Definition of units used in the calculation.

In the figure,

- R is the "detector" radius which subtends the angle θ at the source,
- φ is the angle at which the detector axis is set relative to the beam,
- γ is the angle which is used in finding angular distributions of the radiation,
- d is the distance between the source at the plane of the detector.

The required integral is

$$I = \oint_S W(\gamma)\ dS\ , \tag{A.1}$$

where S is the sector of the annulus. Now

$$dS = \mathrm{Sin}\theta\ d\theta\ d\delta \tag{A.2}$$

and as

$$\mathrm{Cos}(\gamma) = \mathrm{Cos}\theta\ \mathrm{Cos}\phi - \mathrm{Sin}\theta\ \mathrm{Sin}\phi\ \mathrm{Cos}\delta\ , \tag{A.3}$$

Equation (A.1) reduces to

$$\left.\begin{aligned} I &= 2\int_{\theta_1}^{\theta_2}\int_0^{\pi} W(\gamma)\ \mathrm{Sin}\theta\ d\theta\ d\delta \\ W(\gamma) &= W_0[1+A_2P_2(\mathrm{Cos}\gamma)+A_4P_4(\mathrm{Cos}\gamma)] \end{aligned}\right\} . \tag{A.4}$$

where

Hence only the following three integrals need to be evaluated:

$$A \equiv \int_{\theta_1}^{\theta_2}\int_0^{\pi} \mathrm{Sin}\theta\ d\theta\ d\delta \tag{A.5a}$$

$$B \equiv \int_{\theta_1}^{\theta_2}\int_0^{\pi} \mathrm{Cos}^2(\gamma)\ \mathrm{Sin}\theta\ d\theta\ d\delta \tag{A.5b}$$

$$C \equiv \int_{\theta_1}^{\theta_2}\int_0^{\pi} \mathrm{Cos}^4(\gamma)\ \mathrm{Sin}\theta\ d\theta\ d\delta \tag{A.5c}$$

as

$$P_2(\mathrm{Cos}\gamma) = \frac{1}{2}(3\ \mathrm{Cos}^2\gamma - 1)$$

and

$$P_4(\mathrm{Cos}\gamma) = \frac{1}{8}(35\ \mathrm{Cos}^4\gamma - 30\ \mathrm{Cos}^2\gamma + 3)\ .$$

Therefore, by substituting Eqn (A.3) into Eqn (A.5), we obtain Integral A as

$$A = \int_{\theta_1}^{\theta_2}\int_0^{\pi} \mathrm{Sin}\theta\ d\theta\ d\delta = \int_{\theta_1}^{\theta_2} \pi\ \mathrm{Sin}\theta\ d\theta$$

$$= \pi[\mathrm{Cos}\theta_1 - \mathrm{Cos}\theta_2] \tag{A.6}$$

while Integral B gives

$$B = \int_{\theta_1}^{\theta_2}\int_0^{\pi} \mathrm{Cos}^2\gamma\ \mathrm{Sin}\theta\ d\theta\ d\delta$$

$$= \pi\ \mathrm{Cos}^2\phi\left[-\frac{\mathrm{Cos}^3\theta}{3}\right]_{\theta_1}^{\theta_2} + \frac{\pi}{2}\ \mathrm{Sin}^2\phi\left[\frac{\mathrm{Cos}^3\theta}{3} - \mathrm{Cos}\theta\right]_{\theta_1}^{\theta_2} \tag{A.7}$$

and Integral C gives

$$\int_{\theta_1}^{\theta_2}\int_0^{\pi} \mathrm{Cos}^4\gamma\ \mathrm{Sin}\theta\ d\theta\ d\delta$$

$$= \pi\ \mathrm{Cos}^4\phi\left[-\frac{\mathrm{Cos}^5\theta}{5}\right]_{\theta_1}^{\theta_2} + \frac{3\pi}{5}\ \mathrm{Sin}^2\phi\ \mathrm{Cos}^2\phi\left[\mathrm{Sin}^4\theta\ \mathrm{Cos}\theta + \frac{\mathrm{Cos}^3\theta}{3} - \mathrm{Cos}\theta\right]_{\theta_1}^{\theta_2}$$

$$+ \frac{3\pi}{64}\ \mathrm{Sin}^4\phi\left[-5\ \mathrm{Cos}\theta + \frac{5\ \mathrm{Cos}^3\theta}{6} - \frac{\mathrm{Cos}^5\theta}{10}\right]_{\theta_1}^{\theta_2} . \tag{A.8}$$

Now, in terms of integrals A, B and C (Eqns A.6, A.7, A.8)

$$\oint P_2(\text{Cos}\gamma)\ dS = \frac{1}{2}(3(B) - (A)) \tag{A.9}$$

and

$$\oint P_4(\text{Cos}\gamma)\ dS = \frac{1}{8}(35(C) - 30(B) + 3(A))\ . \tag{A.10}$$

The intensity of radiation is then represented by

$$\oint W(\gamma)\ dS = 2W_0A\left\{1 + A_2\left(\frac{3B - A}{2A}\right) + A_4\left(\frac{35C - 30B - 3A}{8A}\right)\right\}.$$

As

$$\oint W_0\ dS = 2W_0A\ ,$$

i.e. isotropic radiation, the geometric attenuation is given by

$$Q_2 = \frac{3B - A}{2A}$$

and

$$Q_4 = \frac{35C - 30B + 3A}{8A}\ .$$

It can be shown that $\frac{B}{A} = \frac{1}{3}$ if $\phi = 54.74°$; for all angles θ_1, θ_2. Hence $Q_2 = 0$ for all angular ranges accepted by the Mini-Orange in its present position. The expression for Q_4 does not simplify easily, but, it can be shown that in the case when $\phi = 54.74°$, then it is given by

$$Q_4 = (\text{Cos}^2\theta_2 + \text{Cos}\theta_2\ \text{Cos}\theta_1 + \text{Cos}^2\theta_1)\left(\frac{35}{72} - \frac{49}{144}(\text{Cos}^2\theta_2 + \text{Cos}^2\theta_1)\right) + \frac{49}{144}\text{Cos}^2\theta_2\ \text{Cos}^2\theta_1 - \frac{7}{48}\ .$$

CHAPTER 3

EXPERIMENTAL RESULTS AND ANALYSIS

3.1 INTRODUCTION

In this chapter, the experimental data taken for the study of the four nuclei ^{116}Te, ^{117}Te, ^{118}Te and ^{119}Te will be discussed, and the derived level schemes presented. As the volume of available data is very large, and as the logic used in all four analyses was similar, only the ^{119}Te analysis will be discussed in detail. Summaries of the analyses of the other three nuclei will then be presented.

In chronological order, ^{119}Te was the first nucleus studied. The task of data analysis was compounded by the lack of any well defined systematic trends — such as those commonly observed in well deformed nuclei. The complexity of the spectrum so derived prompted the decision to study the other nuclei; the hope being that systematic trends may be observed across the mass range. Evidence for any such trends will be discussed in Chapter 4 and Chapter 5.

Levels were assigned on the basis of detailed γ-γ coincidence studies, intensity sums (both in coincidence and singles data) and energy sums. Where quoted, "intensities" refer to intensities, after correction for relative efficiency of detection, relative to an intense transition of the nucleus under study (whose intensity is arbitrarily set to 1000).

The nuclei studied were formed by (HI,xn) reactions which most strongly populate the Yrast states. In the odd mass nuclei, levels based on high spin isomers, rather than the low spin ground states have the greatest population. Such low energy, high spin isomers have been observed in *all* the odd Tellurium nuclei studied so far. As much of the following analysis depends on the correct identification of the high spin isomer in ^{119}Te and ^{117}Te as being of $1h_{11/2}$ neutron quasiparticle nature, a summary of the available evidence will be given. The relevant partial spectra of the odd A Tellurium nuclei is given in Fig. 3.1.

In ^{115}Te, Vajda *et al.* [Va72] determined the high spin isomer's g factor as $g = -.186 \pm .007$, and were able to show its predominant $\nu 1h_{11/2}$ character. In the Tellurium nuclei of mass $A \gtrsim 121$, the isomeric level has been assigned the spin and parity, I^{π} of $11/2^-$ (see [Le80]). This was possible as each of the high spin isomers decays, at least in part, by observable transitions to the ground state. The information on the high spin isomer's decay is summarised in Table 3.1.1. As a result of neutron pick up and stripping experiments (e.g. [Li75] and [Ja64]) it is generally considered that these $11/2^-$ levels are of $\nu 1h_{11/2}$ single particle nature. Such assignments are consistent with shell model predictions.

In line with the systematic trends, which as we have seen, span the mass range presently under study, one could expect that the high spin isomers observed in ^{117}Te and ^{119}Te at approximately 300 keV, are of similar single particle nature to the above. Of these isomers, though, only the spin of the ^{119}Te isomer and the half-lives of each have been measured. The half-lives given in Table 3.1.1, follow the trend observed from the other nuclei. The spin of the ^{119}Te isomer was measured by the atomic beam magnetic resonance technique by Axenston *et al.* [Ax61], and was found to be $I = 11/2$. This supports the above claim.

3.2 ^{119}Te

3.2.1 General

The deduced level scheme for ^{119}Te is presented in Fig. 3.2. Its derivation was based mainly upon 5×10^7 γ-γ coincidence events collected as a result of the reaction ^{110}Pd(^{13}C,4n)^{119}Te at 59 MeV bombarding energy. Additional γ-γ coincidence information from the same reaction, but at 75 MeV bombarding energy was also utilised. This additional information provided further evidence of transitions between the states at high ($I \approx 41/2$ h) angular momentum.

At the commencement of the project, the only information

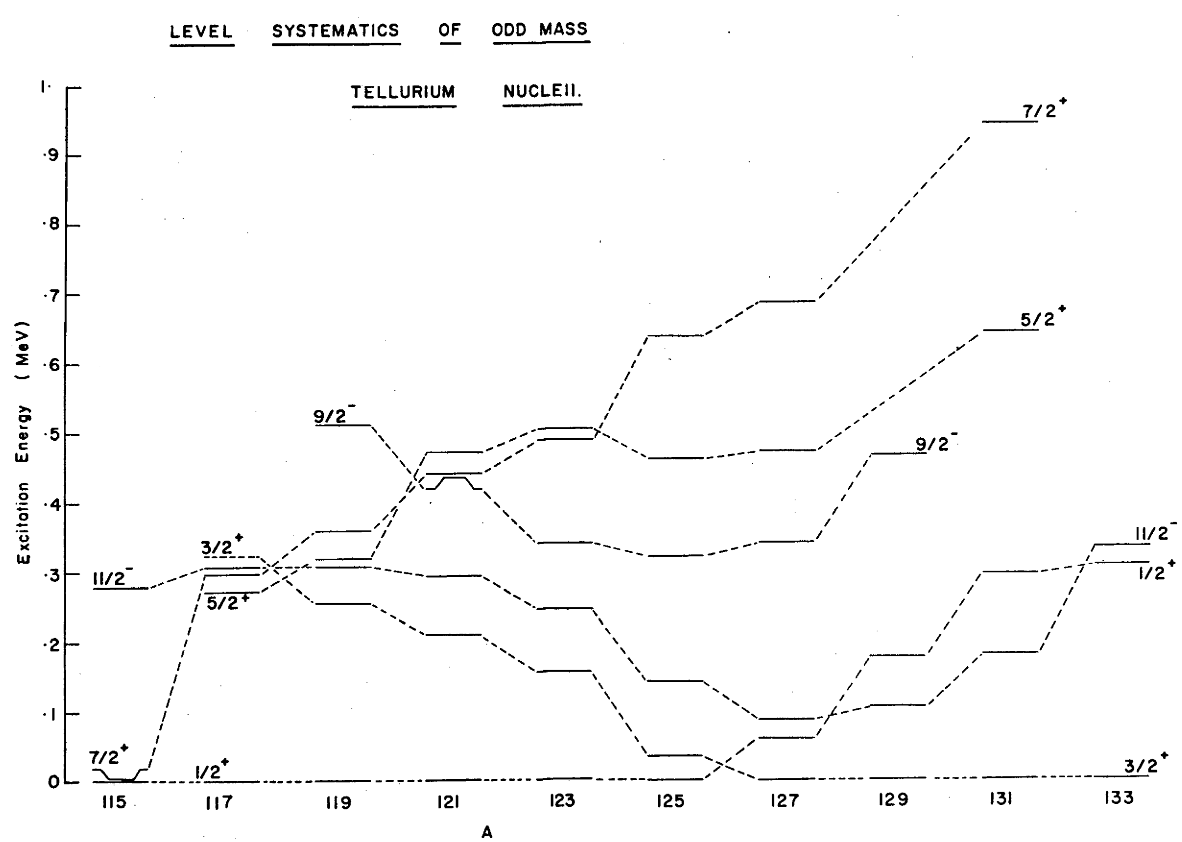

Fig. 3.1: Energy systematics of the low lying states in the odd mass Tellurium nuclei.

Table 3.1.1

High Spin Isomeric Levels in Te Nuclei

A	$T_{1/2}$	M	E_γ	Q_{EC} (a),(b) (MeV)	% γ Decay (b)
115	7.5 μs	M2	279	4.42	(100)
117	103 ms	?	?	3.49	(100)
119	4.7 d	-	-	2.29	(0)
121	154 d	M4	81.8	1.10	90
123	119.7 d	M4	88.5	Stable	100
125	58 d	M4	109.3	Stable	100
127	109 d	M4	88.3	.693	97
129	33.5 d	M4	105.5	1.5	64
131	30 hr	M4	182.2	2.25	22
133	55.4 min	M4	334	2.97	17

(a) Q values of the ground state of the nucleus.

(b) Values obtained from [Le79].

available on the ^{119}Te spectrum was from studies on the decay of ^{119}I (e.g. [Sp70], [Se68]). No information on the high spin states was available. Recently, two papers on ^{119}Te have been published by Hagemann *et al.* [Ha79a] and [Ha79b]. They formed the nucleus by the reaction ^{117}Sn(α,2n)^{119}Te and reported levels with spins of up to $I = 23/2$. The majority of the levels reported by them were based on the ground state band. In contrast, the majority of the levels observed in the present work are based on the previously mentioned high spin isomeric level.

In most cases, the present, independently proposed level scheme agrees with that of Hagemann *et al.* [Ha79b]. However, we observed a 39.8 keV $7/2^+ \rightarrow 5/2^+$ transition, which they did not, and we also found a different placement for the 200.8 keV γ-ray. These differences affect the interpretation of the data, which will be discussed in Chapter 4 and Chapter 5. In addition, we see many more transitions at higher excitation energy and angular momentum.

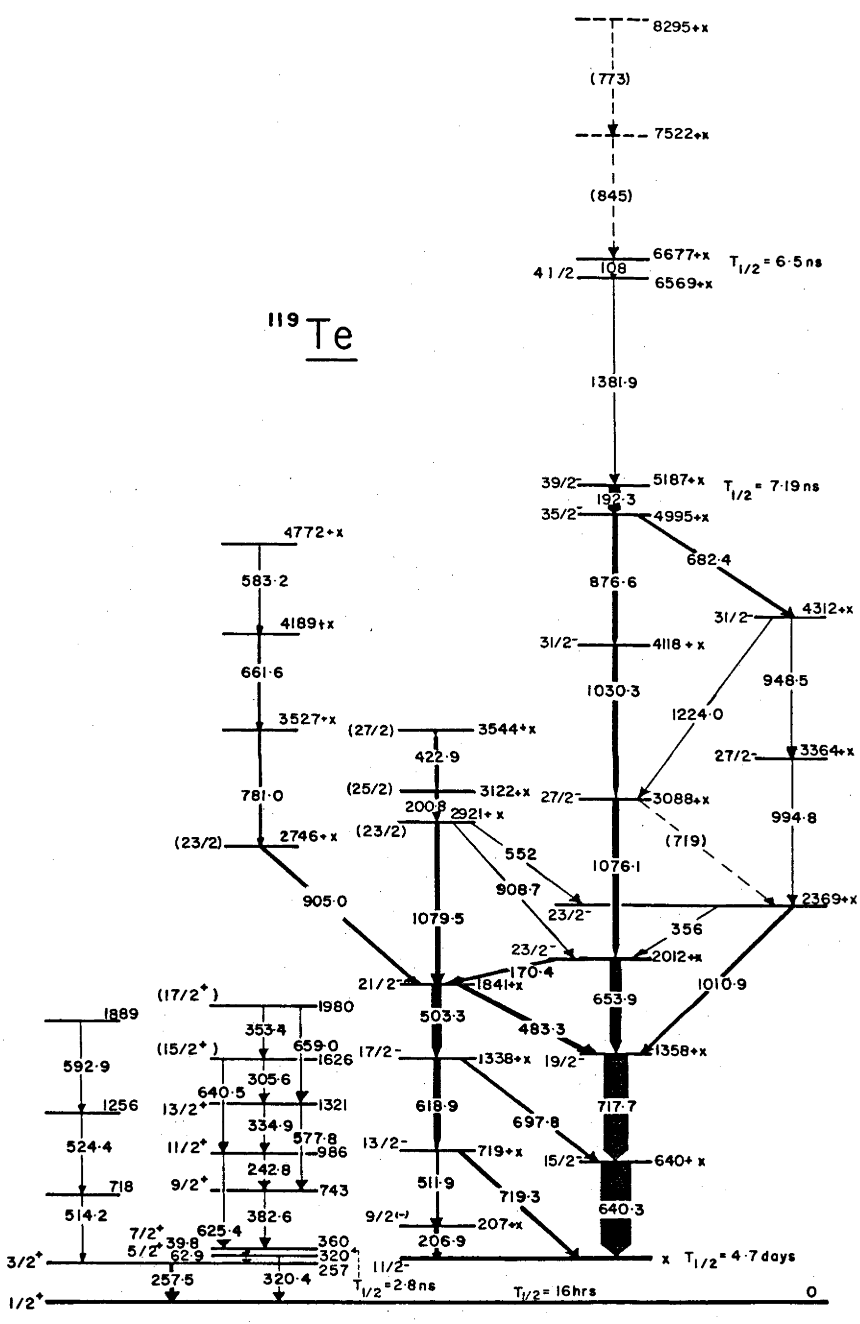

Fig. 3.2: Level spectrum of ^{119}Te deduced from observations following a ^{110}Pd(^{13}C,4n)^{119}Te (59 MeV) reaction.

At present, the excitation of the (assumed) $^{11}/_2{}^-$ isomeric level relative to the ground state is not known precisely. It has been shown that the $^{11}/_2{}^-$ isomer decays solely to ^{119}Sb; mostly by electron capture ($\beta^+ < .7\%$, I.T. $< .03\%$) (e.g. [Du75] and [Ka63]). These studies on ^{119}Sb have determined that the excitation of $^{11}/_2{}^-$ isomeric level in ^{119}Te probably lies between 300 and 320 keV. As no information was obtained in the present study to alter this claim, the energy of the $^{11}/_2{}^-$ isomeric level will here by represented by the value x where it is assumed that $300 \leq x \leq 320$ keV.

3.2.2 Summary of the Data

An example of a singles spectrum, taken with the detector positioned at 55° to the beam, is shown in part (a) of Fig. 3.3. The major transitions which were placed in the ^{119}Te spectrum are marked. Also marked are the transition resulting from Coulomb excitation of the ^{110}Pd target (COULEX), and the first few transitions of the neighbouring ^{118}Te and ^{120}Te nuclei (600, 605, and 615 keV). The relative intensity of these transitions, when compared with the intensity of the 640.3 keV transition (^{119}Te), gives an indication of the cleanliness of the reaction.

After twelve hours of bombardment of the target, the activity spectrum shown in part "b" of Fig. 3.2 was recorded. Now the decay studies of [Du75] and [Ka63] have shown that some gamma rays in ^{119}Sb can be uniquely associated with either the decay of the $^{11}/_2{}^-$ isomeric level (^{119M}Te) or the $^1/_2{}^+$ ground state (^{119g}Te) of ^{119}Te, e.g. the 153 keV transition with ^{119M}Te. The intensity of other transitions in ^{119}Sb also depends on which of the two ^{119}Te states is most populated. Also, the ^{119M}Te has a much longer half-life ($T_{1/2} = 4.7$ days) than that of the ground state ($T_{1/2} = 16$ hrs). So, using the decay scheme of [Du75], we found that the spectrum of Fig. 3.3(b) was only possible if the $^{11}/_2{}^-$ isomeric level was the major product of the reaction. Therefore, the most intense transitions must lead to the isomeric state rather than to the ground state.

The assignment of the 640.3 keV gamma ray to the ^{119}Te nucleus was made on the basis of an excitation function, measured in 3 MeV steps over the range of 53 MeV to 65 MeV. The yield obtained for this

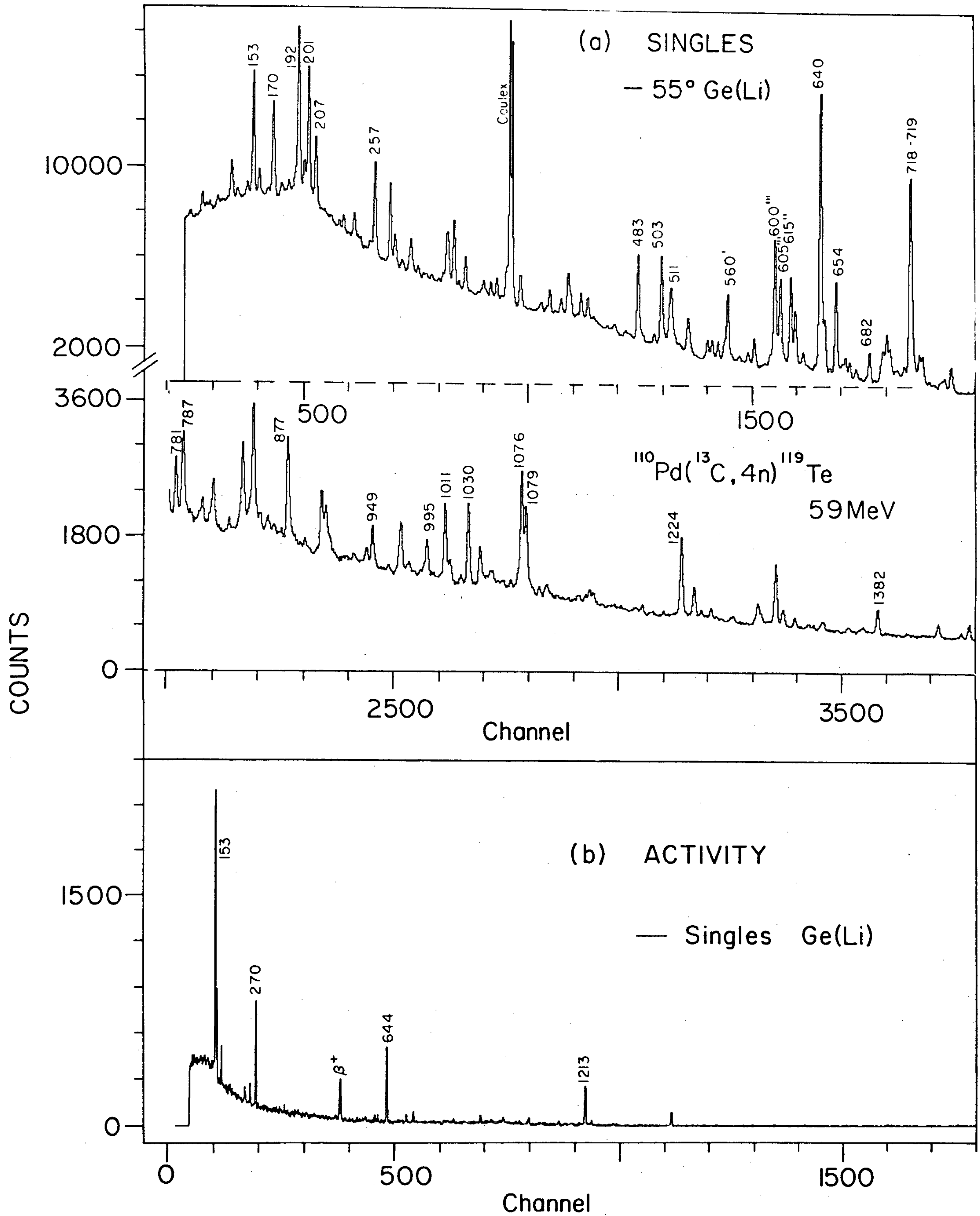

Fig. 3.3: Characteristic singles spectra observed with a Ge(Li) detector at 125° to the beam. (A) In beam. (B) Out of beam activity.

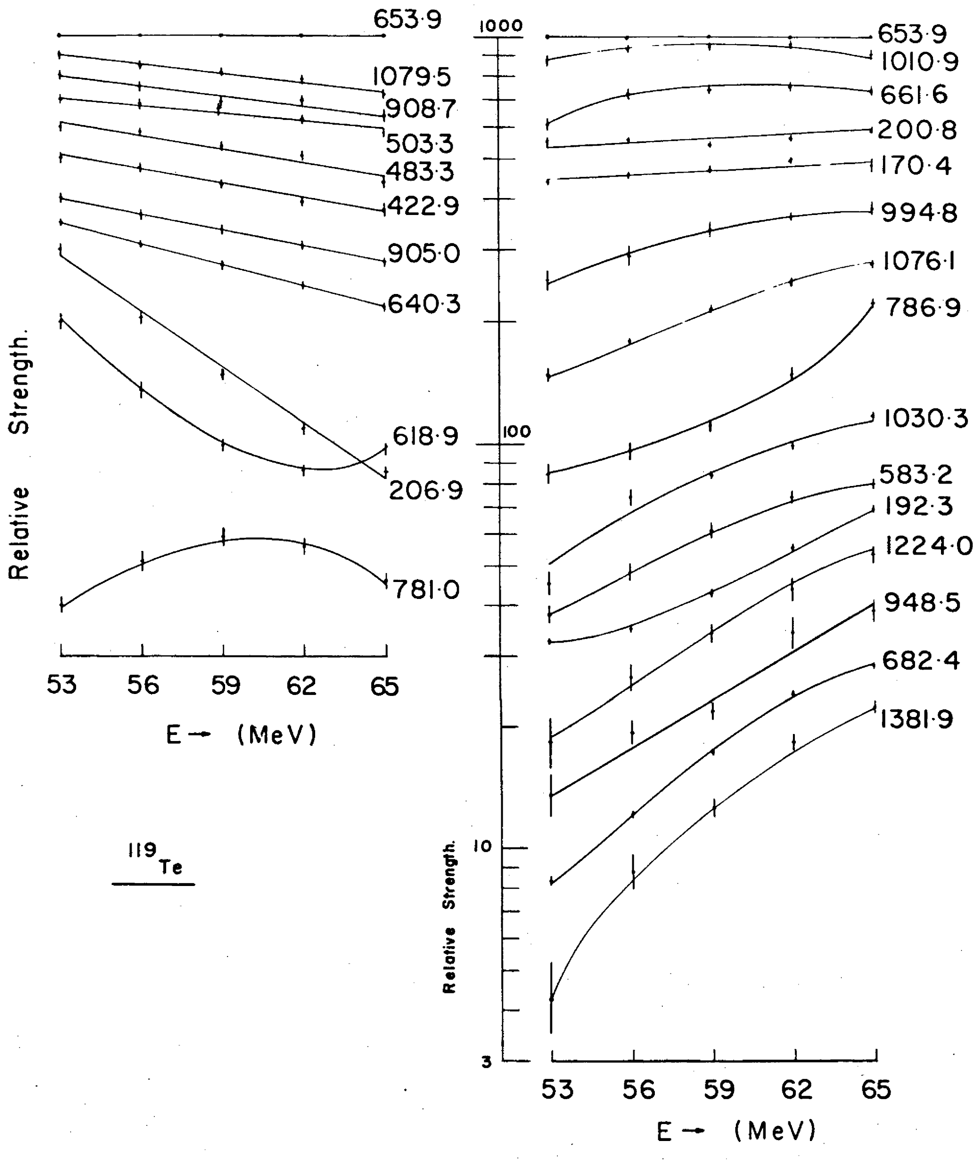

Fig. 3.4: Relative excitation functions of transitions based on the $^{11}/_{2}^{-}$ isomeric level in ^{119}Te.

gamma ray, when compared to the yields of the 605 keV (^{118}Te) and the 560.3 keV (^{120}Te) gamma rays, showed that it most probably belonged to the intermediate nucleus ^{119}Te.

The excitation function of Fig. 3.4 includes all gamma rays which are associated by γ-γ coincidences, both directly and indirectly, with the 640.3 keV gamma ray. The peak areas have been normalised at each energy to that of the 653.9 keV, $23/2^- \rightarrow 19/2^-$ transition. As it is the slope of the graph that conveys information, the values have been offset so as to best display the data. These excitation functions were used as an aid in placing gamma rays into the level scheme.

The intensities of all the transitions assigned to ^{119}Te, measured relative to the intensity of the 640.3 keV transition are given in Table 3.2.1. The measurements were taken at the ^{13}C bombarding energy of 59 MeV. Also given in Table 3.2.1 are the results of the angular distribution measurements and the energy of the initial state of the transition. Some typical examples of the angular distribution measurements are shown in Fig. 3.5. The points are plotted against $\text{Cos}^2\theta$, where θ was the detection angle, and, for convenience, are normalised to their respective values at $\theta = 90°$ ($\text{Cos}^2\theta = 0$). The curves in Fig. 3.5 (also normalised) were determined using the fitted values of A_2 and A_4 given in Table 3.2.1.

The tables of Yamazaki [Ya74] were used to interpret the angular distribution coefficients. To improve the interpretation, values of the attenuation coefficients due to incomplete alignment were found for every transition thought to be of stretched quadrupole nature. These values were then used to determine, by interpolation, the attenuation coefficients for use with transitions of mixed multipolarity. The mixing ratios so determined are presented in Table 3.2.2, together with the initial and final spins for the transitions. The spin convention used for mixing ratios is that used by Yamazaki [Ya74].

The multipolarity for some of the transitions was established by conversion electron measurements. Gamma ray and electron spectra were recorded in both singles mode and in coincidence with neutrons. The coincidence data, by increasing the peak to background ratio (especially effective in the electron spectrum) enabled K conversion

Table 3.2.1

Transition Energies, Gamma Ray Intensities, and Angular Distribution Coefficients for Transitions Observed in the ^{110}Pd(^{13}C,4n)^{119}Te (59 MeV) Reaction. Initial States of Assigned Transitions are also Given.

Transition Energy (a)	Gamma Ray Intensity (c)	A_2 (f)	A_4 (f)	Initial State (keV)
39.8	30 (2) (d)			360
62.9	100 (d)			320
108 (1)	28 (7)			6677 +x
170.4	130 (9)	-.28 (2)	-.02 (2)	2012 +x
192.3	266 (16)	.29 (2)	-.06 (2)	5187 +x
200.8	168 (12)	-.20 (1)	.00 (5)	3122 +x
206.9	94 (7)	.06 (5)	.00 (5)	207 +x
242.8				986
257.5	98 (7)	.01 (3)	.01 (3)	257.5
305 (1)				1626
320.4	45 (10)	.10 (3)	-.01 (3)	320.4
334.9	66 (8)	-.18 (4)	.02 (4)	1321
353.4	12 (8)			1980
356 (1)	24 (6)			2369 +x
382.6	73 (7)	-.34 (4)	.01 (4)	743
422.9	102 (4)	-.45 (4)	.10 (4)	3544 +x
483.3	222 (7)	-.80 (2)	.09 (3)	1841 +x
503.3	252 (8)	.21 (2)	-.02 (2)	1841 +x
511.9 (3)				719 +x
514.2	22 (8)			718
524.4	16 (10)			1256
552 (1)	54 (6)	-.43 (7)	-.01 (7)	2921 +x
577.8	41 (8)			1321
583.2	60 (10)	.09 (3)	-.05 (3)	4772 +x
592.9				1889
618.9	189 (5)	.40 (4)	-.12 (3)	1338 +x
625.4	60 (6)			986
640.3	1000 (c)	.21 (1)	-.02 (1)	640 +x
640.5	< 20			1626

Transition Energy (a)	Gamma Ray Intensity (c)	A_2 (f)	A_4 (f)	Initial State (keV)
653.9	344 (5)	.22 (2)	-.06 (3)	2012 + x
659.0 (3)	54 (8)			1980
661.6 (3)	79 (10)	.24 (8)	-.16 (8)	4189 + x
665.3 (3)				(4373 + x)
682.4	101 (4)	.24 (4)	-.14 (5)	4995 + x
697.8	115 (10)	-.59 (4)	.12 (4)	1338 + x
717.7	951 (10)	.22 (1)	-.02 (1)	1358 + x
719 (1)	< 20 (b)			(3088 + x)
719.3	110 (15)	-.24 (2)	.03 (2)	719 + x
781.0 (2)	100 (7)	.18 (8)	.02 (8)	3527 + x
786.9 (3)				(3708 + x)
876.6 (2)	100 (15) (b)	.27 (3) (c)	-.07 (3) (e)	4995 + x
905.0 (3)	118 (8)	-.37 (4)	.21 (5)	2746 + x
908.7 (3)	77 (9)	-.29 (8)	-.05 (9)	2921 + x
948.5	45 (8) (e)	.24 (6)	-.02 (6)	4312 + x
994.8	61 (5)	.31 (7)	-.10 (8)	3364 + x
1010.9	139 (5)	.13 (4)	.03 (4)	2369 + x
1030.3	146 (5)	.22 (3)	-.06 (3)	4118 + x
1076.1 (2)	245 (5)	.19 (4)	-.03 (4)	3088 + x
1079.5 (2)	162 (5)	.03 (4)	-.04 (4)	2921 + x
1224.0	67 (5)	.34 (8)	.00 (8)	4312 + x
1381.9	56 (8)	.63 (5)	-.01 (6)	6569 + x

(a) Except where given, errors on the transition energies are ±.1 keV.

(b) Presence is inferred from coincidence data.

(c) Singles gamma ray intensities relative to the 640.3 keV gamma ray intensity (except as noted), obtained from a coaxial Ge(Li) detector at 55° to the beam.

(d) Singles gamma ray intensities, relative to the 62.9 keV transition (normalised to 100) obtained from a planar Ge detector at 90° to the beam.

(e) From coincidence data.

(f) Normalised angular distribution coefficient chosen as best fit to the equation

$$W(\theta) = W_0[1 + (A_2)\, P_2(\cos\theta) + (A_4)\, P_4(\cos\theta)] .$$

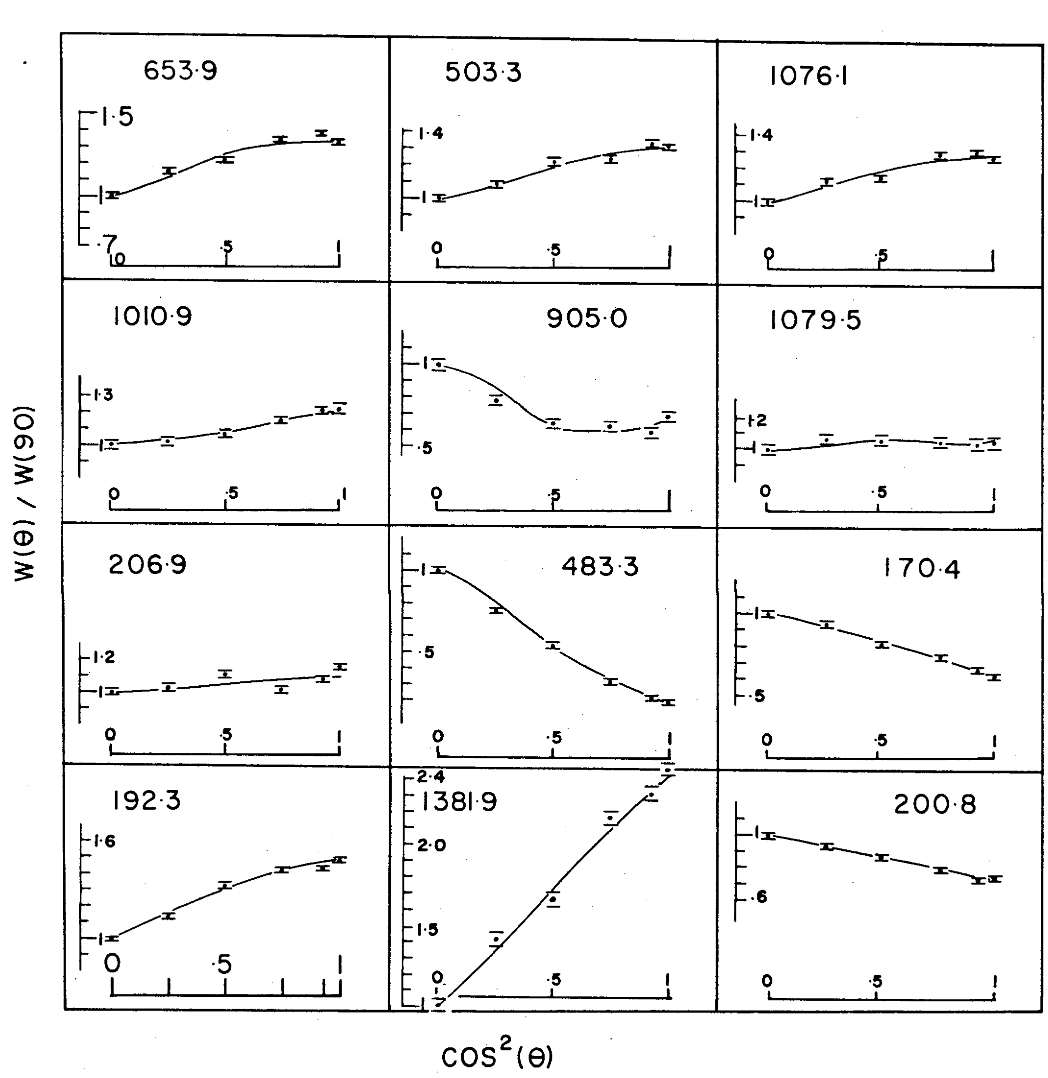

Fig. 3.5: Angular distributions of transitions in ^{119}Te. The curve represents the fitted function $W = W(\theta)/W(90°)$ where $W(\theta) = W_0(1 + A_2P_2(\cos\theta) + A_4P_4(\cos\theta))$.

Table 3.2.2

Mixing Ratios of Dipolar Transitions of ^{119}Te

Energy (keV)	$\delta^{(a),(d)}$	Transition
170.4	$-.16 \leq \delta \leq .11$	$^{23}/_2 \rightarrow ^{21}/_2$
200.8	$\lvert\delta\rvert \leq .04$	$(^{25}/_2) \rightarrow (^{23}/_2)$
206.9	$-.25 \leq \delta \leq -.14$	$^{9}/_2^- \rightarrow ^{11}/_2^-$
483.3	$-.6 \leq \delta \leq 1.5^{(b)}$	$^{21}/_2^- \rightarrow ^{19}/_2^-$
697.8	$-1.7 \leq \delta \leq -1.1$	$^{17}/_2^- \rightarrow ^{15}/_2^-$
719.3	$-.09 \leq \delta \leq -.04$	$^{13}/_2^- \rightarrow ^{11}/_2^-$
905.0$^{(c)}$	$\left\{\begin{array}{l}-5.7 \leq \delta \leq -3.1 \\ 3.3 \leq \delta \leq 8\end{array}\right\}^{(a)}$	$\left\{\begin{array}{l}(^{23}/_2) \rightarrow ^{21}/_2 \\ (^{19}/_2) \rightarrow ^{21}/_2\end{array}\right.$
908.7	$\lvert\delta\rvert > 4^{(b)}$	$^{23}/_2 \rightarrow ^{23}/_2^-$
1079.5	$.15 \leq \delta \leq .23$	$(^{23}/_2) \rightarrow ^{21}/_2$

(a) The A_2 value generally gives two sets of values for δ. The set given is that which is consistent with the measured A_4 values.

(b) Here the maximum value of A_2 is reached. Values of δ given are consistent with measured A_4 values.

(c) Two values of δ are given, one for each possible initial spin. The large positive A_4 (= .21 ± .05) value rules out the $^{23}/_2 \rightarrow ^{23}/_2$ possibility.

(d) The sign convention is that of Yamazaki [Ya74].

coefficients to be determined for the 170.4, 192.3 and 257.5 keV transitions. The coincidence data also made it possible to determine the K conversion coefficient for the 511.9 keV transition.

The electron data was analysed as outlined in Chapter 2. Fortunately no problems arose from overlapping K and L lines in the electron spectra. Absolute normalisation was achieved by using measured [Ba80] and theoretical [Ha68] conversion coefficients for transitions in ^{152}Eu. Examples of the electron spectra are given in Fig. 3.6, and the calculated K conversion coefficients are given in Table 3.2.3. These values are also displayed in Fig. 3.7, where the

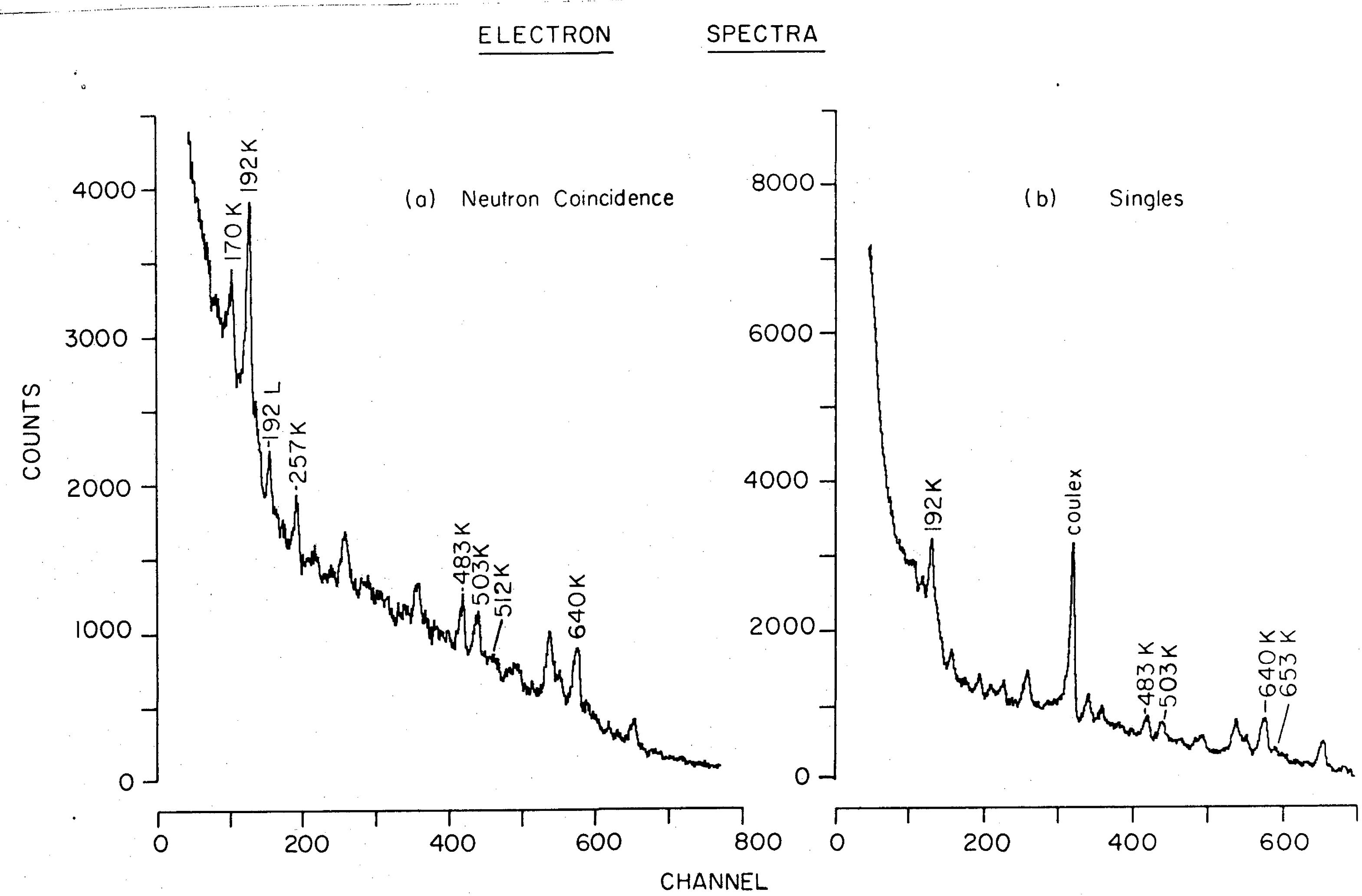

Fig. 3.6: Electron spectra collected with the Mini-Orange spectrometer. (A) In coincidence with neutrons. (b) In singles.

Table 3.2.3

Measured Conversion Coefficients of Transitions of the Reaction $^{110}Pd(^{13}C,4n)^{119}Te$ (59 MeV).

	Transition Energy	α_K
(a)	170.4	$(1.07 \pm .12) \times 10^{-1}$
	192.3	$(.17 \pm .05) \times 10^{-1}$
	257.5	$(3.6 \pm .5) \times 10^{-2}$
	511.9	$(6.0 \pm .9) \times 10^{-3}$
(b)	483.3	$(8.2 \pm 1.2) \times 10^{-3}$
	503.3	$(5.36 \pm .78) \times 10^{-3}$
	640.4	$(4.16 \pm .39) \times 10^{-3}$
	653.9	$(2.86 \pm .41) \times 10^{-3}$

(a) From neutron-gamma, neutron-electron coincidence measurements.

(b) From gamma ray and electron singles measurements.

relation to the theoretical values of pure multipole transitions [Ha68] can be readily seen.

Sufficient data was also obtained on the L shell conversion of the 192 keV transition to enable the K/L ratio to be determined. This is displayed in Table 3.2.4 together with the theoretical values for pure multipole transitions.

It was evident from the γ-γ coincidence data that many transitions showed a small delayed component. By sorting on individual gamma rays leading to the $^{11}/_2{}^-$, x keV level, it was established that there were two separate components to the delayed spectra. One isomeric state was identified as the $^{39}/_2{}^-$ (5187 + x) keV level, the other being identified as lying higher in energy than the $^{41}/_2$ (6569 + x) keV level; of which the most likely candidate was at (6677 + x) keV excitation. The counting rate was too small to determine the half-lives with any accuracy. A neutron-gamma coincidence experiment was used to give a useful counting rate.

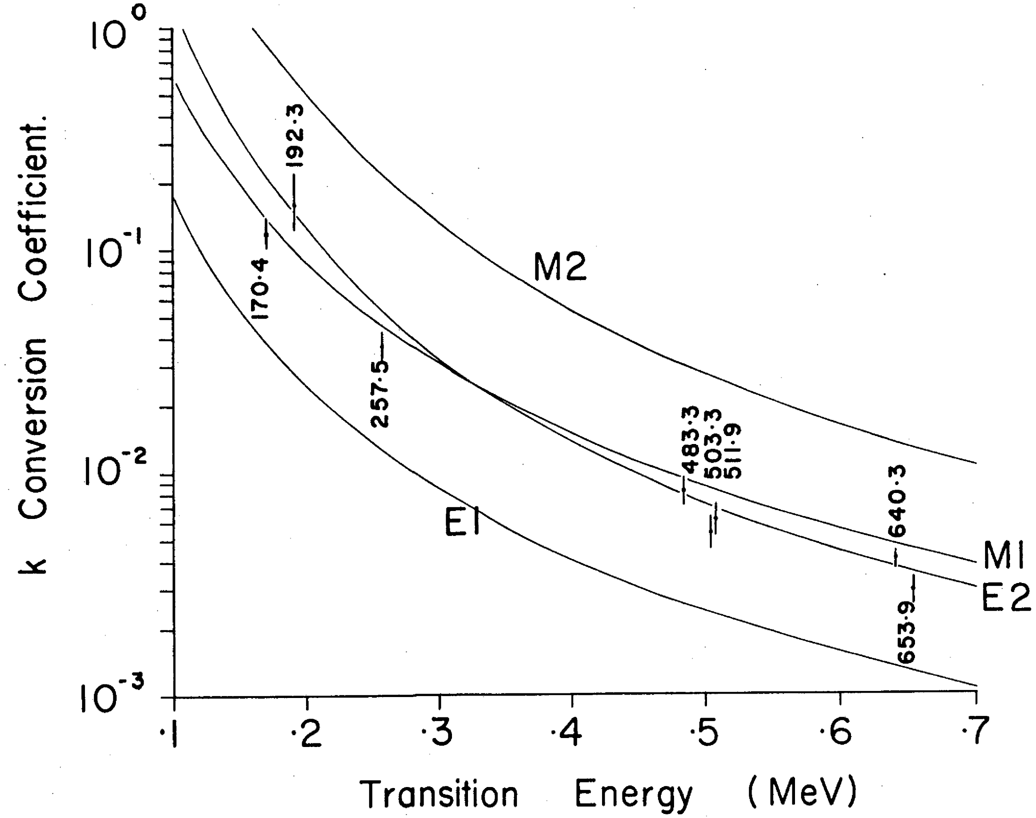

Fig. 3.7: Measured K conversion coefficients in ^{119}Te.

Table 3.2.4

K/L Ratios for the 192.3 keV Transition

Measured	Theoretical[(a)]			
	E1	M1	E2	M2
5.26 ± .55	7.69	7.69	5.0	5.88

(a) Theoretical values obtained from the tables of [Ha68].

A drawback of this technique was that any measurement of the (5187 + x) keV level's decay was necessarily affected by the other isomeric state. This was overcome by the analysis procedure outlined in Chapter 2. In the measurements, the 192 keV transition was observed in a planar Ge detector because the coaxial detector gave inadequate time resolution at the low energy. All other gamma rays were observed in a coaxial detector. The choice of transitions used for this analysis was limited to those least likely to be contaminated by other gamma rays.

Examples of the time spectra obtained are shown in Fig. 3.8. The half life of the higher lying isomeric state was determined from the time spectra of the 1381.9 keV gamma ray as being

$$T_{1/2}(6677 + x) = 6.49 \pm .25 \text{ ns.}$$

This value was used as a parameter in the determination of the half life of the (5187 + x) keV level. The other parameters required for the analysis were; the channel number (≡ time axis) relative to the t = 0 time (prompt time) and the ratio N_1/N_T, where N_1 is the number of transitions affected by only the higher lying of the isomers, and N_T is the number of transitions affected by the lower energy isomer, i.e.

$$\frac{N_1}{N_T} = \frac{I_{(1382)}}{I_{(192)}},$$

(where the intensities are obtained from Table 3.2.1), i.e.

$$\frac{N_1}{N_T} = .21 \pm .03 .$$

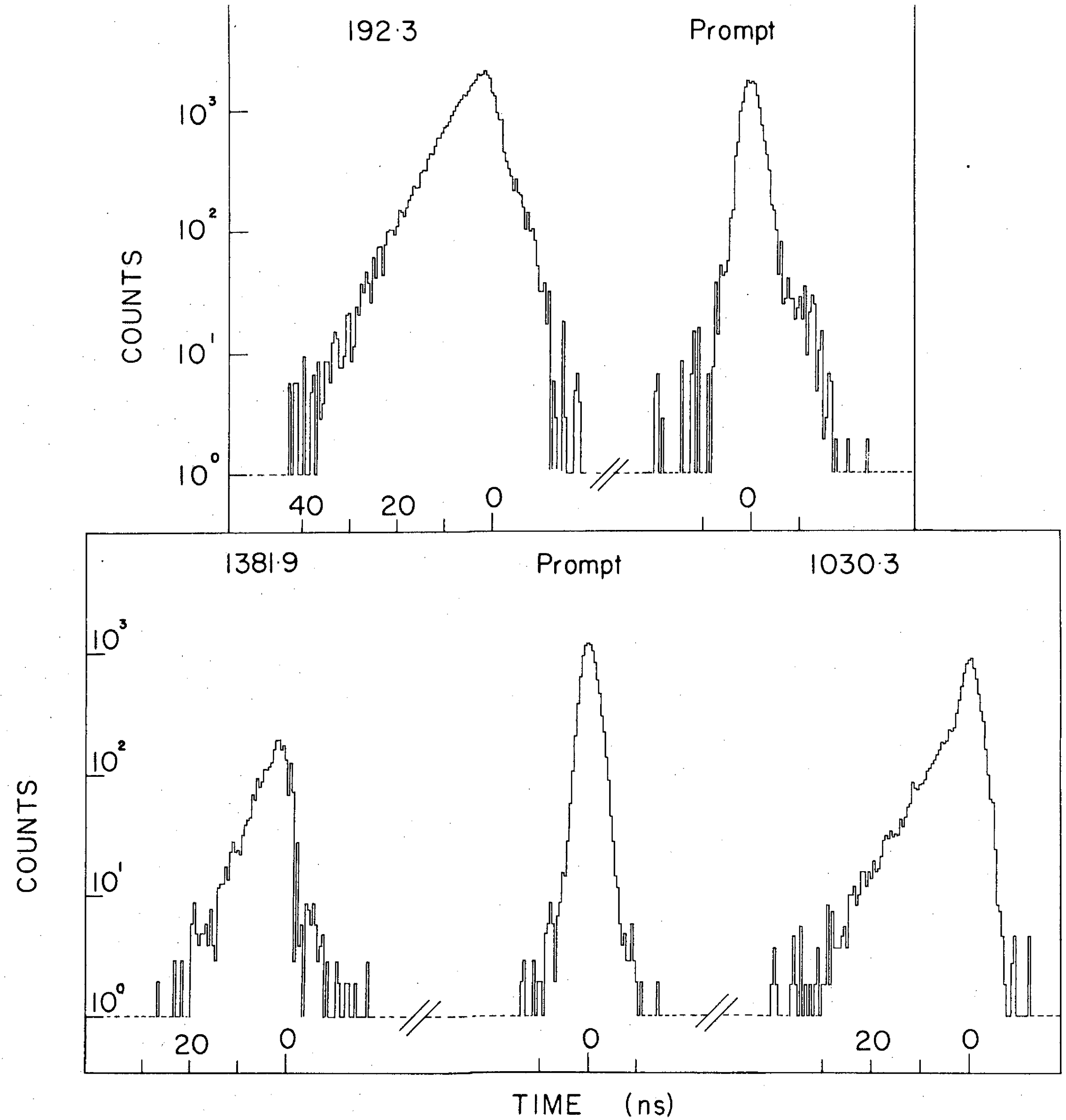

Fig. 3.8: Time spectra obtained in the neutron-gamma coincidence experiment, with, (Top) a planar Ge detector and (Bottom), coaxial Ge(Li) detector.

Table 3.2.5

Determination of the Half Life of the 5187 + x keV Level.[a]

Transition Energy	$T_{1/2}$ (n.s.)
192.3	6.8 ± .10
682.4	7.12 ± .16
876.6	7.17 ± .22
1224.0	7.00 ± .27
1030.3	7.53 ± .20
1076.1	7.06 ± .17
948.5	7.11 ± .29
994.8	7.38 ± .57
1010.9	7.67 ± .39

Average ⇒ $T_{1/2}$ = (7.19 ± .09) n.s.

(a) Input parameters

$$N_F = \frac{N_1}{N_T} = .21 \pm .03$$

$$\lambda_1 = .105 \pm .004 \text{ (channel}^{-1}\text{)} \equiv .107 \pm .004 \text{ (ns}^{-1}\text{)}$$

an error of ±.1 (channel) was used as the uncertainty of time zero.

The results of the individual fits are given in Table 3.2.5. The weighted mean of these values gives

$$T_{1/2}(5187 + x) = 7.19 \pm .09 \text{ ns} .$$

It is interesting to note that the particular combination of parameters needed produces a composite decay curve which appears, at first glance, as a single decay curve. This can be seen in Fig. 3.9 where the fit to the 1224 keV transition's delayed time spectrum is shown in detail.

The 257.5 keV transition also has a delayed component. The half-life of the decay has been previously measured by Hagemann *et al.* [Ha79a] as $T_{1/2}$ = 2.2 ± .2 ns. The present work gives a half life of $T_{1/2}$ = 2.8 ± .2 ns. As the time spectrum of the 39.8 and 62.9 keV gamma

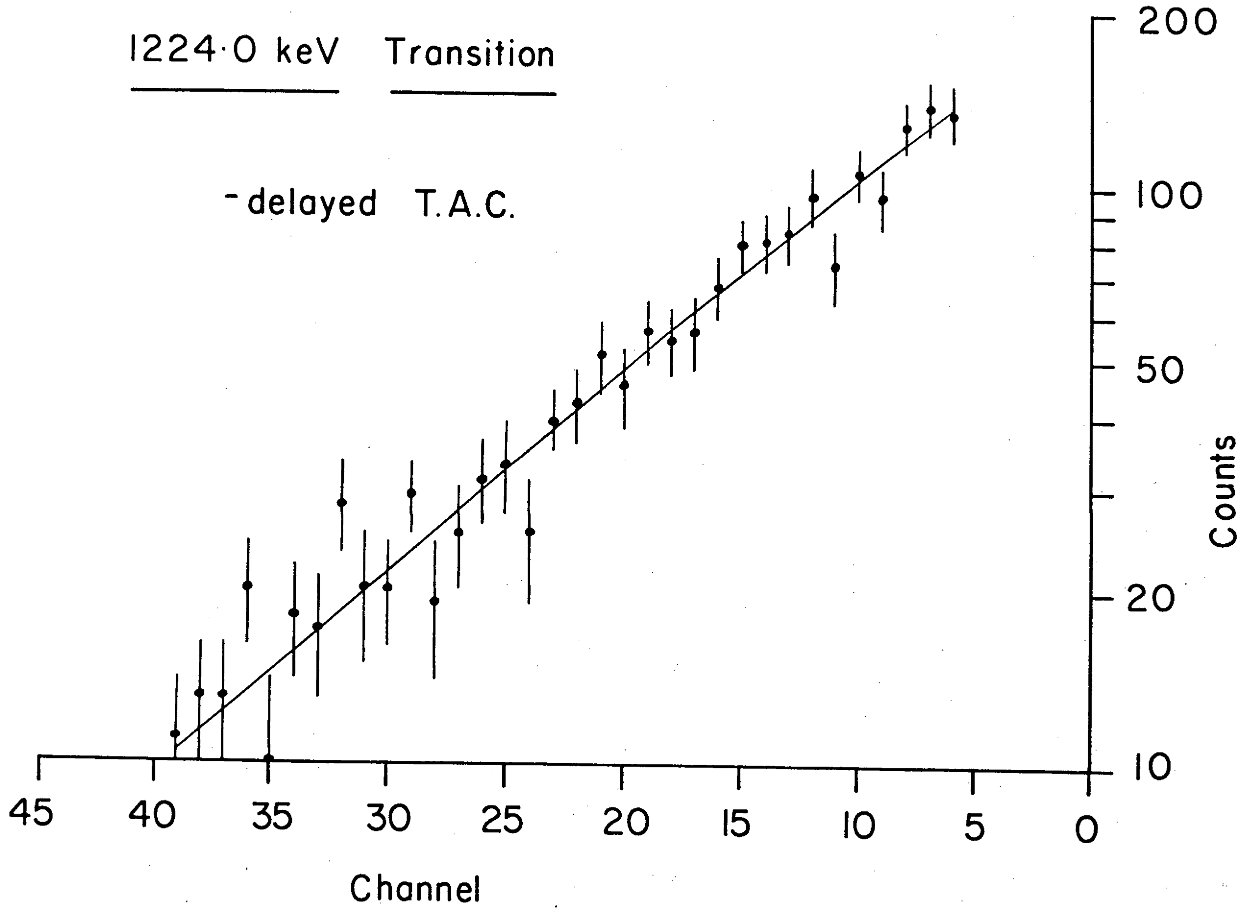

Fig. 3.9: Corrected data plus fit to the delayed time spectum of the 1224.0 keV transition.

rays could not be measured to this accuracy, it is now not certain whether it is the 320 or 360 keV level which is isomeric.

3.2.3 Levels which Decay to the Ground State

The levels have been reported previously by Hagemann *et al.* [Ha79a] and [Ha79b]. They observed many transitions, most of which are seen only weakly, if at all, in the present experiments. However, the observation in the present work, of a 39.8 keV transition alters the placement of the levels.

The 39.8 keV transition was observed to be in coincidence with the 257.5, 320.4 and 625.4 keV gamma rays. The spectrum projected by using a 257.5 keV energy gate is shown in Fig. 3.10 where the two gamma rays of 39.8 and 62.9 keV are clearly visible. Three corrections need to be applied to the peak areas of the 39.8 and 62.9 keV transitions if we are to determine their relative strengths, i.e. for (1) relative efficiency of gamma ray detection, (2) conversion electron emission (which is far more likely than gamma emission at these energies), and (3) angular distribution effects for the measurements were made at 90° to the beam.

The singles relative intensity of the gamma rays (corrected for relative efficiency) was found to be

$$\frac{I_\gamma(39.8)}{I_\gamma(62.9)} = .30 \pm .02 \ .$$

However, to compare the relative *transition* intensities, the conversion coefficients must be known. Now the 62.9 keV transition is known to be M1/E2 ($0 \le \delta < .2$) multipolarity [Ha79b], hence its conversion coefficient can be determined from the tables of [Ha68]. The conversion coefficient of the 39.8 keV transition is then determined from the relation

$$\alpha_T(39.8) = 15.7\,\mathcal{X}\left(\frac{y_1}{y_2}\right) - 1 \ ,$$

where

$$\mathcal{X} = \frac{\text{Transition Intensity (39.8)}}{\text{Transition Intensity (62.9)}} = \frac{I_T(39.8)}{I_T(62.9)}$$

and y_1, y_2 are coefficients representing the effects of the angular

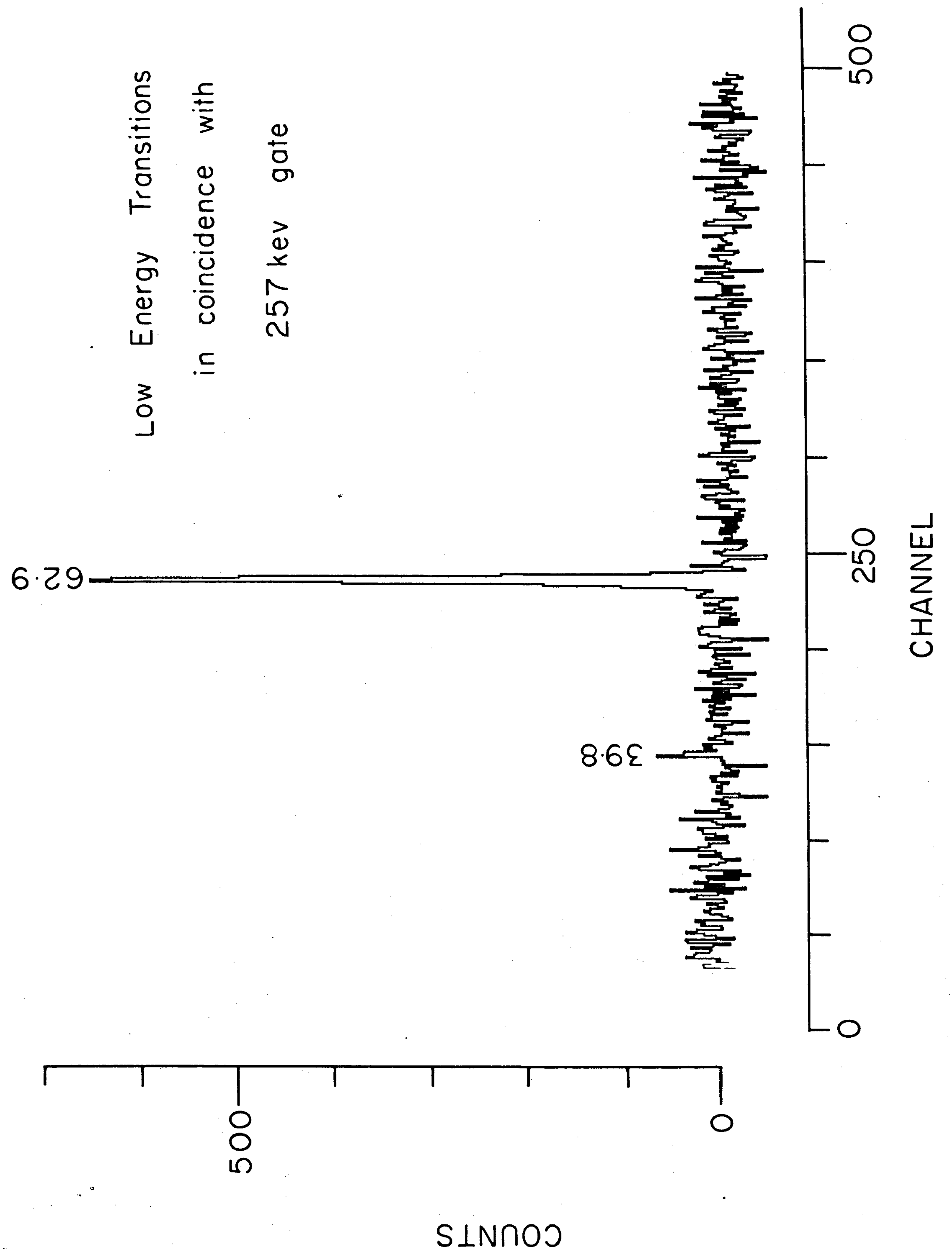

Fig. 3.10: Low energy transitions in coincidence with the 257 keV transition. Observed in a planar Ge detector at 90° to the beam.

distributions of the 39.8 and 62.9 keV gamma rays respectively, i.e.

$$W_{1,2}(90°) = W_0 y_{1,2} = W_0[1 + A_2P_2(\mathrm{Cos}90°) + A_4P_4(\mathrm{Cos}90°)]_{1,2} \cdot$$

As the most probable range of the A_2 attenuation coefficient is $-.3 < A_2 < .3$, the effect of angular distributions would lie in the range $.8 < y_1/y_2 < 1.1$. If the two transitions have similar angular distributions, then $y_1/y_2 \approx 1$.

The minimum intensity that the 39.8 keV transition can have is therefore determined by the smallest conversion coefficient, i.e. pure E1. The minimum is $I_T(39.8)/I_T(62.9) = .3$. [If a pure M1, $I_T(39.8)/I_T(62.9) = .8$.] By examining the interconnection of levels by gamma rays and their relative intensities, we can restrict the possible placement of the 39.8 keV transition to four locations, with appropriate restrictions on its relative intensity. The placements are,

(a) feeding the (proposed) $5/2^+$, 320 keV level

$$\left(\frac{I_T(39.8)}{I_T(62.9)} \approx 1.3\right),$$

(b) feeding the ground state

$$\left(\frac{I_T(39.8)}{I_T(62.9)} > 1.45\right),$$

(c) feeding the level, shown in Fig. 3.2 as $13/2^+$, 1321 keV

$$\left(\frac{I_T(39.8)}{I_T(62.9)} < 53 \pm 13\right),$$

(d) feeding the level, shown in Fig. 3.2 as $(17/2^+)$, 1980 keV

$$\left(\frac{I_T(39.8)}{I_T(62.9)} < 66 \pm 11\right).$$

In case (a), an intensity ratio of 1.3 implies a conversion coefficient of 14 ± 2 for the 39.8 keV transition, i.e. either an E1/M2 ($|\delta| = .05 \pm .01$) or an M1/E2 ($|\delta| = .12 \pm .07$) multipolarity. Case (b) implies similar transitions with only slightly greater mixing ratios, i.e. for relative intensity of 1.5, the transition is of E1/M2

($|\delta| = .06 \pm .01$) or of M1/E2 ($|\delta| = .19 \pm .07$) multipolarity. In the last two cases (c) and (d), the transition would need to be of E1/M2 ($|\delta| < .02$) multipolarity.

Now as the time window used in the gamma sorting included only those events that were prompt or only slightly delayed (< 10 ns), an upper limit to the half life of the 39.8 keV transition can be set (i.e. $T_{1/2}\text{max} \approx 10$ ns). Also, if the transition lies higher in excitation energy than the 257.5 keV transition, then its half life must be less than (or equal to) the 2.8 ns measured for the half life of the 257.5 keV transition. The Weisskopf estimates of the half-lives of various multipolarity 29.8 keV transitions are given in Table 3.2.6 for a $7/2 \to 5/2$ transition.

Using these estimates we can conclude that with E1/M2 multipolarity, any mixing ratio of $|\delta| \gtrsim 2 \times 10^{-4}$ would imply that the M2 transition would be enhanced (assuming $T_{1/2}(39.8) = 10$ ns). This indicates that in placements (c) and (d), the transition would be almost *pure* E1 and that in placements (a) and (b), it would be of M1/E2 multipolarity. These observations preserve the previously proposed [Ha79b] positive parity of the cascade.

Table 3.2.6

Weisskopf Estimates of the Half Life of a 39.8 keV Transition.

Multipolarity	$T^W_{1/2}(7/2 \to 5/2)^{(a)}$
E1	.5 ps
M1	.03 ns
E2	40 μs
M2	.2 ms

(a) Statistical factors included.

The level systematics shown in Fig. 3.1 suggest that an $I^\pi = 7/2^+$ level should exist in ^{119}Te at approximately 300 keV excitation. The systematic trends also suggest that the $I^\pi = 3/2^+$ level lies at an excitation higher than that of 39.8 keV.

We therefore conclude that the 39.8 keV transition is of M1/E2 ($|\delta| \approx .12 \pm .07$) multipolarity and connects a $^7\!/_2{}^+$, 360 keV level with the $^5\!/_2{}^+$, 320 keV level. This is shown in Fig. 3.2.

Some transitions which [Sp70] and [Ha79b] have proposed as feeding the 320.4 keV level are not included in Fig. 3.1 as it is no longer certain to which level they decay.

3.2.4 Levels which Decay to the $^{11}\!/_2{}^-$ (x keV) Isomeric Level

3.2.4.1 Levels connected by the Yrast cascade

Generally, the transitions of which this sequence is comprised, are the most intense transitions observed in the γ-γ coincidence data. There is no observed smooth variation of the transitions' intensities as the level excitation increases. Instead, the fourth most intense transition observed, of 192.3 keV, is placed high in the sequence.

The 640.3 keV transition is placed to directly feed the $^{11}\!/_2{}^-$ (x keV) isomeric level, as it was the most intense transition observed. Also, there was no other combination of transitions which could carry the observed intensity to the $^{11}\!/_2{}^-$ (x keV) level if an attempt was made to place the 640.3 keV transition elsewhere.

The 717.7 keV transition is, in the singles spectrum, one member of a (possible) unresolved triplet of transitions. Two members of this triplet, the 717.7 and 719.3 keV transitions can be easily resolved by peak fitting, or by appropriate gating of the γ-γ coincidence spectra. The possible third member of the triplet (of 719 ± 1 keV) was found only weakly in the coincidence spectra when the 653.9, 717.7 and 1010.9 keV transitions were used as gates. If the transition exists, then it most probably occurs between the $(3088 + x)$, $^{27}\!/_2{}^-$, and the $(2369 + x)$, $^{23}\!/_2{}^-$ states. The branching ratios observed in the coincidence spectra allow an upper limit of 20 to be placed on the transition's singles intensity. Therefore the possible existence of this transition did not significantly affect the energy determination of the other members of the triplet.

The relative placement of the other transitions in the Yrast cascade was based, similarly, on exhaustive intensity comparisons in both singles and gated coincidence spectra. Relative excitation functions as shown in Fig. 3.4 were also used. As the 876.6 keV transition was contaminated in singles data by the $8^+ \rightarrow 6^+$ transition in ^{120}Te, its intensity was estimated from the coincidence data.

Examples of the coincidence spectra are shown in Fig. 3.11, for gate windows of 192.3, 1076.7 and 640.3 keV respectively. The 192 keV gate was sufficiently wide to include part of a contaminant gamma ray (not of ^{119}Te) whose origin was unknown. For intensity determinations, the 192 keV transition could be resolved by peak fitting.

The $^{35}/_{2}^{-}$, (4995 + x) keV level is directly fed by the 192.3 keV transition, and it decays via two major cascades. The intensity of the 192.3 keV transition is consistent with both singles and coincidence intensity sums as measured across these two cascades.

The two levels of highest excitation were deduced from the 75 MeV ^{13}C experiment. The 773 and 845 keV transitions were the only extra transitions observed which could be placed in ^{119}Te. (Care was taken to distinguish the 845 keV transition from that arising from neutron scattering.) As well as being in coincidence with the major ^{119}Te transitions, the time spectrum showed that they occurred earlier than the 192.3 keV transition. This confirms the placement of the two transitions at high excitation. It was not possible to determine the ordering of the transitions from the present data.

All the transitions which make up this cascade from the 640.3 keV up to the 192.3 keV transition have angular distributions which are characteristic of stretched E2 transitions. The multipolarity of the 640.3 and 653.9 keV transitions was confirmed as E2 by conversion coefficient measurements.

Both the K conversion coefficient and the K/L conversion ratio for the 192.3 keV transition are also compatible with stretched E2 transitions. However, after allowing for the large errors, the angular distribution and conversion coefficients may also represent a $^{35}/_{2} \rightarrow ^{35}/_{2}$, E1/M2 transition with a mixing ratio of $|\delta| = .43 \pm .15$. The relation of the partial half-lives of such a transition to the Weisskopf estimates is given in Table 3.2.7, together with similar comparisons for $\Delta J = 2$ transitions. As an enhancement of the M2

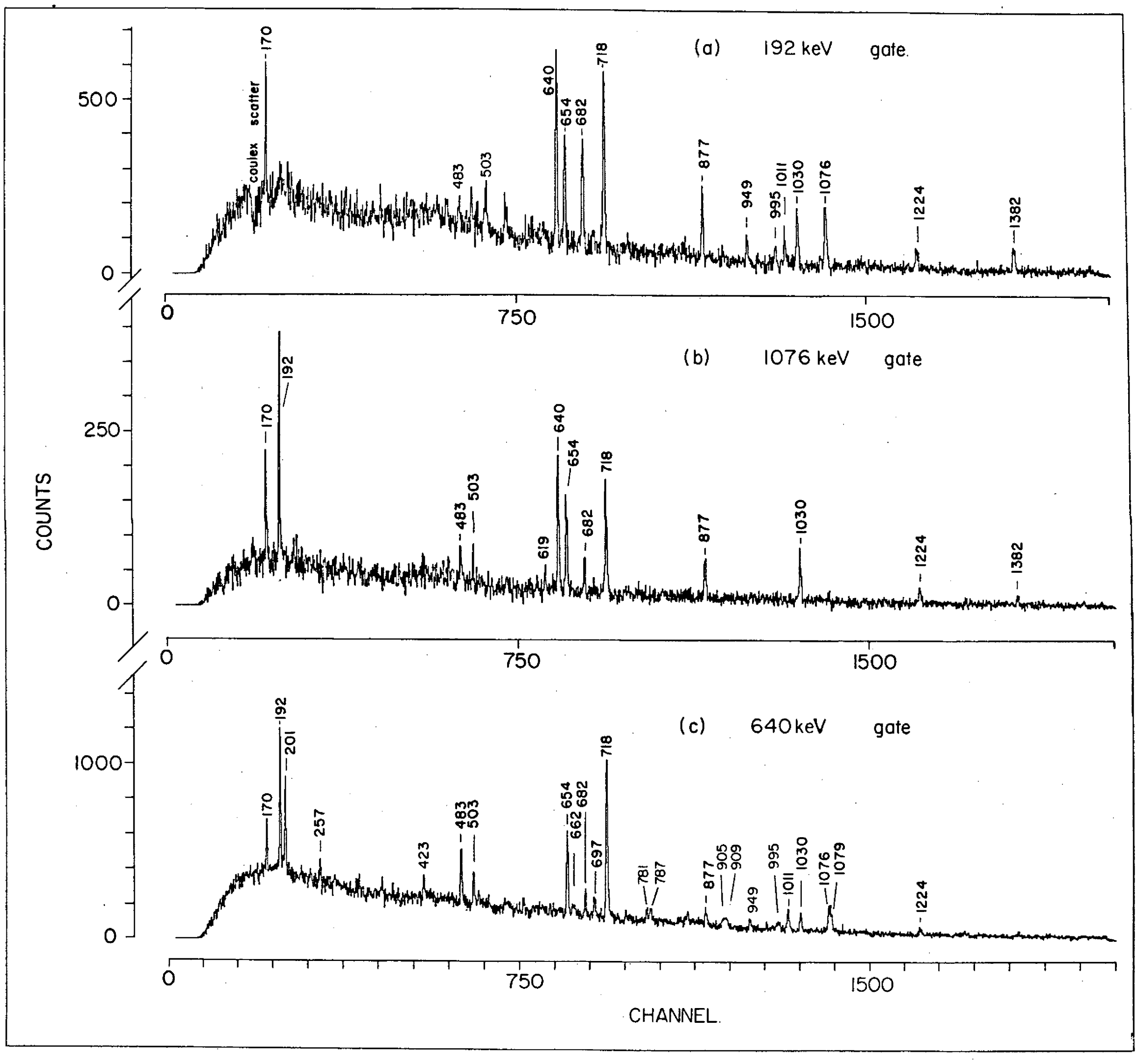

Fig. 3.11: Gated coincidence spectra observed in a coaxial Ge(Li) detector at 125° to the beam.

Table 3.2.7

Decay Possibilities of the (5187 +x) keV, $T_{1/2}$ =7.2 ns Level.

J_i	J_f	M	$T^W_{1/2}$ (ns)[a]	Enhancement (E) or Hindrance (H)
$^{35}/_2$	$^{35}/_2$	E1	.01	1290 H
$^{35}/_2$	$^{35}/_2$	M2	443	14.8 E
$^{39}/_2$	$^{35}/_2$	E2	15.8	2.2 E
$^{39}/_2$	$^{35}/_2$	M2	310	43 E

(a) Weisskopf single particle estimates; statistical factors have been included.

transition is most unlikely (see Chapter 2), the possibility of $^{35}/_2 \rightarrow {}^{35}/_2$ transition occurring can be discounted. This implies that the (5187 +x) keV level has a spin, parity of $I^\pi = {}^{39}/_2{}^-$.

The measured A_2 (A_2^{obs} =+.63 ± .05) of the 1381.9 keV transition is so large that a $\Delta J = 1$ transition is indicated. This implies that the (6569 +x) keV level has a spin of $I = {}^{41}/_2$, and that the mixing ratio of the transition is in the range $+0.82 \leq \delta \leq +1.6$.

3.2.4.2 Other levels below 2012 +x keV excitation

The positioning of the majority of these levels (shown in Fig. 3.1) was constrained by γ-γ coincidence data, energy sums and intensity sums. Excitation functions also support the chosen ordering.

The decision to include a level of (207 +x) keV rather than a level at (511.9 + x) keV was made on the basis of the branching ratio of the (719 +x) keV level. The reasoning was that if the (207 +x) keV level existed, then it would be partially populated by side feeding and partially by decay of the (719 +x) keV level; whereas those transitions of 206.9 keV which were in coincidence with the 618.9 keV transition is dependent on the branching ratio of the (719 +x) keV level. Hence the ratio of the intensities of the 206.9 and 719.3 keV transitions would be higher in singles than when found in coincidence with the 618.9 keV transition, i.e.

$$R_{sing} = \left(\frac{I(206.9)}{I(719.3)}\right)_{(sing)} > R_{coinc} = \left(\frac{I(206.9)}{I(719.3)}\right)_{(618.9 \text{ gated coinc})} .$$

As the observed values are $R_{sing} = .85 \pm .13$ and $R_{coinc} = .34 \pm .15$, the existence of the (207 + x) keV level is proposed. This is in agreement with the level scheme of [Ha79b].

The ordering of all the levels below (2012 + x) keV is similar to that proposed by Hagemann *et al.* [Ha79b]. The present angular distribution measurements and conversion coefficient measurements indicate the proposed spin assignments. (These, too, are in agreement with [Ha79b].) The conversion coefficients also indicate that the 170.4 and 483.3 keV transitions are of M1/E2 multipolarity and that the 503.3 and 511.9 keV transitions are of E2 multipolarity. The conversion coefficient and mixing ratio results are inconsistent if the multipolarity of the $\Delta J = 1$ transitions are E1/M2.

If the 618.9 keV transition is of stretched E2 type, then all the levels of the sequence (i.e. below (2012 + x) keV excitation) are connected by either M1/E2 or E2 transitions. Now as the $T_{1/2} = 4{\cdot}7$ d x keV isomeric level has been assigned a spin, parity of $I^{\pi} = {}^{11}\!/_{2}^{-}$, this implies that all the levels of this sequence have negative parity. As a result of both this work and that of [Ha79b], we can conclude that the identification of these levels has been firmly established. They will now be used as a base to which the remaining gamma rays will be attached.

3.2.4.3 The (2369 + x), (3364 + x) and (4312 + x) keV levels

The (2369 + x) keV level mainly decays to the (1358 + x) keV level by the emission of a 1010.9 keV gamma ray. The coincidence spectrum gated by this transition is shown in Fig. 3.12, part b. The energy window also includes part of another gamma ray, which, it appears, belongs to the spectrum of ^{120}Te. The (2369 + x) keV level also decays by emission of a 356 keV gamma ray. As this transition is unresolved in singles, the estimate of its intensity given in Table 3.2.1 was obtained from the branching ratios observed in the coincidence spectra, and the singles intensity of the 1010.9 keV transition.

As the 682.4 keV transition is observed in coincidence with the

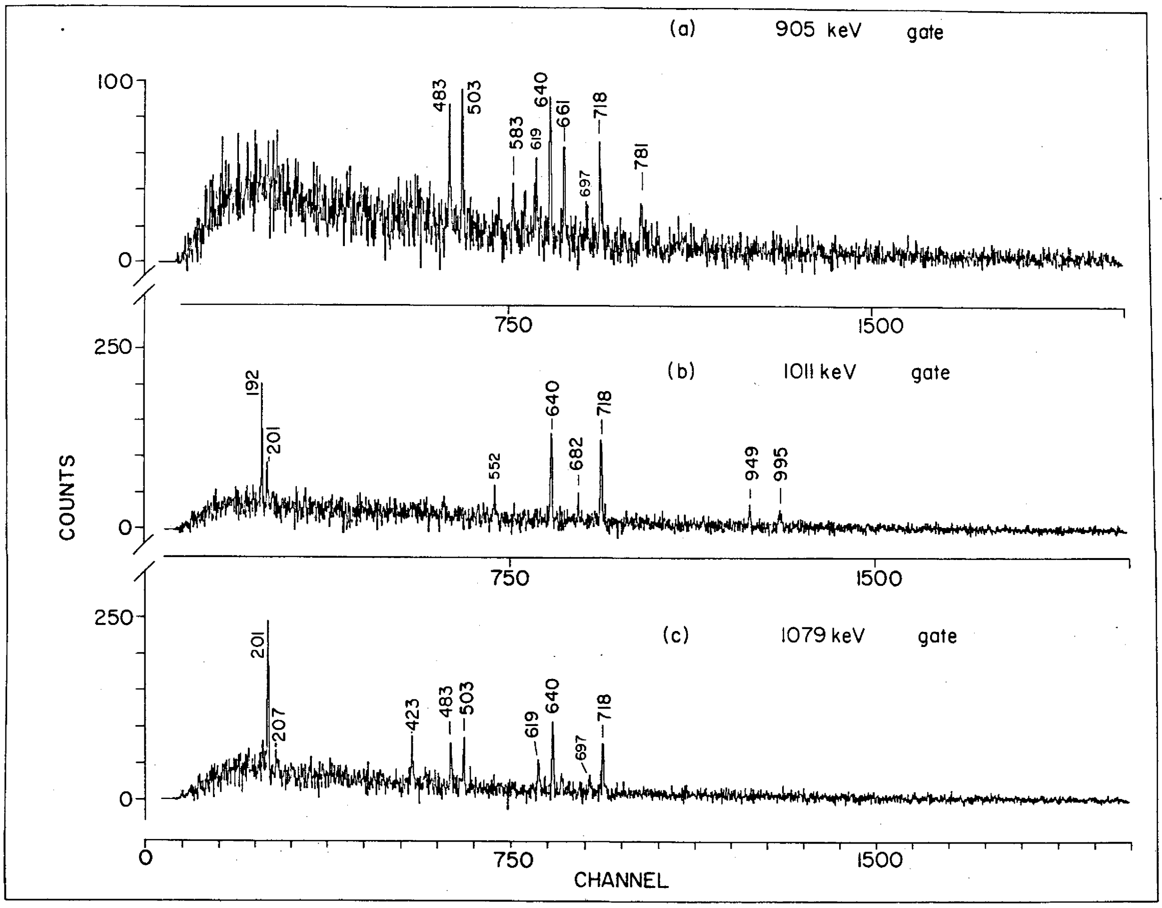

Fig. 3.12: Gated coincidence spectra observed in a coaxial Ge(Li) detector at 125° to the beam.

1224.0, 192.3, and 994.8 and 948.5 keV gamma rays, the (4312 +x) keV level is firmly established. Sums of the gamma ray energies also support the assignment.

The establishment of the (3364 +x) keV level is determined from the intensities of the 948.5 and 994.8 keV transitions when they are in coincidence with the 1010.9 keV transition. The relative intensities found were

$$\left.\frac{I(994.8)}{I(948.5)}\right]_{\substack{\text{1010.9 keV gated} \\ \text{coincidence}}} = \frac{1020 \pm 100}{670 \pm 100} = 1.5 \pm .3 \ .$$

This relation could be expected if the 994.8 keV lay closer to the 1010.9 keV transition than the 948.5 keV transition. The relative excitation functions (Fig. 3.4) weakly supports this ordering.

The 1010.9, 948.5, 994.8, 682.4 and 1224.0 keV gamma rays all have angular distributions consistent with their being stretched E2 transitions. Assuming this multipolarity, the level spins are determined as given in Fig. 3.2. The spin assignments are in accord with those assigned to the Yrast levels. The multipolarity implies that the (2369 +x), (3364 +x) and (4312 +x) keV levels all have negative parity.

3.2.4.4 The (2921 +x), (3122 +x) and (3544 +x) keV levels

The (2921 +x) keV level is strongly populated and decays by three transitions, of 1079.5, 908.7 and 552 keV respectively. The (3122 +x) and (3544 +x) keV levels are determined by the relative intensities of the 200.8 and 422.9 keV gamma rays. These can be seen in the coincidence spectrum gated by the 1079.5 keV gamma ray in Fig. 12, part c. Although the (3544 +x) keV level was populated fairly strongly, no evidence of any feeding transition was found. (The level is not isomeric.)

Relative excitation functions (Fig. 3.4) support the level assignments.

Both the 786.9 and 665.3 keV transitions are unresolved in singles data. They have been placed in ^{119}Te as they are both in coincidence with the 640.3 and 719(d) keV gamma rays. They are also in coincidence with each other. However, there is insufficient evidence with which the placement of the transitions in the level scheme could be made.

Angular distributions of the 1079.5, 908.7, and 552 keV transitions limit the spin of the (2921 + x) keV level to either $I = {}^{21}\!/_2$ or ${}^{23}\!/_2$ as none of the angular distributions are characteristic of stretched E2 transitions. However, if the spin were ${}^{21}\!/_2$, the level would be 1079 keV above the Yrast line, and hence would be unlikely to be populated so strongly. The 200.8 and 422.9 keV transitions are dipolar ($\Delta I = 1$), hence the spin assignments given in Fig. 3.2.

3.2.4.5 The (2746 + x), (3527 + x), (4189 + x) and (4772 + x) keV levels

A detailed study of the coincidence intensities of the four transitions, of 905.0, 781.0, 661.6, and 583.2 keV suggested the above level sequence. The spectrum in coincidence with the 905.0 keV transition is shown in Fig. 3.12, part a. The proposed ordering of the levels is supported by the singles intensities (Table 3.2.1) and relative excitation functions (Fig. 3.4) of the above four gamma rays.

The angular distribution of the 905.0 keV gamma ray indicates a $\Delta J = 1$ transition. If the spin of the (2746 + 1) keV level were $I = {}^{19}\!/_2$, then the level would lie far above the Yrast line and it would be unlikely that it would be populated very strongly. Also, many more transitions would be made possible (e.g. ${}^{19}\!/_2 \rightarrow {}^{19}\!/_2$, ${}^{19}\!/_2 \rightarrow {}^{17}\!/_2^-$, ${}^{19}\!/_2 \rightarrow {}^{17}\!/_2^+$), yet these were not observed.

The spin sequence above the (2746 + x) keV level is not well determined as the angular distributions have relatively large errors. With a positive A_2 and negative A_4, the 661.6 keV gamma ray may be a $\Delta J = 2$ transition. However, the angular distributions of both the 781.0 and 583.2 keV gamma rays may represent either dipole or quadrupole transitions. Spins are therefore not assigned to the levels of this cascade above the (2746 + x) keV level.

3.3 ^{117}Te

3.3.1 General

The deduced level scheme for ^{117}Te is presented in Fig. 3.13. Its derivation was based mainly upon 8×10^7 γ-γ coincidence events collected as a result of the ^{108}Pd(^{13}C,4n)^{117}Te (68 MeV) reaction. The large number of events were required as other reactions were beginning to compete with the 4n reaction channel. As well as the 3n and 5n channels receiving a high population, the pxn and αxn channels were also highly populated; the αxn channels taking approximately 10% of the total reaction cross section.

The 68 MeV bombarding energy, approximately 2 MeV above the optimum bombarding energy for production of the 4n channel, was chosen to preferentially populate the high spin states.

Previous information on ^{117}Te came from the work of Brinkmann *et al.* [Br72] and [Br69b] and that of Hagemann *et al.* [Ha79b]. Information was also available from ^{117}I decay studies [La69] and [Se69]. Brinkmann *et al.* [Br72] showed that the first excited state in ^{117}Te (at 274 keV) was of spin, parity $I^\pi = 5/2^+$. They also indicated the presence of a level of $I^\pi = 7/2^+$ at 296 keV excitation. Hagemann *et al.* [Ha79b] used an (α,2n) reaction and reported on states of spin $I \leq 23/2$ (as in ^{119}Te). The presently proposed negative parity states of spin $11/2 \leq I \leq 23/2$ are in agreement with those proposed by [Ha79b].

The proposed positive parity states, though, are not in general agreement with the work of [Ha79b]. They proposed a level sequence based on the $7/2^+$, 296 keV level which appeared like that of a rotational band. Several of the transitions of that sequence reported by [Ha79b] were not observed in the present experiments. Also, coincidence data indicated a different placement of the 670.1 keV transition.

The excitation energy of the $11/2^-$ ($\sim$ 300 keV) isomeric level ($T_{1/2}$ = 103 ms [Le79]) was previously unknown. The isomer decays via conversion electron and gamma ray emission to the $7/2^+$, 296 keV level [Br69a]. Although the isomeric transition itself has not been observed, Brinkmann *et al.* [Br69a] were able to show that its energy

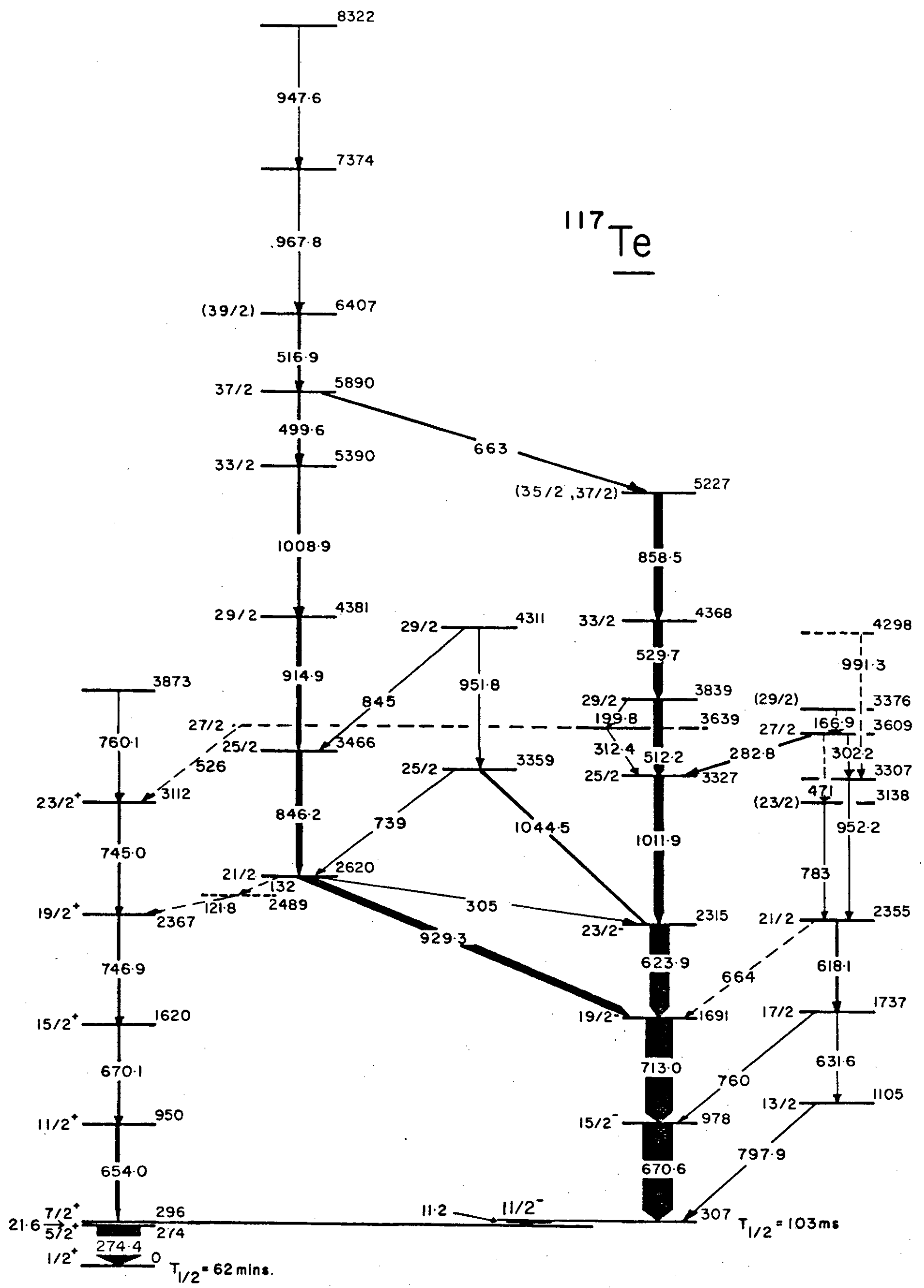

Fig. 3.13: Level spectrum of ^{117}Te deduced from observations following a ^{108}Pd(^{13}C,4n)^{117}Te (68 MeV) reaction.

is less than 32 keV, limiting the excitation of the $^{11}/_{2}^{-}$ level to $E_{11/2^-} \leq 328$ keV.

3.3.2 Summary of the Data

The singles and total coincidence spectra, recorded from a Ge(Li) detector at 125° to the beam are shown in Fig. 3.14. The complexity of the spectra is readily apparent. Those transitions marked thus — *, are from Tin nuclei. The major transitions belonging to the spectrum of ^{116}Te are marked thus — ▲. As an example of the complexity of the spectrum, consider the 512 keV transition. During the analysis it became apparent that there are no fewer than five gamma rays, each from a different nucleus, in the energy region $510 < E_\gamma < 513$ keV.

Some typical examples of the angular distribution measurements are given in Fig. 3.15. The curves in Fig. 3.15 represent the fitted angular distribution function. Values of A_2 and A_4 used were taken from Table 3.3.1. This table also gives the transition energies, the gamma ray relative intensities, and the state from which the transition originated. It will be noticed that several transitions given in Table 3.3.1 are not placed in the level scheme. These are, in general, very weak transitions, often unresolved in the singles spectrum, whose existence in ^{117}Te is based on gamma-gamma coincidence data. The observations, though, are inadequate to uniquely place the transitions in the level scheme of Fig. 3.13.

Relative excitation functions of some of the placed transitions are given in Fig. 3.16. Many of these functions indicated the presence of more than one transition in the energy windows used in determining the relative strengths. The contaminating transitions belong to nuclei other than ^{117}Te.

Although the gamma-gamma coincidence data did not reveal the presence of any new isomeric state, the experience with ^{119}Te led to two further experiments being conducted.

In the first, neutron-gamma coincidences, capable of detecting half-lives greater than 2 ns, failed to show any delayed transition other than the 274 keV gamma ray. The time spectrum of this

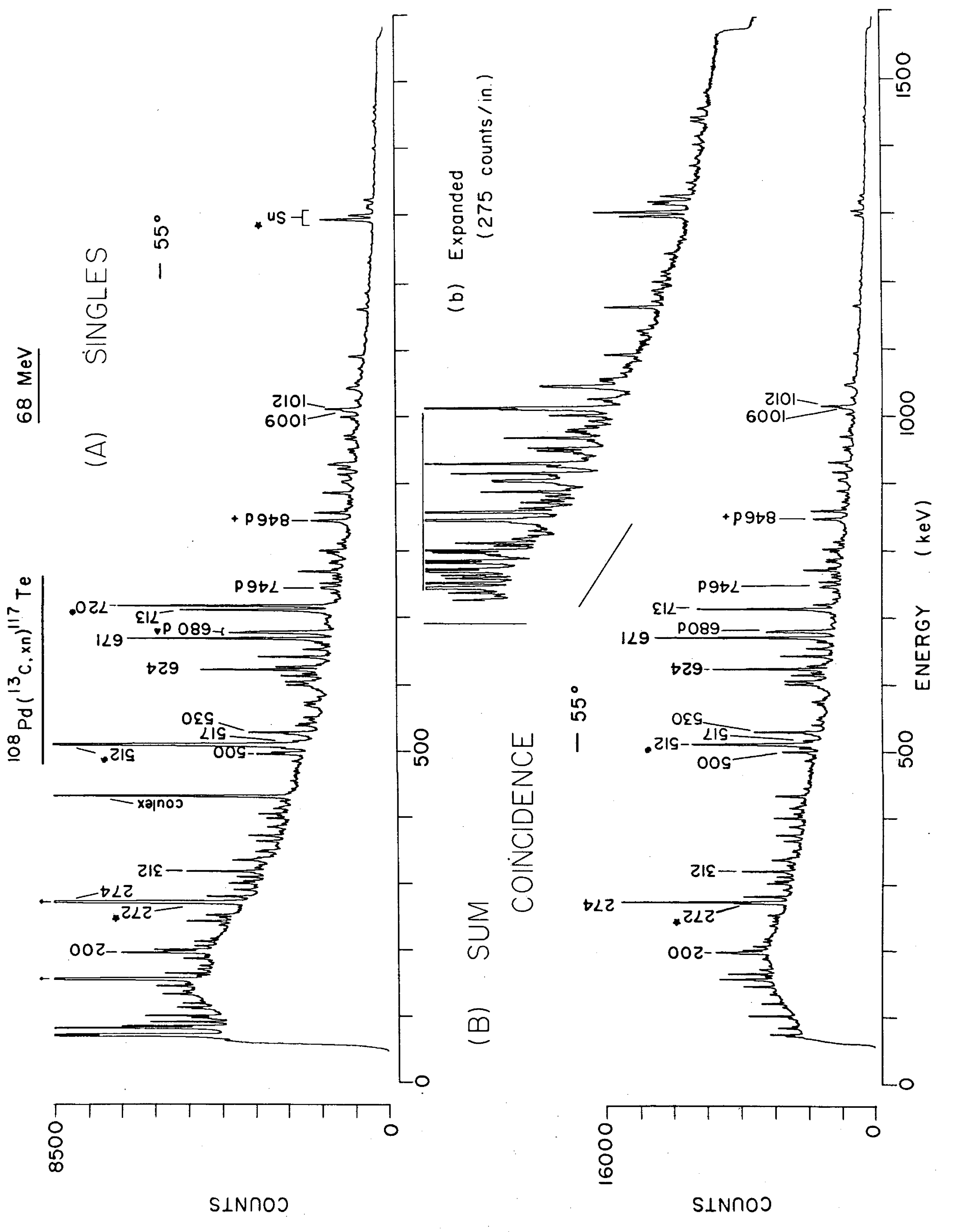

Fig. 3.14: Singles and total coincidence spectra observed following the $^{108}Pd(^{13}C,4n)^{117}Te$ (68 MeV) reaction in a coaxial Ge(Li) detector at 55° to the beam.

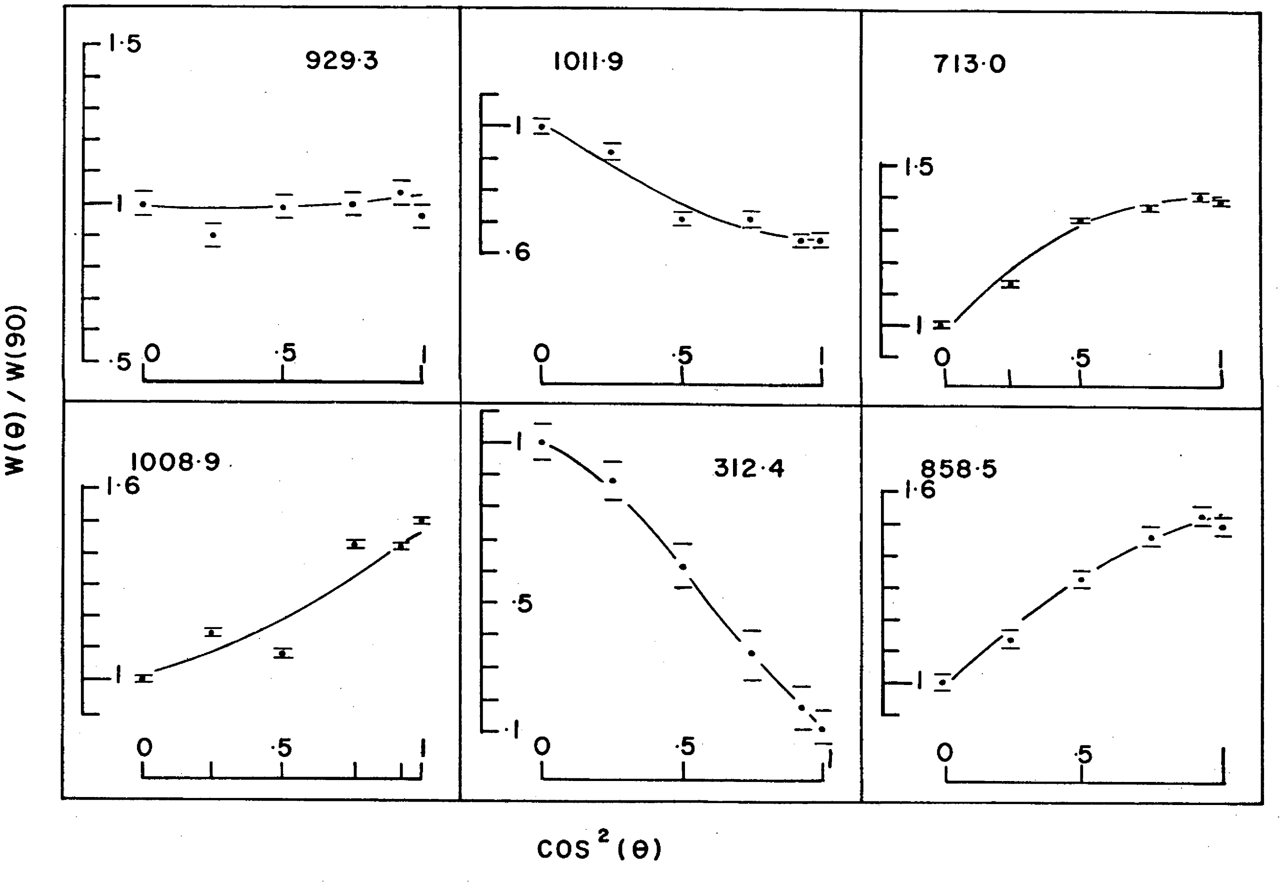

Fig. 3.15: Angular distributions of transitions in ^{117}Te. The curve represents the fitted function $W = W(\theta)/W(90°)$ where $W(\theta) = W_0[1 + A_2P_2(\mathrm{Cos}(\theta)) + A_4P_4(\mathrm{Cos}(\theta))]$.

Table 3.3.1

Transition Energies, Gamma Ray Intensities, and Angular Distribution Coefficients for Transitions Observed in the $^{108}Pd(^{13}C,4n)^{117}Te$ (68 MeV) Reaction. Initial States of Assigned Transitions are also Given.

Transition Energy (a)	Gamma Ray Intensity (b)	A_2 (c)	A_4 (c)	Initial State (keV) (h)
121.8	59 (6)	.27 (16)	-.09 (17)	2489
132 (1)[(e)]	35 (10)			2620
166.9	89 (5)	-.57 (7)	.22 (8)	3376
199.8 [(e)]	55 (10)	-.43 (7)[(f)]	.01 (7)	3839
221 (1)[(e)]	20 (10)			(3138)
274.4	2075 (50)	.02 (1)	-.01 (1)	274
282.8	119 (6)	-.11 (5)	-.02 (6)	3609
302.2 (5)	61 (7)			3609
312.4	68 (5)	-.69 (19)	.14 (20)	3639
327.1 (5)	18 (8)			(d)
340.9 (5)	45 (9)			(d)
407.2 (5)	85 (10)	-.34 (16)	-.02 (18)	(d)
471 (1)	36 (6)			(3609)
487 [(e)]	52 (7)			(2107)
499.6	132 (7)	.21 (5)	-.05 (6)	5890
512.2 [(e)]	300 (15)			3839
516.9	133 (7)	-.01 (5)	.00 (6)	6407
526 (1)[(e)]	25 (10)			(3639)
529.7	341 (10)	.29 (4)	-.09 (5)	4368
618.1	151 (11)	.28 (3)	-.06 (4)	2355
623.9	721 (8)	.28 (1)	-.08 (1)	2315
631.6	86 (9)	.28 (8)	.06 (9)	1737
654.0	154 (8)			950
660.4	48 (9)			(d)
663 (1)[(e)]	80 (15)	-.68 (9)	.20 (11)	5890
664 (1)	20 (15)			(2355)
670.6 [(e)]	1025 (15)	.26 (2)	-.07 (3)	978
670.1 [(e)]	135 (15)			1620
713.0	1000	.26 (2)	-.08 (2)	1691
739 (1)	43 (7)	.28 (14)	-.09 (15)	3359

(g) Peak areas were contaminated by the 847 keV transition resulting from neutron scattering from ^{56}Fe. The strength of this transition is equal to that of the 846.2 keV transition.

(h) Bracketed energies are tentatively assigned levels.

Transition Energy (a)	Gamma Ray Intensity (b)	A_2 (c)	A_4 (c)	Initial State (keV) (h)
745.0 (3)	117 (7)	.34 (6)	-.15 (7)	3112
746.9 (3)	126 (8)	.16 (6)	.03 (7)	2367
760 (1) (e)	68 (9)			1737
760.1 (5) (e)				(3873)
783.0 (3)	113 (8)	-.18 (9)	.02 (10)	3138
797.9	142 (8)	.04 (12)	.23 (14)	1105
810 (1) (e)	35 (15)			(2917)
845 (1) (e)	30 (15)	.24 (3) (g)	-.12 (3)	4311
846.2 (2) (e)	210 (15)			3466
858.5	344 (9)	.31 (3)	-.04 (5)	5227
902.6 (4)	98 (9)			(d)
904.9 (4)	117 (9)			(d)
914.9	171 (9)	.21 (6)	-.03 (7)	4381
929.3	269 (8)	-.01 (5)	.03 (6)	2620
947.6	93 (9)	.12 (17)	-.19 (19)	8322
951.8 (2)	122 (12)	.12 (6)	-.03 (7)	4311
952.2 (2)				3307
967.8	122 (9)	.09 (8)	.03 (9)	7374
991.3 (4)	25 (15)			(4298)
1008.9	151 (8)	.26 (7)	.04 (8)	5390
1011.9	348 (8)	-.32 (4)	.07 (5)	3327
1044.5	122 (7)	.06 (16)	-.23 (18)	3359

(a) Except where given errors on the transition energies are ±.1 keV.

(b) Gamma ray intensities are given relative to the intensity of the 773.0 keV transition. Singles intensities obtained from a coaxial Ge(Li) detector at 55° to the beam direction are given except where note (e) applies.

(c) Normalised angular distribution coefficients chosen as the best fit to the equation $W(\theta) = W_0[1 + (A_2)\ P_2(\mathrm{Cos}\theta) + (A_4)\ P_4(\mathrm{Cos}\theta)]$.

(d) The transition is unplaced in the level scheme presented in Fig. 3.2.3(a).

(e) Data from γ-γ coincidence spectra was used in conjunction with singles data to obtain transition energies and intensities.

(f) Peak areas include a contribution from the 198.4 keV transition in ^{118}Te.

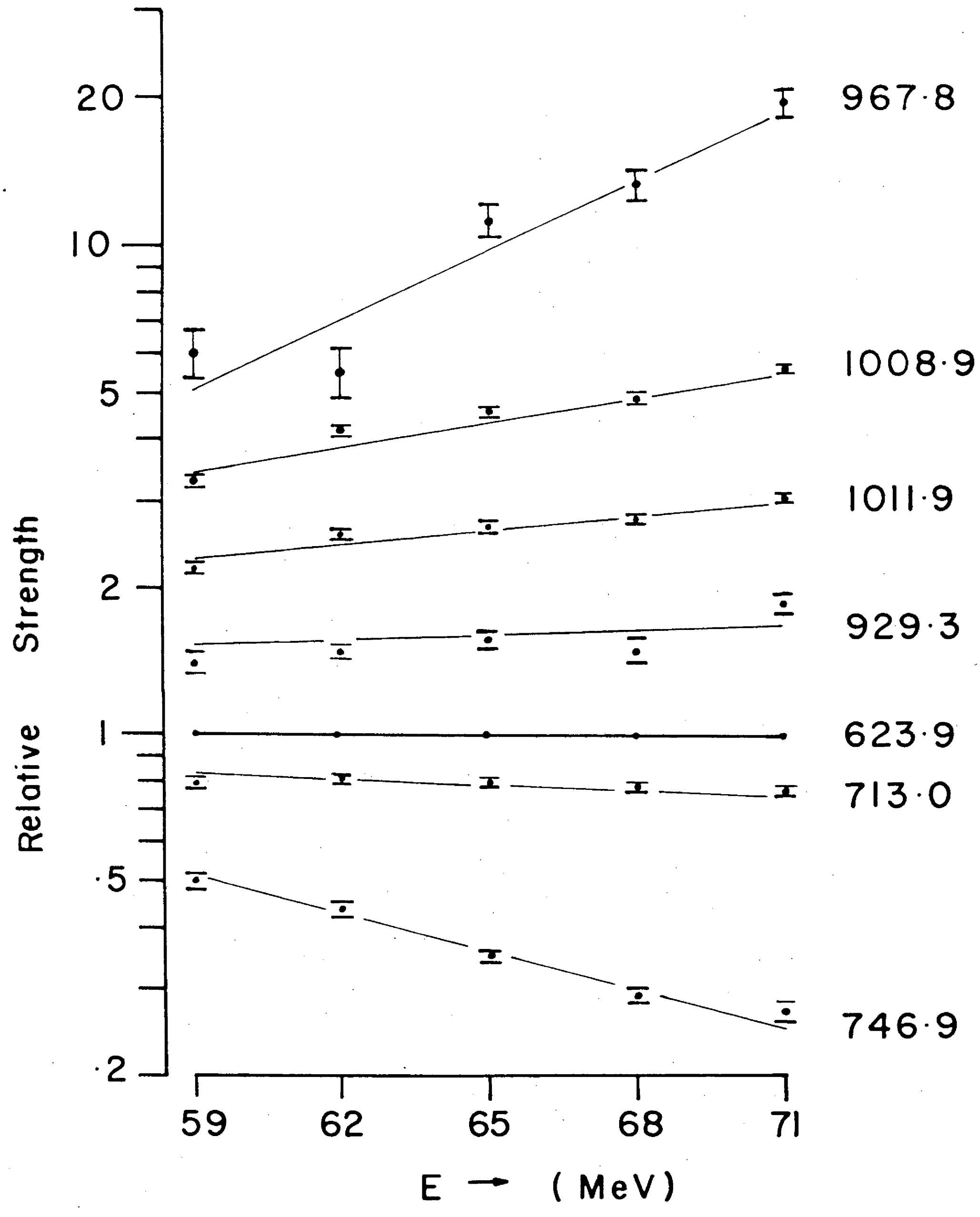

Fig. 3.16: Relative excitation functions of transitions in ^{117}Te.

transition is given in Fig. 3.17, together with a prompt T.A.C. response as measured at a similar energy. The half life determined for the $5/2^+$, 274 keV level was $T_{1/2} = 19.1 \pm .6$ ns, in excellent agreement with previous measurements [Ha79b].

The second experiment used a planar detector to search for any previously unobserved delayed transition. The data was taken in coincidence with a coaxial Ge(Li) gamma ray detector and the time resolution was 5 ns. If any delayed transitions were observed they could then be placed by appropriate gating on the gamma spectra and the time spectra. The relation which the gamma rays hold to isomeric levels is shown in Fig. 3.18(a) for each of the delayed T.A.C. regions. The time range used was sufficient to clearly identify delayed transitions with half-lives of up to the order of a microsecond (in various Tin isotopes). All observed delayed transitions, apart from the 274 keV gamma ray, belonged to the spectra of the Tin isotopes. Also shown in Fig. 3.18 is the total coincidence spectrum of the planar detector.

3.3.3 Levels which Decay to the Ground State

A cascade of five relatively intense transitions of 654.0, 670.1, 746.9, 745.0 and 760.1 keV was observed in delayed coincidence with the 274.4 keV transition, as shown in Fig. 3.19(b).

A detailed analysis of the gamma-gamma coincidence data, using these transition energies as gates, resulted in the ordering of the transitions as given in Fig. 3.13. The energy and intensity of the 670.1 keV transition was obtained from the coincidence data as it was completely hidden in singles by the intense 670.7 keV transition. With the chosen ordering, the observed singles intensities (i.e. not including the 670.1 keV transition) monotonically decrease as the excitation energy increases. The estimated intensity of the 670.1 keV transition is (of course) in agreement with such an observation.

There is no direct evidence for the 296 keV, $7/2^+$ level being the bandhead of the above cascade as the 21.6 keV $7/2^+ \rightarrow 5/2^+$ transition was not observed in the present experiments. As the (HI,xn) reaction mechanism selectively populates levels of Yrast or near Yrast nature,

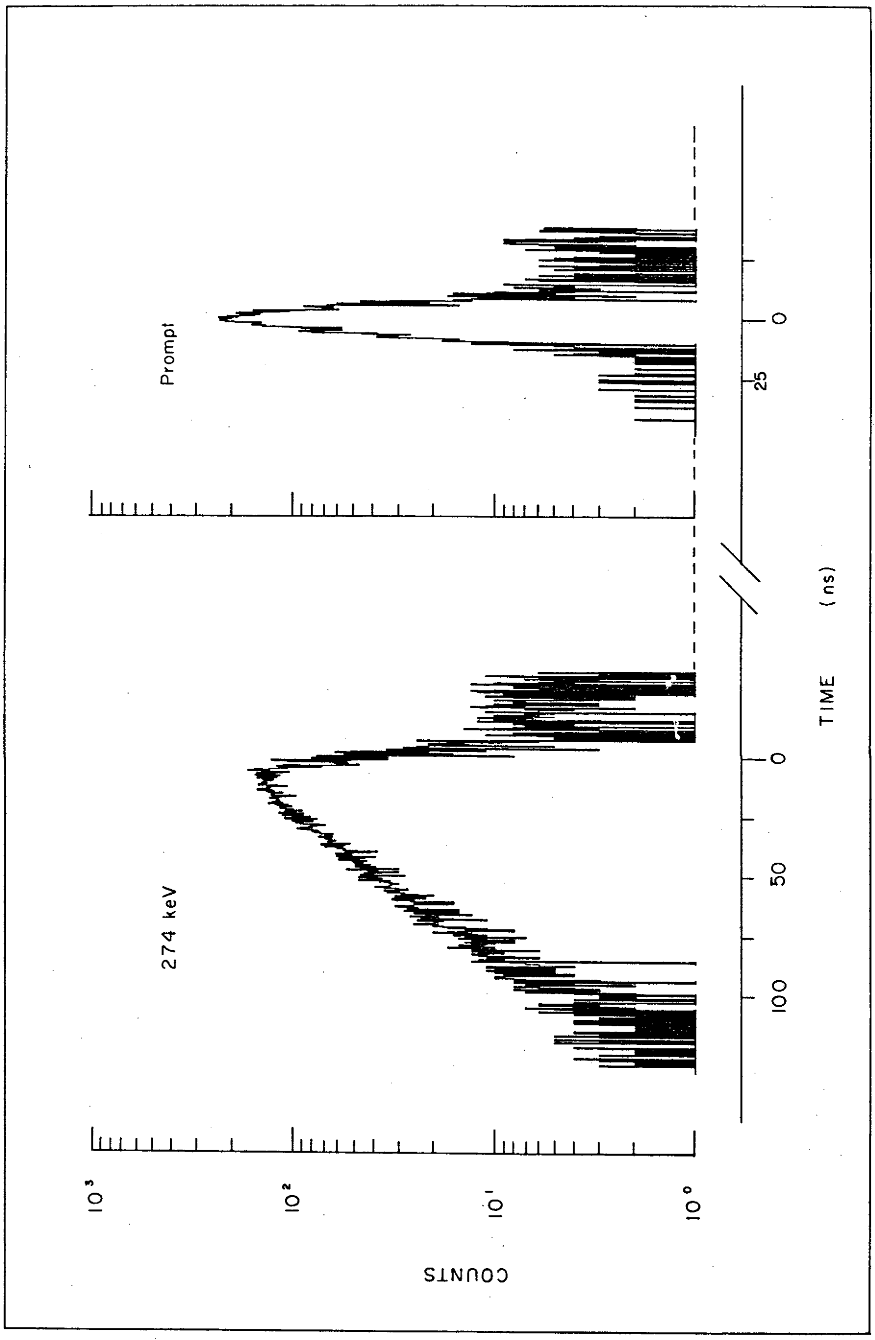

Fig. 3.17: Time spectrum of the 274.4 keV transition. Also shown is the T.A.C. response of a prompt transition of similar energy.

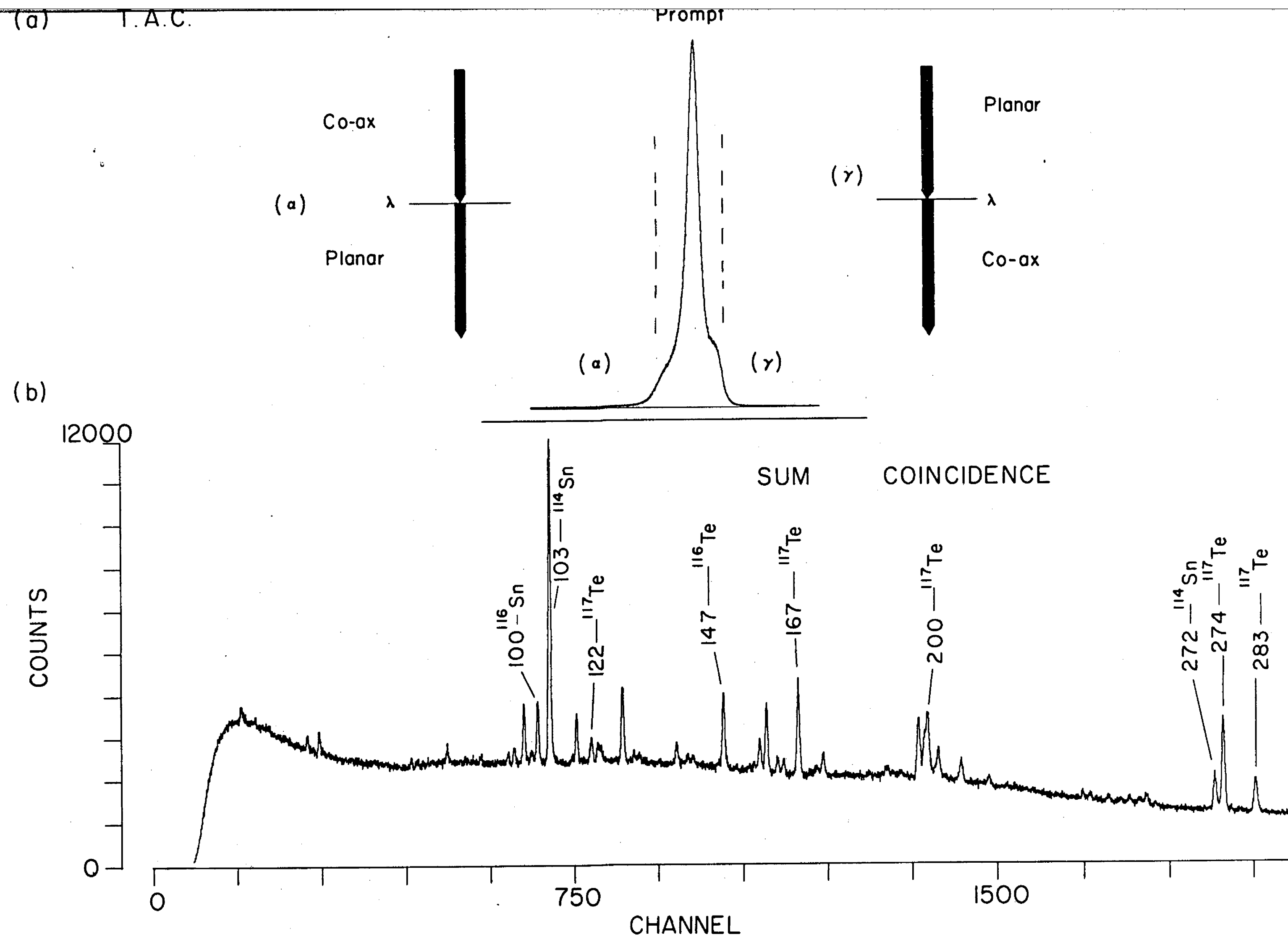

Fig. 3.18: (A) Total coincidence low energy spectrum observed with a planar Ge detector at 90° to the beam. Also shown (B) are the three T.A.C. regions used in the search for delayed transitions.

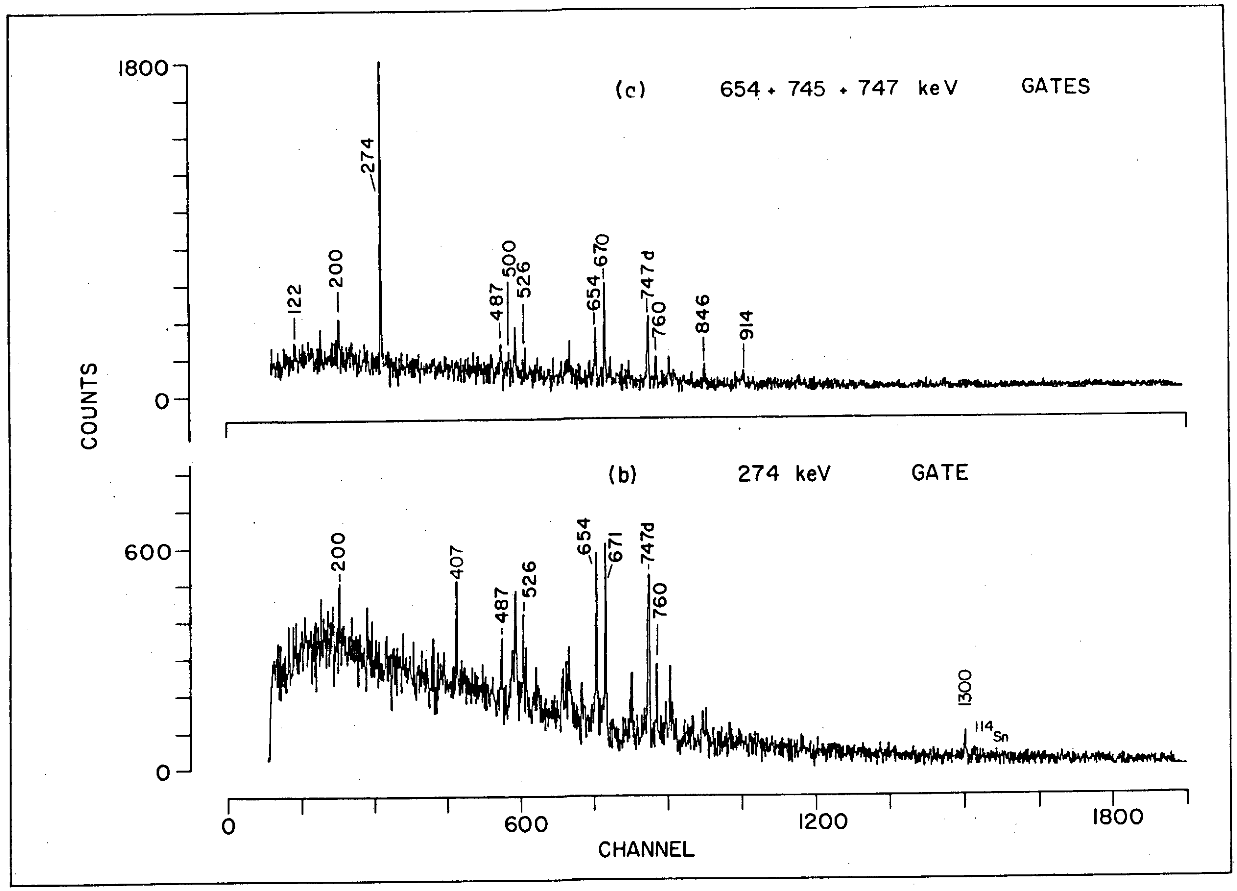

Fig. 3.19: Gated coincidence spectra observed in a coaxial Ge(Li) detector at 55° to the beam.

it is probable that the most intensely observed band is Yrast in nature. As the above mentioned gamma rays are the only intense transitions observed in coincidence with the 274.4 keV transition, they most likely have the $7/2^+$, 296 keV level as bandhead.

The angular distribution of the 654.0, 746.9, and 745.0 keV transitions are compatible with stretched E2 transitions. The angular distribution of the 670.1, 670.6 keV doublet is the same as that of the 713 keV transition, i.e. $A_2 = +.26 \pm .02$ and $A_4 = -.07 \pm .03$. If we assume that the 670.6 and 713.0 keV transitions are of stretched E2 type and have the same angular distribution, then we can determine limits for the value of the A_2 attenuation coefficient of the 670.1 keV transition [$A_2(670)$]. The values of A_2 which would be observed for the doublet, given various distributions of the 670.1 keV transition, are shown in Table 3.3.2. To obtain the observed A_2 values, $.1 < A_2(670.1) < .4$; i.e. the distribution must be similar to that of a stretched E2 transition. The spins are therefore determined as given in Fig. 3.13.

Table 3.3.2

Relation between Attenuation Coefficient of the 670.1 keV Transition and the Values which would be Observed for the Doublet; Given $A_2(670.6) = .26 \pm .02$, $I(670.6) = 1025$, $I(670.1) = 135$.

$A_2(670.1)$	A_2(Observed)
-.2	.21
-.1	.22
0	.23
.1	.24
.2	.25
.3	.265
.4	.28

The spectrum of Fig. 3.19(a) is the sum of the coincidence spectra gated by the 654.0, 745.0 and 746.9 keV transitions. Many of the transitions observed weakly in this spectrum have been placed elsewhere in the spectrum (see §3.3.4). Some "leaking" of intensity from the bands based on the $^{11}/_2^-$ isomeric level to the band based on the $^7/_2^+$, 296 keV level is obviously occurring. This is supported by the observation of the 199.8, 166.9 and 121.8 keV transitions in weak coincidence with the 274.4 keV gamma ray.

Of the transitions which were observed in these coincidence spectra, only six (previously unplaced transitions) can be combined so as to connect the two bands, by three separate decay paths, such that the energies of the levels match. Two of these paths are shown in Fig. 3.13. The third consists of transitions of 487, 810, and 221 keV connecting the 3138 ($^{23}/_2$) and 1620, $^{15}/_2^+$ levels. The difference in energy of the two bands, as determined by the paths is given in Table 3.3.3. The mean value is 11.2 ± .8 keV.

Table 3.3.3

Energy Difference between the Two Cascades (One Based on $^{11}/_2^-$ Isomeric Level, the Other Based on the $^7/_2^+$, 296 keV Level) for the Possible Decay Paths.

Connecting Transitions	Difference in Energies
526	10.2 ± 1.1
132, 121.8	11.9 ± 1.0
487, 510, 221	11.5 ± 1.5

The positioning of these connecting paths could not be confirmed by the gamma-gamma coincidences. The evidence for the assignment of 307.2 keV to the excitation energy of the $^{11}/_2^-$ isomeric level is therefore only circumstantial. The excitation energies given in Fig. 3.13 and Table 3.3.1 all assume this value. Using this value we obtain a hindrance, when compared to the Weisskopf unit of 2400 for the $^{11}/_2^- \rightarrow {}^7/_2^+$ transition.

3.3.4 Levels which Decay to the $^{11}/_2^-$, 307 keV Isomeric Level

3.3.4.1 Yrast and Yrare cascades

The two most intense cascades observed follow a pattern similar to that seen in ^{119}Te, i.e. the Yrast and Yrare cascades are joined both at low (1691 keV) and high (5890 keV) excitation, forming a single cascade below the former and above the latter levels. The members of both cascades and their relative ordering are strongly supported by gamma-gamma coincidence analysis. Examples of the spectra obtained are given in Fig. 3.20. The 929 keV energy window was sufficiently wide to include part of a contaminant gamma ray, apparently belonging to a Tin isotope.

Of the transitions in the dual cascade, only the 967.8, 516.9, 663, 929.3 and 1011.9 keV and, possibly, the 858.5 keV transitions have angular distributions *not* characteristic of stretched E2 transitions. If the 858 keV transition ($A_2^{obs} = .31 \pm .03$, $A_4^{obs} = .04 \pm .05$) were a $\Delta J = 2$ transition, then the 663 keV transition would have to be a $\Delta J = 0$ transition. The spins given in Fig. 3.13 were determined assuming that any $\Delta J = 1$ transitions are probably $J \rightarrow (J-1)$.

3.3.4.2 The 1737 keV and associated levels

Both the 1737 and 1105 keV levels were assigned by Hagemann *et al.* [Ha79b]. The present work confirms their existence but is unable to confirm their spin due to contaminants in the singles spectra of the 760 and 797.9 keV transitions.

The 2355, 3138, 3307 and 4298 keV levels are proposed on the basis of gamma-gamma coincidences. They are supported by the energy sums between the 2555 and 3609 keV levels. The 3609 keV level decays both via this cascade and also in the 282.8 keV transition to the Yrast cascade, joining it at the $^{25}/_{2}$, 3325 keV level.

3.3.4.3 Other levels

The 3639 keV level decays both to the Yrast cascade and to the band based on the $^{7}/_{2}{}^{+}$ 296 keV level. The assignment is supported by the 199.8 keV feeding transition which arises from the decay of the 3839 keV level. Both the 199.8 and 312.4 keV transitions have negative A_2 values, and are consistent with $J \rightarrow J-1$ transitions. This

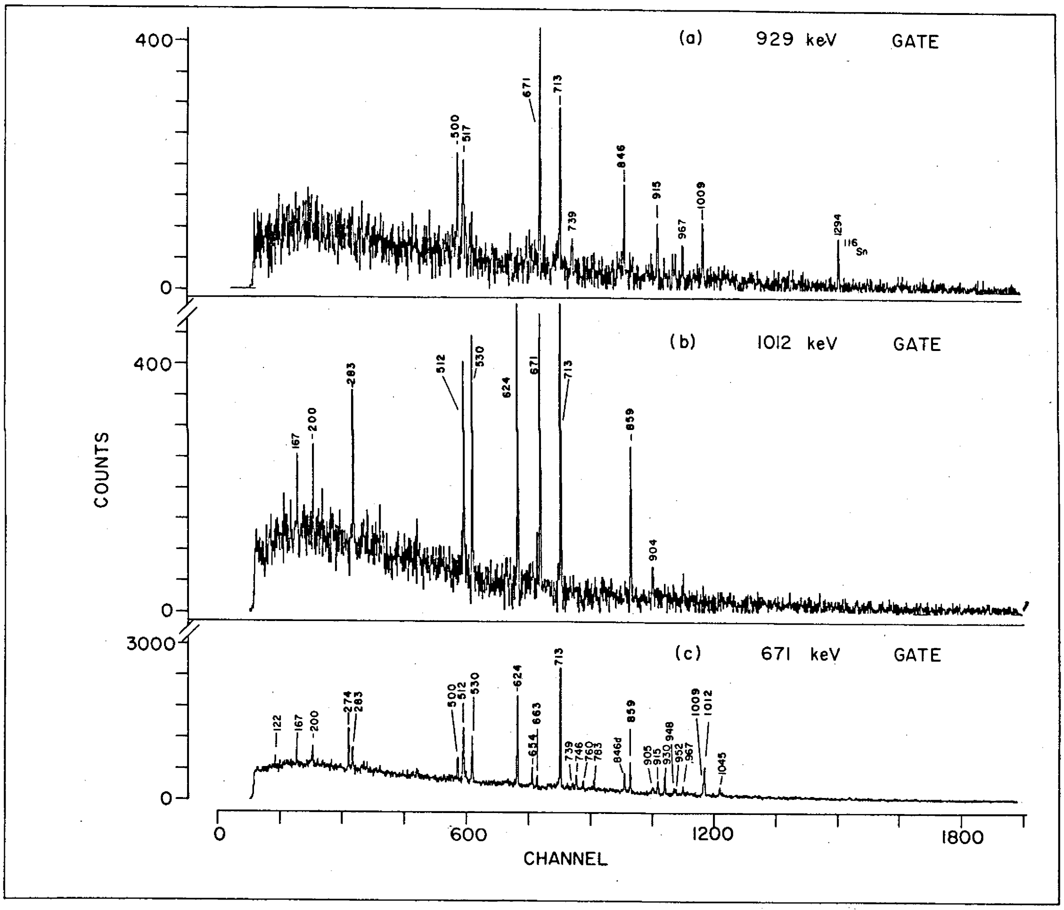

Fig. 3.20: Gated coincidence spectra observed in a coaxial Ge(Li) detector at 55° to the beam.

implies that the 512.2 keV transition is a $\Delta J = 2$ transition, probably stretched E2.

The 3359 and 4311 keV levels are proposed from coincidence data and are supported by energy sums. There is some evidence in the gamma-gamma data to suggest a connection between these levels and levels of higher spin, but the connecting transitions could not be determined.

The level scheme, as presented in Fig. 3.13, is supported by the relative excitation functions displayed in Fig. 3.16.

3.4 ^{118}Te

3.4.1 General

The deduced level scheme for ^{118}Te is presented in Fig. 3.21. Its derivation was based mainly upon 6×10^7 γ-γ coincidence events collected as a result of the ^{110}Pd(^{13}C,5n)^{118}Te (75 MeV) reaction. Additional information from the ^{108}Pd(^{13}C,3n)^{118}Te (68 MeV) reaction was also used.

The transition energies, intensities, and angular distribution coefficients are given in Table 3.4.1. The relative excitation functions are given in Fig. 3.22.

Previous measurements on ^{118}Te have observed states of spin, parity of $I^\pi \leq 8^+$ [Lu69], [Wy73] and [Sp69]. Wyckoff and Draper confirmed the E2 nature of the four transitions between the 8^+, 2573 keV level and the ground state by conversion electron measurements.

A search for low energy ($E_\gamma < 100$ keV) gamma rays and for isomeric states ($T_{1/2} > 2$ ns) produced no positive results.

Examples of the gamma-gamma coincidence spectra are given in Figs. 3.23 and 3.24, the former showing the total coincidence spectrum while the latter shows examples of projected spectra.

3.4.2 Yrast Cascade

The $\Delta I = 2$ sequence is extended to the 10^+, 3360 keV level. Both the 774.1 and 400.7 keV transitions have stretched E2 type angular

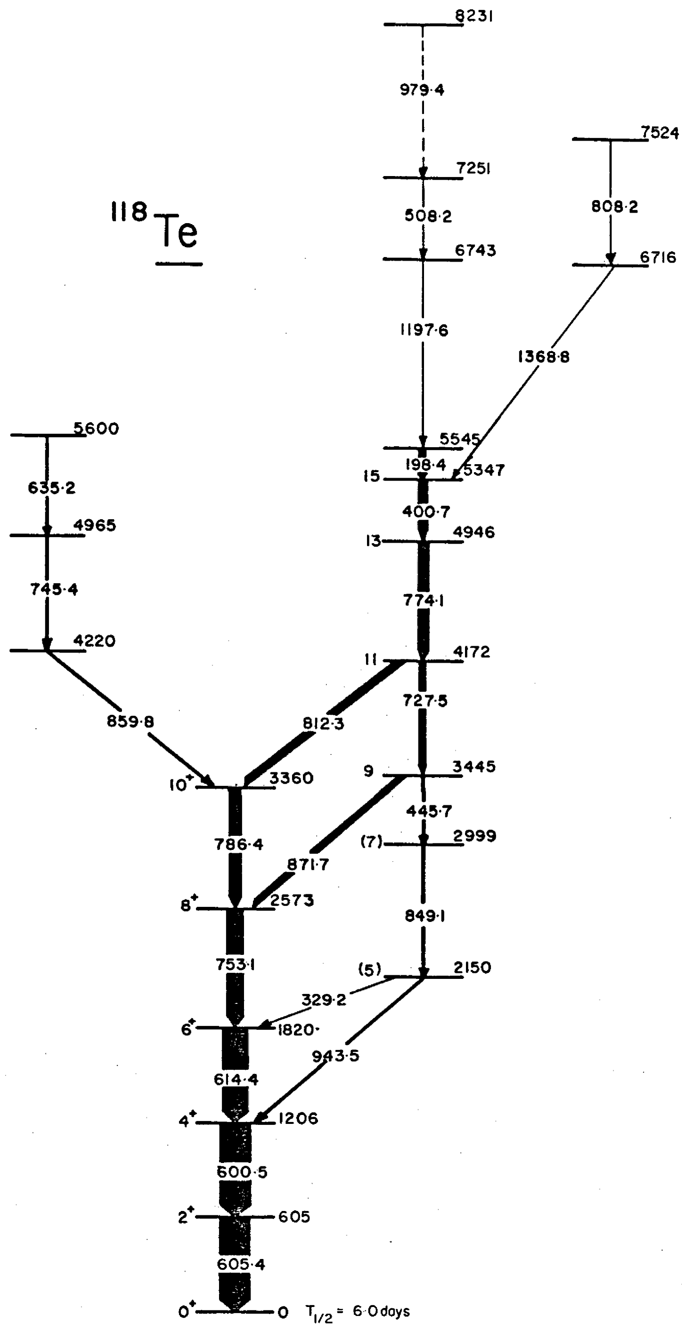

Fig. 3.21: Level spectrum of ^{118}Te deduced from observations following a ^{110}Pd(^{13}C,5n)^{118}Te (75 MeV) reaction.

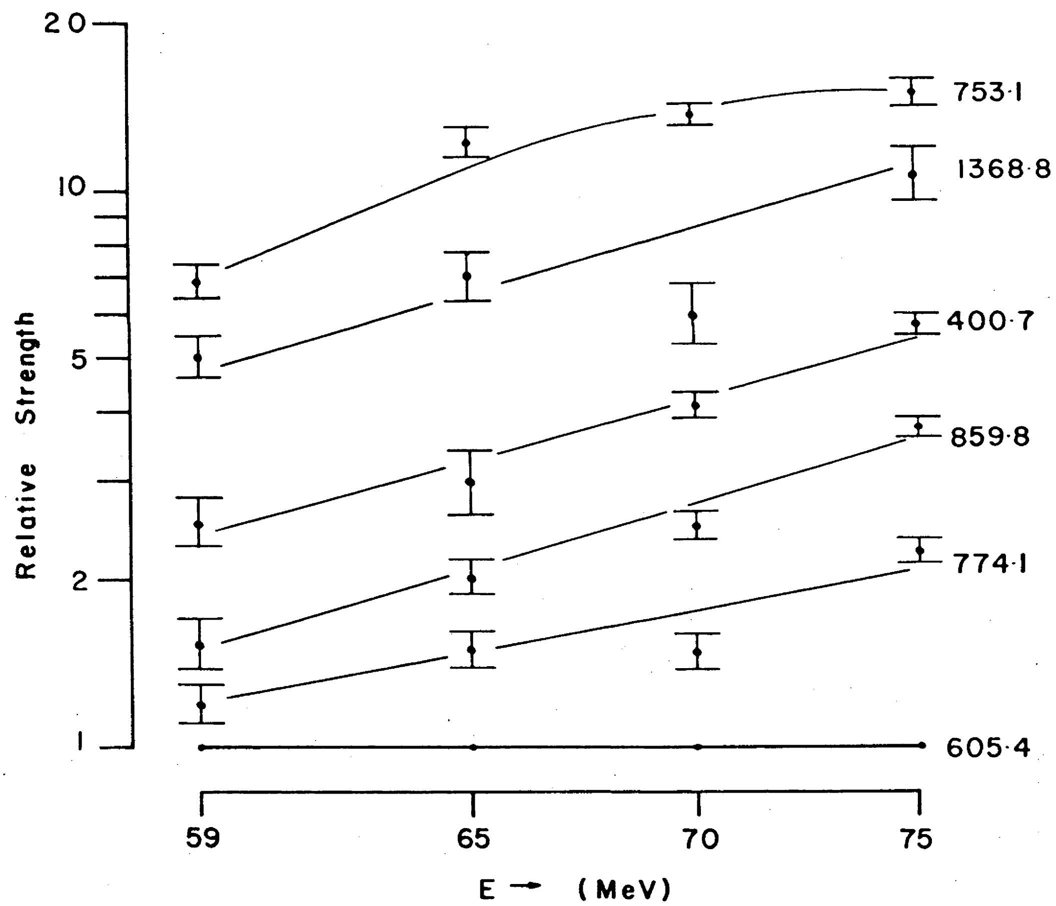

Fig. 3.22: Relative excitation functions of transitions in ^{118}Te.

Table 3.4.1

Transition Energies, Gamma Ray Intensities, and Angular Distribution Coefficients for Transitions Observed in ^{118}Te.

Transition Energy (a)	Gamma Ray Intensity (b)	A_2 (c)	A_4 (c)	Initial State (keV)
198.4 (3)	207 (8)			5545
329.2	66 (5)	.12 (15)	-.04 (16)	2150
400.7	320 (9)	.24 (7)	-.13 (8)	5347
445.7 (2)	101 (6)			3445
508.2 (3)	30 (12)			7251
600.5	1000	.24 (5)	.00 (6)	1206
605.4	1033 (21)	.34 (3)	-.07 (3)	605
614.4	852 (18)	.22 (2)	-.01 (2)	1820
635.2 (2)	119 (7)	.35 (12)	-.16 (13)	5600
727.5	217 (8)	.31 (8)	-.14 (9)	4172
745.4	108 (7)	.34 (6)	-.16 (7)	4965
753.1	587 (14)	.21 (4)	-.05 (4)	2573
774.1	325 (10)	.12 (9)	-.15 (12)	4946
786.4	406 (11)	.28 (3)	-.03 (3)	3360
808.2 (2)	80 (7)			7524
812.3	262 (9)	.00 (08)	.00 (09)	4172
849.1	99 (6)	.22 (12)	.14 (16)	2999
859.8	116 (7)			4220
871.7	197 (8)	-.22 (15)	.11 (17)	3445
943.5	133 (8)	0.0 (2)	-	2150
979.4 (3) (d)	25 (15)			8231
1197.6	54 (6)	-.32 (15)	.24 (17)	6743
1368.8	60 (6)			6716

(a) Except where given errors of the transition energies are ±.1 keV.

(b) Singles gamma ray intensities, observed in a Ge(Li) detector at 5° to the beam direction, of transitions observed in the ^{110}Pd(^{13}C,5n)^{118}Te (75 MeV) reaction are given relative to the intensity of the 600.5 keV transition.

(c) Normalised angular distribution coefficients chosen as the best fit to the equation $W(\theta) = W_0[1 + (A_2)\ P_2(\cos\theta) + (A_4)\ P_4(\cos\theta)]$.

(d) The transition intensity was obtained from γ-γ coincidence data.

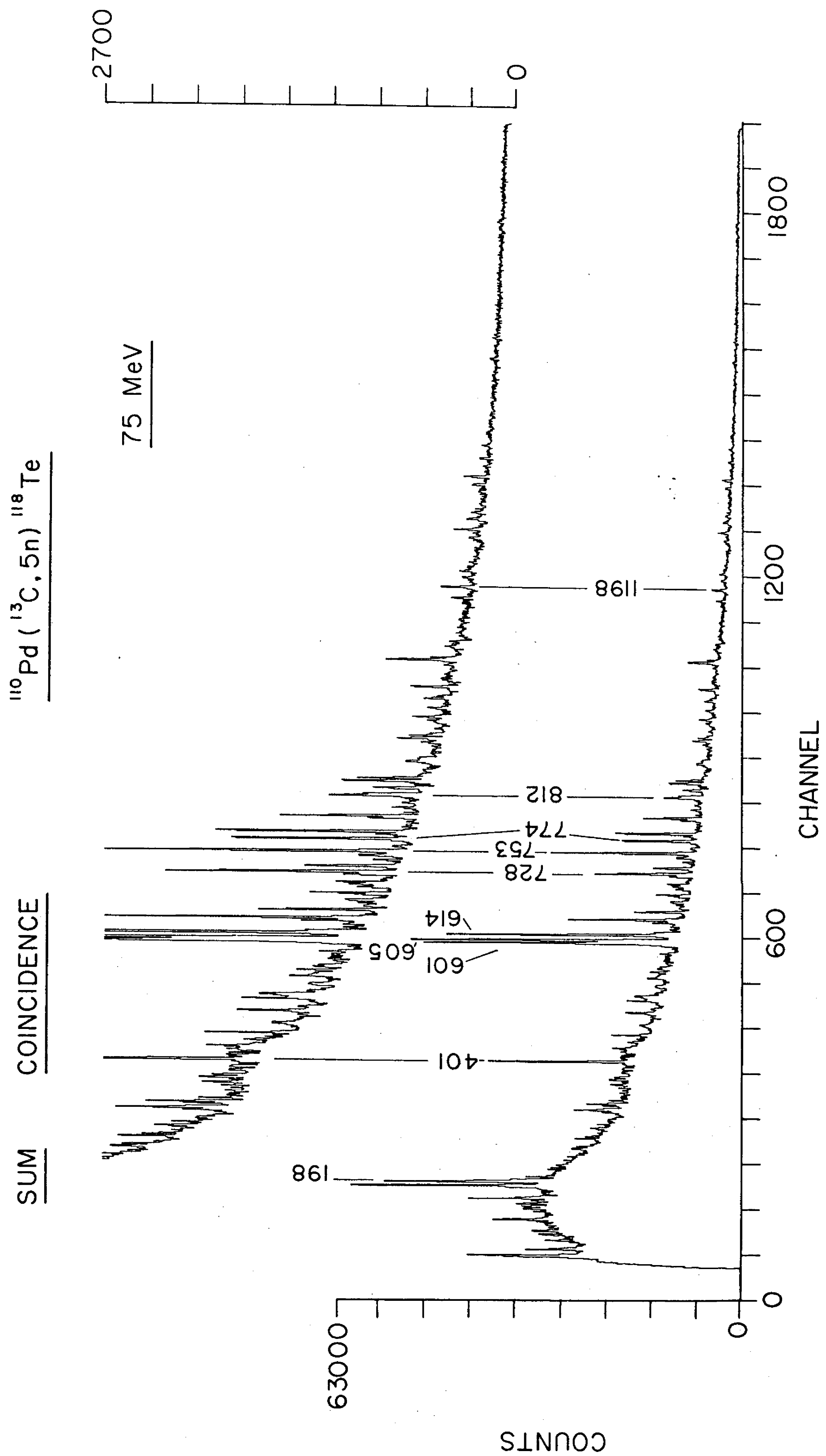

Fig. 3.23: Total coincidence spectra observed in a coaxial Ge(Li) detector at 125° to the beam.

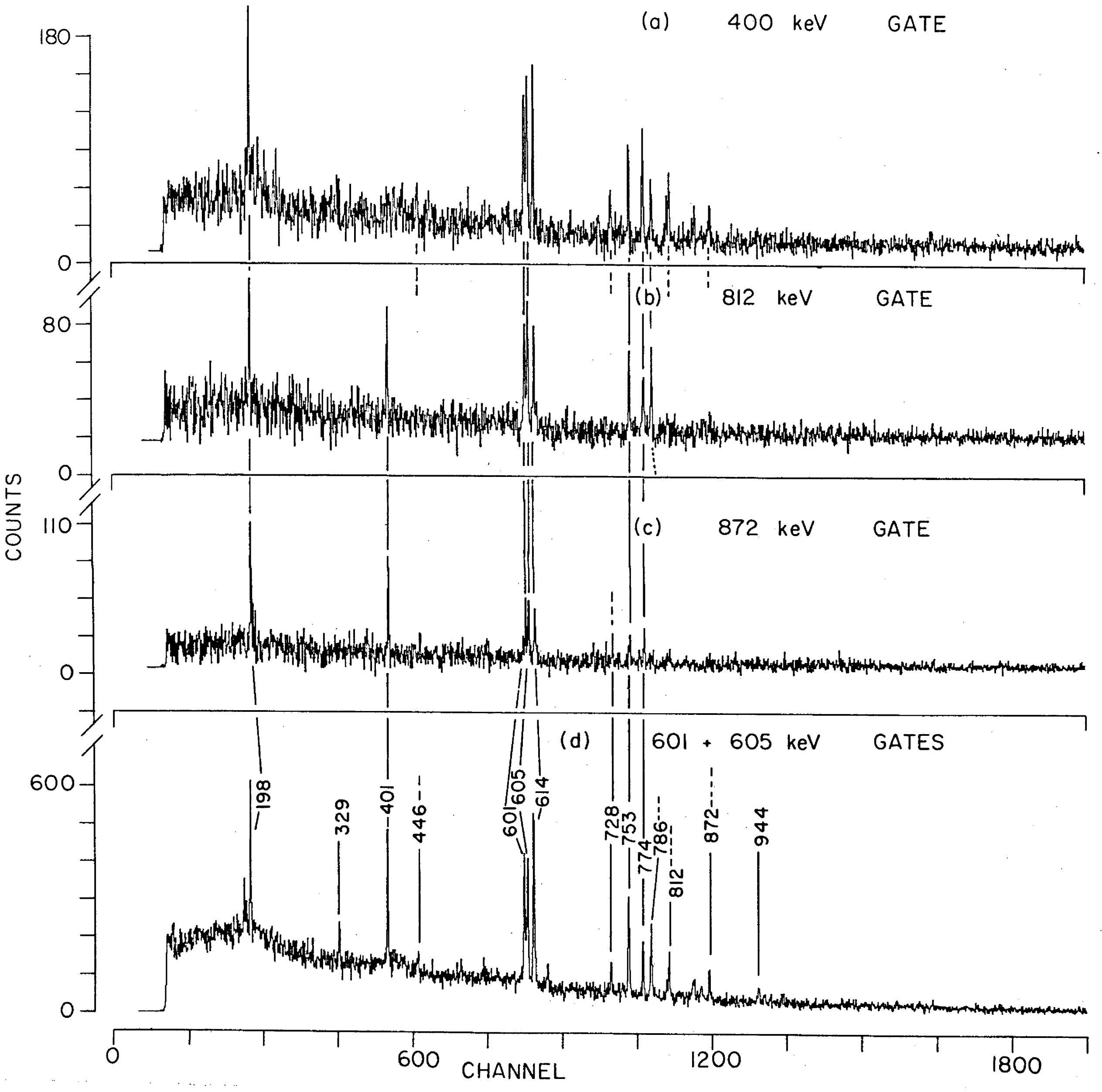

Fig. 3.24: Gated coincidence spectra observed in a coaxial Ge(Li) detector at 125° to the beam.

distributions, but the 812.3 keV transition is isotropic. Assuming that an $I \to (I-1)$ transition is most probable, this implies that the 4172 keV level has spin $I = 11$. It was not possible to determine the angular distribution of the 198.4 keV transition due to contaminant gamma rays (one of which was from ^{19}F).

The Yrast cascade can be traced up to the 8231 keV level, the ordering being determined from gamma-gamma coincidence analysis.

3.4.3 Other Levels

The 3445 keV level is strongly populated. Most of this level's population decays by a $\Delta I = 1$, 871.7 keV transition to the Yrast level at 8^+, 2573 keV. This implies that the 3445 keV level has a spin of $I = 9$. The angular distribution of the 727.5 keV transition (i.e. of E2 nature) supports the assignment of similar $\Delta I = 1$ transitions to the 812.3 and 871.7 keV transitions. Energy sums also support the response.

The 2150 and 2999 keV levels are relatively weakly populated. The angular distributions of the 943.5 and 849.1 keV transitions weakly support the spin assignments of $I = 5$ and 7, respectively, to the levels.

These and the remaining levels were proposed from gamma-gamma coincidence analysis. The excitation functions support the proposed level scheme.

3.5 ^{116}Te

3.5.1 General

The deduced level scheme from ^{116}Te is presented in Fig. 3.25. Its derivation was based mainly upon coincident events collected as a result of the $^{108}Pd(^{13}C,5n)^{116}Te$ (68 MeV) reaction. The 5n channel was well populated in the reaction, the 678.7 keV transition being 56% of the intensity of the 713.0 keV transition in ^{117}Te. Angular distributions and excitation functions were also measured.

Previously Yrast levels of spin, parity $I^\pi \leq 8^+$ have been

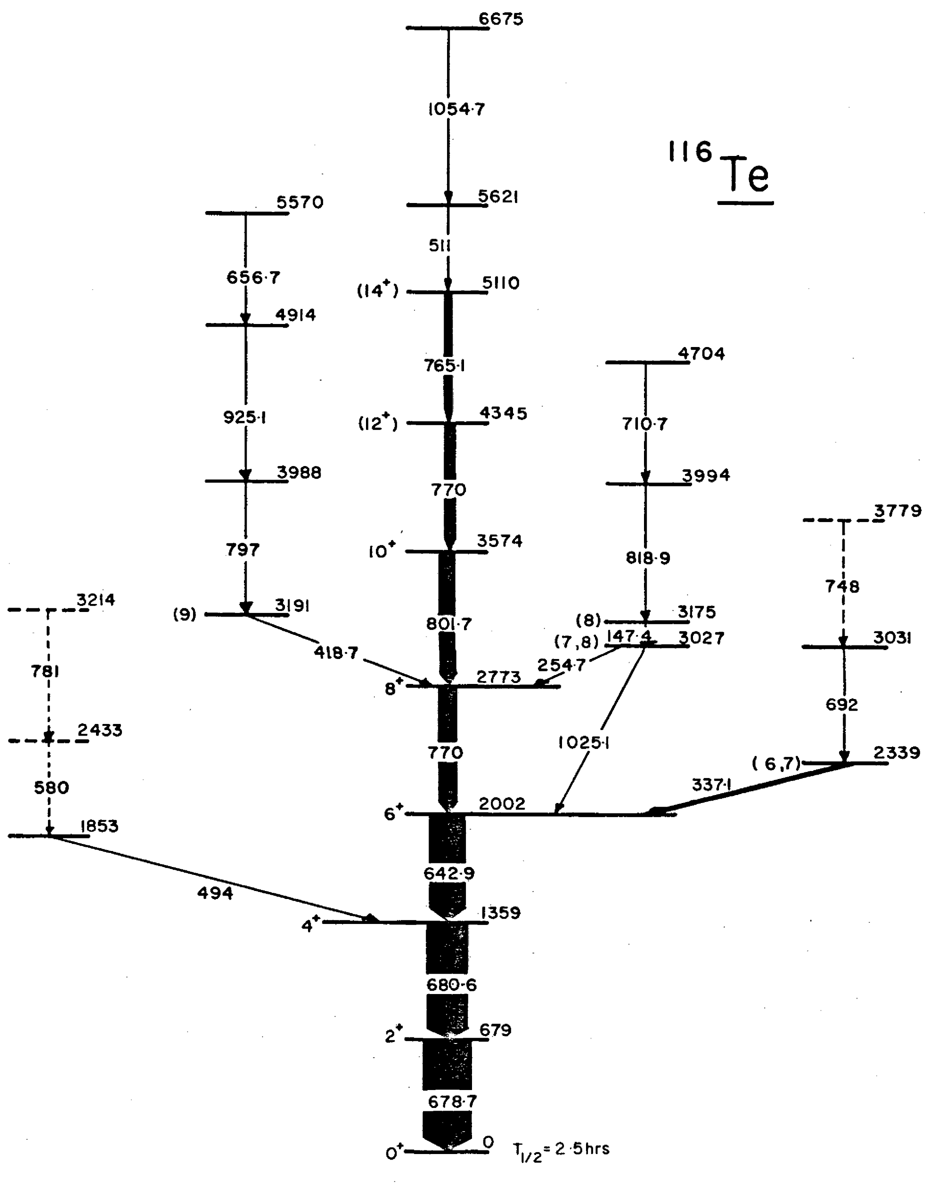

Fig. 3.25: Level spectrum of ^{116}Te deduced from observations following a ^{108}Pd(^{13}C,5n)^{116}Te (68 MeV) reaction.

identified [Lu69], [Wy73], and [Sp69] with the E2 nature of the connecting transitions being confirmed in [Wy73]. The present data is summarised in Table 3.5.1 and examples of the gamma-gamma coincidence spectra are given in Fig. 3.26.

3.5.2 Summary of the Data

Yrast levels have been identified up to 6675 keV excitation and spins have been assigned up to the 5110 keV level on the assumption that the transitions are stretched E2 in character (from the angular distribution data).

The transition at 770 keV was found to be a doublet (see Fig. 3.26). The electron conversion results of [Wy73] should not be affected by this as the higher placed transition was not intense enough to be observed. This was also the case in [Lu69]. The relative placement of the transitions was based on detailed analysis of the coincidence data and the observed singles intensities. The higher placed of 770 keV transitions (4345 $\rightarrow$ 3574 keV) is likely to be a $\Delta J = 2$ transition as the angular distribution of the doublet is similar to that of a stretched E2 transition.

The 3027 keV level decays to both the 2773 and 2002 keV levels. The angular distribution coefficient of the two transitions involved could not be determined for they are very weak. If one assumes that $\Delta I = 1$ or 2 transitions only occur, then the spin of the 3027 keV level is restricted to the values $I = 7,8$.

The 3191 and 2339 keV levels decay by dipolar transitions to the 2773 and 2002 keV levels respectively. Cascades of low intensity gamma rays were found to feed each of the 3191 and 2339 keV levels. No connection between the cascades were found, nor were any other connections to the Yrast cascade observed. The ordering of the levels in the cascades is based on intensities found in the γ-γ coincidence spectra.

A 494 keV transition feeds the 1359 keV level and there is some evidence in the coincidence spectra to suggest the presence of a cascade above the 1853 keV level.

Table 3.5.1

Transition Energies, Gamma Ray Intensities, and Angular Distribution Coefficients for Transitions Observed in ^{116}Te Following the $^{108}Pd(^{13}C,5n)^{116}Te$ Reaction.

Transition Energy (a)	Gamma Ray Intensity (a)	A_2 (c)	A_4 (c)	Initial State (keV)
147.4 (2)	130 (15)	-.09 (16)	-.08 (17)	3027
254.7	41 (6)			3027
337.1	120 (8)			2339
418.7	100 (20)			3191
494 (1)	36 (12)			1853
511 (1)	122 (16)			5621
580 (1)	<30			2433
642.9	1000	.31 (4)	-.09 (4)	2002
656.7	69 (15)	.00 (20)	-.5 (2)	5570
678.7	1457 (22)	.25 (3)	-.08 (3)	679
680.6	1228 (21)	.29 (4)	-.03 (4)	1359
692 (1)	100 (10)			3031
710.7 (2)	40 (10)			4704
748 (1)	40 (12)			3779
765.1	193 (9)	.26 (5)	-.05 (5)	5110
770 (1)	846 (19)	.26 (4)	-.04 (4)	2773
770 (1)				4345
781 (1)	<30			3214
797 (1)	120 (15)			3998
801.7	573 (9)	.27 (7)	-.07 (5)	3574
818.9	81 (10)	.36 (25)	.13 (27)	3994
925.1	90 (10)			4944
1025.1	184 (6)			3027
1054.7	190 (7)			6675

(a) Except where given errors on the transition energies are ±.1 keV.

(b) Singles gamma ray intensities observed in a coaxial Ge(Li) detector at 55° to the beam direction. γ-γ coincidence measurements were used in conjunction with singles measurements to determine the intensities of weak or masked transitions.

(c) Normalised angular distribution coefficients chosen as the best fit to the equation $W(\theta) = W_0[1 + (A_2)\, P_2(\text{Cos}\theta) + (A_4)\, P_4(\text{Cos}\theta)]$.

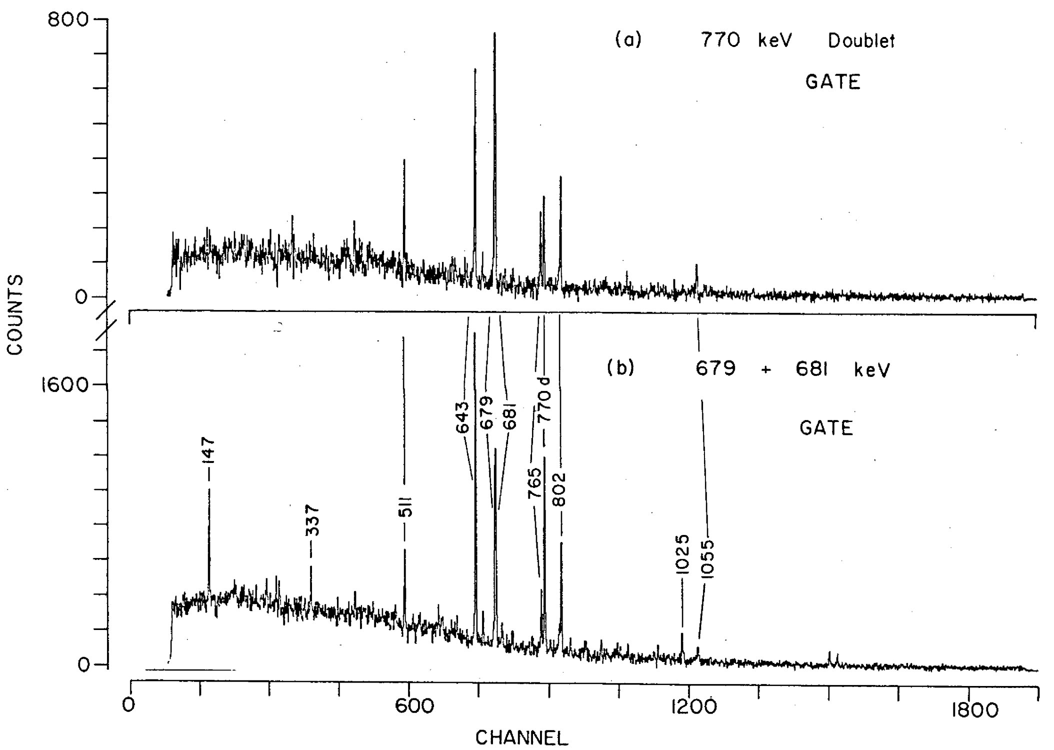

Fig. 3.26: Coincidence spectra observed in a coaxial Ge(Li) detector at 125° to the beam.

3.6 FEEDING PATTERNS IN (HI,xn) REACTIONS

The four level spectra deduced in this chapter are replotted in Figs. 3.27 and 3.28 as E vs. J diagrams. In the figures certain liberties were taken in deciding on spin values.

In ^{116}Te, the Yrast cascade is assumed to consist of $\Delta J = 2$ transitions, and $I = 7$ is assumed for the 3027 keV level. In ^{117}Te, the 4368 keV level is assumed to be of spin $I = {}^{35}/_2$. In ^{118}Te, $I = 16$ is assumed for the 5545 keV level. In ^{119}Te, $I = {}^{23}/_2$ is assumed for both the $(2746 + x)$ and $(2921 + x)$ keV levels.

In this type of plot, one can easily identify the Yrast cascades. As expected, they are comprised of the most intense transitions. The validity of the level schemes is supported by the observation that at no time does any other cascade cross the Yrast cascade. In general, if one considers the average intensity of cascades other than Yrast, one finds that the intensity decreases as one moves further from the Yrast cascade.

In ^{117}Te, where the cascades approach each other near $I = {}^{25}/_2$, one finds an increase in the number of transitions connecting different cascades. This could possibly indicate a high degree of mixing of the nuclear states. In ^{119}Te, however, the cascades are better separated and fewer cross transitions are observed.

It is interesting to note that the "envelope" encompassing the observed levels is quite narrow for ^{116}Te and gradually broadens out as the mass is increased to ^{119}Te.

Also of interest are the following systematics. In all four nuclei there is a splitting of the population among many levels at 2-3 MeV in excitation. The odd nuclei also show a large energy gap at that excitation. There is another energy gap and rapid decrease in intensity at approximately 5 MeV excitation. These energies correspond, roughly, to the energy of breaking one or two pairs of particles respectively.

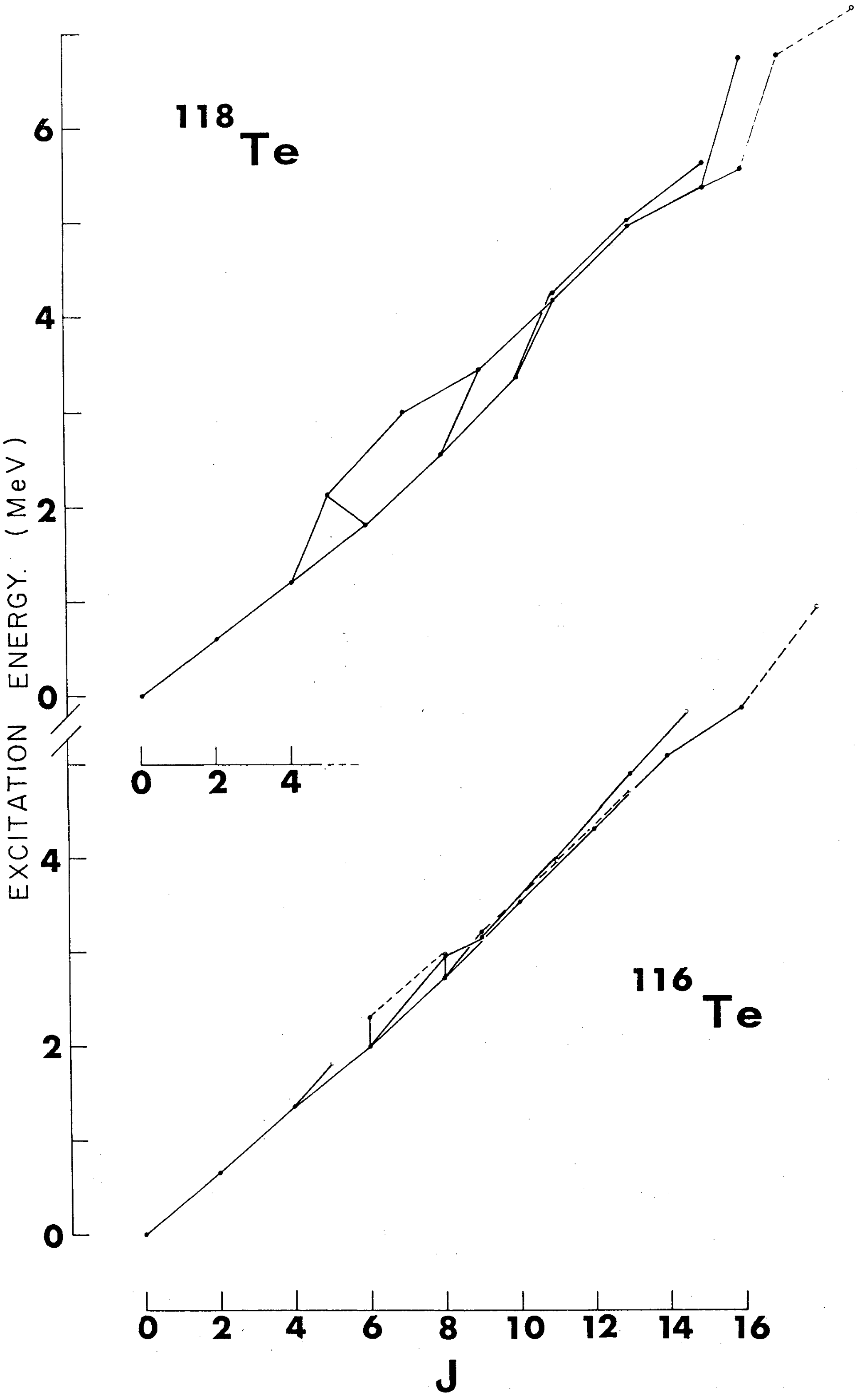

Fig. 3.27: E vs. J plot of the deduced level spectra of ^{118}Te and ^{116}Te.

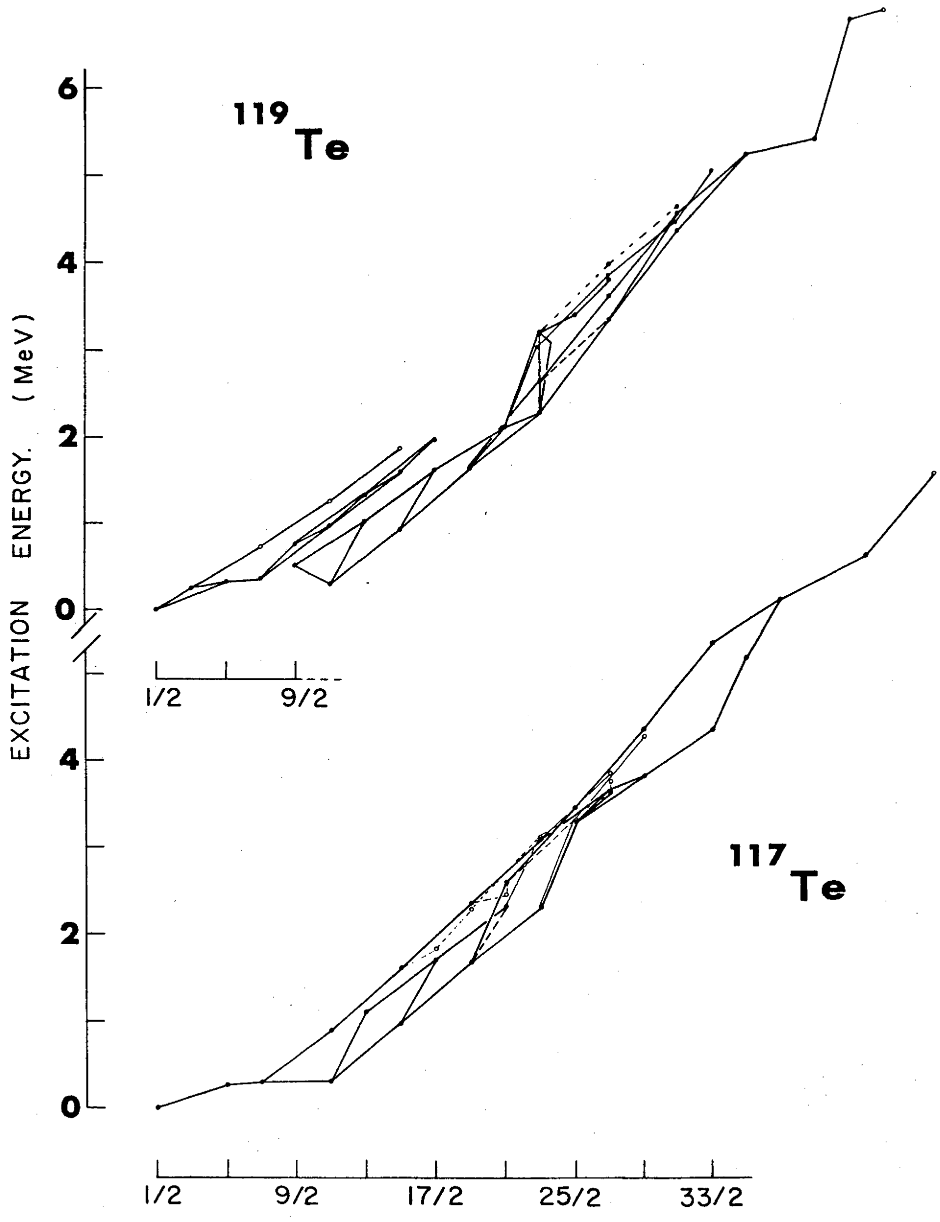

Fig. 3.28: E vs. J plot of the deduced level spectra of ^{117}Te and ^{119}Te.

CHAPTER 4

SINGLE QUASIPARTICLE STATES AND COLLECTIVE EXCITATION

4.1 SINGLE PARTICLE STATES AND NUCLEAR SHAPE

In this section evidence for neutron components to the wavefunctions will be discussed. The effect of such states on an even mass core cannot be found unless some estimate can be made of the shape of the core, before the particle is added to the nucleus. §4.1.2 discusses the shape — and that shape's stability — of the Tellurium nuclei. The major effects of the addition of a neutron to the nuclei are discussed in §4.1.3.

4.1.1 Evidence for Single Neutron Excitations

For the heavier odd mass Tellurium isotopes ($A \geqslant 121$), the dominance of single neutron components in the wavefunctions of several low-excited states has been discussed by Fernandes and Ruo [Fe77]. They carried out neutron pick-up experiments and interpreted the data on the basis of the particle-vibration model. These states include those of spin $J^{\pi} = 1/2^{+}$, $3/2^{+}$, $5/2^{+}$, and $7/2^{+}$ incorporating neutron excitations to the $3s_{1/2}$, $2d_{3/2}$, $2d_{5/2}$ and $1g_{7/2}$ orbitals respectively. Also, supporting evidence of the excitation of a neutron to the $g_{7/2}$ orbital is given by Ionescu-Bujor *et al.* [Io80]. They determined the g factor of the $J^{\pi} = 7/2^{+}$, $T_{1/2} = 85.3$ ns state in ^{121}Te as $g = +.211(3)$, which they could reproduce theoretically only if the wavefunction was predominantly of $1g_{7/2}$ character and by using the results of [Fe77]. Excitation to the $g_{7/2}$ orbital in ^{115}Te has also been discussed by Vajda *et al.* [Va72].

The systematic variation, with nuclear mass, of the energy of the above states was shown in Fig. 3.1. States with similar spins, identified in ^{117}Te and ^{119}Te smoothly extend or "fill in" the trends observed in the other Tellurium nuclei. In particular, the identification, in this work, of the level of spin $J = 7/2$ at 340 keV excitation in ^{119}Te provided a smooth trend which was not previously evident. Similarly, it is not too surprising that the level of $J^{\pi} = 3/2^{+}$ was not observed in ^{117}Te: its excitation, expected from the systematics, would be too high for it to be highly populated in a (HI,xn) reaction.

The fact that the trends in Fig. 3.1 are smooth and slowly varying, suggests that the nature of the levels is not changing rapidly with mass. It is likely then, that the low-lying levels of ^{117}Te and ^{119}Te will have single particle components of their wave-functions similar to those of the heavier nuclei. This has already been discussed in some detail for the $11/2^{-}$ level [$1h_{11/2}$ orbital] in Chapter 3.

Support for the proposal that the low-excited positive parity states are the result of single neutron excitations is provided by the observed decay modes of the levels in question. The observed and known transitions (of interest here) for ^{117}Te and ^{119}Te are summarised in Table 4.1.1. The table also gives the measured half-lives of the $5/2^{+}$ levels and, for completeness, includes the possible, but not observed, transition $7/2^{+} \rightarrow 3/2^{+}$ in ^{119}Te.

The fifth column of Table 4.1.1 gives the Weisskopf estimates of the (partial) half-lives of the initial levels on the assumption of stretched $\Delta J = 1$ or $\Delta J = 2$ transitions occurring [see Chapter 2]. The hindrance factors so determined for both $5/2^{+}$ levels [column 6] are consistent with the expectation that the wavefunctions for these levels have very substantial single particle components.

Half-lives for the $7/2^{+}$ levels could not be determined experimentally, and possible reasons are provided by examination of the Weisskopf estimates for those levels' decay, as given in Table 4.1.1. Even if hindrances for the $7/2^{+} \rightarrow 5/2^{+}$ transition were taken to be the same as those found for the $5/2^{+}$ levels' decays (i.e. effectively assuming pure single particle transitions), the lifetime of the $7/2^{+}$ levels would be too short to be measured by the technique used in the present experiments.

Table 4.1.1

Decay of Levels of Spin $7/2^+$ and $5/2^+$ in ^{117}Te and ^{119}Te

A	J_i^π	J_f^π	E_{TR} [keV]	Multipolarity [stretched]	Partial $T_{1/2}$(exp) [ns]	$T_{1/2}$[W][(a)] [ns]	H[(a)]
117	$7/2^+$	$5/2^+$	21.6	M1		.19	
117	$5/2^+$	$1/2^+$	274.4	E2	19.1	5.4	3.5
119	$7/2^+$	$5/2^+$	39.8	M1		.03	
119	$7/2^+$	$3/2^+$	[102.7][(b)]	E2		215	
119	$5/2^+$	$3/2^+$	63.5	M1	.05	.02	2.7[(c)]
119	$5/2^+$	$1/2^+$	320.4	E2	6.8	2.5	2.7[(c)]

(a) Weisskopf estimates — see Chapter 2.

(b) Not observed.

(c) Allowance is made for observed branching ratios.

It is also interesting to consider why the 102.7 keV transition $7/2^+ \to 3/2^+$ in ^{119}Te was not observed. From the Weisskopf estimates of Table 4.1.1, we find that the intensity of this transition would be approximately 1.4×10^{-4} of the intensity of the alternative $7/2^+ \to 5/2^+$ transition — which would make the probability of identification very small. Any mutual collectivity in the wavefunctions of $7/2^+$ and $3/2^+$ levels would enhance the probability of the E2 transition's detection. The fact that it was *not* observed weakly supports the assumption of a single particle transition.

So therefore all the available experimental evidence is consistent with the assumption that the wavefunctions of the $1/2^+$, $5/2^+$ and $7/2^+$ levels of ^{117}Te and ^{119}Te and the $3/2^+$ level of ^{119}Te are predominantly of single neutron character.

4.1.2 Single Particle States in Deformed Nuclei

It is difficult, if not impossible, to reconcile the relative excitations of the single neutron states of ^{117}Te and ^{119}Te with predictions of the spherical shell model (outlined in Chapter 1). We therefore need to consider the single particle energies in a range of deformed nuclei, i.e. in deformed potentials. At present, we do not know the shape of the Tellurium nuclei, so all common types of deformation must be considered.

The most commonly observed deformation is a "stretching" or "squashing" of the spherical shape to produce a spheroid with an axis of cylindrical symmetry. This "stretching" is measured by the quadrupole deformation parameter β, as described in Chapter 1. We will also consider hexadecapole (ε_4) and triaxial (γ) deformations.

The single particle states in a spheroidal potential which has $\beta > 0$ were considered first by Nilsson in 1955 [Ni55]. That treatment has since been modified and extended, e.g. [Ni69], [Gu67]. In an axially deformed potential, coupling between states of the same spin and parity occurs. Whereas this interaction may be large for states within a major oscillator shell, it is usually quite small between different oscillator shells [i.e. between N and ($N \mp 2$) shells]. The interaction between states in different shells was sometimes ignored in calculations, but it can be approximately included if the parameters of the calculation are based on a different deformation parameter, ε_2, instead of β. Although the exact relationship between ε_2 and β is complicated, to first order it is simply

$$\varepsilon_2 \approx .95\ \beta\ . \tag{1}$$

The Hamiltonian of a particle in a deformed modified harmonic oscillator potential can be written in the form [Ni55]

$$H = H_o + H_c + H_{corr}\ , \tag{2}$$

where H_o is the spherically symmetric part of the Hamiltonian, H_c represents the coupling of the particle to the axis of deformation, and

$$H_{corr} = C\ \underset{\sim}{l}\cdot\underset{\sim}{s} + D(\underset{\sim}{l}^2 - \langle l^2 \rangle)\ . \tag{3}$$

Here, the first term represents the spin-orbit coupling. The second term includes a centrifugal correction ($\underset{\sim}{l}^2$) which serves to depress states of high angular momentum. The final term is a modification, introduced in [Gu67], which is proportional to the average value of $\underset{\sim}{l}^2$.

The parameters of Eqn (3), C and D, need to be chosen such that known single particle levels are reproduced. It is more usual, though, to adjust the related parameters, κ and μ, defined by

$$\kappa = -\tfrac{1}{2}\frac{C}{\hbar\overset{0}{\omega}_0} \tag{4a}$$

and

$$\mu = \frac{2D}{C}, \tag{4b}$$

where $\overset{0}{\omega}_0$, the frequency of oscillation at zero deformation, is given by [Ni55]

$$\hbar\overset{0}{\omega}_0 = 41\ A^{-1/3}\ . \tag{4c}$$

These parameters are chosen because within any one oscillation shell, the level *sequence* is determined by the parameter μ, while the total energy *spread* is determined, primarily, by the parameter κ. In fitting the observed levels of both the Actinide nuclei ($A \sim 242$) and the rare earth nuclei, Nilsson *et al.* [Ni69] found that κ and μ vary with mass according to the relations (assumed linear)

$$\left.\begin{aligned} \mu_n &= .624 - \frac{1.234\ A}{1000} \\ \kappa_n &= 0.0641 - \frac{0.0026\ A}{1000} \end{aligned}\right\}\ \text{neutrons}$$

$$\left.\begin{aligned} \mu_p &= 0.493 + \frac{0.649\ A}{1000} \\ \kappa_p &= 0.0766 - \frac{0.0779\ A}{1000} \end{aligned}\right\}\ \text{protons}\ . \tag{5}$$

These relations predict that for mass $A = 128$, the parameters that should be used to predict neutron single particle levels are $\mu_n = .4660$ and $\kappa_n = .0638$. Using these parameters, the level scheme of Fig. 4.1 was derived. If Eqns (5) *are* applicable in this mass region, then Fig. 4.1 should be sufficient for the prediction of neutron energies for most of the Tellurium nuclei.

However, it is instructive to note the dependence of the orbitals' energy at zero deformation ($\varepsilon_2 = 0$), as a function of κ and μ. This is shown in Figs. 4.2a, 4.2b and 4.3 for the $3s_{1/2}$, $2d_{3/2}$ and $1h_{11/2}$ orbitals. Figs. 4.2 show, firstly, the sensitivity of the energy of

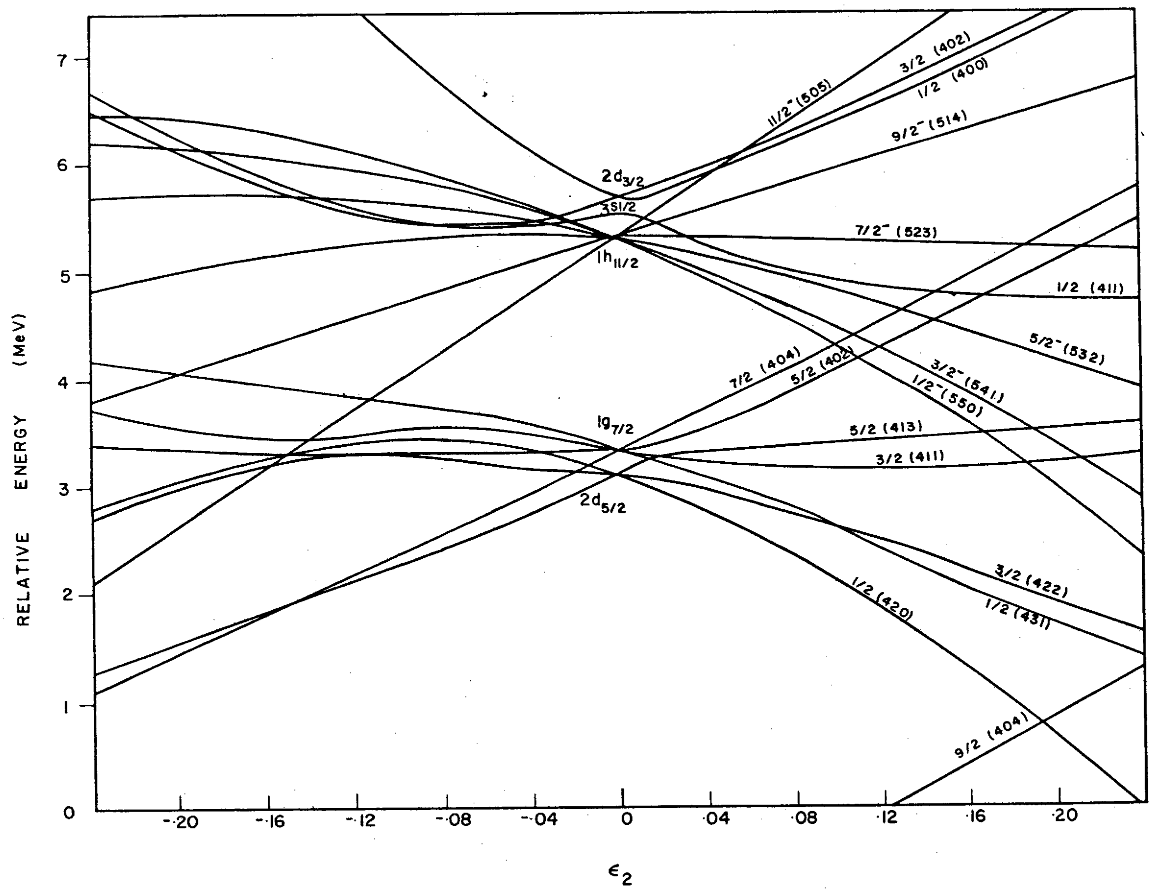

Fig. 4.1: Neutron Nilsson level diagram for $A = 128$ nuclei, using constants $\kappa_n = .0638$ and $\mu_n = .4660$ ($\varepsilon_4 = 0$).

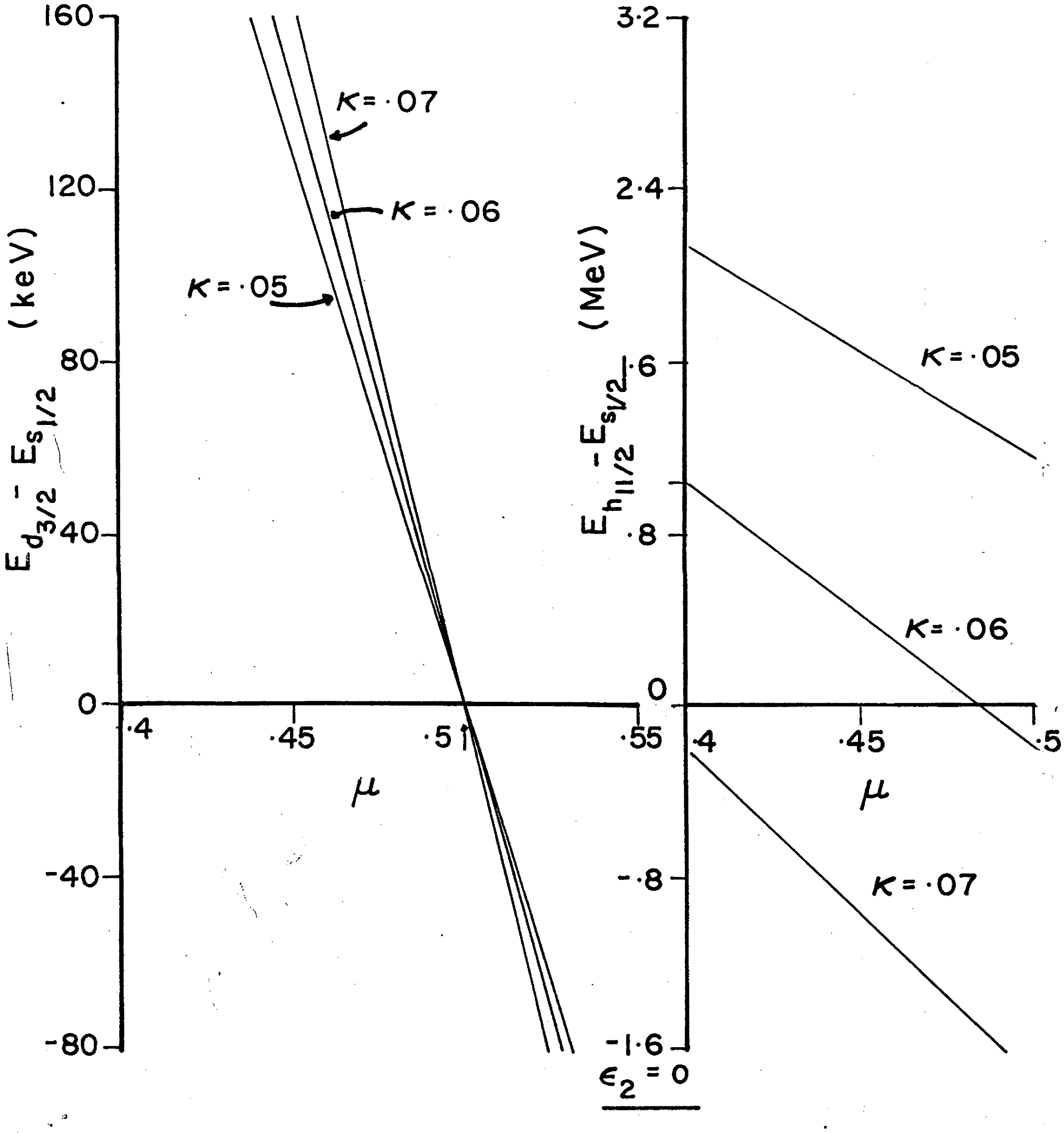

Fig. 4.2: Relative excitation of the $1h_{11/2}$, $2d_{3/2}$ and $3s_{1/2}$ neutron orbitals at $\varepsilon_2 = 0$ — determined as a function of κ_n and μ_n.

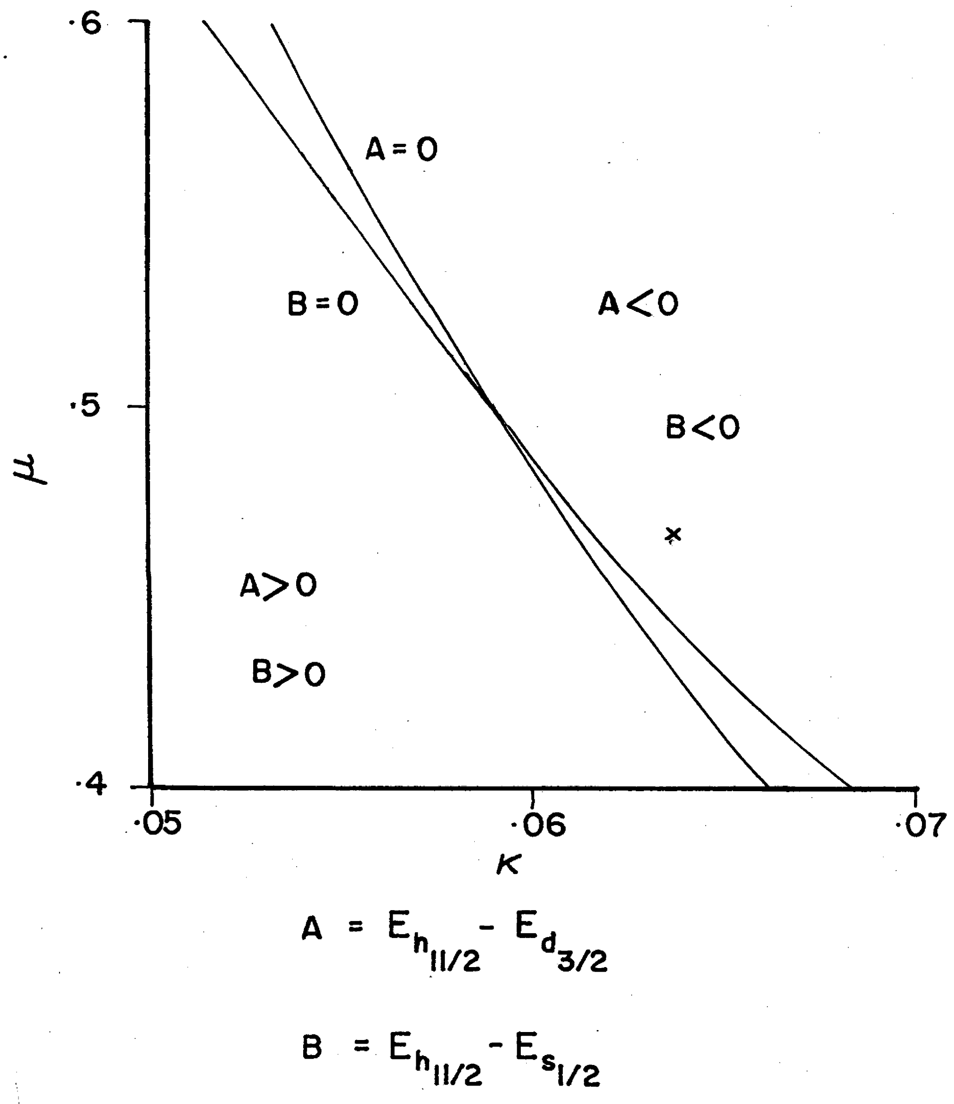

Fig. 4.3: Locii of points in the κ,μ plane where the $1h_{11/2}$ orbital has the same energy, at zero deformation, as the $3s_{1/2}$ or the $2d_{3/2}$ neutron orbitals.

the $h_{11/2}$ orbital to the value of κ. This is not surprising as the $1h_{11/2}$ orbital is a member of the fifth oscillator shell, in contrast to the fourth oscillator shell membership of the $3s_{1/2}$ and $2d_{3/2}$ orbitals. Also, it is evident that the ordering of the $3s_{1/2}$ and $2d_{3/2}$ orbitals is inverted at $\mu = .5$, independent of the value of κ. Although not shown, this is also the case for the $1g_{7/2}$ and $2d_{5/2}$ orbitals.

The effect of κ and μ on the level ordering is more clearly seen in Fig. 4.3, where the two lines represent the loci of values for which, at zero deformation, the $1h_{11/2}$ orbital is at the same energy as either the $3s_{1/2}$ and $2d_{3/2}$ orbitals. The κ and μ values used in the determination of Fig. 4.1 are denoted by a cross. This figure will be used in a later section for the determination of representative κ and μ values.

If we wish to consider higher order axially symmetric deformations, then potentials of the "box" form shown in Fig. 4.4 must be treated. These potentials were treated in [Ni69], with single particle levels being predicted similar to those in Fig. 4.5. This figure can be immediately compared with Fig. 4.1, as all the parameters, apart from ε_4, are the same. The main difference that is observed is found at small quadrupole deformations. The degeneracy at $\varepsilon_2 = 0$, found in Fig. 4.1, is no longer present in Fig. 4.5, and is replaced by a splitting, in energy, of levels of the same j value but different Ω. The *ordering* of the levels is also effected. At larger ε_2 values, the diagrams appear very similar.

Axially asymmetric potentials, however, produce much more complicated single particle level schemes than shown in either Fig. 4.1 or 4.5. Such level schemes have been discussed by T.D. Newton [Ne60] and Larsson [La73].

The complexity is the result of neither j nor Ω being good quantum numbers in the triaxial region, $0° < \gamma < 60°$. Therefore, all states of similar parity can interact, resulting in levels which may change structure many times between $\gamma = 0°$ and $\gamma = 60°$, or even, for any one value of γ, if ε_2 is changed. One point that such level schemes have in common with their axial symmetric partners is that "intruder" or "unique parity" orbitals are relatively pure in structure, due to a

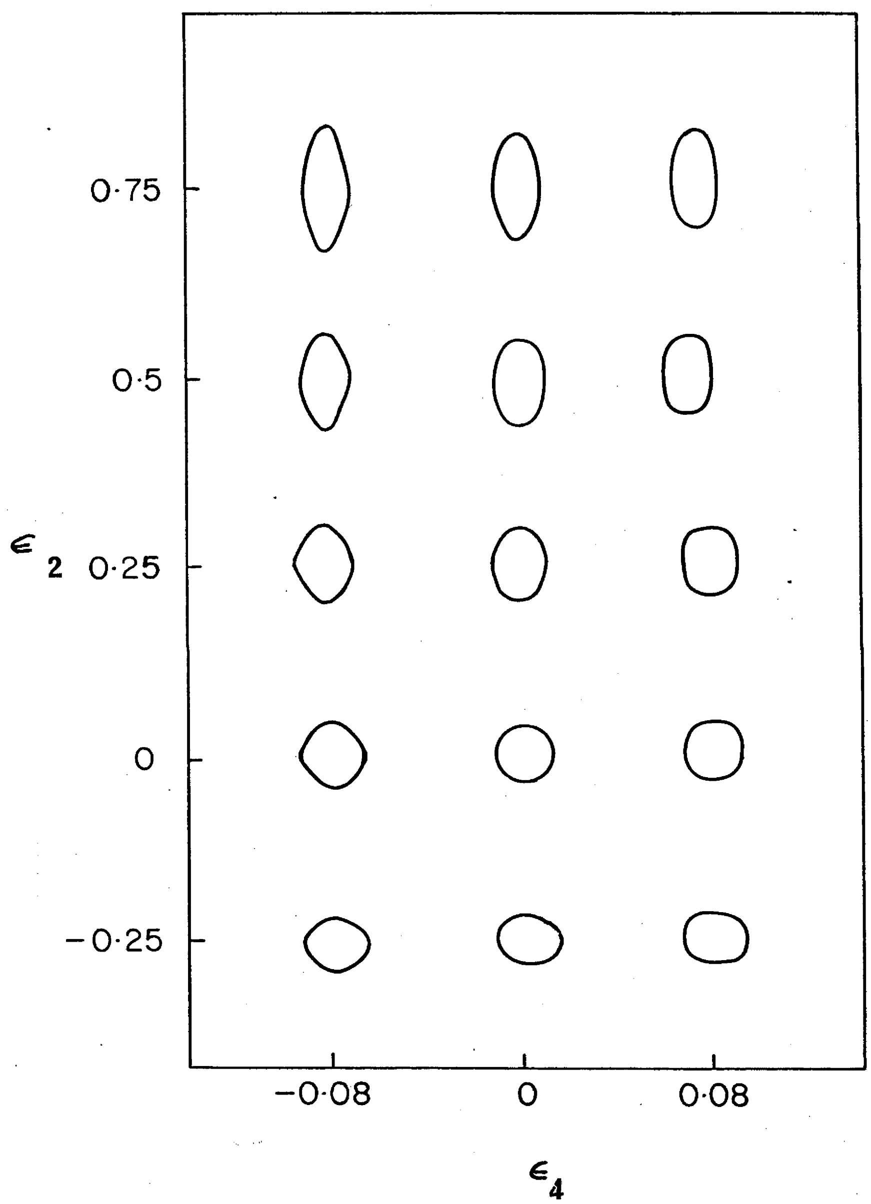

Fig. 4.4: Nuclear shapes in the plane of the deformation parameters ε_2 and ε_4. A sphere corresponds to $\varepsilon_2 = 0$ and $\varepsilon_4 = 0$. Spheroids have $\varepsilon_4 = 0$.

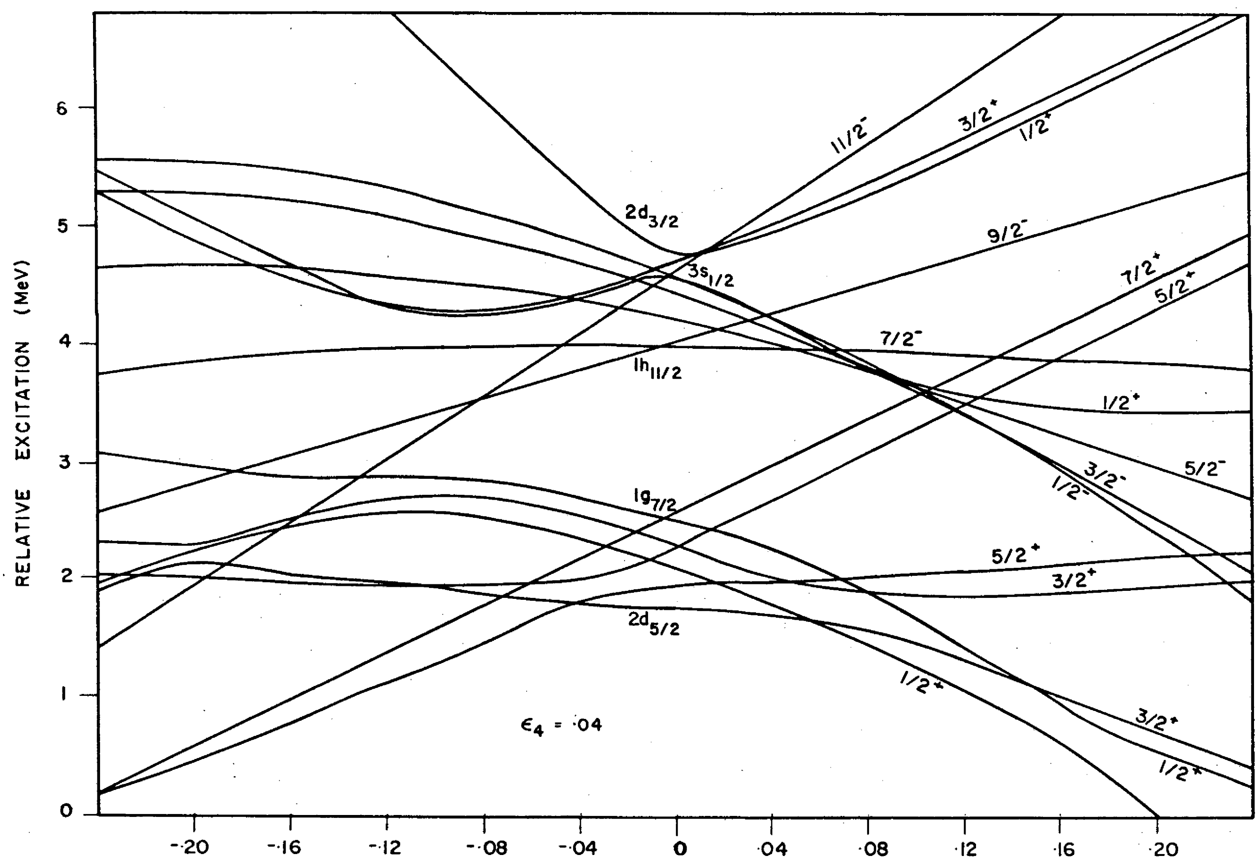

Fig. 4.5: Neutron Nilsson level diagram for A = 128 nuclei.
Parameters as for Fig. 4.1 except ε_4 = .04.

large energy gap between them and the next level of that parity.

The energies of levels in the triaxial region vary smoothly from $\gamma = 0°$ to $\gamma = 60°$, as shown in Fig. 4.6 for the $1h_{11/2}$ orbitals. If one ignored the quasicrossing points and traced levels with similar character, one would find patterns similar that that of Fig. 4.6 made up from levels having the same j value in the axially symmetric limits (i.e. the level scheme can be represented by Fig. 4.6 superimposed many times). Because of this smooth behaviour, one can, for a first approximation only, estimate the energy of levels in the triaxial region by simply making a linear interpolation of the relevant levels between the prolate and oblate extremes.

4.1.3 Effect of the Single Neutron Levels on the Nuclear Shape

For the calculation of single particle levels, we need to know both the shape of the Tellurium nuclei and values for κ and μ.

To find applicable values for κ and μ, it is helpful to consider the nearby Tin nuclei. These single closed shell nuclei can be considered as being stiffly spherical, due to the high excitation energy (> 1 MeV) of the first 2^+ state in the even mass nuclei. The ground state of the odd Tin nuclei would then give an indication of the neutron level ordering at zero deformation. It is found that for masses A = 123, 125 and 127, the ground state spin is $11/2^-$. With the $1/2^+$ ground state of the lower mass nuclei and $3/2^+$ ground state of the higher mass nuclei, this suggests the level ordering (in increasing energy) of $3s_{1/2}$, $1h_{11/2}$, $2d_{3/2}$. It is also possible that pairing of $1h_{11/2}$ particles may be energetically favoured even if the $h_{11/2}$ orbital lies above the $2d_{3/2}$ for the lower mass numbers. This, however, does not seriously affect the following discussion.

If we assume that the two extra protons of the Tellurium nuclei primarily affect the softness of the nuclei, without otherwise affecting the neutron distribution, then the level order suggested above for the Tin nuclei could be taken to apply for the Tellurium nuclei. As we can see in Fig. 4.3, this ordering greatly restricts the choice of κ and μ. As μ is the more quickly varying parameter of Eqn (5), we will maintain a value for κ similar to that used in Fig.

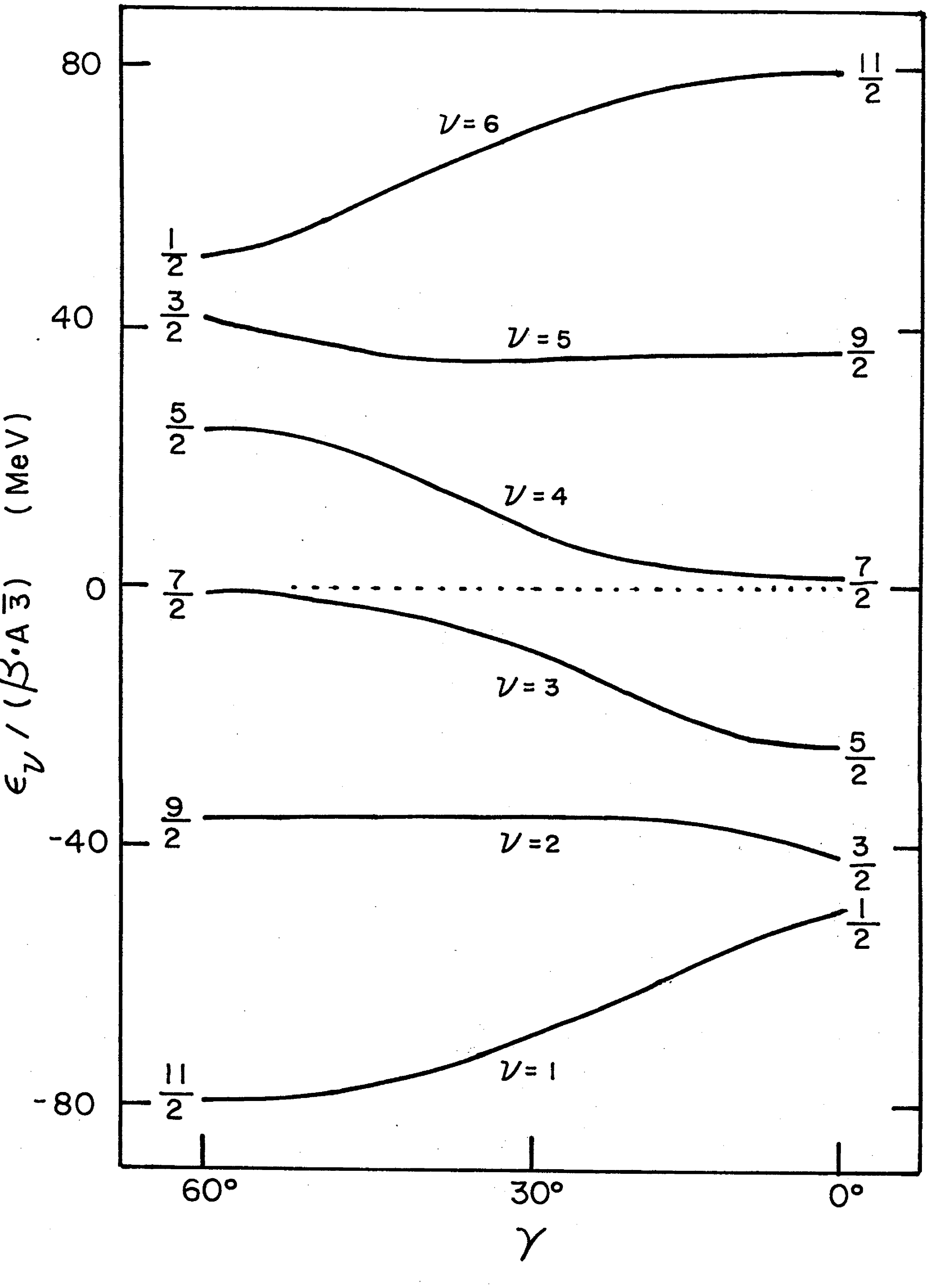

Fig. 4.6: Neutron particle level energies, ϵ_ν, in the triaxial region for a $j = {}^{11}\!/_2$ neutron. Level spins in the symmetric limits ($\gamma = 0°, 60°$) are given. For hole states, the level ordering $\nu = 1,6$ would be reversed. Level energies are normalised so that $\sum_{\nu=1}^{6} E_\nu = 0$; $\nu = 1, 2, .. j+\frac{1}{2}$.

4.1. In future sections we will use the values $\kappa = .065$, $\mu = .412$ in the determination of single neutron levels for the Tellurium levels. It is obvious that many other sets of parameters would be equally valid. Apart from the reason given above, the only other reason to choose this set is that it produces a separation of the $3s_{1/2}$ and $2d_{3/2}$ at zero deformation that is comparable to the observed values.

However, if the nuclei were axially deformed, we should expect to find some nucleus of mass $A < 134$ having a ground state of spin $J^{\pi} = 11/2^-$. We have already seen, in Fig. 3.1, that although the excitation energy of the $11/2^-$ state becomes quite low, at no time does it become the ground state. Before considering this in detail, we will look at the information which is available on the shape of the even mass Tellurium nuclei.

Estimates of the average deformations of the even mass nuclei with $120 \leqslant A \leqslant 130$ have been made by Habs *et al.* [Ha74]. Values computed using data from their tables are presented in Table 4.1.2 — the corresponding potential energy surfaces were shown in Chapter 1. All of these nuclei have a mean value for the asymmetry parameter of $\gamma \approx 30°$ [i.e. Cos $3\gamma \approx 0$], but are γ-soft, as indicated by the large values of σ(Cos 3γ), which represents the spread in the values of Cos 3γ.

As the potentials of Fig. 1.10 all have a minimum at $\beta = 0$, the large β_{rms} values in Table 4.1.2 indicate the softness of the nuclei to quadrupole deformations; the softest nuclei being ^{122}Te. The smooth decrease of both β_{rms} and $\sigma(\beta^2)$ (spread in the possible values of β^2) from ^{122}Te to ^{130}Te reflects a stiffening of the spherical shape as the neutron shell closure at ^{134}Te is approached. The possible beginning of a similar trend for the lower masses may be reflected in the values of β_{rms} and $\sigma(\beta^2)$ for ^{120}Te. This may be caused by a "subshell" closure at $N = 64$ (^{116}Te). For at small deformations, $|\beta| < .1$, when both the $1g_{7/2}$ and $2d_{5/2}$ orbitals are filled, these orbitals are well separated, in energy, from the $3s_{1/2}$, $1h_{11/2}$, $2d_{3/2}$ group. This occurs for all the potential shapes considered previously. The "subshell" so formed does have an observable effect on the Tin nuclei, e.g. ^{114}Sn ($N = 64$) has a higher $E_{2_1^+}$ energy than either ^{112}Sn or ^{116}Sn. The subshell may also be the

Table 4.1.2

Deformation of Even Tellurium Nuclei

A	$<\beta^2>$	$\sigma(\beta^2)$	β_{rms}	$\sigma(\text{Cos } 3\gamma)$
120	3.017×10^{-2}	1.808×10^{-2}	.174	.570
122	3.331×10^{-2}	1.896×10^{-2}	.183	.596
124	3.035×10^{-2}	1.824×10^{-2}	.114	.607
126	2.500×10^{-2}	1.513×10^{-2}	.158	.588
128	1.915×10^{-2}	1.146×10^{-2}	.138	.628
130	1.580×10^{-2}	9.546×10^{-3}	.126	.633

cause of some of the observed perturbations in the Tellurium nuclei.

On comparing the discussions on both the even and odd mass nuclei, we are in a position to qualitatively understand the manner in which the neutron orbitals are filled, for this depends on both the level ordering and the nuclear shape.

If there is a subshell closure at $N = 64$, then ^{116}Te would be only slightly deformed, and we can consider this nucleus as being a "core" to which other neutrons are added. The addition of one neutron would result in spin $1/2^+$ as the $3s_{1/2}$ orbital is energetically favoured for small ($|\beta| < .1$) deformations. However, as the Coriolis energy is proportional to the spin of a particle, a pair of neutrons added to the ^{116}Te "core" may energetically favour the lowest level (labelled $\nu = 1$ in Fig. 4.6) of the $1h_{11/2}$ orbital. As we can see in Fig. 4.6, this orbital does not particularly favour any gamma orientation, so the gamma softness, observed in the heavier nuclei, should also be present in ^{118}Te.

Now as the $\nu = 1$ level of the $h_{11/2}$ orbital decreases in energy as β increases (see Fig. 4.1 for the extreme $\gamma = 0$, $60°$ cases), adding a pair to this level should also tend to increase the axial deformation of the nucleus, thereby softening the nucleus.

In this manner, the ground state configurations of $^{116-122}Te$ can be produced as presented in Table 4.1.3. For ^{122}Te, the $\nu = 1$, 2, and 3 levels of the $1h_{11/2}$ orbital are filled. In adding pairs to the $\nu = 4$,

Table 4.1.3

Possible Configurations of Neutrons Outside a ^{116}Te "Core"

A	Configuration Added to ^{116}Te
117	$s_{1/2}$
118	$(h^{2}_{11/2})_{\nu=1}$
119	$(h^{2}_{11/2})_{\nu=1}\ s_{1/2}$
120	$(h^{4}_{11/2})_{\nu=1,2}$
121	$(h^{4}_{11/2})_{\nu=1,2}\ s_{1/2}$
122	$(h^{6}_{11/2})_{\nu=1,2,3}$
123	$(h^{6}_{11/2})_{\nu=1,2,3}\ s_{1/2}$
124	$(h^{8}_{11/2})_{\nu=1,2,3,4}$
125	$(h^{8}_{11/2})_{\nu=1,2,3,4}\ s_{1/2}$
126	$(h^{8}_{11/2})_{\nu=1,2,3,4}\ s^{2}_{1/2}$
127	$(h^{8}_{11/2})_{\nu=1,2,3,4}\ s^{2}_{1/2}\ d_{3/2}$
128	$(h^{10}_{11/2})_{\nu=1,2,3,4,5}\ s^{2}_{1/2}$
129	$(h^{10}_{11/2})_{\nu=1,2,3,4,5}\ s^{2}_{1/2}\ d_{3/2}$
130	$(h^{12}_{11/2})_{\nu=1,2,3,4,5,6}\ s^{2}_{1/2}$

5, or 6 levels, smaller β deformations are energetically preferred (again with respect to Fig. 4.1) so, as observed in Table 4.1.2, the softness is maximal in ^{122}Te.

The ground state spins of the four next heaviest nuclei depend very much on the relative excitations of the three orbitals $3s_{1/2}$, $1h_{11/2}$ and $2d_{3/2}$. The observed spin sequence can be reproduced if one assumes that in placing a pair of neutrons in the $\nu = 4$ level of the $1h_{11/2}$ orbital, the resulting average energy is less than the average energy of the $3s_{1/2}$ orbital. For the heavier nuclei, if the average energy of a neutron in the $2d_{3/2}$ orbital is less than if it were placed in the $\nu = 5$ or 6, $1h_{11/2}$ orbits, then the $3/2^{+}$ ground state is reproduced.

The configurations which must be added to ^{116}Te to produce these results are summarised in Table 4.1.3.

The manner in which the $h_{11/2}$ orbital is gradually filled also explains why the energy of the $11/2^-$ state slowly reduces to its minimum value in ^{127}Te, this being the nucleus in which the competition between the $2d_{3/2}$ and $1h_{11/2}$ orbits for the position of the ground state is strongest.

This discussion has highlighted the softness of the Tellurium nuclei and its possible cause. However, the excitation of a neutron from the ground state to another orbital may polarise the nucleus. The shape of the nucleus in excited states must therefore be found by some other method before the Nilsson model or its derivatives can be used to determine single particle energies.

4.2 COLLECTIVE EXCITATIONS IN THE EVEN TELLURIUM NUCLEI

4.2.1 The Vibrational Model

The level schemes of all the even Tellurium nuclei studied so far have displayed a sequence of levels which are almost equally spaced in energy. The main members of these sequences, shown in Fig. 4.7, reproduce energy spacings expected of nuclei which are good vibrators (see Chapter 1). If, however, this correspondence is examined in detail, certain anomalies begin to show.

A first measure of the vibrational character of a nucleus is the ratio of the excitation of a level of spin J (E_J) to that of the 2_1^+ level's energy ($E_{2_1^+}$), i.e. $R_J = E_J/E_2$. This is given in Table 4.2.1 for the 2_1^+, 4_1^+, 6_1^+, 8_1^+ and 10_1^+ levels of a perfect harmonic vibrator. These integer values can be compared with the values of R_J as determined from the observed energy levels of ^{116}Te and ^{118}Te. At low spin the observed and theoretical values match well, there being less than 2% difference in the values up to $J = 6$. At higher spin, the deviations increase, becoming 11% for the 10^+ level in ^{118}Te, indicating the breakdown of the assumption of a good vibrator.

Another indication of the vibrational nature of a nucleus is the presence of the triplet of levels of spin 0_2^+, 2_2^+, 4_1^+ (see Chapter 1). Of this two phonon triplet, only the 4_1^+ state has been identified in

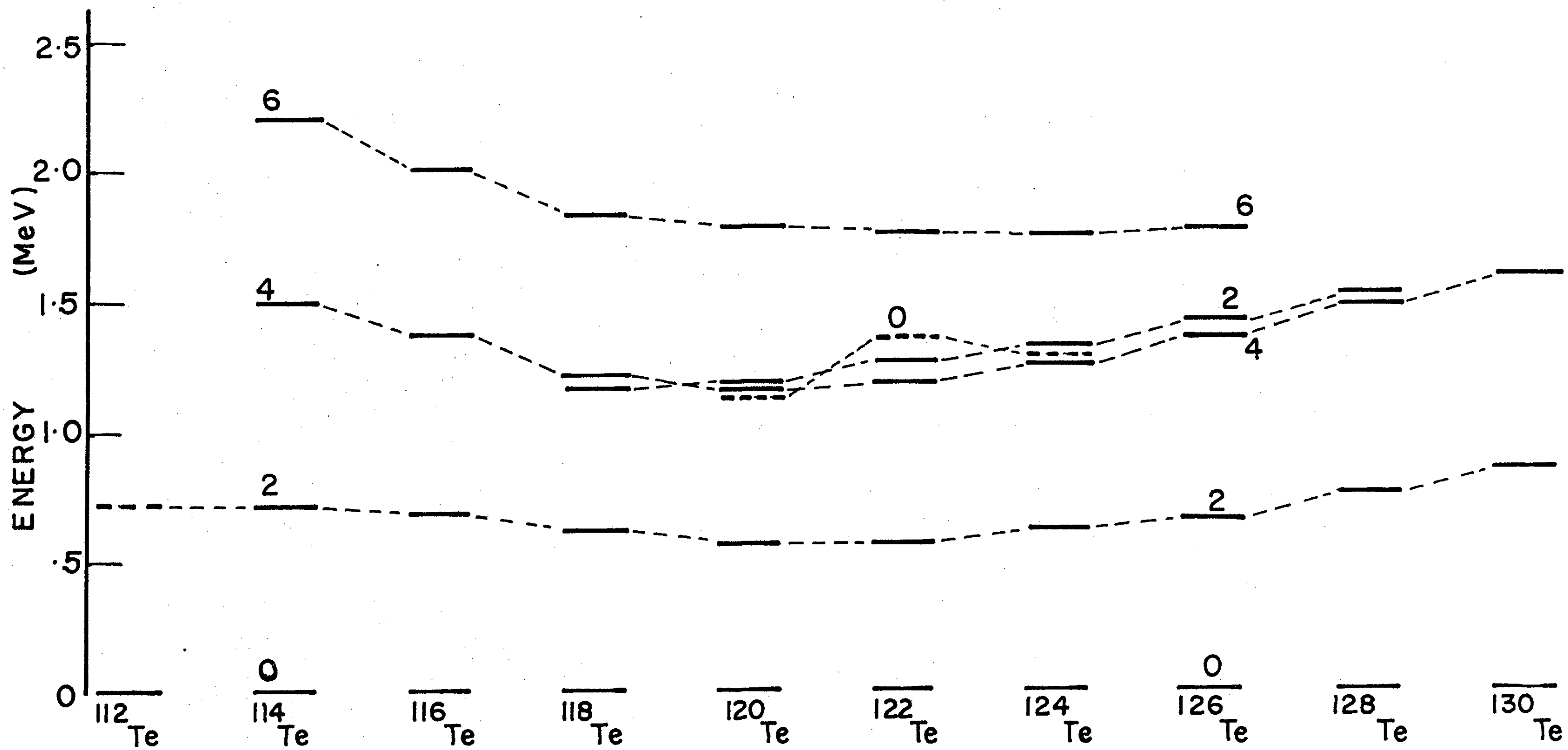

Fig. 4.7: Energy systematics of low spin (I ≤ 6) states in the even Tellurium isotopes.

Table 4.2.1

Values of R_J

J^{π}	"Good Vibrator"	^{116}Te	^{118}Te
2_1^+	1	1	1
4_1^+	2	2.00	1.99
6_1^+	3	2.95	3.01
8_1^+	4	4.09	4.25
10_1^+	5	5.27	5.55

both ^{116}Te and ^{118}Te. A possible 2_2^+ state has been suggested for ^{118}Te [Sp69], but no 0_2^+ states, at the required energy, have been observed in either nucleus. The situation is similar in the heavier Tellurium nuclei, for only in ^{120}Te and ^{122}Te has a 0_2^+ level been identified at an energy similar to that of the 4_1^+ level.

These levels and all the known 2_2^+ levels are shown in Fig. 4.7. Given the assumption of vibrational nuclei, any difference between the energy of these 2_2^+ and 4_1^+ levels must be caused by anharmonic effects. This difference is more clearly seen in Fig. 4.8. The curve, drawn only to guide the eye, peaks at approximately mass 122 and exhibits a distinct skewness at mass 126, the nucleus where, according to the arguments of the previous section, the $3s_{1/2}$ orbital is filled for the first time. It is clear, from this figure, that any anharmonic effect capable of producing the observed energy differences is intimately related to the filling of the $1h_{11/2}$ orbital.

The above two sets of observations seriously weaken any argument based on the pure harmonic vibrational nature of the even Tellurium nuclei. Further deviations from this assumption are found in the observed static quadrupole moments of the 2^+ states in $^{122-130}Te$ [K175], [Ba74]. These moments were found to have non-zero magnitude and negative sign. They can be reproduced if one considers, in addition to the effect of a vibrational potential, the coupling, to the potential of the two protons outside the $Z = 50$ proton shell [Lo70], [De74].

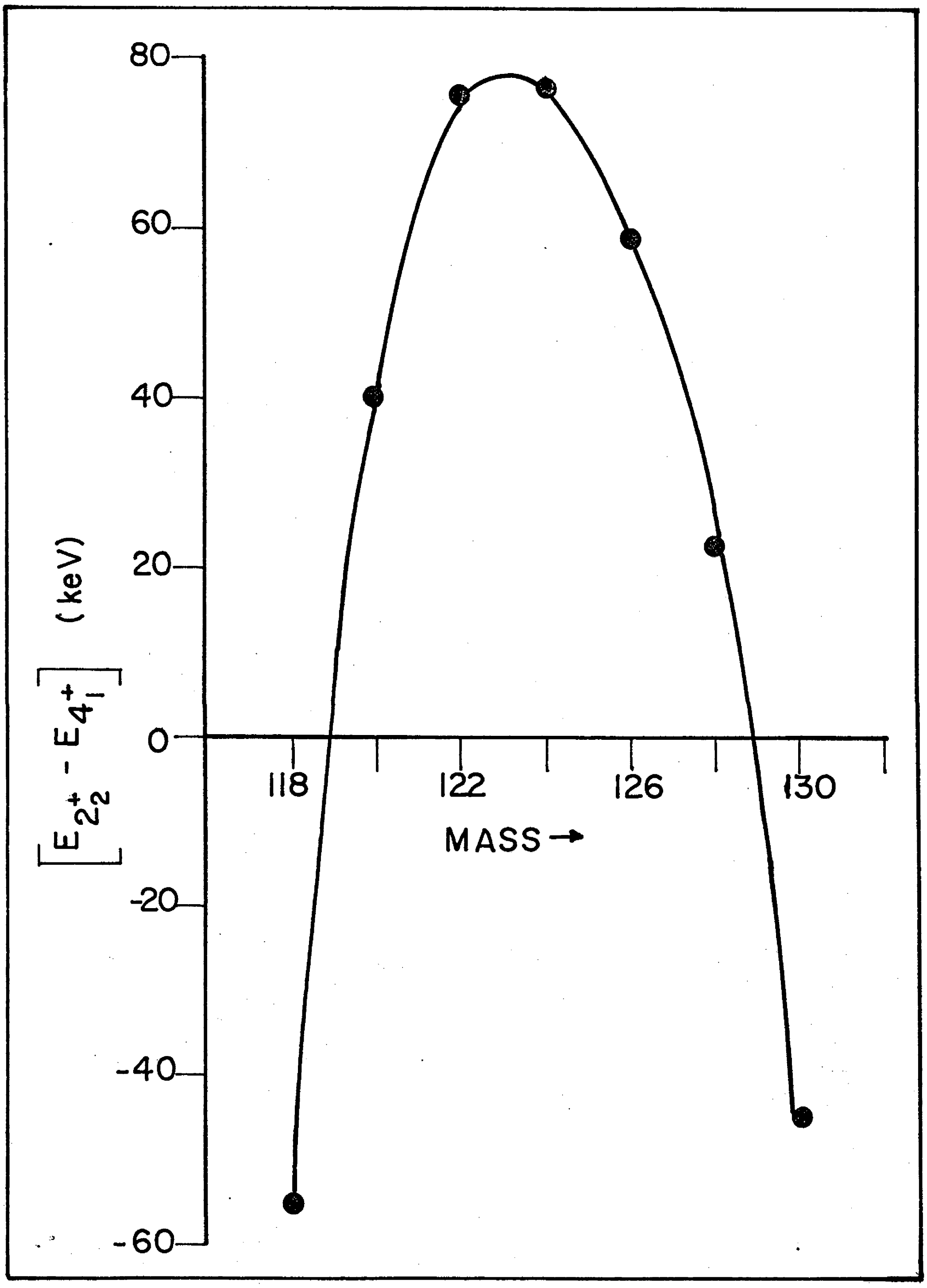

Fig. 4.8: Energy differences observed in the two phonon triplet of states of the even Tllurium isotopes.

Of the predictions made by these calculations, one is that the 0_2^+ state would be at high excitation, which is compatible with its non-observation. It is possible that the lack of experimentation has caused this. It is interesting to note, also, that the later, and more detailed work, [De74], failed to reproduce the excitation of 2_2^+ states; consistently high values being predicted.

It is obvious from these comments that although the vibrational model appears, superficially, to be adequate, the actual situation is far more complex. Neutron excitation, and possibly proton excitations as well, may play an important role in the determination of the level schemes, and hence the level wavefunctions.

4.2.2 Variable Moment-of-Inertia Model

One feature of the results of the proton-vibration coupling model of [Lo70] and [De74] is that the set of levels of spin 2_1^+, 4_1^+, 6_1^+, and 8_1^+ have similar properties. The rates of transitions between these states were also shown to be larger than those to other states. This behaviour resembles that expected of a distorted rotational band. In terms of the rigid rotor model (see Chapter 1), the behaviour would imply a different value of the moment-of-inertia for every level.

Evidence of such distorted rotational bands has long been known. They occur very frequently and are best displayed in the Mallmann Curves [Ma59] as shown in Fig. 4.9. These curves are found by plotting the experimental R_J values against R_4. On such a plot, rigid rotors would lie on the upper limit, $R_4 = {}^{10}/_3$, of the curves. The regularity of the curves suggests the presence of some underlying cause.

The Variable Moment-of-Inertia model (V.M.I.), [Sc76], is a phenomenological model capable of treating distorted rotational bands. With it, one assumes that the moment-of-inertia increases steadily with spin. *No* assumptions as to the cause of the increase are made and so the model does not depend on axial symmetry for its success.

The energy levels are determined from the relation

$$E_J(=\mathcal{I}_J) = \tfrac{1}{2}C(\mathcal{I}_J - \mathcal{I}_0)^2 + \tfrac{1}{2}\frac{J(J+1)}{\mathcal{I}_J} \qquad (1)$$

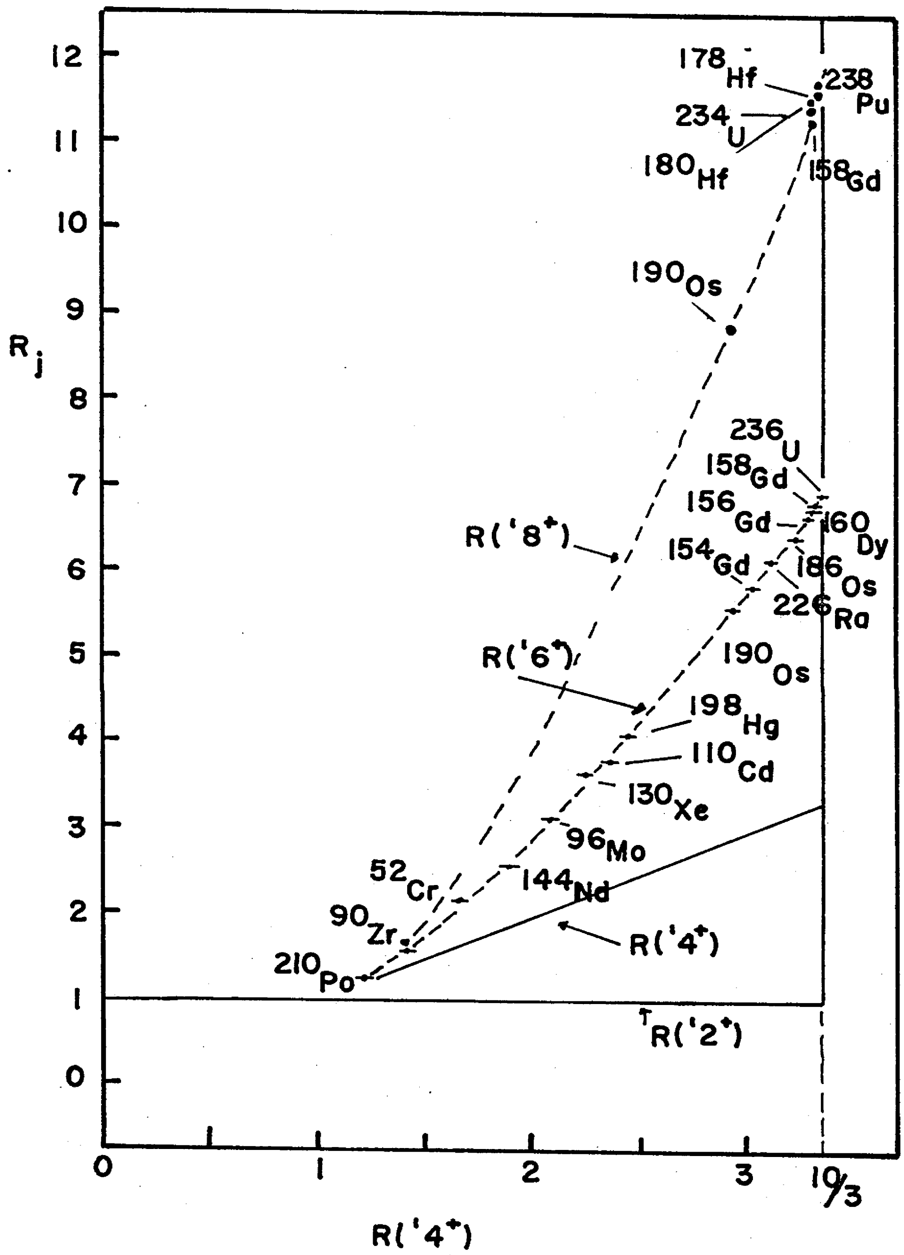

Fig. 4.9: Mallmann Curves. Empirical ratios E_6/E_2 [R(^{1}6+)] and E_8/E_2 [R(^{1}8+)] as functions of E_4/E_2.

with the equilibrium condition

$$\frac{\partial E(\mathcal{I}_J)}{\partial \mathcal{I}_J} = 0 , \tag{2}$$

where $\mathcal{I}_J$ is the moment-of-inertia of the state of spin J measured in units of $\hbar$. ($\mathcal{I}_0$ is the ground state moment-of-inertia) and C is a stiffness parameter. Using Eqns (1) and (2), $\mathcal{I}_J$ can be determined as the root of the equation,

$$\mathcal{I}_J^3 - \mathcal{I}_0 \mathcal{I}_J^2 = \frac{J(J+1)}{2C} \tag{3}$$

which has only one real root for any finite and positive value of $\mathcal{I}_0$ and C.

The natural limits of the V.M.I. model lie in the range $2.23 \leqslant R_4 \leqslant {}^{10}/_{3}$, that is, deformed nuclei. The success of the model can be estimated from its ability to reproduce the Mallmann Curves in Fig. 4.9. These curves, though, appear to extend to lower values of R_4 than 2.23. This extension can be fitted by the V.M.I. model if it is extended to include negative values of $\mathcal{I}_0$. In the extended mode, $\mathcal{I}_0$ changes character so that it then represents a measure of the "increased resistance to departure from spherical symmetry". The extended V.M.I. model is valid in the region $1.82 \leqslant R_4 \leqslant 2.23$, the "spherical" region, and it is to this region that most of the Tellurium nuclei belong.

Nuclei *are* found with $R_4 < 1.82$ (Fig. 4.9), but, with few exceptions, they are singly or doubly magic nuclei.

Before proceeding to fit $\mathcal{I}_0$ and C by using the observed energy levels of Tellurium nuclei, we need to examine the validity of the initial assumptions. We need to show that the levels comprise a *single* band built on the ground state, and that the moment-of-inertia does slowly increase with spin. These conditions may not apply above an excitation energy of 2Δ, where two quasiparticle states, and bands based on them, may be observed.

If the moment-of-inertia is varying only slowly, then it can be estimated from the transition energies. As

$$\Delta E_J = E_{(J)} - E_{(J-2)} \approx \frac{(4J-2)}{2\mathcal{I}_J} \tag{4a}$$

we obtain

$$2\mathcal{I}_J \approx \frac{(4I-2)}{\Delta E_J}. \qquad (4b)$$

($\mathcal{I}_J$ is in units of $\hbar$.) This can then be plotted against the square of the rotational frequency, also estimated from the transition energy, for the quantisation of angular momentum satisfies

$$\mathcal{I}_J w = \sqrt{J(J+1)}\,\hbar . \qquad (5a)$$

Then

$$(\hbar w)^2 \approx \left(\frac{\Delta E_J}{[J(J+1)]^{\frac{1}{2}} - [(J-2)(J-1)]^{\frac{1}{2}}}\right)^2 \qquad (5b)$$

— for large J this approaches $\Delta E_J^2/4$. Such a plot then produces a conventional "backbending" plot. The V.M.I. model is applicable whenever a smooth curve of positive slope is obtained.

In Fig. 4.10, transitions up to $8_1^+ \rightarrow 6_1^+$ are used to provide the estimates of Eqns (4) and (5) for the nuclei $^{114-126}$Te. A large backbend is observed for most of the Tellurium nuclei at the 6_1^+ level. It is similar to what is commonly observed, albeit at higher spin, in deformed nuclei (e.g. [Dr80]). The "S" shape so formed signals the presence of a band other than the ground state band.

The *degree* of the backbend (as measured by the acuteness of the angle of the curve) is minimal for ^{118}Te and ^{120}Te, and increases as the mass is increased or decreased. Also, the nuclei heavier than ^{118}Te show a *decrease* in the moment-of-inertia from the 6_1^+ to the 8_1^+ level. In Fig. 4.11, the plots for ^{116}Te and ^{118}Te are extended to include all levels connected in cascade by $\Delta J = 2$ transitions. The sharp oscillations in these curves indicate the invalidity of a one band V.M.I. model at spins higher than 4^+.

We cannot, then, justify the use of all available level energies as parameters in fitting $\mathcal{I}_0$ and C, as was done in [De74].

Using only the two level energies $E_{2_1^+}$ and $E_{4_1^+}$ to determine $\mathcal{I}_0$ and C, we can find all levels predicted by the V.M.I. model. These are given, for ^{116}Te and ^{118}Te in Table 4.2.2, and are used to determine the curves marked V.M.I. in Fig. 4.11. On comparing the curves in Fig. 4.11, one can see that ^{118}Te deviates less from a soft rotor than does ^{116}Te.

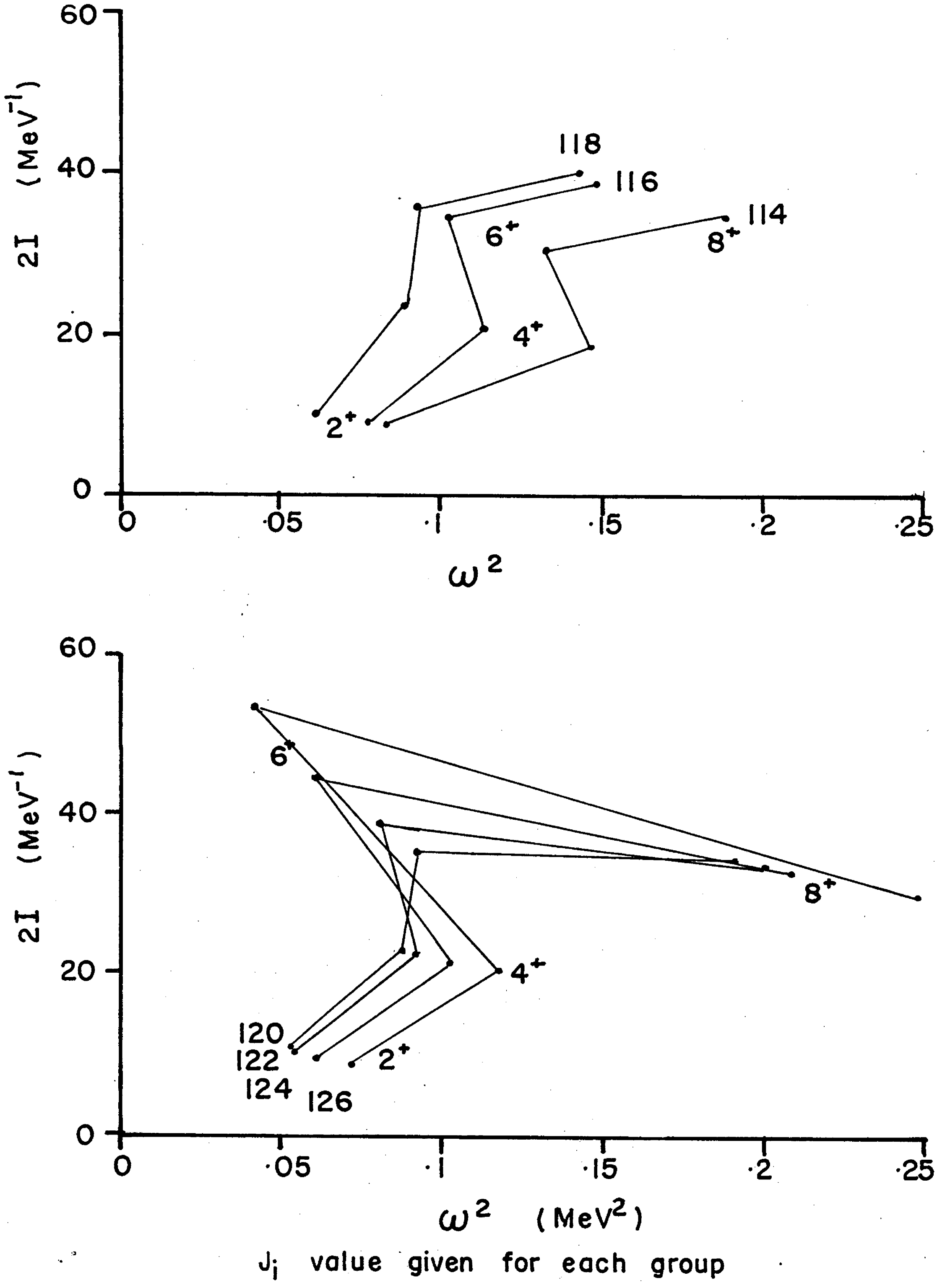

Fig. 4.10: Backbending plots of the even Tellurium nuclei, including transitions up to the $8^+ \rightarrow 6^+$ transitions.

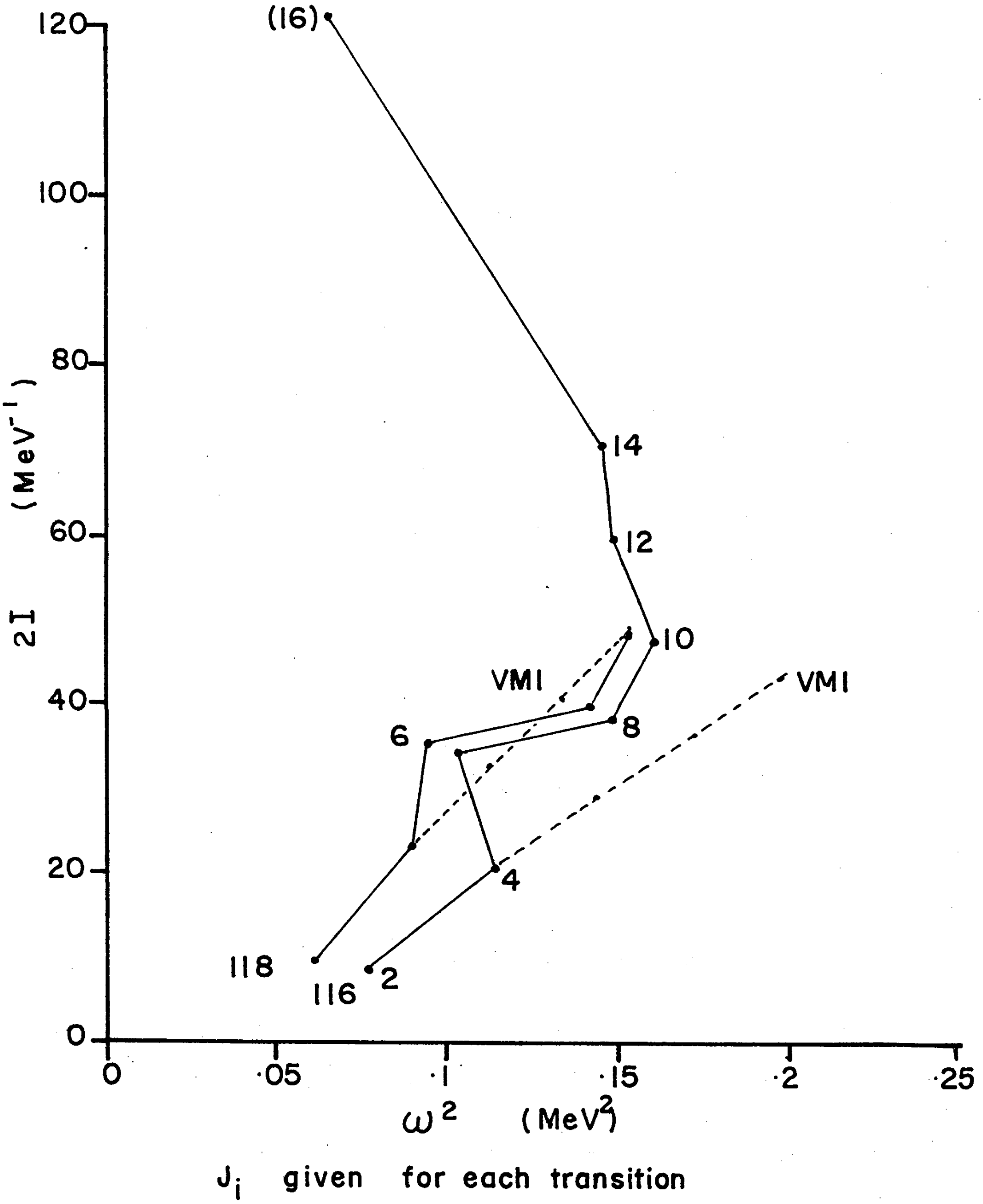

Fig. 4.11: Backbending plots of the nuclei ^{116}Te, ^{118}Te. All observed Yrast E2 transitions are included. The dotted curves represent predictions of the extended V.M.I. model.

Table 4.2.2

Level Energies Predicted by the V.M.I. Model for $^{116,118}Te$

Level Spin	MeV A = 116	MeV A = 118
2^+	.679	.606
4^+	1.359	1.206
6^+	2.124	1.880
8^+	2.957	2.613
10^+	3.848	3.398

The deviations are due to either neutron or proton quasiparticle excitations, which were introduced in the previous section. In fact, level wavefunctions predicted by the proton-vibration coupling model of [De74] suggest that *only* the 2_1^+ level (in the heavier Tellurium nuclei) is of a predominantly collective nature. The 6_1^+ levels have mostly 2-proton configurations, while the 4_1^+ levels are a mixture of collective and particle excitations. The model of [De74] is, of course, unable to predict the neutron components of the level wavefunctions.

Neutron-proton interactions may also play an important role in determining the level energies. In [Sh53], it was shown that these interactions are at a maximum when the neutrons and protons are in the same orbit; this situation may occur in the Tellurium nuclei at low energies.

This was proposed by Scharff-Goldhaber [Sc74] as a reason why the *proton* particle-hole asymmetry, about the magic number $Z = 50$, is so masked for the Te-Cd nuclei. This can be seen in Fig. 4.12, where R_4 is plotted against neutron number, in contrast to the symmetry of the Pd-Xe nuclei (50 ± 4 protons).

In summary, the V.M.I. model, though not applicable to all energy levels is helpful at pinpointing non-collective effects and giving some insight as to their causes. A further example of the effect of the neutron subshell closure at $N = 64$ is seen in Fig. 4.12, where the value of R_4 reaches a local minimum at ^{116}Te.

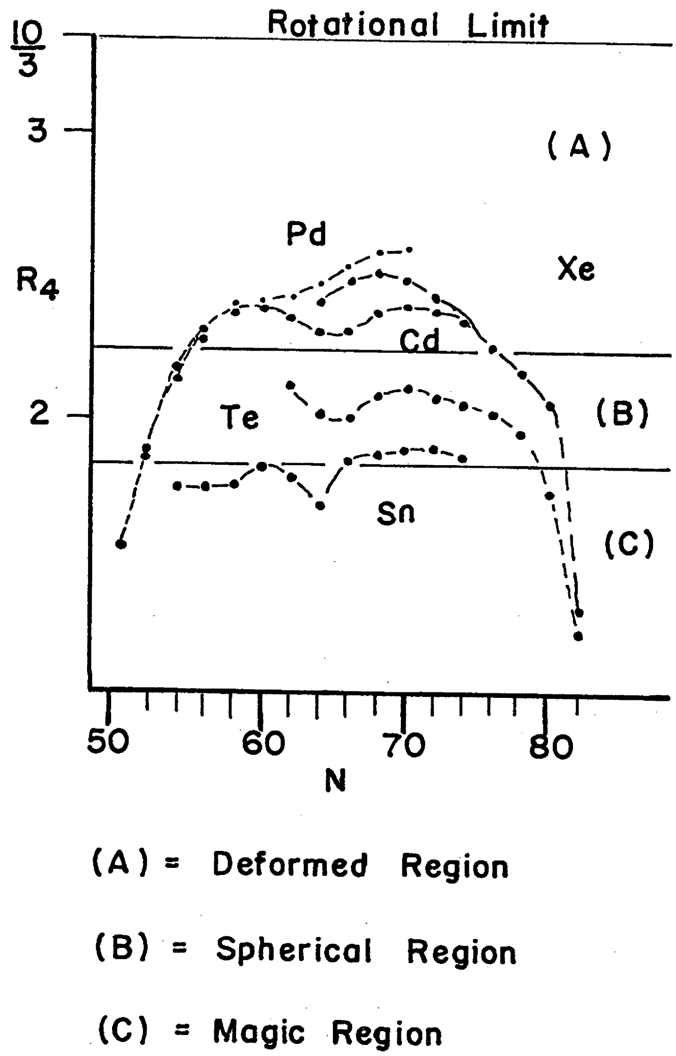

Fig. 4.12: R_4 values for Z = 46 (Pd), 48 (Cd), 50 (Sn), 52 (Te) and 54 (Xe) are plotted against neutron number. The three regions of the V.M.I. model are indicated.

4.2.3 Triaxiality of the Even Tellurium Isotopes

The varying moments-of-inertia discussed in the previous section do not exclude the possibility of stable gamma deformations occurring, for as we have seen, the nuclei are γ-soft. Such a situation occurs in the Os-Pt region, where potential energy surfaces indicate γ-soft even nuclei, yet the odd mass spectra indicate cases having definite gamma deformations [Me75a].

This anomaly may have been resolved (for the Os-Pt region) by Satapathy *et al.* [Sa80], who, by a fully microscopic model, were able to reproduce a γ-minimum in the potential energy surfaces of the even nuclei. Such a detailed calculation has not been performed for the Tellurium nuclei, so we must consider the available data for evidence of triaxiality. The lack of states of sufficient collectivity, however, prevents a detailed examination of the triaxiality of these nuclei.

The energy levels of an even mass triaxial rotor are shown in Fig. 4.13 [Da58]. Notice that the 2_2^+ state becomes quite low in energy for gamma values $20° < \gamma < 40°$, as does the 3_1^+ state — but no 0_2^+ state is predicted.

As we have already discussed the observed 2_2^+ states in Tellurium nuclei are quite low in energy (close to the 4_1^+ state) and few 0_2^+ states, at low energy, have been observed. The observed 3_1^+ states, shown in Fig. 4.7, all lie closer to the 6_1^+ state than the 4_1^+ state. A state, possibly of spin 3_1^+, has been observed in ^{118}Te at 1704 keV excitation by Sakai [Sa74]. Because of this high excitation, they may not be purely collective in character, and hence should not be compared too rigorously with the triaxial rotor predictions.

These observations are compatible with the triaxial rotor description of the even Tellurium nuclei, although further work, especially on the 0_2^+ states, is obviously desirable.

If we assume that the Tellurium nuclei *are* triaxial rotors, we can then determine the moment-of-inertia of the ground states and the γ deformation. This is possible as [Da58] gives, for the energies of the 2_1^+ and 2_2^+ states,

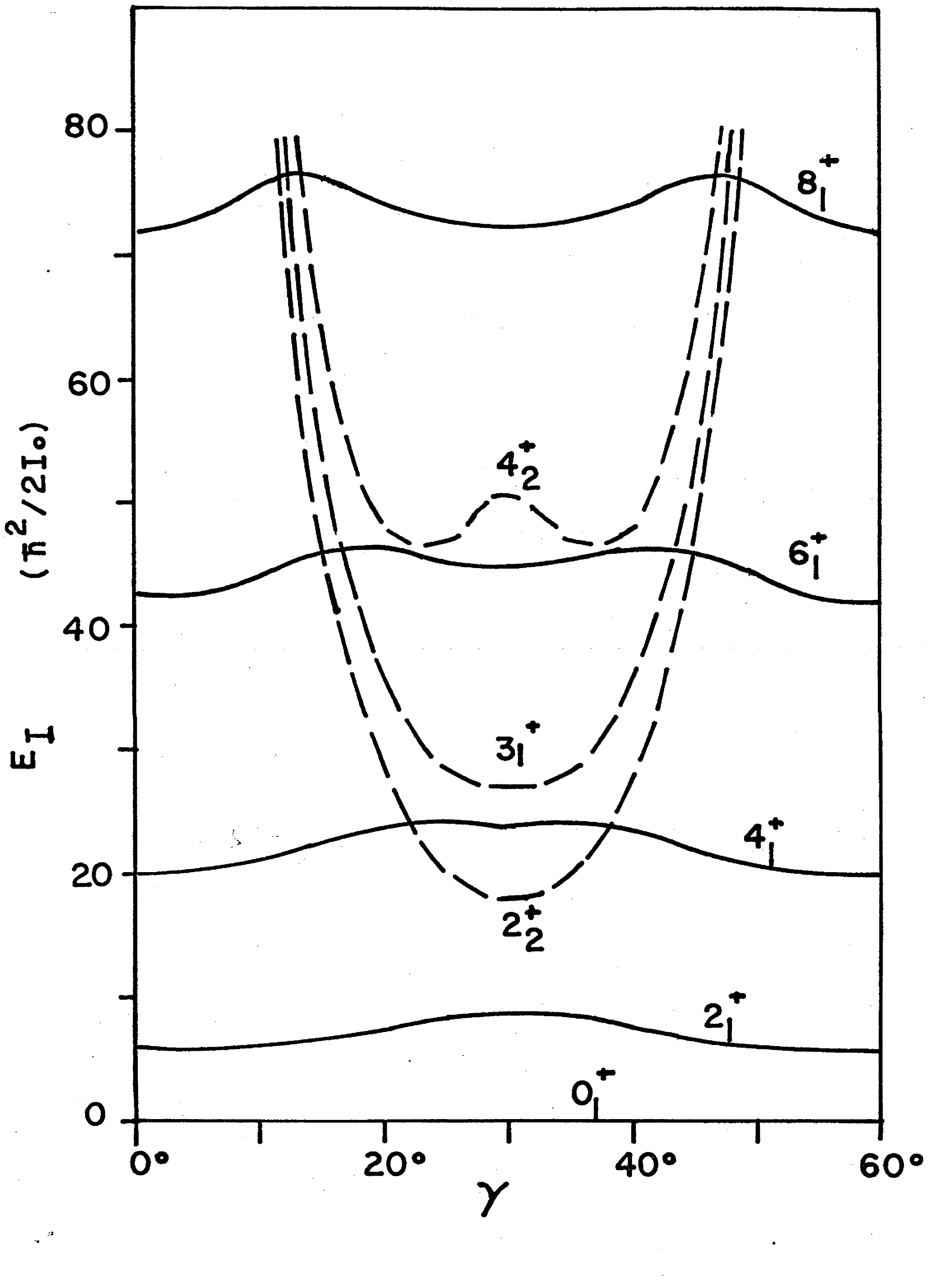

Fig. 4.13: Energy levels for an even triaxial rotor in the triaxial region. Energies are in units of $[\hbar^2/2I_0]$.

$$E_{2^+_{1,2}} = \frac{6\hbar^2}{2\mathcal{I}_0} \times \left\{\frac{9 \mp \sqrt{81 \pm 72\ \mathrm{Sin}^2(3\gamma)}}{4\ \mathrm{Sin}^2(3\gamma)}\right\} .$$

From the experimental ratio $E_{2^+_2}/E_{2^+_1}$, which has a minimum value of 2, we can find γ, and hence $\mathcal{I}_0$. These are given in Table 4.2.3 for $^{116-126}$Te. As a 2^+_2 state has not been observed in ^{116}Te, and as the calculated ratio in ^{118}Te is smaller than theoretically possible, both these nuclei are assumed to have deformations of $\gamma = 30°$. As expected, the values follow the trends observed in the other parameters studied, i.e. γ is a minimum and $\mathcal{I}_0$ a maximum at ^{122}Te.

Table 4.2.3

Moment-of-Inertias Determined Using the Triaxial Rotor Model

A	$E_{2^+_2}/E_{2^+_1}$	γ [±.5°]	$2\mathcal{I}_0/\hbar^2$ [MeV^{-1}]
116	-	[30°]	13.3
118	1.90	[30°]	14.9
120	2.14	27°	15.7
122	2.23	26.5°	15.6
124	2.20	26.5°	14.5
126	2.14	27°	13.3
128	2.05	28.5°	12.0

The conclusion of these studies on the even nuclei is that collective excitations are dominant only at low spin and excitation. Quasiparticle excitations dictate the behaviour of the nuclei at spins as low as 6^+ and even possibly 4^+.

4.3 ODD MASS NUCLEI

4.3.1 Introduction

A most important point in a discussion of the odd mass Tellurium nuclei is the softness and sphericity of their even mass cores. The shape of such nuclei is often influenced by the presence of an unpaired particle in a manner that is different in kind, as well as magnitude, to half the effect that an additional *pair* of particles would be. Examples of this have been observed in the Iodine [Va77] and Thallium [Ne70] nuclei, and also, as mentioned in Chapter 1, in the Antimony nuclei.

Of the available orbitals for a neutron, the energy of some [e.g. [404 $1/2^+$]] and [550 $1/2^-$]] change rapidly for a given change in deformation when compared to nearby [e.g. [523 $7/2^-$]] orbitals — see Fig. 4.1. Thus the shape of the odd nucleus will depend on both the Fermi level and on the orbital occupied by the extra neutron.

To estimate the effect of such shape polarisation, one requires a detailed calculation of the nuclear potential energy surface, as well as a representative single particle level scheme. As the first condition has not been met for ^{117,119}Te, and the latter can be only approximated [see §4.1], the polarising effects can be estimated only after rigorous attempts at understanding the observed spectra have been made. Yet a qualitative understanding is useful as a guide to which model is appropriate!

The effect of a neutron occupying the $1h_{11/2}$ orbital has been discussed in §4.1. From this we obtain an expectation that the placement of a neutron in this orbital would result in no pronounced preference for prolate or oblate shapes.

A similar case was made for a neutron occupying the highest orbital of the $g_{7/2}$ j-shell, but it can be seen in Fig. 4.1 that the orbital rises in energy more quickly for nuclei being deformed prolately than oblately. This effect is due to the presence of other states of positive parity with similar spin. As the Fermi level of ^{117,119}Te lies above the $g_{7/2}$ orbital at $\beta = 0$, this may result in prolate shapes having a slight energy preference.

The possibility that different shapes may exist in different excited levels of Tellurium nuclei makes it difficult, yet vital, to interpret the level schemes. It is no longer valid to interpret ^{119}Te, say, as a neutron quasiparticle (or quasihole) coupled to a ^{118}Te (or ^{120}Te) core, where we can assume that the properties of the core are those of ^{118}Te (or ^{120}Te). For now the core, and its properties, may have been altered due to a change of shape.

It follows, then, that the usual method of determining the degree of coupling between the quasiparticle and core is of limited value. That is, the required value of "a", given by

$$a = \frac{[E_{(I+2)} - E_{(I)}]_{\text{odd mass nucleus}}}{[E_{(I+2-j)} - E_{(I-j)}]_{\text{core nucleus}}},$$

is not known as neither E(I+2-j) nor E(I-j) is known. We can however use the associated qualitative observation that if levels of spin I = (j+1),(j+2) are observed such that [E(j+2) - E(j+1)] is roughly equal to [E(j+1) - E(j)], then strong coupling of the particle to the deformation of the core may be occurring. This is seen in the bands built on the $7/2^+$ levels in the ^{119}Te and ^{121}Te nuclei [Ha79].

On the other hand, if the level of spin (j+1) does not occur, or occurs near, in energy to the (j+2) level, then either weak coupling or decoupling of the particle and the core may be occurring.

If the weak coupling approach of de-Shalit [Sh62] can be applied, one would expect to see multiplets of levels whose spins take all the values, $|j - R| \leqslant I \leqslant |j + R|$ (where R is the rotational angular momentum of the core). It is true, though, that the lower spin members of any given multiplet may not be observed in a (HI,xn) reaction, due to the feeding pattern. Such a coupling could apply to the bands built on the $11/2^-$ levels, but it is not capable of explaining the presence, nor the energy systematics, of the $9/2^-$ level observed in the odd Tellurium nuclei of mass greater than A = 117.

Considering the expectations of a triaxially deformed core, it is natural to investigate the observed bands in terms of a quasiparticle coupled to a triaxially deformed core. This will be discussed in the following sections with a view to not only fitting the energy levels, but also to attempt to determine the shape of the core in each case.

4.3.2 Triaxial Rotor Plus Particle Model

4.3.2.1 Introduction

The model to be developed here is, with only a minor variation, that of Meyer-ter-Vehn [Me75a]. The variation, to be described later, does not alter the basic successes enjoyed by this model, amongst which is its ability to describe all coupling strengths between weak and strong as a function of the deformation parameters β and γ. The model also predicts the existence of a level of spin $I^{\pi} = 9/2^{-}$ in the Tellurium nuclei and is capable of reproducing the systematic behaviour of the level as the number of neutrons is altered.

4.3.2.2 Wavefunctions

We commence the discussion by considering the properties of a triaxial core. For simplicity, the Davydov approximation is used [Da58] which fixes the collective wavefunction at its average values, thereby assuming a rigid shape. This is indeed a serious limitation of the model, especially in a region of such soft nuclei, but it is only by examining the effect of the inadequacies of this approximation that we can hope to fully understand the behaviour of a soft triaxial rotor.

The energy levels of such an (even mass) triaxial rotor were given in Fig. 4.6 and, as discussed in §4.2.3, are capable of representing what is known of the even Tellurium nuclei below ~ 3 MeV in excitation.

The semi-axes of the rigid rotor can be described by

$$R_{\kappa} = R_0\left[1 + \sqrt{\frac{5}{4\pi}}\,\beta\,\mathrm{Cos}\left(\gamma - \frac{2\pi}{3}\kappa\right)\right] ; \qquad \kappa = 1,2,3 , \tag{1}$$

where R_0 is the radius of the sphere of equivalent volume and κ refers to the relevant axes. This ellipsoid shape generates a deformation potential which is given by

$$V_p = k(r)\,\beta\left\{\mathrm{Cos}^2\,Y_{20}(\theta,\phi) + \frac{\mathrm{Sin}\gamma}{\sqrt{2}}\,[Y_{22}(\theta,\phi) + Y_{2-2}(\theta,\phi)]\right\} , \tag{2}$$

where the $Y_{2\mu}$ are spherical harmonics and $k(r)$ determines the radial dependence of V_p.

The moment-of-inertia parameter is chosen to vary with γ as would be expected from irrotational flow, so that

$$\mathcal{I}_{\kappa} = \mathcal{I}_0 \times \frac{4}{3}\,\mathrm{Sin}^2\left(\gamma - \frac{2\pi}{3}\kappa\right) , \qquad \kappa = 1,2,3 \tag{3}$$

and we are required to adjust only $\mathcal{I}_0$. The variation of the moment-of-inertia, given by Eqn (3), are displayed in Fig. 4.14 for the range $0 \leqslant \gamma \leqslant 180°$.

The odd nucleon which is coupled to the core is considered as a quasiparticle or quasihole. It is in this aspect, that the Meyer-ter-Vehn calculation differs most from the calculation of Pashkevich and Sardaryon [Pa65]. For ease of calculation, the quasiparticle is restricted to a single j shell, which is an assumption that can be only approximately correct at best. However, for many cases, including those treated in later sections, it can be shown that the assumption is not unreasonable.

The particle and hole contributions to the Hamiltonian can be explicitly accounted for by using a 2×2 matrix notation. It also allows for a simple representation of the coupling of particles and holes by the pairing interaction. Thus the total Hamiltonian of the system is

$$H = H_P + H_R , \tag{4}$$

where H_R is the Hamiltonian of the core which is given by

$$H_R = \left(\sum_{\kappa=1}^{3} \frac{(I_\kappa - j_\kappa)^2}{2\mathcal{I}_\kappa} \right) \begin{pmatrix} 1 & 0 \\ 0 & 1 \end{pmatrix} \tag{5}$$

and H_P is the Hamiltonian of the particle, given by

$$H_P = (\varepsilon_j - \lambda_F) \begin{pmatrix} 1 & 0 \\ 0 & -1 \end{pmatrix} + V_P \begin{pmatrix} 1 & 0 \\ 0 & -1 \end{pmatrix} + \Delta \begin{pmatrix} 0 & 1 \\ 1 & 0 \end{pmatrix} , \tag{6}$$

where $(\varepsilon_j - \lambda_F)$ is the energy of the state (ε_j) relative to the Fermi energy (λ_F), V_P is taken from Eqn (2), and Δ is the pairing energy.

The fact that Eqn (4) is invariant under rotations of 180° (in γ) allows the wavefunctions to be written in the form

$$\psi_{IM,\alpha} = \sum_{K\Omega\tau} C_{K\Omega}^{(I,j,\alpha)} \left(D_{MK}^{(I)} \chi_{\Omega\tau}^{(j)} + (-)^{(I-j)} D_{M-K}^{(I)} \chi_{\Omega\tau}^{(j)} \right) , \tag{7}$$

where $D_{MK}^{(I)}$ denote rotational D-functions,

$\chi_{\Omega\tau}^{(j)}$ denote the particle (hole) amplitude: $\tau = \pm 1$ distinguishes particles (+) from holes (−),

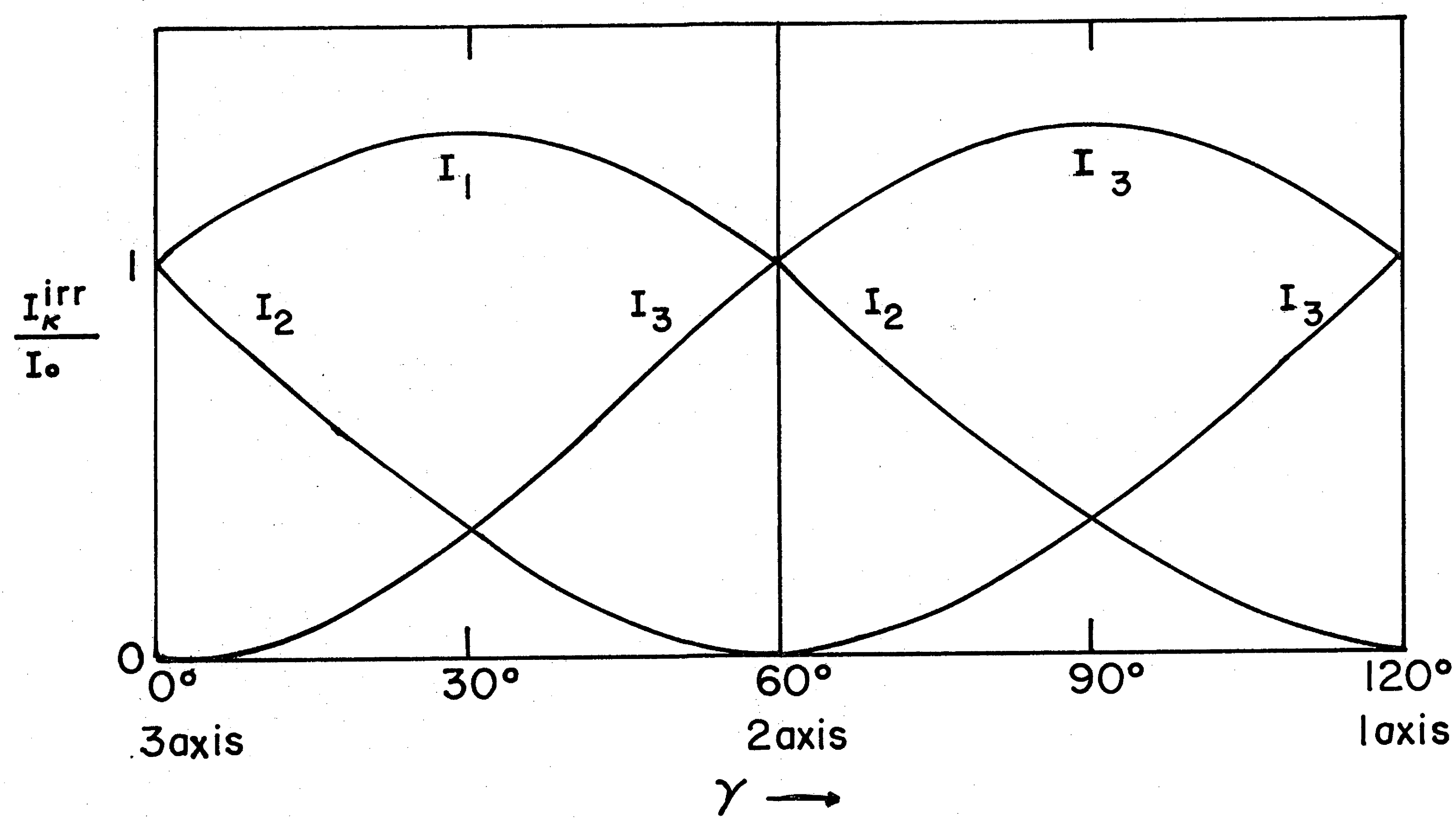

Fig. 4.14: Variation of the moments-of-inertia with γ. Axes given are as used in the particle plus triaxial rotor model.

α labels all states of angular momentum I,

and the summation is restricted to

$$|\kappa| \leqslant +I$$

$$|\Omega| \leqslant j$$

$$(\kappa + j) \text{ is even}$$

$$(\Omega + j) \text{ is even}$$

$$\tau = \pm 1 .$$

As well as the occurrence of D_2 symmetry, other symmetries arise from the six equivalent domains of the (β,γ) space, and from the cyclic permutations of the potential V_P (see Eqn (2)). It can be shown [Me75a] that because of the symmetries, a particle coupled to a core represented by parameters β, γ, λ_F has the same energy spectrum as a hole coupled to a core with parameters β, $(60° - \gamma)$, $-\lambda_F$, i.e.

$$E_n^{(I,j)} - (\beta,\gamma,\lambda_F;\ \text{particle}) = E_n^{(I,j)}(\beta,(60-\gamma),-\lambda_F;\ \text{hole}) . \quad (8)$$

It should be noted, though, that such a parameter transformation also involves a transformation of the axes such that

$$(\hat{1},\hat{2},\hat{3}) \rightarrow (\hat{3},\hat{1},\hat{2}) . \quad (9)$$

4.3.2.3 Moments and transition probabilities

The reduced matrix elements of the electric quadrupole and magnetic dipole are given [Me75a] in the form

$$\langle I',\alpha' \| Q^{(C)} \| I,\alpha\rangle = F^{(C)}_{I'\alpha',I\alpha}\, Q_0 \quad (10a)$$

$$\langle I',\alpha' \| Q^{(P)} \| I,\alpha\rangle = F^{(R)}_{I'\alpha',I\alpha}\, q_{sp} \quad (10b)$$

and, for $(I',\alpha') \neq (I,\alpha)$

$$\langle I',\alpha' \| M \| I,\alpha\rangle = F^{(1)}_{I'\alpha',I\alpha}(\mu_{sp} - g_R j) , \quad (10c)$$

where (C) and (P) represent the core and particle components respectively,

Q_0 $(= 3/\sqrt{5\pi}\, R_0^2\, Z\beta)$ is the intrinsic charge quadrupole moment,

q_{sp} and μ_{sp} are the single particle values for the electric and magnetic moments respectively,

g_R (= Z/A) is the gyromagnetic ratio of the core,

and the F factors contain the effect of the rotating core on the matrix elements.

It can be shown [Me75a] that from Eqns (10), one obtains for the spectroscopic electric quadrupole and magnetic moments (for particle calculations)

$$Q_{I\alpha}^{(sp)} = \begin{pmatrix} I & 2 & I \\ -I & 0 & I \end{pmatrix} \langle I\alpha \| Q \| I\alpha \rangle \tag{11a}$$

and

$$\mu_{I\alpha} = g_R I + \begin{pmatrix} I & 1 & I \\ -I & 0 & I \end{pmatrix} \langle I\alpha \| M \| I\alpha \rangle , \tag{11b}$$

where $\begin{pmatrix} I & 2 & I \\ -I & 0 & I \end{pmatrix}$ is a Wigner 3j-symbol. Also, the reduced transition probabilities and mixing ratios are found to be

$$B(E2;I\alpha \rightarrow I'\alpha') = \frac{5}{16\pi} \frac{|\langle I'\alpha' \| Q \| I\alpha \rangle|^2}{(2I+1)} \tag{12a}$$

$$B(M1;I\alpha \rightarrow I'\alpha') = \frac{|\langle I'\alpha' \| M \| I\alpha \rangle|^2}{(2I+1)} \tag{12b}$$

$$\delta(I\alpha \rightarrow I'\alpha') = 0.7\ E_\gamma^2 \sqrt{\frac{5}{16\pi}} \frac{\langle I'\alpha' \| Q \| I\alpha \rangle}{\langle I'\alpha' \| M \| I\alpha \rangle} , \tag{13}$$

where $E_\gamma = [E_{(I,\alpha)} - E_{(I'\alpha')}]$ (MeV).

In the case of calculations involving quasiholes, the sign, only, of $Q^{(sp)}$ and δ are changed. The other parameters expressed in Eqns (11), (12), (13) are not altered.

4.3.2.4 Model parameters

Of the parameters in the model, β, γ, and λ_F are varied in order to obtain a reasonable fit to an experimentally determined level scheme. The other parameters are assigned values which are consistent with the general trends in nuclear behaviour. For example, the strength (K) of the deformed field of the core is taken as

$$K = \frac{206}{A^{1/3}} \text{ (MeV)} \tag{14}$$

which is consistent with the splitting of the $h_{11/2}$ shell in the Nilsson level scheme. Although the derivation of this relation assumed axial symmetry, Eqn (14) is here assumed to also hold for triaxial deformations.

To determine the inertia parameter, $\mathcal{I}_0$, we make use of a general empirical rule as originally shown by Gradzins [Gr62], i.e.

$$E_{(2_1^+)}\ B(E2;2_1^+\rightarrow 0^+)\ \approx\ (2.5\pm 1)\times 10^{-3}\times Z^2\ A^{-1}\quad [\mathrm{MeV\ (eb)^2}]\ . \tag{15}$$

It is in the interpretation of this rule that the present model differs from the model of Meyer-ter-Vehn [Me75a]. Here we assume general triaxial conditions rather than the limiting case of axial symmetry [Me75a]. This extension is possible as Eqn (15) is quite general, there being no attempt in [Gr62] to limit the data for fitting to that from axial symmetric nuclei.

It can be shown (e.g. [Da58], [Me75a]) that for triaxially deformed (even) nuclei,

$$E_{(2_1^+)}\ B(E2;2_1^+\rightarrow 0^+)\ =\ \frac{3}{16}\,\frac{\hbar^2 Q_0^2}{\pi\mathcal{I}_0}\,X(\gamma)\ Z(\gamma) \tag{16a}$$

where

$$X(\gamma)\ =\ \frac{9-\sqrt{81-72\ \mathrm{Sin}^2(3\gamma)}}{4\ \mathrm{Sin}^2\ 3\gamma} \tag{16b}$$

and

$$Z(\gamma)\ =\ \tfrac{1}{2}\left\{1+\frac{(3-2\ \mathrm{Sin}(3\gamma))}{\sqrt{9-8\ \mathrm{Sin}(3\gamma)}}\right\}. \tag{16c}$$

The variation of $X(\gamma)$ and $Z(\gamma)$ with γ are shown for convenience in Fig. 4.15, from which it can be seen that at $\gamma=0$, both $X(\gamma)$ and $Z(\gamma)$ are equal to unity, reducing Eqn (16a) to the result for axial symmetry, as required. It is also obvious that large differences between this approach and those depending on axial symmetry will occur for large values of γ ($\gamma\approx 30°$).

After substituting for the static quadrupole moment in Eqn (16a) and equating relations (16) and (15), we obtain

$$\frac{\hbar^2}{2\mathcal{I}_0}\ =\ \frac{204}{\beta^2\ A^{7/3}\ X(\gamma)\ Z(\gamma)} \tag{17}$$

which reduces to the relation shown in [Me75a] at $\gamma=0$, $60°$, etc. The appearance of the functions $X(\gamma)$ and $Z(\gamma)$ in relation to (17) affects

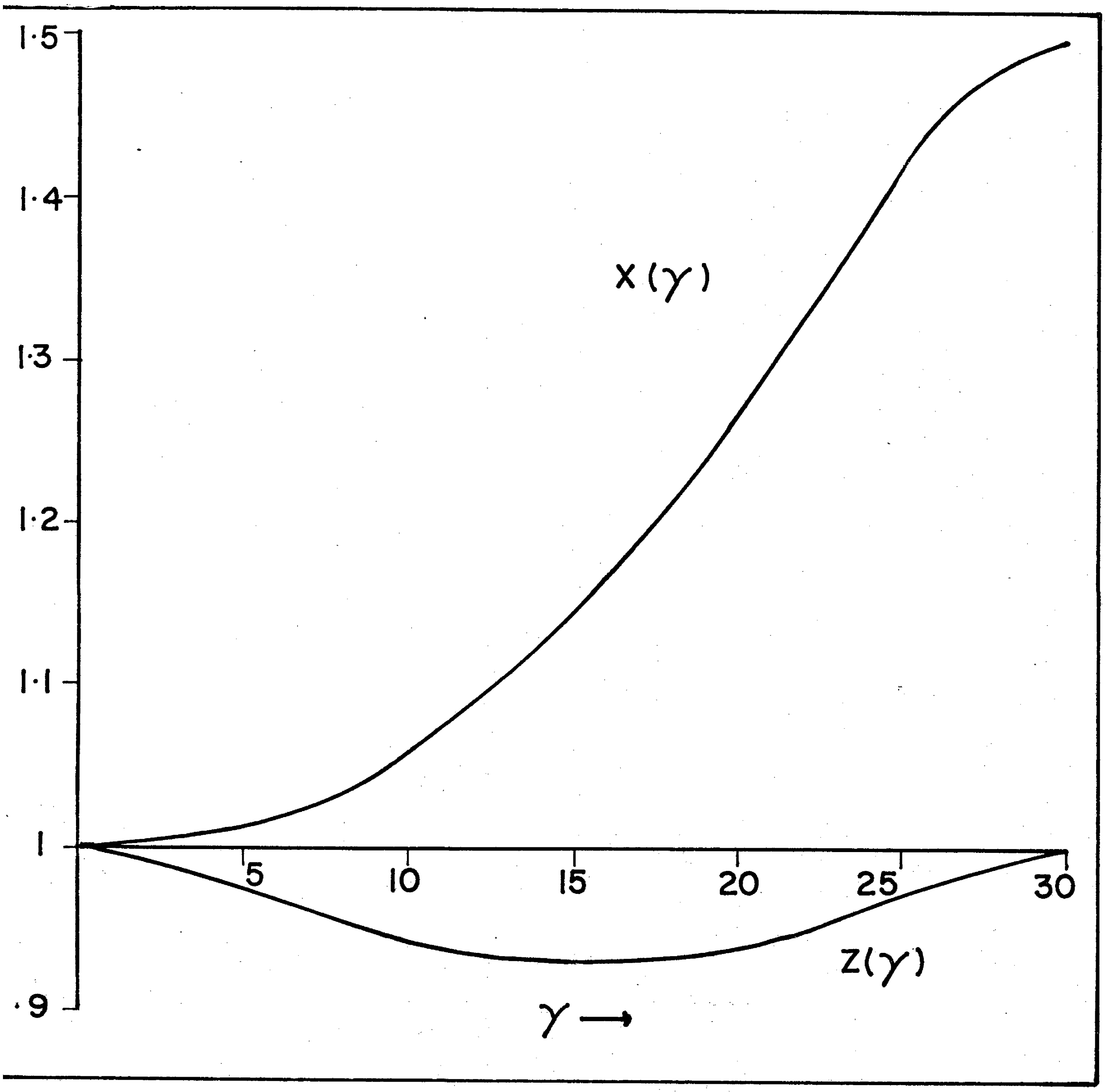

Fig. 4.15: Variation of X(γ) (Eqn 16(b)) and Z(γ) (Eqn 16(C)) over the region of $0 \leq \gamma \leq 30°$. Both curves are symmetrical about $\gamma = 30°$.

the best fit parameter values for any given data set in a way that can only be determined by the use of a computer calculation. Significant effects could be expected in the best fit value of β. The present model, making use of the formula for the energy of $I = 2_1^+$ level of an even triaxial rotor as [Me75a] and §4.2

$$E_{2_1^+} = \frac{(6)\hbar^2}{2\mathcal{I}_0} X(\gamma) \tag{18}$$

predicts a deformation parameter

$$\beta = \left(\frac{1224}{A^{7/3}\ E_{2_1^+}\ Z(\gamma)}\right)^{1/2} \tag{19}$$

which differs by up to 20% from the prediction of [Me75a] and [Da58], namely,

$$\beta = \left(\frac{1224\ X(\gamma)}{A^{7/3}\ E_{2_1^+}}\right)^{1/2} . \tag{20}$$

The lowering of the value of β, which is observed, explains, to some extent, the origin of some discrepancies which occur in the literature. For example, in [Sh79], great detail was used to describe the bands built on levels of spin $I^\pi = 9/2^+$ in the Antimony nuclei, as rotational bands in nuclei having deformations of $\beta \sim .16 \rightarrow .2$. Yet calculations using the model of [Me75a] suggested nuclei with $\beta \sim .32$ (for ^{115}Sb). While the present model does not completely rectify the situation, it does succeed in giving smaller values of β ($\beta \sim .27$ for ^{115}Sb).

4.3.3 Choice of Parameters and Fitting Procedure for Particle-Triaxial Model

The variable parameters, γ, β, and λ_F, are represented in the calculations by γ, $E_{2_1^+}$, and FER. $E_{2_1^+}$, related to β by Eqns (18) and (19), is the energy of the first 2^+ state of the even mass core. The use of this parameter allows for a rapid comparison of the core with the (A-1) nucleus. FER is a measure of the extent to which the Fermi level intrudes the j-shell, and is given by

$$\mathrm{FER} = \frac{\lambda_F - E_{\varepsilon_1}}{E_{\varepsilon_2} - E_{\varepsilon_1}} , \tag{21}$$

where for particle (hole) calculations, E_{ε_1} is the energy of the lowest (highest) energy particle state of the j-shell and E_{ε_2} is the energy of the next lowest (highest) particle state of the j-shell. If the Fermi level lies outside the j-shell, then FER is set to zero.

To estimate FER, the single neutron energies were found, using the Nilsson model, linearly interpolated to the γ value required [see §4.1]. λ_F was then found by solving the equations (22), (23)

$$V_j^2 = \tfrac{1}{2}\left(1 + \frac{(\varepsilon_j - \lambda_F)}{\sqrt{\Delta^2 + (\varepsilon_j - \lambda_F)^2}}\right) \tag{22}$$

and

$$N = 2 \sum_j V_j^2 , \tag{23}$$

where V_j represents the probability of occupancy of the j quasi-particle state and N is the total number of neutrons.

Also needed was the neutron gap parameter, determined from the approximation

$$2\Delta_n \approx [M(Z,N-1) - M(Z,N)] - [M(Z,N-2) - M(Z,N-1)] . \tag{24}$$

For ^{118}Te, $Z = 52$, $N = 66$ and $A = 118$. Hence

$$2\Delta_n = 2M(117) - M(118) - M(116) , \tag{25}$$

where 117, 118, 116 refer to Tellurium nuclei of those masses. As

$$\begin{aligned} M(116) &= 115.90825 \text{ a.m.u.} \\ M(117) &= 116.90859 \text{ a.m.u.} \\ M(118) &= 117.90590 \text{ a.m.u.} , \end{aligned} \tag{26}$$

$$\Delta_n = 1.42 \text{ MeV} . \tag{27}$$

This value was used for all calculations on both the odd-mass Tellurium nuclei considered.

The difficulty in estimating these parameters is that β must be known in order to determine FER, yet FER must be known in order to estimate β. The procedure used to overcome this is as follows.

A starting value for FER was assumed and E_{2^+} and γ varied until the experimental level scheme had been reproduced. Generally, these fitted values could not reproduce the value of FER as estimated above. This new value of FER was then taken as the input for a repeat of the procedure, as summarised in Fig. 4.16. Eventually the procedure converges, and a consistent solution (in terms of FER, E_{2^+} and γ) is reached. The parameter values corresponding to the consistent solution are here taken to represent the "fitted parameters".

The restriction in the calculations of the rigid core assumption (mentioned in the previous section) has only minimal impact if the rotor is well deformed. Such nuclei *are* generally quite rigid. However, the softness of the Tellurium nuclei requires the imposition of some restrictions to the choice of levels to be used in the fitting procedure.

The choice used for all the calculations was to attempt to fit only those levels which are suspected of having similar core rotational content. The fitted parameters so determined should then define a "shape" of the core which is related to some average shape for the levels fitted. Comparison between predicted and experimental energies of the other levels should give some indication of the effects of core softness.

4.3.4 Interpretation of the Negative Parity States

The levels to be discussed in this section form the cascades in ^{117}Te and ^{119}Te which end at the $I^{\pi} = 11/2^-$ levels. If these cascades are to be examined as rotational bands by the use of the triaxial rotor model, then the applicability of restricting the calculation to a single j shell should be tested. A relevant measure of the purity of the j quantum number is the value of $\langle j^2 \rangle$.

If j is a good quantum number, then

$$\langle j^2 \rangle = j(j+1) \qquad (28)$$

which, for the $h_{11/2}$ orbital is 35.75. However, many states of sufficient spin and with similar parity may contribute to the wave-function of one orbital and hence affect the mean. For any orbital we will define $\langle j^2 \rangle$ as

$$\langle j^2 \rangle \approx \sum_j D^2_{j\Omega}\, j(j+1) \; , \qquad (29)$$

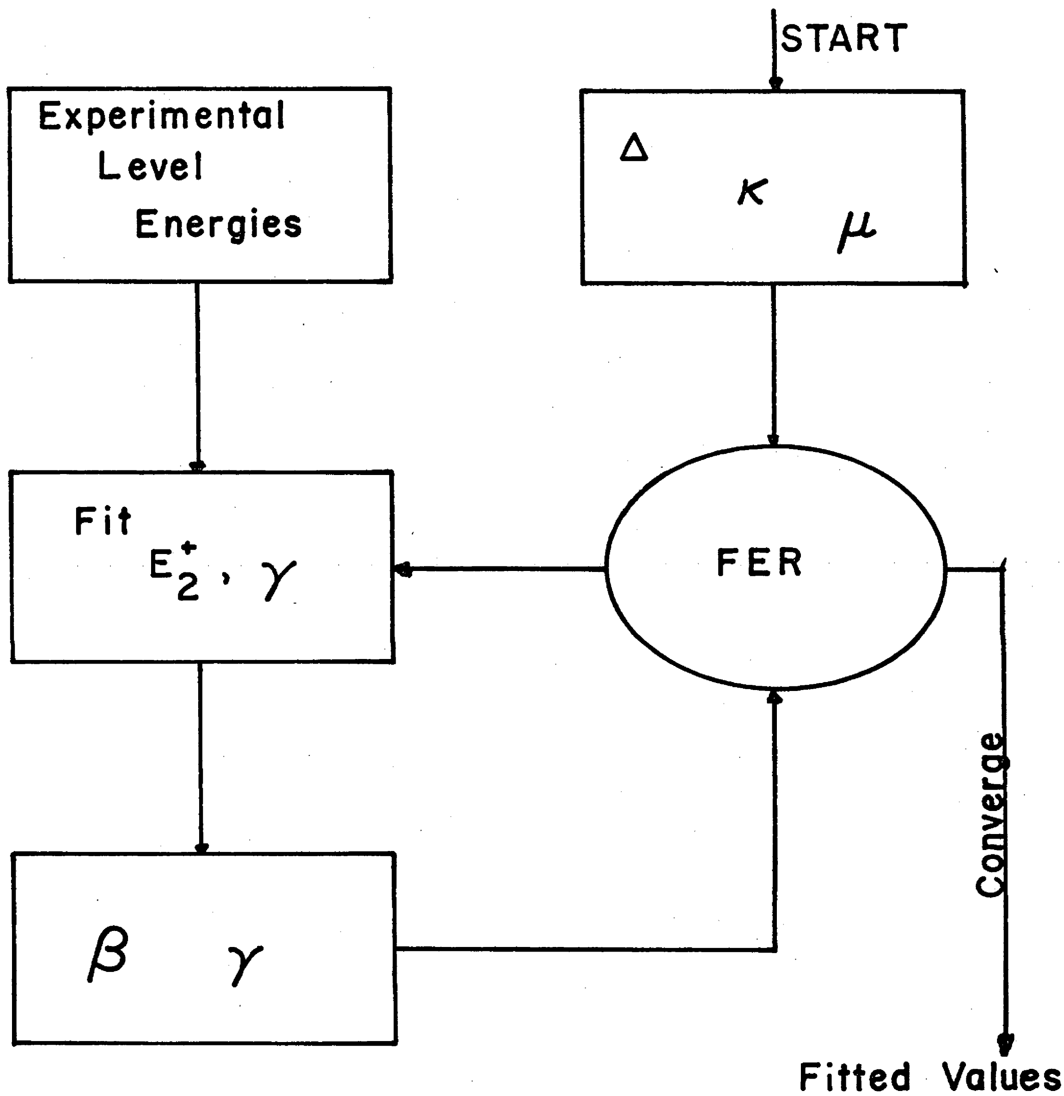

Fig. 4.16: Procedure used to compute values for E_2+, γ and β.

where the $D_{j\Omega}$ are the expansion coefficients of the Nilsson state of the odd particle in the spherical basis. The results of Eqn (29) of course depend on the deformation at which the $D_{j\Omega}$ are evaluated. They are found not to change rapidly with deformation except where pseudo-crossings of two states (of similar K,π) occurs.

The $D_{j\Omega}$ have been evaluated for the $1h_{11/2}$ neutron shell at $\beta = .165$ and $\gamma = 0°$, and these are presented in Table 4.3.1. The value of $\langle j^2 \rangle$ for each of the orbitals is also presented. The $1h_{11/2}$ (intruder) orbitals have reasonably pure j quantum numbers, as expected from the large energy gap, at small deformations, between the $1h_{11/2}$ orbital and the other orbitals of the $N = 5$ major oscillator shell.

Table 4.3.1

$D_{j\Omega}$ Coefficients for the $h_{11/2}$ Orbitals at $\beta = .165$

State	$K \backslash j$	$^{11}/_2$	$^9/_2$	$^7/_2$	$^5/_2$	$^3/_2$	$^1/_2$	$\langle j^2 \rangle$
[505]	$^{11}/_2$	1						35.75
[514]	$^9/_2$	.998	-.053					35.72
[523]	$^7/_2$	.992	-.064	.108				35.47
[532]	$^5/_2$	.981	-.060	.182	-.015			35.03
[541]	$^3/_2$	.968	-.044	.244	-.011	.033		34.60
[550]	$^1/_2$	.957	-.017	.282	-.012	.061	-.010	34.12

It will be shown later that the β deformation chosen for the evaluation of the elements of Table 4.3.1 is similar to the fitted values of β for both ^{117}Te and ^{119}Te. As it was not possible to evaluate Eqn (29) at the fitted deformations (β,γ), the results of Table 4.3.1 are assumed to be sufficient to justify restricting the calculation to a single j shell.

The levels whose energies were to be fitted by the model were chosen as those of spin $I = {}^{15}/_2$ and $I = {}^{13}/_2$. In ^{119}Te (and ^{121}Te), these levels appear to be members of bands similar in appearance to decoupled bands built on levels of $(j,K) = ({}^{11}/_2, {}^{11}/_2)$ and $({}^{11}/_2, {}^9/_2)$ respectively. As such their spin could be considered as consisting of a particle of (j,K) above, coupled to a core rotation [i.e. $(j,K)\otimes R$] such that $R=2$ for both levels. Hence, one may hope that one set of core parameters will be sufficient to apply to both levels.

Although no $9/2^-$ level was observed in ^{117}Te, levels of spin $I = 15/2$ and $13/2$ were again chosen as candidates for the fitting procedure.

Initially the value of the parameter FER was allowed to vary between the limits $0 \leqslant \mathrm{FER} \leqslant 2.5$ and the following general observations were made (all energies being measured relative to that of the $I = 11/2$ level):

- As FER increases, the energy of the $I^\pi = 9/2^-$ level decreases.
- The minimum energy of the $9/2^-$ level, at any given value of FER, increases as β decreases.
- At no value of FER could a set of the parameters E_{2^+},γ be found that was capable of simultaneously reproducing the energies of the levels of spin $I = 9/2$, $13/2$, and $15/2$.
- In fitting only the levels of spin $I = 13/2$ and $15/2$, the fitted parameters E_{2^+} and γ varied slowly and smoothly with FER.

However, it was not possible to find a fit to the two levels for values of FER greater than two.

The first point illustrates that the systematic behaviour of the $9/2^-$ level in the Tellurium nuclei, as seen in Fig. 3.1, is a natural result of the addition of neutrons causing a rise in the Fermi level. The fact that the $9/2^-$ level always (in Tellurium) lies higher, in energy, than the $11/2^-$ level (Fig. 3.1) indicates the small (β) deformation of these nuclei.

Using these observations as a base, the procedure shown in Fig. 4.16 was followed, until the fitted parameters were obtained as,

$$\text{for } ^{119}\text{Te} \qquad \begin{aligned} E_{2^+} &= .659 \text{ MeV } [\beta = .164] \\ \gamma &= 31.5^\circ \\ \mathrm{FER} &= 1.42 \end{aligned} \tag{30a}$$

and for ^{117}Te $\quad E_{2^+} = .657$ MeV $[\beta = .167]$

$$\gamma = 28.7° \tag{30b}$$

$$\text{FER} = 0.94\ .$$

The level schemes corresponding to these sets of parameters are shown in Fig. 4.17, together with the experimentally determined level schemes. Only the Yrast levels of those calculated are shown.

In both nuclei, the calculated energies deviate markedly from the experimental values at spins greater than $I = {}^{15}\!/_2$, highlighting the severity of the rigid core assumption. The calculations are able to reproduce the relative closeness of the levels of spin $I = {}^{17}\!/_2$ and ${}^{19}\!/_2$, but are unable to predict the position, relative to the ${}^{23}\!/_2$ level, of the ${}^{21}\!/_2$ level in ^{119}Te.

In ^{119}Te, the position of the ${}^{9}\!/_2^-$ level is predicted as lying much higher in energy than observed. Attempts were made to fit the energies of the ${}^{9}\!/_2$ and ${}^{13}\!/_2$ levels, ignoring all others, but no set of parameters could be found to satisfy such criteria.

In ^{117}Te, a ${}^{9}\!/_2^-$ level is predicted at a reasonably low energy but has not been confirmed by the experimental results.

The nature of the predicted levels can be revealed by considering their wavefunctions. Information is contained in the parameters $C^{(Ij\alpha)}_{\underset{\sim}{K}\underset{\sim}{\Omega}}$ of Eqn (7) where $\underset{\sim}{K}$ and $\underset{\sim}{\Omega}$, if considered as averaged projections of $\vec{I}$ and $\vec{j}$ on one of the axes, can be used for an approximate classification of the wavefunction. The definition of $\underset{\sim}{K}$ and $\underset{\sim}{\Omega}$ is illustrated in Fig. 4.18, but it should be remembered neither $\underset{\sim}{K}$ nor $\underset{\sim}{\Omega}$ are good quantum numbers. We will use the $\hat{2}$ axis, as defined in Eqn (3) as the projection axis, for the moment-of-inertia about this axis approaches zero at 60° and the axis then becomes the oblate symmetry axis.

The square of the amplitudes of the Yrast levels ($\alpha = 1$), are given in Table 4.3.2 for ^{119}Te, and in Table 4.3.3 for ^{117}Te. The amplitudes are normalised such that

$$\sum_{\underset{\sim}{K}\,\underset{\sim}{\Omega}} \left(C^{\,Ij\,(\alpha=1)}_{\underset{\sim}{K}\,\underset{\sim}{\Omega}}\right)^2 = 1\ . \tag{31}$$

In interpreting the values of C^2 in Tables 4.3.2 and 4.3.3, the

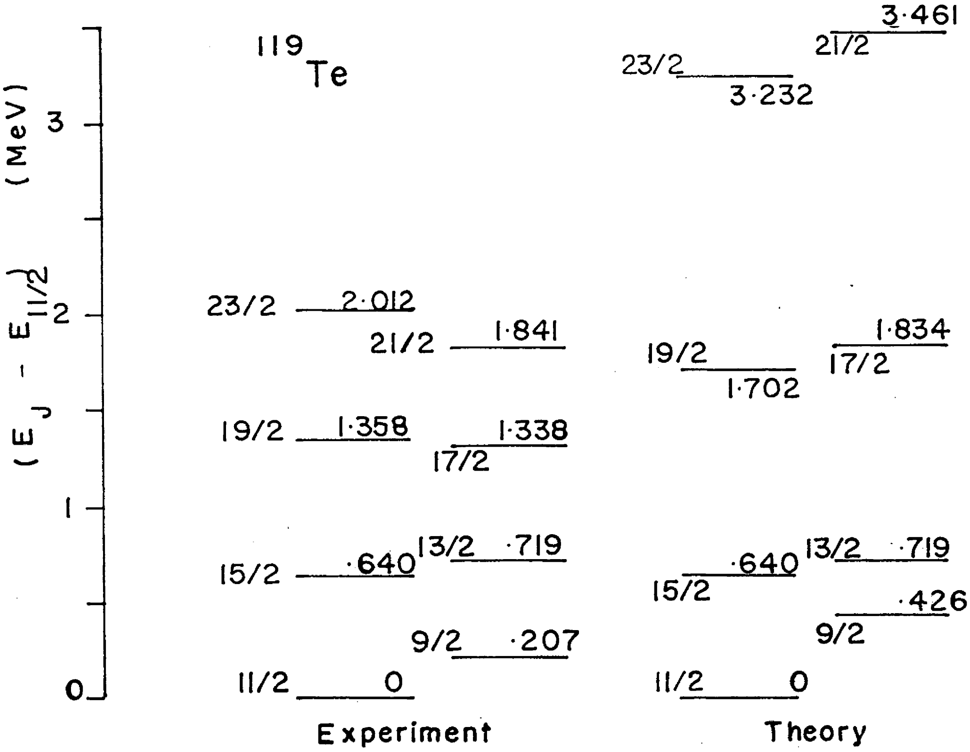

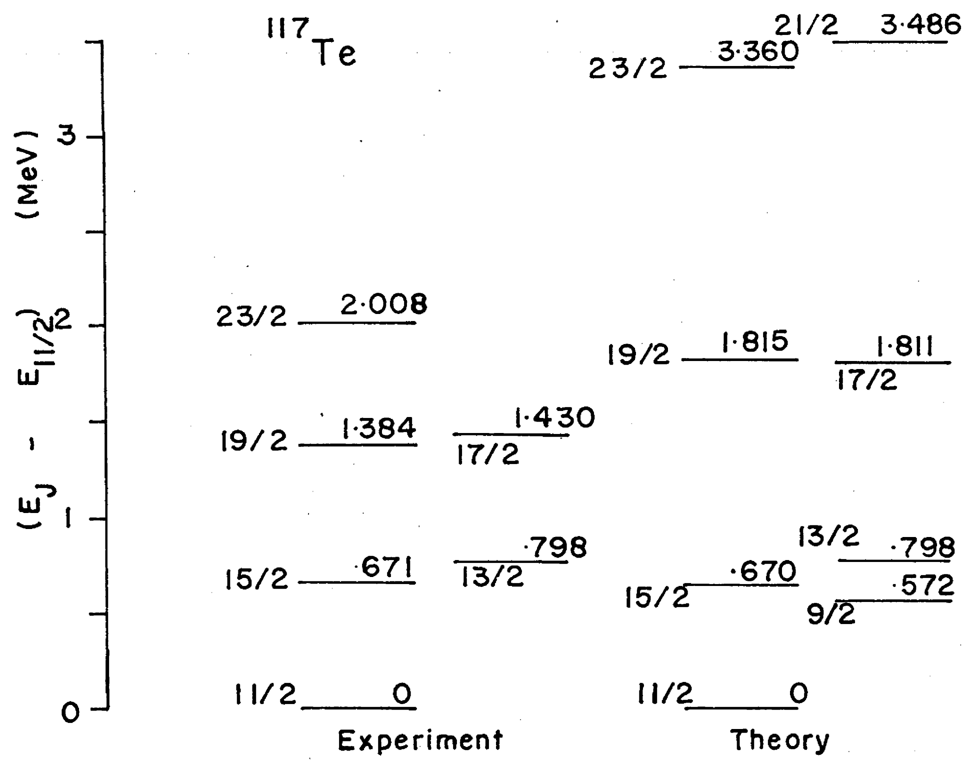

Fig. 4.17: Experimental and theoretically produced energy levels of the $1h_{11/2}$ bands in ^{119}Te and ^{117}Te. Calculations are described in the text.

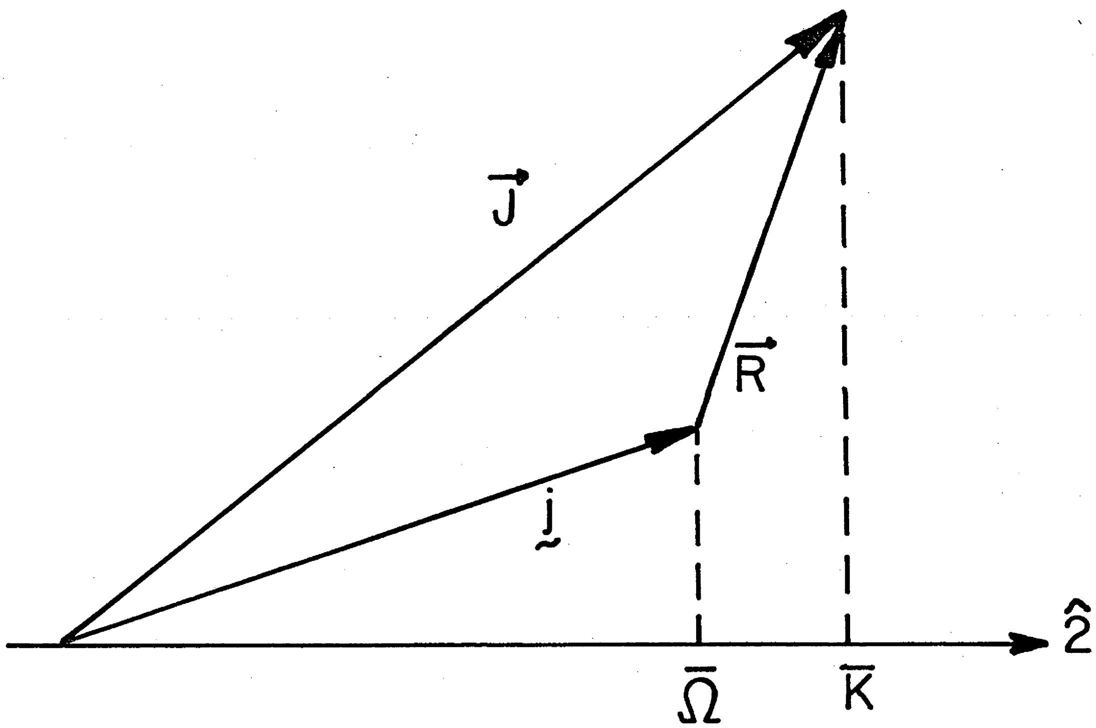

Fig. 4.18: Definition of $\underset{\sim}{K}$ and $\underset{\sim}{\Omega}$, the averaged projections of $\underset{\sim}{I}$ and $\underset{\sim}{j}$ on the $\hat{2}$ axis.

Table 4.3.2

Calculated Wavefunctions $(C_{K\Omega})^2$ of the Yrast Levels in the $h_{11/2}$ Band of ^{119}Te

Wavefunction for $J = 9/2$, $E = 426$ MeV State

K \ Ω	11/2	7/2	3/2	1/2	5/2	9/2
7/2	.022	.305	.018			
3/2		.012	.039	.015		
1/2			.011	.004		
5/2				.020	.135	.021
9/2					.007	.380

Wavefunction for $J = 11/2$, $E = 0.0$ MeV State

K \ Ω	11/2	7/2	3/2	1/2	5/2	9/2
11/2	.182					
7/2		.200	.006			
3/2		.007	.096	.011		
1/2			.011	.080	.010	
5/2				.010	.133	.002
9/2					.002	.252

Wavefunction for $J = 13/2$, $E = .719$ MeV State

K \ Ω	11/2	7/2	3/2	1/2	5/2	9/2
11/2	.228	.015				
7/2		.235	.001			
3/2		.006	.034			
1/2			.002	.003	.005	
5/2					.108	.003
9/2					.005	.343
13/2						.010

Wavefunction for $J = {}^{15}/_2$, $E = .640$ MeV State

$K \backslash \Omega$	$^{11}/_2$	$^7/_2$	$^3/_2$	$^1/_2$	$^5/_2$	$^9/_2$
$^{15}/_2$	.056					
$^{11}/_2$	.030	.039				
$^7/_2$		.141	.026			
$^3/_2$		.011	.138	.025		
$^1/_2$			.023	.132	.018	
$^5/_2$				.025	.145	.003
$^9/_2$					.028	.098
$^{13}/_2$						.059

Wavefunction for $J = {}^{17}/_2$, $E = 1.834$ MeV State

$K \backslash \Omega$	$^{11}/_2$	$^7/_2$	$^3/_2$	$^1/_2$	$^5/_2$	$^9/_2$
$^{15}/_2$	.176	.001				
$^{11}/_2$	.046	.102				
$^7/_2$		.138	.012			
$^3/_2$		.011	.033			
$^1/_2$			.004	.004	.010	
$^5/_2$				.002	.085	.006
$^9/_2$					.039	.131
$^{13}/_2$						.198
$^{17}/_2$						

Wavefunction for $J = {}^{19}/_2$, $E = 1.702$ MeV State

$K \backslash \Omega$	$^{11}/_2$	$^7/_2$	$^3/_2$	$^1/_2$	$^5/_2$	$^9/_2$
$^{19}/_2$	.004					
$^{15}/_2$	.027	.002				
$^{11}/_2$	.010	.070	.002			
$^7/_2$		.093	.055	.002		
$^3/_2$		.013	.134	.042	.001	
$^1/_2$			.034	.138	.024	
$^5/_2$			.001	.048	.121	.004
$^9/_2$				.002	.062	.048
$^{13}/_2$					.001	.062
$^{17}/_2$						.003

Wavefunction for $J = {}^{21}/_2$, $E = 3.461$ MeV State

$K \backslash \Omega$	$^{11}/_2$	$^{7}/_2$	$^{3}/_2$	$^{1}/_2$	$^{5}/_2$	$^{9}/_2$
$^{19}/_2$	.024					
$^{15}/_2$	.085	.002				
$^{11}/_2$	.037	.093				
$^{7}/_2$	.002	.149	.005	.002		
$^{3}/_2$		.034	.043	.011	.003	
$^{1}/_2$		.001	.027	.005	.038	
$^{5}/_2$			.003	.001	.104	.017
$^{9}/_2$				.001	.034	.121
$^{13}/_2$						.143
$^{17}/_2$						.014
$^{21}/_2$						

Wavefunction for $J = {}^{23}/_2$, $E = 3.232$ MeV State

$K \backslash \Omega$	$^{11}/_2$	$^{7}/_2$	$^{3}/_2$	$^{1}/_2$	$^{5}/_2$	$^{9}/_2$
$^{23}/_2$						
$^{19}/_2$	.006					
$^{15}/_2$	.013	.010				
$^{11}/_2$	.005	.069	.007			
$^{7}/_2$		.068	.072	.004		
$^{3}/_2$		.013	.125	.054	.001	
$^{1}/_2$			.042	.135	.027	
$^{5}/_2$			.003	.065	.102	.003
$^{9}/_2$				.006	.075	.029
$^{13}/_2$					.008	.045
$^{17}/_2$						.011
$^{21}/_2$						

Table 4.3.3

Calculated Wavefunctions $(C_{K\Omega})^2$ of the Yrast Levels in the $h_{11/2}$ Band of ^{117}Te

Wavefunction for $J = 9/2$, E = .572 MeV State

K \ Ω	11/2	7/2	3/2	1/2	5/2	9/2
7/2	.057	.242	.028	.001		
3/2		.016	.021	.016	.001	
1/2		.001	.011	.002	.010	.001
5/2			.001	.023	.084	.035
9/2					.018	.434

Wavefunction for $J = 11/2$, E = 0.0 MeV State

K \ Ω	11/2	7/2	3/2	1/2	5/2	9/2
11/2	.353	.001				
7/2	.001	.141	.009			
3/2		.010	.050	.010		
1/2			.010	.040	.010	
5/2				.010	.077	.007
9/2					.006	.266

Wavefunction for $J = 13/2$, E = .798 MeV State

K \ Ω	11/2	7/2	3/2	1/2	5/2	9/2
11/2	.337	.021	.001			
7/2	.005	.157				
3/2		.014	.018	.001		
1/2			.003	.002	.008	
5/2					.061	.015
9/2				.001	.004	.318
13/2						.033

Wavefunction for $J = {}^{15}\!/_2$, $E = .670$ MeV State

$K \backslash \Omega$	$^{11}\!/_2$	$^{7}\!/_2$	$^{3}\!/_2$	$^{1}\!/_2$	$^{5}\!/_2$	$^{9}\!/_2$
$^{15}\!/_2$	.197					
$^{11}\!/_2$	.039	.060	.001			
$^{7}\!/_2$	.001	.095	.027	.001		
$^{3}\!/_2$		.013	.074	.021	.001	
$^{1}\!/_2$			.019	.068	.017	
$^{5}\!/_2$			.001	.023	.084	.006
$^{9}\!/_2$				.001	.036	.088
$^{13}\!/_2$					.001	.124

Wavefunction for $J = {}^{17}\!/_2$, $E = 1.811$ MeV State

$K \backslash \Omega$	$^{11}\!/_2$	$^{7}\!/_2$	$^{3}\!/_2$	$^{1}\!/_2$	$^{5}\!/_2$	$^{9}\!/_2$
$^{15}\!/_2$	.267	.001				
$^{11}\!/_2$	.059	.091				
$^{7}\!/_2$	.002	.095	.011			
$^{3}\!/_2$		.012	.018			
$^{1}\!/_2$			.003	.002	.009	
$^{5}\!/_2$				.002	.051	.010
$^{9}\!/_2$					.034	.116
$^{13}\!/_2$						.213
$^{17}\!/_2$						.002

Wavefunction for $J = {}^{19}\!/_2$, $E = 1.815$ MeV State

$K \backslash \Omega$	$^{11}\!/_2$	$^{7}\!/_2$	$^{3}\!/_2$	$^{1}\!/_2$	$^{5}\!/_2$	$^{9}\!/_2$
$^{19}\!/_2$	.018					
$^{15}\!/_2$	.049	.004				
$^{11}\!/_2$	.016	.077	.004			
$^{7}\!/_2$	.001	.086	.053	.003		
$^{3}\!/_2$		.017	.100	.040	.002	
$^{1}\!/_2$		.001	.034	.100	.026	
$^{5}\!/_2$			.002	.045	.017	.007
$^{9}\!/_2$				.003	.063	.056
$^{13}\!/_2$					.004	.084
$^{17}\!/_2$						.010

Wavefunction for $J = {}^{21}\!/_2$, $E = 3.486$ MeV State

$K \backslash \Omega$	$^{11}\!/_2$	$^{7}\!/_2$	$^{3}\!/_2$	$^{1}\!/_2$	$^{5}\!/_2$	$^{9}\!/_2$
$^{19}\!/_2$	.071					
$^{15}\!/_2$	.118	.006				
$^{11}\!/_2$	.043	.091				
$^{7}\!/_2$	.004	.110	.007	.001		
$^{3}\!/_2$		.031	.027	.005	.003	
$^{1}\!/_2$		.002	.017	.003	.028	.001
$^{5}\!/_2$			.003		.069	.020
$^{9}\!/_2$					.035	.109
$^{13}\!/_2$					.001	.158
$^{17}\!/_2$						.033
$^{21}\!/_2$						

Wavefunction for $J = {}^{23}\!/_2$, $E = 3.360$ MeV State

$K \backslash \Omega$	$^{11}\!/_2$	$^{7}\!/_2$	$^{3}\!/_2$	$^{1}\!/_2$	$^{5}\!/_2$	$^{9}\!/_2$
$^{23}\!/_2$	.001					
$^{19}\!/_2$	.015					
$^{15}\!/_2$	.021	.017				
$^{11}\!/_2$	.008	.073	.011			
$^{7}\!/_2$	.001	.065	.067	.007		
$^{3}\!/_2$		.017	.099	.051	.003	
$^{1}\!/_2$		.001	.041	.105	.029	
$^{5}\!/_2$			.005	.060	.087	.006
$^{9}\!/_2$				.009	.073	.034
$^{13}\!/_2$					.013	.057
$^{17}\!/_2$						.022
$^{21}\!/_2$						.001

following points are helpful:

- The value of β is similar in both nuclei.

- ^{119}Te is, approximately, as oblate ($\gamma_{fit} = (30+1.5)°$) as ^{117}Te is prolate ($\gamma_{fit} = (30-1.3)°$).

- These imply similar moments-of-inertia for the two nuclei, but about different axes, i.e.

$$^{119}I_1 \approx {}^{117}I_1 \tag{32a}$$

$$^{119}I_2 \approx {}^{117}I_3 \tag{32b}$$

$$^{119}I_3 \approx {}^{117}I_2 \,. \tag{32c}$$

- As the nuclei have γ deformations close to 30°, the moment-of-inertias about the $\hat{2}$ and $\hat{3}$ axes will not differ greatly. In fact, there is less than 20% difference between them.

The only major difference between the two nuclei lies with the Fermi level. The deeper penetration of the j-shell which is involved in ^{119}Te makes the likelihood of complete alignment of the neutron with any axis less than in ^{117}Te. This is reflected in the wave-functions of the $^{11}/_2{}^-$ level, where, for example,

$$\left(C^{11/2,11/2}_{11/2,11/2}\right)^2 = \begin{cases} .353 & \text{for } ^{117}\text{Te} \\ .182 & \text{for } ^{119}\text{Te} \,. \end{cases} \tag{33}$$

Now, a neutron, in a high-j shell, has an oblate density distribution which is axially symmetric about the direction of its angular momentum $(\vec{j})$. So as the neutron prefers to couple to the core in such a way that the mass overlap is maximised, it has a tendency to align with the $\hat{2}$ axis. Thus strongest coupling will occur for $\gamma = 60°$, but in the present situation the β deformation is so small that the coupling will be very weak.

The neutron also has a tendency to align its angular momentum with that of the rotating core, for complete alignment minimises the energy due to centrifugal and Coriolis effects.

Another point is that as the moment-of-inertia about the $\hat{2}$ axis drops to zero at $\gamma = 60°$, rotation about this axis becomes increasingly unfavourable and $\vec{R}$ is forced into the $(\hat{1},\hat{3})$ plane.

It is possible, then, to recognise two "groups" of levels from

Tables 4.3.2 and 4.3.3; one in which $\vec{j}$ and $\vec{R}$ are "more or less" aligned, and the second where $\vec{j}$ is aligned with the $\hat{2}$ axis. The two "groups" rapidly lose their identity as the spin is increased, and the wavefunctions become very mixed. This mixing occurs more rapidly for ^{119}Te due to the increased value of FER.

The first group consists of those levels with $I = j + R$ $(R = 0, \pm 2, \pm 4, \ldots)$ and appear similar to the rotation-aligned coupling scheme of axially symmetric nuclei. In ^{117}Te, the group is, initially, partially aligned with the $\hat{2}$ axis as the moment-of-inertia about the $\hat{3}$ axis is smallest. In ^{119}Te, where the situation is reversed, $\vec{j}$ and $\vec{R}$ are partially aligned perpendicular to the $\hat{2}$ axis. By projecting the wavefunctions on different axes, it can be shown that $\vec{j}$ and $\vec{R}$ are aligned with the $\hat{3}$ axis in ^{119}Te. This "group" of levels forms a "favoured" band as these were found to be the most populated in the experiments.

The second group consists of those levels of spin $I = j + R + 1$ $(R = 0, \pm 2, \pm 4, \ldots)$ and form an "unfavoured" band. It is obvious from the $C^2_{\underset{\sim}{K\Omega}}$ coefficients of Tables 4.3.2 and 4.3.3 that this band is not a perfect "deformation-aligned" band in the sense that the core rotation is not completely perpendicular to the $\hat{2}$ axis. The major components of the wavefunction are, however, those of a deformation aligned band.

The identity of these two bands are not easy to determine because of the weak coupling and the similarity of the moments-of-inertia about the $\hat{2}$ and $\hat{3}$ axes.

The decay rates calculated for transitions occurring between levels of interest are given in Tables 4.3.4 and 4.3.5. The tendency of levels in the "unfavoured" band" to decay to members of the "favoured" band is most noticeable.

It is ^{119}Te that is the more successful at retaining population in the "unfavoured" band. This is in accord with the experimental results where the $9/2^-$ level, observed in ^{119}Te, is not observed in ^{117}Te. The experimental and theoretical branching ratios for the decay of the $17/2^-$ and $13/2^-$ levels, given in Table 4.3.6, show this in more detail. Although the theoretical branching ratios for the $13/2^-$ level may be overestimated (caused by the extremely small rate for the

Table 4.3.4

Decay Rates Calculated for Transitions in ^{119}Te

Transition	Transition Probability (ps^{-3})
$9/2 \to 11/2$	.06
$13/2 \to 9/2$	$.22 \times 10^{-3}$
$13/2 \to 11/2$	.47
$15/2 \to 11/2$	.14
$17/2 \to 11/2$	1.7
$17/2 \to 15/2$	1.2
$19/2 \to 15/2$	2.5
$21/2 \to 17/2$	17
$21/2 \to 19/2$	7.4
$23/2 \to 19/2$	19

Transitions are between levels whose wavefunctions are tabulated in Tab.e 4.3.2.

Table 4.3.5

Decay Rates Calculated for Transitions in ^{117}Te

Transition	Transition Probability (ps^{-1})
$9/2 \to 11/2$	.71
$13/2 \to 9/2$	$.27 \times 10^{-6}$
$13/2 \to 11/2$	2.0
$15/2 \to 11/2$	.17
$17/2 \to 13/2$	1.0
$17/2 \to 15/2$	2.8
$19/2 \to 15/2$	3.3
$21/2 \to 17/2$	20
$21/2 \to 19/2$	9.6
$23/2 \to 19/2$	20

Transitions are between levels whose wavefunctions are tabulated in Table 4.3.3.

Table 4.3.6

Branching Ratios of $^{13}/_2^-$ and $^{17}/_2^-$ States

		Fraction: $\dfrac{I_{17/2-15/2}}{I_{17/2-13/2}}$	$\dfrac{I_{13/2-11/2}}{I_{15/2-9/2}}$
^{117}Te	Theor	2.8	7.4×10^{6}
	Obs	<.79	very large
^{119}Te	Theor	.70	2136
	Obs	.88	>.85

$^{13}/_2^- \rightarrow {}^9/_2^-$ transition), the *observed* trend between the nuclei is reproduced.

In Table 4.3.7, the calculated and observed mixing ratios are given for the interband transitions. A serious failure of the model occurs here, for it is unable to reproduce the sign of the mixing ratio. (This also occurs when the standard Meyer-ter-Vehn calculations are made.) Much care was taken to ensure that the definition of mixing ratio used in the Meyer-ter-Vehn calculations was the same as used in the interpretation of angular distributions in this work (i.e. Yamazaki [Ya67]). However, as the model successfully predicts the sign of mixing ratios in many other cases (e.g. [Me75b]), the failure here appears to be indicative of effects occurring which are outside the scope of the model.

The predicted electric quadrupole and magnetic dipole moments are given in Table 4.3.8. None of these have, as yet, been measured, but it is interesting to compare the magnetic moment of the $^{11}/_2^-$ levels with the measured g factor of the $^{11}/_2^-$ level in ^{115}Te [Fa79], given as

$$g^{115}_{11/2^-} = -0.186 \pm .007 \; . \qquad (34a)$$

For the heavier nuclei the corresponding factors can be determined from the data of Table 4.3.8 as

Table 4.3.7

Mixing Ratios

Transition	Nucleus	δ_{Th}	δ_{Obs}
$9/2 \to 11/2$	119	-.249	$-.25 \leqslant \delta \leqslant -.14$
$13/2 \to 11/2$	119	+.5689	$-.09 \leqslant \delta \leqslant -.04$
$17/2 \to 15/2$	119	+1.928	$-1.7 \leqslant \delta \leqslant -.1.1$
$21/2 \to 19/2$	119	+2.647	$\delta \approx -.82$
$13/2 \to 11/2$	117	+.326	-
$17/2 \to 15/2$	117	+.764	-

Table 4.3.8

Calculated Electric Quadrupole and Magnetic Dipole Moments for Yrast States of the $h_{11/2}$- Bands in ^{119}Te and ^{117}Te

J	^{119}Te Q_2(eb)	^{119}Te μ(nm)	^{117}Te Q_2(eb)	^{117}Te μ(nm)
$9/2$	-.386	-1.145	-.452	-1.105
$11/2$	-.300	-1.055	-.594	-1.033
$13/2$	-.124	-.444	-.302	-.398
$15/2$	-.095	-.204	-.502	-.180
$17/2$	-.375	.421	-.523	.444
$19/2$	.004	.659	-.176	.699
$21/2$	-.141	1.428	-.348	1.451
$23/2$	.034	1.526	-.112	1.577

$$g^{117}_{11/2^-} = -.188 \qquad (34b)$$

$$g^{119}_{11/2^-} = -.192 \qquad (34c)$$

which are very similar to the above measurement.

The interpretation of the negative parity states by this model has given some useful insights as to the nature of the nuclear states.

As the odd neutron is not strongly coupled to the core, effects, such as the two-proton excitations seen in the even mass Tellurium isotopes (which cannot be incorporated into the present model), may have a significant impact on the level scheme. The fits would undoubtedly be improved if a Variable Moment-of-Inertia was used, as shown for similar cases in [V178]. Further refinement could be made by extending the particle space for the odd neutron as in [La78]. The most useful extension would be to include the $2f_{7/2}$ shell, as these orbitals contribute most (apart from the $h_{11/2}$ orbitals) to the $D^2_{j\Omega}$ coefficients of Eqn (29).

Recently the Xenon isotones of ^{117,119}Te, ^{119}Xe and ^{121}Xe, have been examined by the standard Meyer-ter-Vehn calculations [Ch81]. The level schemes are reproduced in Fig. 4.19. They concluded that the $9/2^-$ level was higher in energy than the $11/2^-$ level as a result of a small value of γ. In contrast, it was shown here that, in Tellurium, the small value of β caused the raising of the $9/2^-$ level (relative to the $11/2^-$ level).

4.3.5 Interpretation of the Positive Parity States

The triaxial rotor plus particle model is a particularly favourable model to use in the interpretation of the band built on the $7/2^+$ level in ^{119}Te. It is able, in a very simple way, to reproduce the observed "squeezing" of both the $9/2^+$ and $11/2^+$ levels, and of the $13/2^+$ and $15/2^+$ levels. Here, the "squeezing" refers to the $9/2^+$ (or $13/2^+$) level lying closer in energy to the $11/2^+$ ($15/2^+$) level than the $7/2^+$ ($11/2^+$) level. The first effect occurs when gamma is increased from zero, and is particularly noticeable for $20° < \gamma < 30°$. Given that one affects a fit to levels of spin $9/2^+$ and $11/2^+$, the second effect occurs when FER is increased from zero. As a result, the observed behaviour can be reproduced without the addition of any other variables.

The model presented here limits the calculation to within a single j shell. However, mixing of the $g_{7/2}$ orbitals with other orbitals certainly occurs, and this is reflected in the $D^2_{j\Omega}$ coefficients given in Table 4.3.9. These values were evaluated at the

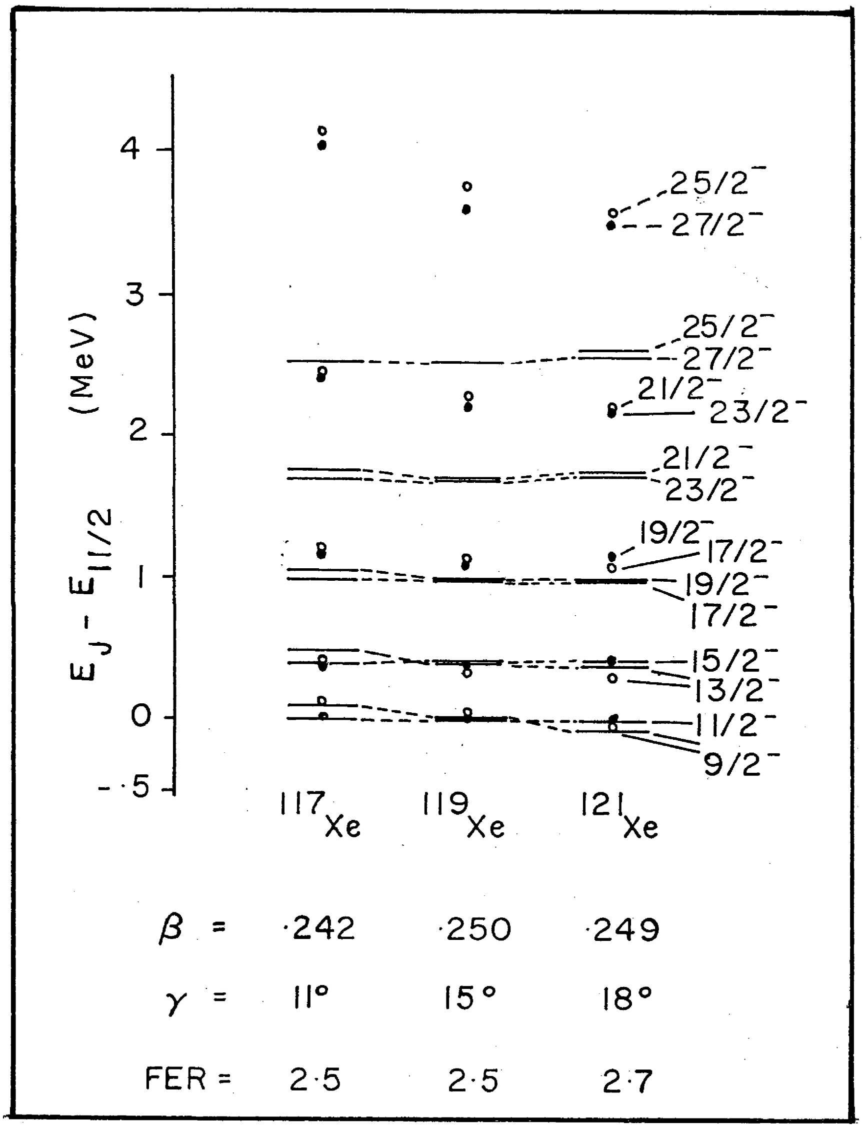

Fig. 4.19: $1h_{11/2}$ band structure in odd-A Xe nuclei. The dots represent the results of theoretical calculations using the given parameters.

Table 4.3.9

$D_{j\Omega}$ Coefficients for the $g_{7/2}$ Orbitals at $\beta = .237$

State	$K \backslash j$	$9/2$	$7/2$	$5/2$	$3/2$	$1/2$	$\langle j^2 \rangle$
[404]	$7/2$	.1084	.9941				15.86
[413]	$5/2$	.1910	.9353	−.2999			15.47
[422]	$3/2$	.2920	.8056	−.3801	.3481		14.05
[431]	$1/2$	.3690	.5660	−.3556	.5280	−.371	10.68

deformation $\beta = .237$, $\gamma = 0°$ and show, compared to the "pure" value ($\langle j^2 \rangle = 15.75$), the estimated $\langle j^2 \rangle$ drop off rapidly for $\Omega = 3/2$ and $K = 1/2$ orbitals.

It appears that if only $\Omega = 7/2$ and $K = 5/2$ orbitals were involved in the excitation of the band, then the restriction of the calculation to a single j shell may not be detrimental. The situation becomes more complex, though as γ is increased from zero, for then all orbitals of the same parity are able to mix. The amount of mixing only becomes large when the orbitals are near in energy (e.g. quasicrossing points). If such mixing is occurring to a great degree, then it will manifest itself in the calculation by, firstly, requiring a larger value for the FER parameter as mixing of the states effectively reduces the gap between the uppermost and next uppermost orbitals. Secondly, the degree of agreement between the calculated and experimental results will not be very good.

The fitting procedure, as previously outlined, was conducted for ^{119}Te only, there being insufficient data available from the ^{117}Te experimental results. The levels fitted were those of spin $I = 9/2$ and $11/2$, the fitted parameters being determined as

$$\begin{aligned} E_{2^+} &= .321 \text{ MeV} \qquad (\beta = .238) \\ \gamma &= 24.4° \\ \text{FER} &= .39 \,. \end{aligned} \tag{35}$$

The experimental and calculated level schemes are shown in Fig. 4.20. It is immediately obvious that the fit here is much better than

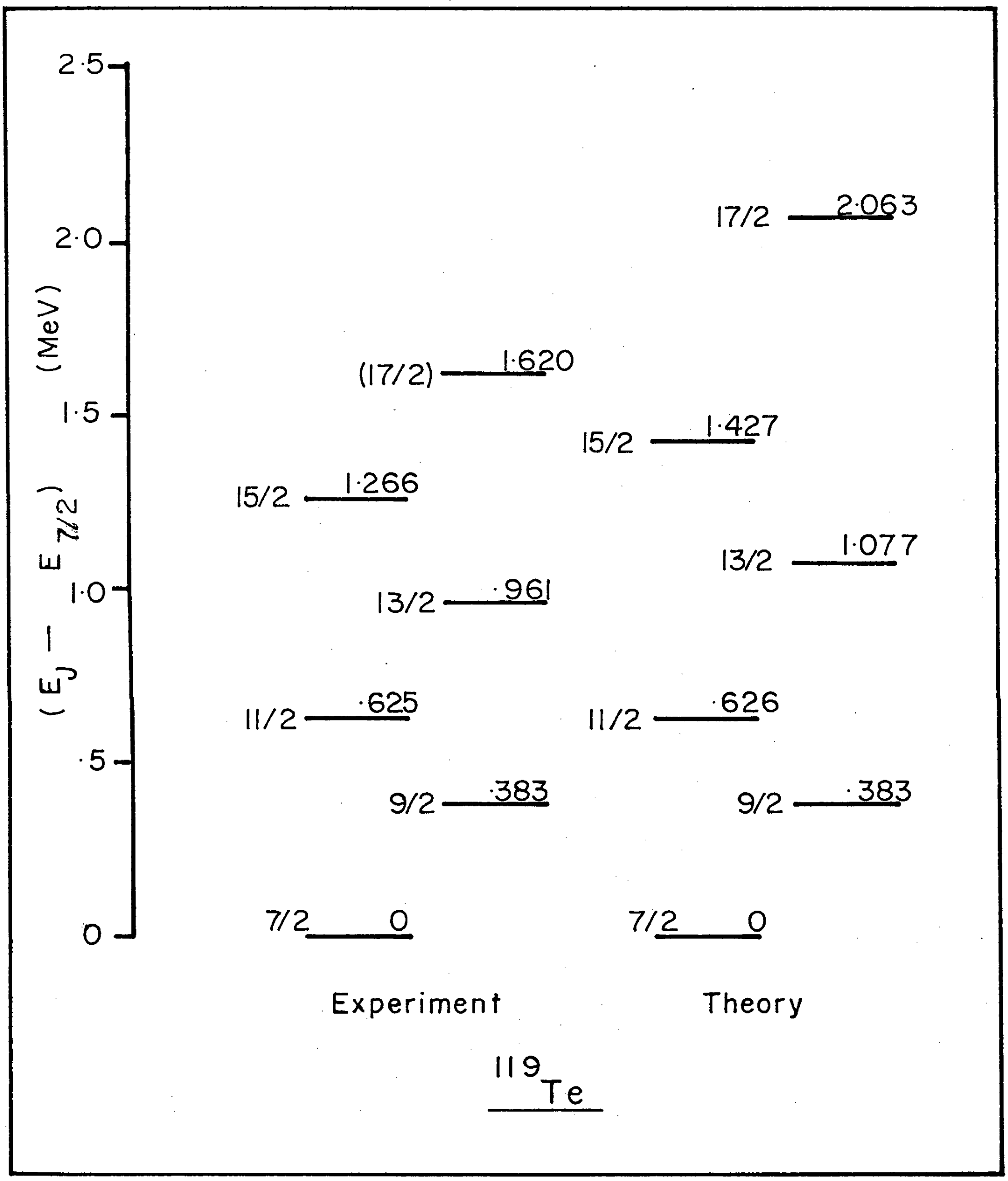

Fig. 4.20: Experimental and theoretically produced energy levels of the $7/2^+$ band in ^{119}Te. Calculations are described in the text.

those obtained for the negative parity states. This is a consequence largely of the increased deformation providing a base for stronger coupling of the neutron hole, which, in turn, is less likely to alter the shape of the core (any more). The fit could, again, be improved by the introduction of a Variable Moment-of-Inertia.

It is interesting to note the ratio of the energies of the levels of spin $I = {}^{15}\!/_{1}$ and ${}^{13}\!/_{2}$. This ratio is given by

$$R_{th} = \frac{E_{15/2^+}}{E_{13/2^+}} = 1.32 \tag{36a}$$

and

$$R_{exp} = 1.32 \,. \tag{36b}$$

Such agreement is probably fortuitous, but it is an indication that the rotational content of the core is probably similar to the calculated content, even though the shape of the core is different. A more sensitive measure of the "squeezing" of these levels is the ratio

$$S_{th} = \frac{(E_{13/2^+} - E_{11/2^+})}{(E_{15/2^+} - E_{13/2^+})} = 1.29 \,, \tag{37a}$$

where

$$S_{exp} = 1.10 \,. \tag{37b}$$

This ratio varies rapidly with FER and the experimental value (Eqn (37b)) can be reproduced if a value of FER = .37 is used. The fitted solution is then not self-consistent, but the slight difference — between this value and the fitted value for FER (Eqn (35)) — is possibly indicative of only a slight amount of mixing occurring in the single particle states.

The wavefunctions of the Yrast states, for which the $\left(C^{Ij}_{\underset{\sim}{K\Omega}}\right)^2$ values are given in Table 4.3.10, are much less mixed than in the negative parity cases. All the states show almost complete alignment of the neutron hole's spin with the $\hat{2}$ axis, and the admixture of $\Omega = {}^1\!/_2$ or ${}^3\!/_2$ states is very small. This is consistent with the initial assumptions. A detailed breakup of the components of the wavefunctions show that the observed band has almost equal contributions from a ($\underset{\sim}{K} = {}^7\!/_2$, $\underset{\sim}{\Omega} = {}^7\!/_2$) normal rotational band, and a rotational band

Table 4.3.10

Calculated Wavefunctions of the Yrast Levels in the $g_{7/2}$ Band of ^{119}Te

Wavefunction for $J = 7/2$, $E = 0.0$ MeV State

K \ Ω	7/2	3/2	1/2	5/2
7/2	.896	.010		
3/2	.006	.005	.001	
1/2		.001	.001	.002
5/2			.004	.074

Wavefunction for $J = 7/2$, $E = .382$ MeV State

K \ Ω	7/2	3/2	1/2	5/2
7/2	.817	.005		
3/2	.018	.012	.001	
1/2			.001	.004
5/2			.006	.004
9/2				.003

Wavefunction for $J = 1/2$, $E = .626$ MeV State

K \ Ω	7/2	3/2	1/2	5/2
11/2	.447	.003		
7/2	.334	.008		
3/2	.018	.020	.004	
1/2		.005	.009	.013
5/2			.007	.103
9/2			.001	.028

Wavefunction for J = $^{13}/_{2}$, E = 1.077 MeV State

$K \backslash \Omega$	$^{7}/_{2}$	$^{3}/_{2}$	$^{1}/_{2}$	$^{5}/_{2}$
$^{11}/_{2}$	.410	.002		
$^{7}/_{2}$	.350	.011		
$^{3}/_{2}$	.025	.017	.001	
$^{1}/_{2}$		.001	.001	.010
$^{5}/_{2}$			.006	.113
$^{9}/_{2}$			.001	.050
$^{13}/_{2}$				

Wavefunction for J = $^{15}/_{2}$, E = 1.427 MeV State

$K \backslash \Omega$	$^{7}/_{2}$	$^{3}/_{2}$	$^{1}/_{2}$	$^{5}/_{2}$
$^{15}/_{2}$	.008			
$^{11}/_{2}$	.236	.001		
$^{7}/_{2}$	.267	.020	.001	
$^{3}/_{2}$	.035	.058	.015	.002
$^{1}/_{2}$	.001	.021	.036	.042
$^{5}/_{2}$		.001	.018	.172
$^{9}/_{2}$			.002	.064
$^{13}/_{2}$				

Wavefunction for J = $^{17}/_{2}$, E = 2.063 MeV State

$K \backslash \Omega$	$^{7}/_{2}$	$^{3}/_{2}$	$^{1}/_{2}$	$^{5}/_{2}$
$^{15}/_{2}$	.027			
$^{11}/_{2}$	.314	.002		
$^{7}/_{2}$	.300	.018		
$^{3}/_{2}$	.044	.027		.001
$^{1}/_{2}$	.001	.003	.002	.026
$^{5}/_{2}$			.007	.143
$^{9}/_{2}$			.002	.083
$^{13}/_{2}$				.001
$^{17}/_{2}$				

built on the ($\underset{\sim}{K} = {}^{11}/_2$, $\underset{\sim}{\Omega} = {}^7/_2$) gamma band head. The only other component to appreciably add to the wavefunction is that of a normal rotational band built on the ($\underset{\sim}{K} = {}^5/_2$, $\underset{\sim}{\Omega} = {}^5/_2$) state.

The calculated transition probabilities and mixing ratios for transitions between the Yrast levels are given in Tables 4.3.11 and 4.3.12. The branching ratios of the levels of spin $I \geqslant {}^{11}/_2$, determined from Table 4.3.11, are given in Fig. 4.21, which clearly shows the reproduction, by the theory, of the experimental trends. The agreement, not unexpectedly, is worse for the higher spin states. The calculation *is*, in this case, able to reproduce the observed sign of δ, and also gives excellent agreement with the magnitude of the mixing ratio as determined by [Ha79b].

Table 4.3.11

Transition Probabilities for Transitions between Yrast States in the $g_{7/2}$ Band of ^{119}Te

Transition	Transition Probability (ps^{-1})
$^9/_2 \rightarrow {}^7/_2$	$.75 \times 10^{-1}$
$^{11}/_2 \rightarrow {}^7/_2$	.17
$^{11}/_2 \rightarrow {}^9/_2$	$.11 \times 10^{-1}$
$^{13}/_2 \rightarrow {}^9/_2$	.35
$^{13}/_2 \rightarrow {}^{11}/_2$	.11
$^{15}/_2 \rightarrow {}^{11}/_2$	.82
$^{15}/_2 \rightarrow {}^{13}/_2$	$.64 \times 10^{-1}$
$^{17}/_2 \rightarrow {}^{13}/_2$	3.0
$^{17}/_2 \rightarrow {}^{15}/_2$	.35

Transitions are between states whose wavefunctions are tabulated in Table 4.3.10.

The calculated electric quadrupole and magnetic moments, of the Yrast states, are given in Table 4.3.13. None of these have as yet been measured in ^{119}Te, but we can compare the magnetic moment of the $^7/_2{}^+$ level in ^{119}Te with that of a similar level in ^{121}Te. In ^{121}Te, there is a band built on the $^7/_2{}^+$ state, which appears very similar in character to the band in ^{119}Te [Ha79b]. The magnetic moment of the $^7/_2{}^+$

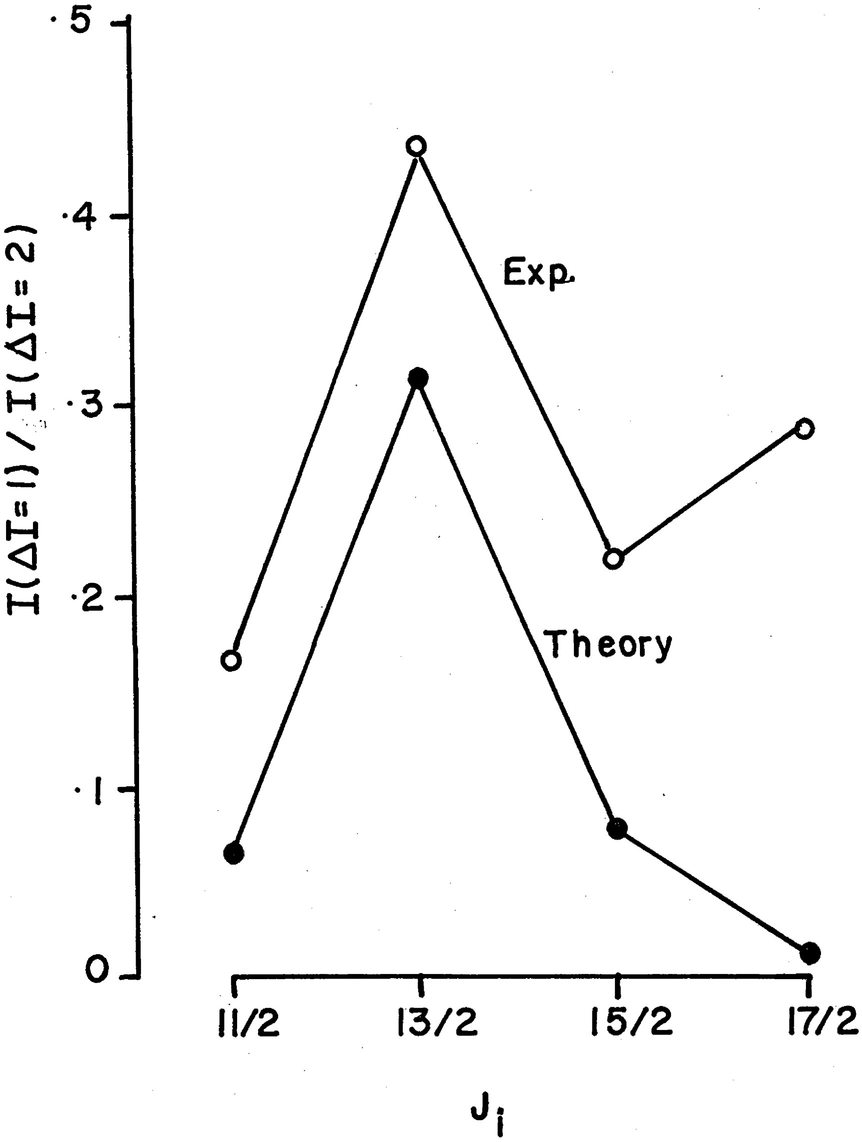

Fig. 4.21: Experimental and theoretical branching ratios in the $^7/_2{}^+$ band of ^{119}Te.

Table 4.3.12

Calculated Mixing Ratios of $\Delta J = 1$ Transitions in the $g_{7/2}$ Band of ^{119}Te

Transition	δ
$9/2 \rightarrow 7/2$	-.245
$11/2 \rightarrow 9/2$	-.051
$13/2 \rightarrow 11/2$	-.254
$15/2 \rightarrow 13/2$	-.116
$17/2 \rightarrow 15/2$	-.375

Table 4.3.13

Calculated Electric Quadrupole and Magnetic Dipole Moments for Yrast States of the $g_{7/2}$ Band in ^{119}Te

J	Q_2 (eb)	μ(nm)
$7/2$	1.311	.991
$9/2$	.478	1.487
$11/2$	1.019	1.879
$13/2$	.580	2.363
$15/2$	.143	2.776
$17/2$	.157	3.274

band head in ^{121}Te has been measured [Io80] as,

$$\mu_{121} = +.738\ (\pm.010)\ \text{nm}$$

which is similar to the value calculated for the bandhead in ^{119}Te (Table 4.3.13).

It has been demonstrated here that the triaxial rotor plus particle model could be used successfully in the interpretation of positive parity levels in ^{119}Te. In ^{117}Te, however, there is little information that can be utilised.

The large energy spacings of the quadrupole transitions, together with the absence of any dipole transitions, suggest a small β

deformation of the core. The coupling of a $g_{7/2}$ neutron hole to such a core would be weak and would indicate that the observed pattern of levels comprises part of a decoupled band.

Having 65 neutrons, the Fermi level in ^{117}Te would be lower than in ^{119}Te. This implies a larger value for the parameter FER, but such a tendency is offset, to some degree, by a decrease in deformation. The other parameter, γ, is as difficult to determine. On the strength of the fitted values found for γ in the other bands in ^{117}Te and ^{119}Te, it is not unreasonable to expect a large value for the parameter, i.e. $\gamma \approx 30°$.

Although no fitting procedure could be meaningfully attempted, a check was made to show the consistency of the triaxial rotor plus particle model with the above discussions. The level scheme was calculated for a $g_{7/2}$ neutron hole, using the parameters $\gamma = 30°$ and FER = .4. It was found that when the $11/2^+$ level was fitted, the deformation of the core was $\beta \approx .187$.

The $9/2^+$ level was then predicted as having a similar energy to the $11/2^+$ level, which would make the transitions between these levels much harder to observe. If γ is kept constant and FER is allowed to vary between the limits $0 \leqslant \text{FER} < .6$, this pattern is repeatedly found; the β deformation varying only slowly within the limits $.18 \leqslant \beta \leqslant .19$.

For this range of β and $\gamma = 30°$, a value of FER $\approx .4$ is found by interpolation of the Nilsson model. This is consistent with the above observations.

Variation of the asymmetry parameter may significantly alter the situation as the energies of both the $11/2^+$ and $9/2^+$ levels are strongly dependent on the value of γ. In all of the above cases, a slightly prolate nucleus would lower the $9/2^+$ level relative to the $11/2^+$ level, and in a slightly oblate nucleus, the $9/2^+$ level would rise above the $11/2^+$ level. This argument highlights the uncertainty in the shape of the mass 116 core, the best estimate being $\beta < .2$ and $\gamma \approx 30°$.

4.3.6 Discussion

In the previous sections, the shapes of the nuclei ^{117,119}Te were determined as a function of the orbital in which the odd neutron resided. This information is summarised in Table 4.3.14, where the corresponding parameters for the (A-1) even Tellurium nuclei are also given (from Table 4.3.3).

Table 4.3.14

Parameters of the Core of the Tellurium Nuclei

	116	117,$h_{11/2}$*	117,$g_{7/2}$*	118	119,$h_{11/2}$*	119,$g_{7/2}$*
$\hbar^2/2\mathcal{I}_0$	75	73	n.a.	67	74	38
β	$\sim .17$	.167	$< .2$	$\sim .17$	.164	.238
γ	$\sim 30°$	28.7°	$\sim 30°$	$\sim 30°$	31.5°	24.4°

* The orbital occupied by the odd particle.

It is obvious from this table, that the addition of a neutron to an $h_{11/2}$ orbital does not greatly affect the shape of the even mass core, at least for small amounts of core rotation. The only parameter which does change significantly is the Fermi level. The rise in Fermi level and the slight increase in the moment-of-inertia ($\mathcal{I}_0$) from ^{117}Te to ^{119}Te are together responsible for the majority of the differences in the nuclei's negative parity level schemes.

In contrast, when the odd neutron occupies the $g_{7/2}$ orbital, the shape of the core is significantly altered. The β deformation increases and there is a sharp rise in the value of $\mathcal{I}_0$. This, together with the Fermi level lying near the top of the j-shell produces the observed strong coupling spectrum of ^{119}Te. The effects are not as marked in ^{117}Te, which reflects the increase in the resistance to deformity of the ^{116}Te over that of the ^{118}Te core.

It was mentioned earlier that the inclusion of a Variable Moment-of-Inertia would considerably improve the fit of the higher spin levels, but this would be at the cost of including many extra variables, including β and γ values for every rotational state of the core. Calculations with so many variables become quite unwieldy, and so one is forced to make some other simplifying assumptions.

Other approaches which may also reproduce the observed level schemes include the consideration of the β and γ deformations as dynamic variables. The γ-unstable potential model of Wilets and Jean [Wi56] has been shown [Br69] to have the capability of reproducing spectra similar to those of the odd Tellurium nuclei.

The consideration of hexadecapole deformations may be particularly pertinent, especially for the heavier Tellurium nuclei. When attempts were made to extend the present set of calculations (which assume quadrupole deformations only) to the heavier Tellurium nuclei, difficulties in obtaining a consistent (as defined earlier) solution were found. After further investigation, it was noted that these arose partly from the nearness in energy of the $^{15}/_{2}^{-}$ and $^{13}/_{2}^{-}$ levels, but were mostly due to the ordering of these two levels. As discussed in [Br69], the introduction of hexadecapole deformation is capable of reversing this order, which may then allow consistent solutions to be found.

The addition of these extra degrees of freedom reinforces the notion of a soft core. To reach an understanding of the interplay of the above effects requires theories more complex than that mentioned here, yet they must still be manageable. One such theory, the interacting boson-fermion model, is at present being investigated in this region [Mo80]. This theory, with the use of only several parameters, is able to incorporate implicitly extra effects such as the two proton particle excitations observed in the even mass Tellurium nuclei.

The effect of particle excitations has been ignored in the triaxial rotor plus particle model. This is a reasonable assumption only if the odd neutron is decoupled from the core. Then, the core effectively ignores the presence of the extra particle and should behave in a fashion similar to the (N-1) nucleus.

For the higher spin states, multi-quasiparticle components of the wavefunction will increase in importance and these will be discussed in the next chapter.

CHAPTER 5

MULTIPLE-QUASIPARTICLE STATES

5.1 INTRODUCTION

As illustrated in Chapter 4, the influence of multiple quasiparticle states becomes evident at very low spins as a result of the high rotational frequencies of the collective motion of the cores. The successful competition of quasiparticle excitation over the core excitations is expected to increase as the spin and excitation energy of the levels are increased, so it is important to examine these effects.

As also illustrated in Chapter 4, the deformation of a Tellurium nucleus is sensitive to the orbitals occupied by the unpaired particles. Without a proper knowledge of the core's shape, the energies of the quasiparticles cannot be meaningfully estimated. However, the combined energy of any one "set" of quasiparticles is not expected to change rapidly as the nuclear mass changes, so much information is often obtained from a study of the energy systematics of levels of various spin. In this region of soft, transitional nuclei, the four Tellurium nuclei presently studied are the *only* examples where discrete states of spin greater than $I = {}^{27}\!/_{2}$ have been reported. Any discussion of energy systematics is therefore limited in scope and the following discussion relies on the summation of energy systematics of various "low" ($I \leqslant 10$) spin states.

Here we will limit the discussion, for neutron quasiparticle excitation, to the orbitals $3s_{1/2}$, $2d_{3/2}$, $2d_{5/2}$, $1g_{7/2}$, and $1h_{11/2}$, giving maximum spins of 10^+, ${}^{27}\!/_{2}$ (+ or −), 17^-, and ${}^{39}\!/_{2}{}^-$ for the situations where two, three, four or five quasiparticles are excited, respectively. Although this range is also available for proton excitations, the following discussion will generally be limited to the

$1g_{7/2}$ and $2d_{5/2}$ orbitals, which can couple to produce a maximum spin of $I^{\pi} = 6^{+}$.

The assignment of quasiparticle configurations to a particular state depends, not only on the level's spin, parity and excitation, but also on the decay modes of the nucleus, i.e. how the state interacts with others. In the following, the states are discussed according to increasing quasiparticle number. As a result, some of the tentative assignments may appear, initially, to be based on weak arguments. It is the overall level scheme and observed modes of decay which ties the arguments together.

5.2 REVIEW OF SYSTEMATIC TRENDS

5.2.1 States Produced by Proton Excitations

The energy systematics of some of the low-lying states of the odd mass Antimony nuclei are presented in Fig. 5.1. The states presented are those which have been interpreted [Sh79], [Va71], [Se70] as being mostly single proton states (although the $9/2^{+}$ state is best interpreted as a 2p - 1h state. If we take these energies as a guide to the proton quasiparticle energies in the Tellurium nuclei, then we could expect that configurations involving the $2d_{5/2}$ and $1g_{7/2}$ orbitals would be most energetically favourable. Configurations involving either of the other two orbitals would lie at much higher energies. This is consistent with the results of Lopac's calculations [Lo70] (and see Chapter 4) which show that the 6^{+} state of the even Tellurium nuclei is dominated by the two proton configurations $(\pi g^{2}_{7/2})$ and $\pi(g_{7/2}, 2d_{5/2})$.

States involving these proton configurations in their wave-function could also be expected to rise in energy as the nuclear mass decreases from 119. Indeed, the energy of the 6^{+} state rises, from ^{118}Te to ^{116}Te, by an amount that is approximately equal to the difference between the $7/2^{+}$ level energy in ^{117}Sb and ^{115}Sb.

5.2.2 States Produced by Neutron Excitations

Most noticeable of this category are the states of spin 5^{-} and 7^{-}

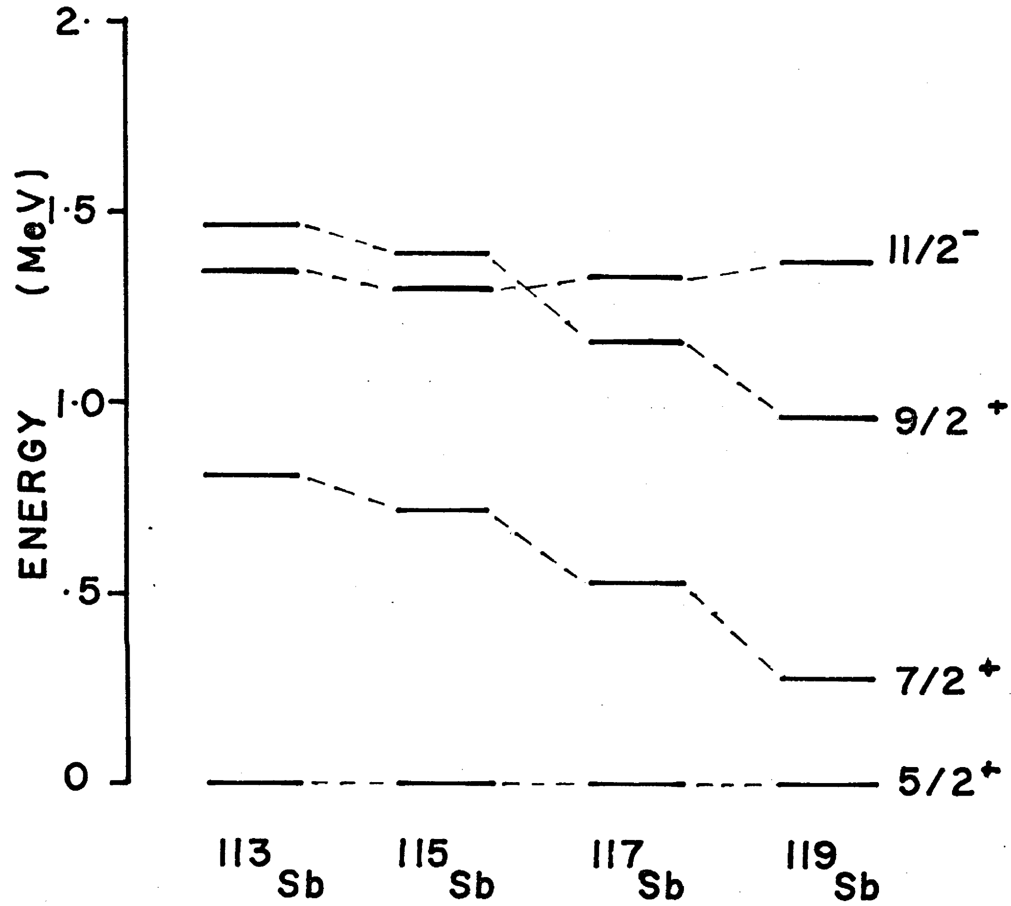

Fig. 5.1: Low energy proton quasiparticle states in $^{113}Sb - ^{119}Sb$.

found in the even Tellurium nuclei. Dzhelepov [Dz69] has pointed out the non-collective nature of these states and so they must involve the excitation of a particle to the $h_{11/2}$ neutron subshell, this being the only orbital at low enough excitation energy having negative parity. Neutron configurations which can give these spins are $\nu(h_{11/2}, 2d_{3/2})$ for $I^{\pi} = 7^-$ and 5^- and $\nu(h_{11/2}, 3s_{1/2})$ for the $I^{\pi} = 5^-$ state only. Both of these states decrease in energy as the mass increases (see Fig. 5.2), such behaviour being consistent with the assumed configurations.

States of similar spin are also observed in the even Tin nuclei where they often exhibit isomerism. They have been interpreted in a manner similar to the above, and so provide support for the two neutron interpretation. In addition, the g factor measurements of [Bo72] and [Is79] indicate very pure two quasineutron states for these levels in the Tin nuclei. This is supported by the theoretical work of Arvieu [Ar63], who estimates the contributions to the wavefunctions as, for example,

$$|^{114}\mathrm{Sn}, 7^-\rangle = .9949|\nu|h_{11/2}, \nu 2d_{3/2}\rangle + \ldots$$

and

$$|^{118}\mathrm{Sn}, 7^-\rangle = .9999|\nu|h_{11/2}, \nu 2d_{3/2}\rangle + \ldots .$$

Also observed in some of the even Tin nuclei are isomeric states of spin $I^{\pi} = 10^+$. These have been interpreted [Is79] as being of $(\nu h^2_{11/2})$ configuration, this being the only configuration capable of reproducing both spin and parity in the correct energy range. Similar 10^+ states have been identified in the Tellurium nuclei, but have not been identified as uniquely $(\nu 1h^2_{11/2})$ configurations.

The energy of these states vary with nuclear mass in a manner that is similar to the energy variation of the 7^- state. Now the systematics of the 7^- states depend on two different orbitals — the $1h_{11/2}$ and the $2d_{3/2}$. If the 10^+ states were of $\nu(1h^2_{11/2})$ configuration, the systematics would depend on only the one orbital. They would have the one particle in common, so the difference between the energies of the 10^+ and 7^- states should reflect the energy differences between the other two orbits. We have already seen that particles in the $1h_{11/2}$ orbital lie at approximately the same energy as those in the $2d_{3/2}$ orbital (Chapter 4). The similar trends of the 7^- and 10^+ states are therefore consistent with the assumption of a

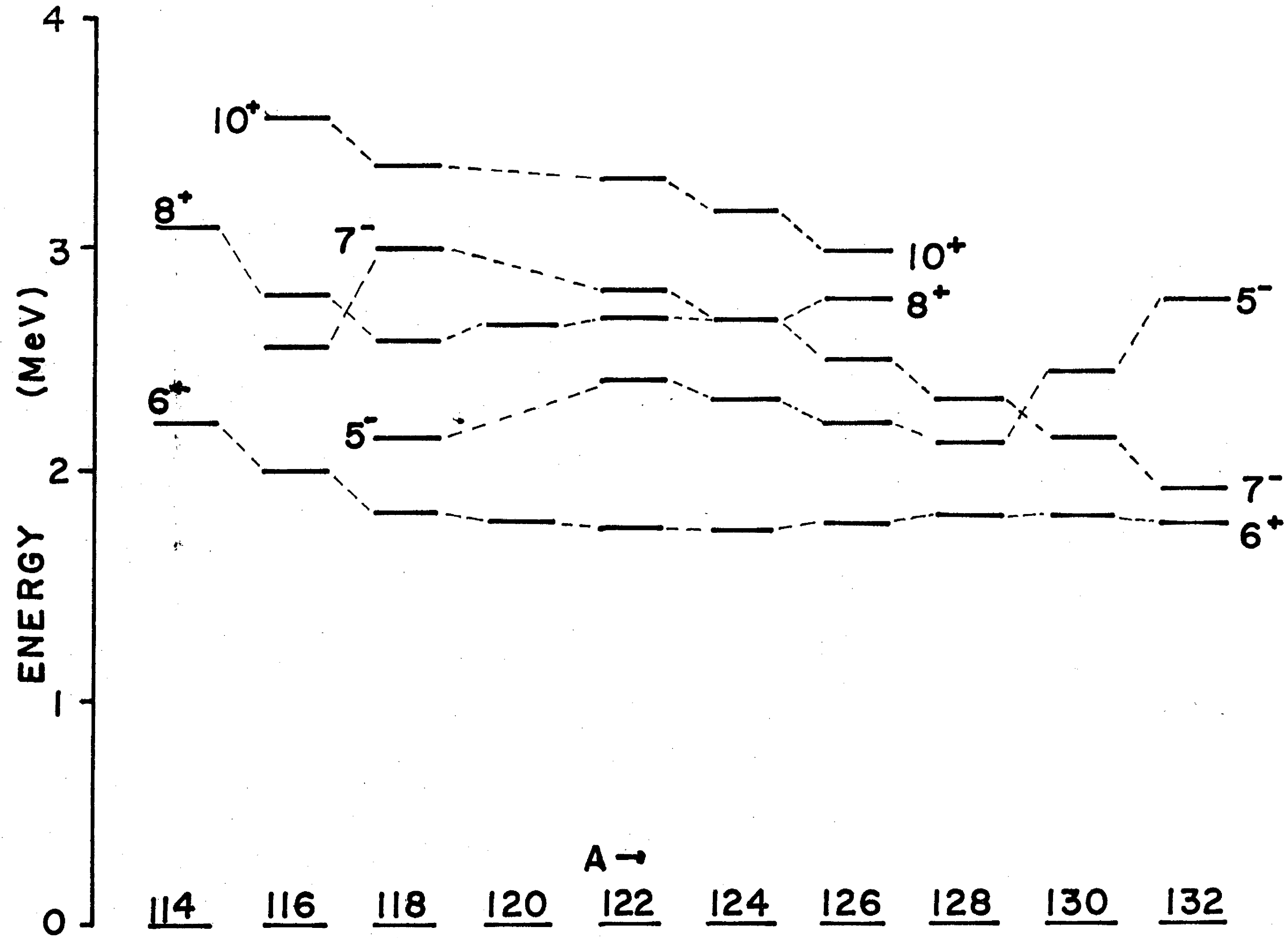

Fig. 5.2: Systematics of states of spin I = 5, 7, and 10 in the even Tellurium nuclei.

$\nu 1h^2_{11/2}$ configuration for the 10^+ states.

5.2.3 States Involving Proton-Neutron Excitations

Evidence of a single proton plus single neutron quasiparticle excitations are found in the neighbouring odd-odd Antimony nuclei. Of the levels observed in the nuclei of mass $A \leqslant 118$, the most striking examples are the ground states ($I^\pi = 3^+$) and the 8^- isomeric states. It has been shown [e.g. [Ka76]) that the ground state wavefunction consists of a rather pure ($\pi 2d_{5/2}$, $\nu 3s_{1/2}$) component, while that of the isomeric states contain rather pure ($\pi 2d_{5/2}$, $\nu 1h_{11/2}$) components. As the Antimony mass is increased, the excitation energy of the 8^- level drops, reflecting the increasing penetration of the $h_{11/2}$ neutron shell which is occurring.

The systematic behaviour of these states aids in the determination of the relative positions of any two proton, one-neutron quasiparticle states in the odd Tellurium nuclei.

Also, one proton, two neutron quasiparticle states have been identified in several of the odd mass Antimony nuclei (e.g. [Sh79], [Fa79]). Of these, the most definite are the isomeric levels of $I^\pi = 19/2^-$ in ^{115}Sb, $25/2^+$ in ^{117}Sb, and $27/2^+$ in ^{119}Sb. The state in ^{115}Sb has been identified as a $2d_{5/2}$ proton coupled to the 7^-, ^{114}Sn core excitation. The other two states are identified as having a $2d_{5/2}$ or $1g_{7/2}$ proton, respectively, coupled to the 10^+ excitations of the Tin cores. These assignments are consistent with the systematic behaviour of both the core and single proton excitation energies.

5.3 MULTIPLE QUASIPARTICLE EXCITATIONS IN $^{116-119}$Te

5.3.1 Two Quasiparticle Excitations (^{116,118}Te)

The extension of the energy systematics of the 6^+ states to ^{116,118}Te (see Fig. 5.2) shows a smooth behaviour indicating little change in their structure. This behaviour, combined with the observations of §5.2 supports the proposed two quasiproton configuration. The large backbend observed in the plot of Fig. 4.10, which indicates small collective contribution, also supports the quasiparticle interpretation. However, the quite high excitation which is reached in ^{116}Te ($E_{6^+} = 2002$ keV) makes possible the inclusion of less favoured two quasiparticle states in the wavefunction. Any such "contamination" of the wavefunction would most likely be due to the $\nu(1g_{7/2}, 2d_{5/2})$ or $\nu(1g^2_{7/2})$ configurations.

Apart from these states, all other two quasiparticle states of sufficiently high spin and sufficiently low energy to be observed, must include at least one unpaired neutron in the $h_{11/2}$ shell. These include the 5^-, 7^- and 10^+ states as previously described.

There is also no evidence available to support the existence, in the heavier Tellurium nuclei, of two quasiproton states involving the $1g_{9/2}$ or $1h_{11/2}$ orbitals.

In Chapter 3, it was established that the 2150 keV and 2999 keV states in ^{118}Te had spins of $I = 5$ and 7 respectively. In ^{116}Te, two possible candidates for an $I = 7$ state were observed. They are the $I = (6,7)$ state at 2339 keV, and the $I = (7,8)$ state at 3027 keV. No state of $J = 5$ was observed in ^{116}Te.

If one assumes that the 3072 keV state in ^{116}Te has spin $I = 7$, then this and the 2999 keV state in ^{118}Te form a continuation of the smooth curve of the 7^- states as shown in Fig. 5.2. It is therefore plausible to assume that these states in ^{116}Te and ^{118}Te have the same parity and structure as have the $I = 7$ states in the heavier Tellurium nuclei, i.e. $I^\pi = 7^-$, $\nu(1h_{11/2}, 2d_{3/2})$.

This is supported by the following observation. For a spin of $I = 7$ to be formed by two quasiparticles, one of the particles must be either a neutron or proton in the $1h_{11/2}$ orbital, or a proton in the $1g_{9/2}$ orbital. As there is no evidence for such states in the heavier Tellurium nuclei, it is plausible that these possibilities may be ignored.

By analogy, the 2150 keV level in ^{118}Te can be tentatively associated with the levels of $I^\pi = 5^-$ in the heavier nuclei. The association is weaker than the above for the systematic trend of the states, with mass, is not extended as smoothly (see Fig. 5.2).

The level at 3455 keV excitation in ^{118}Te was shown to have spin $I = 9$ (see Chapter 3). Once again, a $1h_{11/2}$ neutron is probably involved in the wavefunction. This infers either a $\nu(1h^2_{11/2})$, 9^+, or a $\nu(1h_{11/2},1g_{7/2})$, 9^- state. If the arguments concerning the 2999 keV, $I = 7$ state are upheld, then the possible decay modes of the 3445 keV level are:

(a) If $I^\pi = 9^+$:— via an 447 keV M2 transition to the 2999 keV level and via an 871 keV M1/E2 transition to the 2574 keV level;

(b) If $I^\pi = 9^-$:— via an 447 keV E2 transition to the 2999 keV level and via an 871 keV E1/M2 transition to the 2574 keV level.

Using single particle estimates from Chapter 2, the branching ratios, for both the above cases are of the order,

$$\frac{T_{sp}(447)}{T_{sp}(871)} \approx 0\left\{\frac{(.447)^5}{(.871)^3} \times \frac{1}{197^2}\right\}$$

$$\approx 0[10^{-6}] \ .$$

As suggested in Chapter 2, E2 transitions are likely to be enhanced, relative to the single particle estimate, while M2 transitions are commonly hindered. As the 447 keV transition *is* observed, the probability of it being of E2 nature must be higher than that of it being an M2 transition.

It is therefore suggested that negative parity and configuration $\nu(1h_{11/2},1g_{7/2})$ are associated with the 3445 keV state.

The 10^+ level observed in both ^{116}Te and ^{118}Te smoothly extend (see Fig. 5.2) the systematics of the 10^+ levels in the heavier Tellurium nuclei. If the previous arguments (§5.3.1) are valid, it is then likely that the configuration $\nu(1h^2_{11/2})$ is a dominant component of the wavefunction of these states.

5.3.2 Three Quasiparticle States in ^{117,119}Te

There are only a few basic combinations of quasiparticles which control the complexity of the observed level schemes. These are: a neutron (most likely of the $h_{11/2}$ shell) coupled to two protons, and the combination of three neutrons producing either odd parity states (odd number of $h_{11/2}$ neutrons) or even parity states (even number of $h_{11/2}$ neutrons).

Levels of the configuration $(\nu h_{11/2}, \pi g^2_{7/2})$ or $(\nu h_{11/2}, \pi 1g_{7/2}, \pi 2d_{5/2})$ are more likely to be observed in ^{119}Te than in ^{117}Te.

This is because the proton configurations (here represented by the 6^+ states) are lower in energy in ^{118}Te than in ^{116}Te. Also, the energy of the $h_{11/2}$ neutron, relative to the other single quasineutron states is generally lower in ^{119}Te than in ^{117}Te.

For the purposes of this discussion we will tentatively identify the 3138 keV level of ^{117}Te and the 2369 keV level of ^{119}Te respectively as being comprised mostly of these configurations — both levels have $I = {}^{23}/_2$ (the maximum for the configurations) while the level of ^{119}Te also has been shown to have negative parity. Further reasons for this identification will become obvious, as the discussion proceeds.

Of the three-neutron configurations, it is informative to note the combinations possible when an extra neutron is coupled to the 10^+ core state. These, summarised in Table 5.3.1, can also be interpreted as the coupling as shown in the third column of the table. The right hand side of the coupling equation approximately represents levels (of that spin) of the (A-1) nucleus.

Table 5.3.1

Couplings of Three Quasineutrons

Coupling (One)	Spin I^π	Coupling (Two)	Configuration
$h_{11/2} \otimes 10^+$	${}^{27}/_2{}^-$	$h_{11/2} \otimes 10^+$	$\nu(h^3_{11/2})$
$g_{7/2} \otimes 10^+$	${}^{27}/_2{}^+$	$h_{11/2} \otimes 9^-$	$\nu(h^2_{11/2}, g_{7/2})$
$d_{5/2} \otimes 10^+$	${}^{25}/_2{}^+$	$h_{11/2} \otimes 8^-$	$\nu(h^2_{11/2}, d_{5/2})$
$d_{3/2} \otimes 10^+$	${}^{23}/_2{}^+$	$h_{11/2} \otimes 7^-$	$\nu(h^2_{11/2}, d_{3/2})$
$s_{1/2} \otimes 10^+$	${}^{21}/_2{}^+$	$h_{11/2} \otimes 5^-$	$\nu(h^2_{11/2}, s_{1/2})$

In ^{119}Te, the first four of these configurations can be tentatively identified with the levels at (3088 + x) (${}^{27}/_2{}^-$), (3544 + x) (${}^{27}/_2{}^+$), (3122 + x) (${}^{25}/_2{}^+$), and (2921 + x) (${}^{23}/_2{}^-$) keV excitation as these show relative excitations similar to those of the single quasiparticle states at lower excitation (i.e. with $I^{\pi} = {}^{11}/_{2}^{-}$, ${}^{7}/_{2}^{+}$; ${}^{5}/_{2}^{+}$ and ${}^{3}/_{2}^{+}$). This would imply negative parity for the 2421 +x keV level.

The pattern is similar in ^{117}Te for there, the ${}^{25}/_{2}^{+}$, 3327 keV level, the most strongly populated of these four 3qp levels, is lowest in energy, as is the ${}^{5}/_{2}^{+}$ level of the four 1qp levels. Following this analogy the ${}^{27}/_{2}$ level at 3639 keV excitation would consist, mostly, of the $\nu(h^2_{11/2}, g_{7/2})$ configuration. It is not certain whether the negative parity state of $\nu(h^3_{11/2})$ has been observed as the parity of the levels is unknown. Also, just as the ${}^{3}/_{2}^{+}$ level was not observed in ^{117}Te (due to its (presumed) too high excitation for observation following a (HI,xn) reaction) the 3qp coupling ($d_{3/2} \otimes 10^+$) was not observed, probably for similar reasons.

Next, consider the 2620 keV, $I = {}^{21}/_{2}$ level in ^{117}Te. To obtain this spin through a coupling of three quasiparticles, one must have at least one neutron occupying the $1h_{11/2}$ shell, giving as most likely combinations $\nu(1h^2_{11/2}, s_{1/2})$ and $\nu(h_{11/2}, d_{3/2}, g_{7/2})$ — where only the maximum spin of the coupling is considered. Other combinations are of course possible. Neutron configurations only are considered for reasons outlined in §5.2.1.

Looking at ^{119}Te, we find that the only observed state of $I = {}^{21}/_{2}$ is at (1841 +x) keV excitation and has negative parity.

Previously (Chapter 4) this level was treated as being part of the level scheme created by a particle coupled to a rotating triaxial core. The calculations, though, grossly overestimated the energy of the state, and could not reproduce its position relative to the (2012 +x) keV, ${}^{23}/_{2}^{-}$ state. This inaccuracy may be partially explained if the state has some 3qp component.

Assuming for the moment that this state has a similar 3qp structure to that of the 2620 keV level of ^{117}Te, one must conclude that because of the parity, the latter of the above configurations applies, i.e. $\nu(h_{11/2}, d_{3/2}, g_{7/2})$. Such a conclusion is supported by the rapid lowering, relative to the other 1qn orbitals of the $d_{3/2}$ state from ^{117}Te to ^{119}Te. (As evidenced by the observation of the ${}^{3}/_{2}^{+}$ and ${}^{23}/_{2}^{+}$ states in ^{119}Te.) It is also strongly supported by the observed decay paths. In neither nuclei was a transition observed which directly connected the $^{25}/_{2}{}^{(+)}$, (3122 + x) keV (of proposed $\nu(h^2_{11/2}, 2d_{5/2})$) state the $^{21}/_{2}$ state in question, yet most of the population of the $^{23}/_{2}$, (2921 + x) keV (proposed $\nu(h^2_{11/2}, d_{3/2})$) state in ^{119}Te decays to the $^{21}/_{2}{}^{-}$ (1841 + x) keV state. This could be expected if the states involved rather pure three quasiparticle configurations as one expects that transitions involving the change of orbital of only one particle are more likely to proceed than if two particles had to change orbitals.

Using this argument one could expect to observe a transition in ^{117}Te, connecting the $^{25}/_{2}$, 3327 keV state to the $^{21}/_{2}$, 2620 keV state if the lower state had positive parity (i.e. $\nu(h^2_{11/2}, 2d_{5/2}) \Rightarrow \nu(h^2_{11/2}, 3s_{1/2})$. Such a transition was not observed. Hence, on the basis of these arguments, we propose that the $^{21}/_{2}$, 2620 keV level in ^{117}Te should be identified with the $\nu(h_{11/2}, 2d_{3/2}, 1g_{7/2})$ configuration.

Other supporting evidence, though less distinct, arises from the fact that some of the population of the level decays to the band built on the $^{7}/_{2}{}^{+}$ level, indicating at least some $1g_{7/2}$ neutron component in the wavefunction.

The possibility of some $\nu(1h_{11/2}, 1g_{7/2}, 2d_{5/2})$ component in the least excited $^{23}/_{2}{}^{-}$ level of both nuclei (i.e. 2315 keV in ^{117}Te and 2012 + x keV in ^{119}Te) is thereby indicated by analogy. In general, then, it is seen that the major decay paths between the three quasiparticle states in either nucleus are consistent with the argument that only one particle changes orbitals at any one time, and that *that* particle changes from a higher to a lower excited orbital as determined from the low spin one quasiparticle states.

5.3.3 Four Quasiparticle States in ^{116,118}Te

There is only a little indication of the presence of "pure" 4qp states in ^{116}Te. It consists of the "lowering" in energy of the I = (16), 5621 keV state. This occurs because the transition which connects this state to the I = (14), 5110 keV state, (of 511 keV), is much lower in energy than any other transition which is part of the cascade to the ground state. Such behaviour in fact appears to be merely a magnification of an effect seen at lower spin. By splitting

Table 5.3.2

Pattern Formed by High and Low Spin Cascades in ^{116}Te

Transition	Energy (keV)		Approximate Behaviour		Energy (keV)	Transition
$2^+ \to 0^+$	679	$\to$	$\sim x$	$\leftarrow$	770	$(12) \to 10^+$
$4^+ \to 2^+$	681	$\to$	$\sim x$	$\leftarrow$	765	$(14) \to (12)$
$6^+ \to 4^+$	643	$\to$	$< x$	$\leftarrow$	511	$(16) \to (14)$

the ($\Delta I = 2$) cascade into two parts as is shown in Table 5.3.2, we see that a pattern is formed at low spin and repeated at high spin. This strongly suggests that the high spin states are formed by coupling the 10^+, $(\nu h^2_{11/2})$ (3574 keV) state with the 2^+, 4^+, and 6^+ states of a $^{(116-2)}$Te core. This gives as the most likely component for the $I = (16)$ (5621 keV) state, the configuration $(\nu h^2_{11/2}, \pi g_{7/2}, \pi d_{5/2})$.

In ^{118}Te, the situation is similar, in that the 6^+ core state appears to be coupled to two neutron configurations, but, in this case, the configurations $\nu(h_{11/2}, 3s_{1/2})$, $\nu(h_{11/2}, 2d_{5/2})$ and $\nu(h_{11/2}, 1g_{7/2})$ appear to be sufficiently low energy to compete with the $\nu(h^2_{11/2})$ configuration. This is seen in Table 5.3.3, where the couplings mentioned above are shown to reproduce the observed spins. Table 5.3.4 shows that after extraction of the core excitation, by considering energy differences, the sysematic behaviour of levels of high spin is approximately similar to that of the two quasineutron levels.

5.3.4 Five Quasiparticle States in ^{117,119}Te

We will consider first for each nucleus those states which have the fewest possible 5qp representations. These include all states of spin $I = {}^{37}/_2$ or ${}^{39}/_2$.

In ^{117}Te, states of each of these spins are observed (at 5890 and 6407 keV respectively, and possibly 5227 keV) and their interpretation will be based on the three quasiparticle nature of the lower spin states. If the interpretation of the ${}^{21}/_2$, 2620 keV level is correct

Table 5.3.3

Coupling of Quasineutrons and Quasiprotons in ^{118}Te

NEUTRONS		⊗ PROTONS		⇒ FINAL SPIN
Configuration	I^π	Configuration	I^π	I^π
$h_{11/2}, s_{1/2}$	5^-	$g_{7/2}, d_{5/2}$	6^+	11^-
$h_{11/2}, d_{5/2}$	7^-	$g_{7/2}, d_{5/2}$	6^+	13^-
$h_{11/2}, g_{7/2}$	9^-	$g_{7/2}, d_{5/2}$	6^+	15^-
$h^2_{11/2}$	10^+	$g_{7/2}, d_{5/2}$	6^+	16^+

Table 5.3.4

Pattern Formed by High and Low Spin Cascades in ^{118}Te

Transition	Energy	Transition	Energy
(16) → (15)	198	$10^+ \rightarrow 9^{(-)}$	-85
15 → 13	400	$9^{(-)} \rightarrow 7^{(-)}$	445
13 → 11	774	$7^{(-)} \rightarrow 5^{(-)}$	849

(§5.3.2). Then the $I = 37/2$ level will have negative parity as is the case for the $\nu(h_{11/2}, 2d_{3/2}, 1g_{7/2})$ configuration. With the orbitals under consideration, there is only one method of coupling five quasiparticles to produce $I^\pi = 37/2^-$, i.e. $\nu(h^3_{11/2}, 1g_{7/2}, 2d_{3/2})$. Such a configuration allows a simple, single neutron transition from this state to a level which has a majority of the above three quasiparticle configuration.

If the level at 6407 keV excitation ($I = (39/2)$) has negative parity, then the configurations $(\nu h^3_{11/2}, \nu g^2_{7/2})$, $(\nu h^3_{11/2}, \nu g_{7/2}, \nu 2d_{5/2})$, $(\nu h^3_{11/2}, \pi g^2_{7/2})$, and $(\nu h^3_{11/2}, \pi g_{7/2}, \pi 2d_{5/2})$ are possible. The first two of these (all neutrons) have four particles in orbits common to the proposed wavefunction of the $I = 37/2$ state. This suggests that these five neutron components will figure strongly in the wavefunction of the state. If, however, the 6407 keV level has positive parity, then the $\nu(h^4_{11/2}, g_{7/2})$, $(\nu h^2_{11/2}, \nu g_{7/2}, \pi g^2_{7/2})$, or the $(\nu h^2_{11/2}, \nu g_{7/2}, \pi g_{7/2}, \pi 2d_{5/2})$

configurations are possible. For similar reasons to before, it is expected that the neutron configuration would be dominant in the wavefunction.

The range of configurations possible for the state at 5227 keV excitation in ^{117}Te is even larger, for neither spin nor parity is determined uniquely. As we have proposed neutron configurations for the states at both higher and lower excitation, the most dominant component in the wavefunction of the state is probably similar. The neutron configurations which can couple towards the possible wavefunctions are presented in Table 5.3.5. It is difficult to refine our choice of preferred configurations, but, if the basis of only allowing one neutron transitions is chosen, then the following configurations would be preferred: $\nu(h^3_{11/2}, d_{5/2}, d_{3/2})$ or $\nu(h^2_{11/2}, g_{7/2}, d_{5/2}, d_{3/2})$ producing $I^\pi = 35/2^-$ or $35/2^+$ respectively. It should be noted that the 6407 keV → 5227 keV transition, which was *not* observed would then require a two-neutron transition.

Table 5.3.5

Possible Configurations of the 5227 keV Level of ^{117}Te

I^π	$37/2^+$	$35/2^-$	$35/2^+$
Configuration	$\nu(h^4_{11/2}, 2d_{5/2})$	$\nu h^5_{11/2}$	$\nu(h^2_{11/2}, g^3_{7/2})$
	$\nu(h^2_{11/2}, g^2_{7/2}, d_{5/2})$	$\nu(h^3_{11/2}, 2d^2_{5/2})$	$\nu(h^2_{11/2}, g_{7/2}, 2d^2_{5/2})$
		$\nu(h^3_{11/2}, 2d_{5/2}, 2d_{3/2})$	$\nu(h^2_{11/2}, g_{7/2}, 2d_{5/2}, 2d_{3/2})$

In ^{119}Te, a state of $I^\pi = 39/2^-$ is observed at (5187 + x) keV excitation. That this state decays by an *E2* transition which is only slightly enhanced (see Chapter 3), is an indication of the pure quasi-particle nature of the wavefunction. The possible configurations were mentioned earlier (for ^{117}Te), but here, it is more probable that proton excitations form part of the wavefunction. This distinction is obtained from the pattern of the decay of the nucleus from this level. It is seen in Fig. 3.6, to decay via the states which have wavefunctions incorporating the $(\nu h^3_{11/2})$ or $(\nu h_{11/2}, \pi g_{7/2}, \pi d_{5/2})$

configurations. A strong proton component of the wavefunctions of all the states in the cascade to the $^{23}/_{2}^{-}$, (2369 + x) keV ($\nu h_{11/2}, \pi g_{7/2}, \pi d_{5/2}$) state would enhance intraband transitions over out-of-band transitions such as possibly those to the positive parity three quasineutron states. This suggests that the configurations ($\nu h^3_{11/2}, \pi g_{7/2}, \pi d_{5/2}$) or ($\nu h^3_{11/2}, \pi g^2_{7/2}$) are most likely to comprise the $^{39}/_{2}^{-}$ level.

The level to which the $^{39}/_{2}^{-}$ level directly decays ($I^{\pi} = {}^{35}/_{2}^{-}$, (4995 + x) keV) could then be a mixture of configurations, including ($\nu h^5_{11/2}$), ($\nu h^3_{11/2}, \nu d^2_{5/2}$), ($\nu h^3_{11/2}, \pi d^2_{5/2}$), and ($\nu h_{11/2}, \nu g_{7/2}, \nu d_{5/2}, \pi g_{7/2}, \pi d_{5/2}$).

5.3.5 Very High Spin States in $^{116-119}$Te

To obtain levels with spin greater than I = 16, I = $^{39}/_{2}$ (for the even and odd nuclei respectively), and still retain four or five quasiparticle configurations, we must consider the excitation of the protons to the higher energy, high spin states, $\pi 1g_{9/2}$ and $\pi 1h_{11/2}$. In all four nuclei studied there are some levels observed at very high excitations that may incorporate such configurations.

The most probable examples occur in ^{119}Te, where we find a large energy gap (of 1382 keV) between the isomeric $^{39}/_{2}^{-}$ state and the next observed level (at 6569 + x keV). Above that, there is the isomeric level at (6677 + x) keV excitation, suggesting pure quasiparticle configurations.

Of the possible configurations from which these states can be constructed, likely five quasiparticle configurations are ($\nu h^3_{11/2}, \pi 2d_{5/2}, \pi g_{9/2}$) for the $^{41}/_{2}$ state, and ($\nu h^3_{11/2}, \pi 2d_{5/2}, \pi h_{11/2}$) for the isomeric state at (6677 + x) keV excitation. Now consider only the proton part of these and the ($\nu h^3_{11/2}, \pi 2d_{5/2}, \pi g_{7/2}$) configurations. The discussion of §5.2.1 suggested a large energy difference between the $\pi g_{7/2}$ and $\pi g_{9/2}$ orbitals. This would be reflected in the energies of relevant two proton configurations. Also, (from Fig. 5.1), the $\pi g_{9/2}$ orbital lies only slightly lower in energy than the $\pi h_{11/2}$ orbital for ^{117}Sb and ^{119}Sb. Using these observations, we can reconstruct the spins and relative energies observed in these five quasiparticle in ^{119}Te, as summarised in Table 5.3.6, by considering a four quasi-particle "set", coupled to different proton quasiparticles. The

Table 5.3.6

Possible Configurations of High Spin States of ^{119}Te and Comparison of Energy Systematics with States in Antimony

	^{119}Te				Average of ^{117}Sb and ^{119}Sb (a)		
Level Energy (b)	I^π Obs	Proposed Configuration	I^π (Conf)	Observed Energy Diff. (b)	Average Energy Diff.	Configuration	Level Energy (b)
5187 + x	$39/2^-$	$(\nu h^3_{11/2}, \pi 2d_{5/2}) \otimes \pi g_{7/2}$	$39/2^-$			$\pi g_{7/2}$	398.5
				1382	667		
6569 + x	$41/2$	$(\nu h^3_{11/2}, \pi 2d_{5/2}) \otimes \pi g_{9/2}$	$41/2^-$			$\pi g_{9/2}$	1065.5
				108	278.5		
6677 + x	-	$(\nu h^3_{11/2}, \pi 2d_{5/2}) \otimes \pi h_{11/2}$	$43/2^+$			$\pi h_{11/2}$	134.4

(a) Average ≡ [(level energy in ^{117}Sb) + (level energy in ^{119}Sb)]/2.

(b) Energies in keV.

"average" of the two Antimony nuclei is used in an attempt to more accurately reflect the situation in ^{119}Te (which can be thought of as an approximate ^{118}Sb core plus a neutron).

Of course, a perfect match of the results within Table 5.3.6 cannot be expected, for many other effects, such as different deformations and particle interactions alter the single particle energies. The matching is, however, good enough to suggest that the proposed configurations play an important role in the wavefunction of the states.

^{118}Te also exhibits a large energy gap above the (proposed) $(\nu h^2_{11/2}, \pi g_{7/2}, \pi d_{5/2})$, 16^+ state before another level is observed (i.e. at 6716 keV and 6742 keV). In this nucleus, though, the two quasi-neutron configuration $\nu(h_{11/2}, g_{7/2})$ has a similar excitation to that of the $\nu(h^2_{11/2})$ configuration. This is also seen in the excitation energy of the proposed (2n + 2p) configurations — see Table 5.3.7. It is then reasonable to expect similar energies to occur when the two neutrons are coupled to other two proton configurations. On this basis, the configurations proposed for the 6742 and 6716 keV states are as shown in Table 5.3.7.

If these levels decay by the act of only a single proton changing orbits (i.e. $1g_{9/2} \rightarrow 1g_{7/2}$), then the observed decay pattern (i.e. 6742, $(17^+) \rightarrow 5545$, (16^+) and 6716, $(16^-) \rightarrow 5347$, (15^-)) is reproduced. In fact it was the observed decay pattern which suggested the different neutron configurations for the 6716 and 6742 keV levels; for otherwise, a decay similar to that of ^{119}Te might be expected. The proposal of a $g_{9/2}$ proton in the configurations of the states is consistent with the relative energies of the proton orbitals averaged over ^{115}Sb and ^{117}Sb.

Unfortunately, there is insufficient evidence to support configuration proposals for the very high spin states of ^{116}Te and ^{117}Te.

5.4 DISCUSSION

Not all of the observed levels have been assigned a quasiparticle configuration, as such an exercise would be impossible with the

Table 5.3.7

Levels of ^{118}Te Involving Proposed $\nu(h_{11/2},g_{7/2})$ or $\nu(h^2_{11/2})$ Configurations

Proposed Configuration	I^{π} Conf	Observed Energy (keV)	Proposed Configuration	I^{π} Conf	Observed Energy (keV)
$\nu(h_{11/2},g_{7/2})$	9^-	3445	$\nu(h^2_{11/2})$	10^+	3360
$\nu(h_{11/2},g_{7/2}),\pi(g_{7/2},2d_{5/2})$	15^-	5347	$\nu(h^2_{11/2}),\pi(g_{7/2},2d_{5/2})$	16^+	5545
$\nu(h_{11/2},g_{7/2}),\pi(g_{9/2},2d_{5/2})$	16^-	6716	$\nu(h^2_{11/2}),\pi(g_{9/2},2d_{5/2})$	17^+	6742

present state of knowledge. The levels for which quasiparticle configurations have been proposed are all states relatively well populated in the (HI,xn) reactions. Nor have we considered the effect of core rotation in contributing to the wavefunction of the high spin states. Coupling of the quasiparticles to collective core excitations does occur, and probably contributes a major part towards the wavefunctions of some states — most likely those lying between the previously assigned three and five quasiparticle states in ^{117}Te and ^{119}Te.

Generally, the quasiparticle assignments have reflected the fact that as the nuclear mass increases (that is, as the $h_{11/2}$ neutron orbital becomes more fully occupied), the energy required to excite one or more particles into the $h_{11/2}$ orbital decreases. They also show that two-proton excitations are found at lower energy in the heavier nuclei. It is slightly confusing in that both these processes are first noticed in the Yrast states at the same mass number, i.e. $A = 119$. This accounts for the marked difference in the level schemes of the two odd nuclei ^{117}Te and ^{119}Te.

The assignments are supported by the observation that the observed decay pattern can be reproduced by assuming the levels decay by only one particle changing orbit, or by two particles coupling to form zero angular momentum. This assumption is reasonable as the transposition of several particles will be less likely to proceed, and hence, observed.

No deformation-aligned rotational bands based on any of the multiple quasiparticle states were found. Now, as most of the observed transitions are of high energy (> 500 keV), this suggests that the deformation of the nuclear core is small in all cases.

The lack of rotational bands and the strong influence of shell effects on level energies is in agreement with the work of Simon *et al.* [Si79]. They determined that core rotation occurs significantly only at spins above approximately 30 $\hbar$ (for neutron deficient Tellurium nuclei). It is interesting to note that this is similar to the spin obtained if *all* $N = 4$ shell orbitals contained unpaired neutrons, i.e. $I = 33$. They also concluded that shell effects played an important role at all spins.

Such core rotational behaviour provides many paths by which a highly excited nucleus can decay. The nucleus is then unlikely to reach the Yrast line until a low spin value is reached. In Tellurium, below spin 30 ħ, there is little competition to the statistical decays (see Chapter 2) and hence the nucleus quickly reaches the Yrast line.

5.5 SUMMARY

The present work has provided level schemes, of four Tellurium nuclei, up to excitation energies of greater than 6.5 MeV. Analysis of the low excited states has provided evidence of single particle excitations in the odd mass nuclei, and collective rotational motion in all nuclei.

By using a variation of the Meyer-ter-Vehn triaxial rotor plus particle model [Me75a], we were able to show the different effects on the shape of the nucleus provided by the excitation of particles to different orbitals. The model was not sufficiently able to completely describe all the low lying levels due both to other deformations occurring and to the effects of multiple quasiparticle excitations. This latter effect was most vividly displayed by the "backbending" plots of §4.2, where large "backbends" were formed at spin 6 ħ in the even mass nuclei. The triaxial rotor model, though, was sufficient to indicate that in the bands based on the $11/2^-$ levels, the deformation was small and the extra neutron was only loosely coupled to the core.

Quasiparticle excitations were shown to play a major role in the structure of many of the excited levels, with said structure determining a level's decay mode.

The effect of a neutron subshell closure at $N = 64$ is reflected in the high spin states of ^{118}Te and ^{119}Te, each of which can be described as a ^{114}Sn core to which are coupled two proton quasiparticles and two or three quasineutrons. The increased stiffness expected in nuclei close to (sub)-shell nuclei affects the energy of the proton excitations such that in ^{117}Te, three quasineutron excitations are more favourable (than 1n - 2p excitations).

In the light of these observations, it is not surprising that no set of Nilsson-model parameters have yet been found to adequately predict the quasiparticle energies. To determine any such parameters, one would need information on the shape of the nucleus in every state for which the model is to be used; an unenviable task.

Any further attempts at analysis of these nuclei should be made with a theory that considers all modes of excitation. One such, is the Interacting Boson Model [Ar76], for even nuclei, and the Interacting Boson-Fermion Model [Ia79] for odd mass nuclei. An extension of these theories to explicitly predict multiple quasi-particle states would also be desirable.

On the experimental side, the observations made here would be supported and enhanced by extension of the knowledge of discrete high spin levels to the heavier and lighter Tellurium nuclei. However, one is limited in the heavier nuclei by the practical limitations of beam, target, and energy considerations. It is highly unlikely that Tellurium nuclei of $A > 122$ can be studied to very high spin.

Formation of the more neutron-deficient Tellurium nuclei in high spin states is possible by (HI,xn) reactions, but proton and alpha evaporation channels will become more populated. To observe "clean" spectra from these reactions may require measurements to be made in anti-coincidence with a charged particle detector.

An experimental difficulty is found in that there are only a few very intense transitions in any of the nuclei studied. Also, many transitions have similar energies. The difficulty in unravelling the experimental results, though great, is rewarded by a more thorough understanding of the nucleon-nucleon interactions in this mass region.

It would also be fruitful to examine the very high spin states of the neutron deficient Xenon nuclei. The study of [Ch81] showed that the nuclei are more deformed than the Tellurium nuclei, giving at the one time, both a greater number of levels before multiple quasi-particle excitations need be considered, and a more stable deformation (on which to base theoretical calculations).

Such a study would complement the present work, giving the ability to compare energies of levels in the direction of both neutron and proton change. This should enable the effects of penetration of the $\nu h_{11/2}$ shell, and proton excitations to be separated.

REFERENCES

[Ar63] Arvieu, R., *Ann. de Phys.* 8 (1963) 407.

[Ar76] Arima, A. and Iachello, F., *Ann. Phys.* 99 (1976) 253.

[Ax61] Axenstein, S., Liljegren, G. and Lindgren, I., *Arkiv für Fysik* 20 (1961) 473.

[Ba74] Barrette, J., Barrette, M., Haroutunran, R., Lamourex, G. and Monaro, S., *Phys. Rev. C* 10 (1974) 1166.

[Ba80] Baglin, C.M., *Nuclear Data Sheets* 30 (1980) 1.

[Be74] Bell, R.A.I., Dept. of Nucl. Phys. Int. Report, ANU-P/606 (1974).

[Bo72] Borsaru, M., Herskind, B., Kalish, R. and Nakai, K., *Proc. of Int. Conf. of Nucl. Moment and Nucl. Structure* (1972).

[Br69] Brinckmann, H.F., Heiser, C. and Hagemann, U., *Nucl. Phys.* A123 (1969) 689.

[Br72] Brinckmann, H.F., Fromm, W.D., Heiser, C., Rotter, H., Clark, D.D., Hansen, N.J.S. and Pedersen, J., *Nucl. Phys.* A193 (1972) 236.

[Br79] Bron, J., Hesselink, W.H.A., Van Poelgeest, A., Zalmstra, J.J.A., Vitzinger, M.J., Verheul, H., Heyelej, K., Waroguier, M., Vincx, H. and Van Isacker, P., *Nucl. Phys.* A318 (1979) 335.

[Ch78] Chowdry, P., Piel, Jr., W.F., Garg, U. and Fossen, D.B., *Abstract B.A.P.S.* 23 (1978) 962.

[Ch81] Chowdhury, P., Garg, V., Sjoreen, T.P. and Fossen, D.B., *Phys. Rev. C* 23 (1981) 733.

[Cl72] Cline, D., *Proc. of Int. Conf. of Nucl. Moment and Nucl. Structure*, Osaka (1972) p.377.

[Da58] Davydov, A.S. and Fillipov, G.F., *Nucl. Phys.* 8 (1958) 237.

[De74] Degrieck, E. and Van Den Berghe, C., *Nucl. Phys.* A231 (1974) 141.

[Di66] Diamond, R.M., Matthias, E., Newton, J.O. and Stephens, F.S., *Phys. Rev. Letters* 16 (1966) 1205.

[Dr77] Dracoulis, G.D., Walker, P.M. and Johnston, A., Dept. of Nucl. Phys. Int. Report, ANU-P/674 (1977).

[Dr80] Dracoulis, G.D., Fahlander, C. and Fewell, M.P., *Phys. Rev. Letters* 45 (1980) 1831.

[Du75] Duffait, R., Charvet, A. and Chery, R., *Z. Phys.* A272 (1975) 315.

[Dz69] Dzhelepov, D.S., Peker, L.K. and Vorobev, V.D., *Izv. Akad. Nauk SSSR (Ser. Fiz.)* 33 (1969) 562.

[Ed52] Edmonds, A.R. and Flowers, B.H., *Proc. Roy. Soc.* A214 (1952) 515.

[El34] Elsasser, W., *J. de Phys. et Rad.* 5 (1934) 625.

[Fe55] Feingold, A.M. and Frankel, S., *Phys. Rev.* 97 (1955) 1025.

[Fe77] Fernandes, M.A.G. and Rao, M.N., *J. Phys. G* 3 (1977) 1397.

[Fa79] Faber, S.R., Young, L.E. and Bernthal, F.M., *Phys. Rev. C* 19 (1979) 720.

[Ga70] Gabrakov, S., Zhelev, Zh., Zaitseva, N.G., Penev, I. and Sabirov, S.S., *Akad. Nauk SSR Bull. Phys. Ser.* 34 (1970) 1825.

[Gn71] Gneuss, G. and Greiner, W., *Nucl. Phys.* A171 (1971) 449.

[Go76] Gowdy, G.M. Xenoulis, A.C., Wood, J.L., Baker, K.R., Fink, R.W., Weil, J.L., Kern, B.D., Hofstetter, K.J., Spejewski, E.H., Mledkodaj, R.L., Carter, H.K., Schmidt-Ott, W.D., Lin, J., Bingham, C.R., Riedlinger, L.L., Zganjar, E.F., Sastry, K.S.R., Raniayya, R.V. and Hamilton, J.M., *Phys. Rev. C* 13 (1976) 1601.

[Gr62] Grodzins, L., *Phys. Letters* 2 (1962) 88.

[Gu67] Gustafson, C., Lamm, I.L., Nilsson, B. and Nilsson, S.G., *Ark. Fys.* 36 (1967) 613.

[Ha68] Hager, R.S. and Seltzer, E.C., *Nuclear Data* A4 (1968) 1.

[Ha74] Habs, D., Klewe-Nebenius, H., Wisshak, K., Löhken, R., Nowicki, G. and Rebel, H., *Z. Physik* 267 (1974) 149.

[Ha79a] Hagemann, U., Keller, H.J., Protochristow, C.L. and Stary, F., *Z. Phys.* A290 (1979) 399.

[Ha79b] Hagemann, U., Keller, H.J., Protochristow, C.L. and Stary, F., *Nucl. Phys.* A329 (1979) 157.

[He76] Heyde, K., Waroquier, M., Vincx, H. and Van Isaker, P., *Phys. Lett.* 64B (1976) 135.

[Ia79] Iachello, F. and Scholten, O., *Phys. Rev. Lett.* 43 (1979) 679.

[Io80] Ionescu-Bujor, M., Iordachescu, A., Ivanov, E.A. and Plostinaru, D., *Phys. Lett.* 90B (1980) 65.

[Is75] Ishii, M., *Nucl. Inst. and Meth.* 127 (1975) 53.

[Jo64] Jolly, R.K., *Phys. Rev. B* 136 (1964) 683.

[Ka63] Kantele, J. and Fink, R.W., *Nucl. Phys.* 43 (1963) 187.

[Ka76] Kamerans, R., Jongsma, H.W., Ketel, T.J., Van der Wey, R. and Verheul, H., *Nucl. Phys.* A266 (1976) 346.

[Ke71] Kerek, A., *Nucl. Phys.* A176 (1971) 466.

[Ke72] Kerek, A., Kownacki, J., Marelius, A. and Phil, J., *Nucl. Phys.* A149 (1972) 64.

[Kl75] Kleinfeld, A.M., Mäggi, G. and Werdecker, D., *Nucl. Phys.* A248 (1975) 342.

[Ko60] Kocker, C., Mitchell, A., Creager, C. and Nainan, T., *Phys. Rev.* 120 (1960) 1348.

[Kr70] Krane, K.S. and Steffan, R.M., *Phys. Rev. C* 2 (1970) 724.

[Ku68] Kumar, K. and Baranger, M., *Nucl. Phys.* A110 (1968) 529.

[La69] Ladenbauer-Bellis, I.M., Bakhru, H. and Luzzati, A., *Phys. Rev.* 187 (1969) 1739.

[La73] Larsson, S.E., *Physica Scripta* 8 (1973) 17.

[La78] Larsson, S.E., Leander, G. and Ragnarsson, I., *Nucl. Phys.* A307(1978) 189.

[Le79] Lederer, C.M. and Shirley, V.S. (eds.), *Table of Isotopes*, 7th ed. (1979).

[Li75] Lien, J.R., Vaagen, J.S. and Grue, A., *Nucl. Phys.* A253 (1975) 165.

[Li77] Lien, J.R., Lunde Nilsen, C., Nilsen, R., Vold, P.B., Graue, A. and Løuhøiden, G., *Can. J. Phys.* 55 (1977) 463.

[Lo70] Lopac, U., *Nucl. Phys.* A155 (1970) 513.

[Lu69] Luukko, A., Kerek, A., Rezanka, I. and Herrlander, C.J., *Nucl. Phys.* A135 (1969) 49.

[Ma49] Mayer, M.G., *Phys. Rev.* 75 (1949) 1969.

[Ma59] Mallmann, C., *Phys. Rev. Lett.* 2 (1959) 507.

[Ma66] Malmsten, G., Nilsson, Ö. and Andersson, I., *Ark. Fys.* 33 (1966) 361.

[Ma68] Mariscotti, M.A.J., Scharff-Goldhaber, G. and Buck, B., *Phys. Rev.* 178 (1968) 1864.

[Ma74a] Der Mateosian, E. and Sunyar, A.W., *Atomic Data and Nuclear Data Tables* 13 (1974) 391.

[Ma74b] Der Mateosian, E. and Sunyar, A.W., *Atomic Data and Nuclear Data Tables* 13 (1974) 407.

[Me75a] Meyer-ter-Vehn, J., *Nucl. Phys.* A249 (1975) 111.

[Me75b] Meyer-ter-Vehn, J., *Nucl. Phys.* A249 (1975) 141.

[Mo63] Morinaga, H. and Gugelot, P.C., *Nucl. Phys.* 46 (1963) 210.

[Mo80] Morrison, I., private communication (1980).

[Ne60] Newton, T.D., *Can. J. Phys.* 38 (1960) 70.

[Ne70] Newton, J.O., Cirilov, S.D., Stephens, F.S. and Diamond, R.M., *Nucl. Phys.* A148 (1970) 593.

[Ne74] Newton, J.O., in *Nuclear Spectroscopy and Reactions, Part C* (J. Cerny, ed.), Academic Press (1974) p.185.

[Ni55] Nilsson, S.G., *Mat. Fys. Medd. Dan. Vid. Selsk.* 29, No. 16 (1955).

[Ni69] Nilsson, S.G., Chin Fu Tsang, Sobiczewski, A., Szymański, Z., Wycech, S., Gustafson, C., Lamm, I.-L., Möller, P. and Nilsson, B., *Nucl. Phys.* A131 (1969) 1.

[Pa65] Pashkevich, V.V. and Sardaryan, R.A., *Nucl. Phys.* 65 (1965) 401.

[Ri70] Riedinger, L.L., Johnson, N.R. and Hamilton, J.H., *Phys. Rev. C* 2 (1970) 2358.

[Ro53] Rose, M.E., *Phys. Rev.* 91 (1953) 610.

[Rø80] Rødland, T., Vaagen, J.S. and Lien, J.R., *Nucl. Phys.* A338 (1980) 13.

[Sa74] Sakai, M., *Izv. Akad. Nauk Fiz.* 38 (1974) 758.

[Sa79] Satem Vasconcelos, S., Rao, M.N., Veta, N. and Appoloni, C.R., *Nucl. Phys.* A313 (1979) 333.

[Sa80] Satpathy, L., Ansari, A., Sahu, R. and Satpathy, M., *Proc. of Int. Conf. on Nucl. Phys.*, Berkeley Abstracts (1980) p.350.

[Sc68] Scharff-Goldhaber, G. and Goldhaber, A.S., *Phys. Rev. Lett.* 24 (1968) 1349.

[Sc74] Scharff, G. and Goldhaber, M., *J. Phys. A* 7 (1974) L121.

[Sc76] Scharff-Goldhaber, G., Dover, C.B. and Goodman, A.L., *Ann. Rev. Nucl. Sci.* 26 (1976) 239.

[Se64] Segré, E., *Nuclei and Particles*, W.A. Benjamin, Inc. (1964), New York.

[Se68] Sergolle, H., *Comp. Rend.* B266 (1968) 633.

[Se69] Sergolle, H., Albouy, G., Lagrange, J.M., Pautrat, M. and Horenbeeck, J.U., *Comp. Rend.* B283 (1969) 701.

[Se70] Sen, S. and Sinha, B.K., *Nucl. Phys.* A157 (1970) 497.

[Si64] Sikkeland, T., *Ark. Fys.* 36 (1964) 539.

[Si65] Siegbahn, H., *Alpha, Beta and Gamma-Ray Spectroscopy*, North-Holland Publ. Co. (1965).

[Si79] Simon, R.S., Diamond, R.M., El Masri, Y., Newton, J.O., Sawa, P. and Stephens, F.S., *Nucl. Phys.* A313 (1979) 209.

[Sh62] De Shalit, A., *Phys. Rev.* 122 (1962) 1530.

[Sh53] De Shalit, A. and Goldhaber, M., *Phys. Rev.* 92 (1953) 1211.

[Sh79] Shroy, R.E., Gaigalas, A.K., Schatz, G. and Fossan, D.B., *Phys. Rev. C* 19 (1979) 1324.

[Sp69] Spejewski, E.H., Hopke, P.K. and Loeser, Jr., F.W., *Phys. Rev.* 186 (1969) 1270.

[Sp70] Spejewski, E.H., Hopke, P.K. and Loeser, Jr., F.W., *Nucl. Phys.* A146 (1970) 182.

[St75] Stephens, F.S., *Rev. Mod. Phys.* 47 (1975) 43.

[Va71] Van den Berghe, G. and Heyde, K., *Nucl. Phys.* A163 (1971) 478.

[Va72] Vajda, S., Iordăchescu, A., Ivanov, E. and Pascovici, G., *Phys. Lett.* 42B (1972) 54.

[Va77] Van Isaker, P., Waroquier, M., Vincx, H. and Heyde, K., *Nucl. Phys.* A292 (1977) 125.

[Vi78] Vieu, Ch., Larsson, S.E., Leander, G., Ragnarsson, I., De Wieclawik, W. and Dionisio, J.S., *J. Phys. G* 4 (1978) 1159.

[Wa70] Warner, R.A. and Draper, J.E., *Phys. Rev. C* 1 (1970) 1069.

[Wa76] Walters, W.B. and Mayer, R.A., *Phys. Rev. C* 14 (1976) 1925.

[Wi56] Wilets, J. and Jean, M., *Phys. Rev.* 102 (1956) 788.

[Wy73] Wyckoff, W.G. and Draper, J.E., *Phys. Rev. C* 8 (1973) 796.

[Ya67] Yamazaki, T., *Nuclear Data A* 13 (1976) 1.